Functional renormalization group beyond the perturbative regime

Dissertation

der Mathematisch-Naturwissenschaftlichen Fakultät
der Eberhard Karls Universität Tübingen
zur Erlangung des Grades eines
Doktors der Naturwissenschaften
(Dr. rer. nat.)

vorgelegt von
MSc Nils Wentzell
aus Essen

Tübingen
2016

Gedruckt mit Genehmigung der Mathematisch-Naturwissenschaftlichen Fakultät der
Eberhard Karls Universität Tübingen.

Tag der mündlichen Qualifikation:	7.9.2016
Dekan:	Prof. Dr. Wolfgang Rosenstiel
1. Berichterstatter:	Prof. Dr. Sabine Andergassen
2. Berichterstatter:	Prof. Dr. Alessandro Toschi
3. Berichterstatter:	Assistant Professor Adolfo Avella

Abstract

This thesis aims at developing new schemes for the treatment of correlation effects in condensed matter systems using quantum field theoretical approaches. In particular, our goal is to extend the description of correlation physics at the two-particle level. This is necessary for an unbiased treatment of condensed matter systems that exhibit electronic correlations and competing ordering tendencies. In this respect, the functional renormalization group (fRG) approaches have surely contributed substantially over the last years, as they account for all scattering channels and their mutual feedback effects in an unbiased way. In spite of its flexibility, the application of the fRG is limited by its inherent perturbative nature. To go beyond the conventional weak-coupling implementations, we discuss the general idea to extend fRG based computational schemes by using an exactly solvable interacting reference problem as starting point for the RG flow. The systematic expansion around this solution accounts for a non-perturbative inclusion of correlations at both, the one-particle (self-energy) and two-particle (vertex functions) level. The full treatment of the two-particle vertex functions, however, poses a huge limitation to the numerical performance, not only in the fRG, but in several forefront many-body algorithms. In this perspective, we provide a detailed diagrammatic analysis of the frequency and momentum structures of the vertex functions, together with their physical interpretation. This constitutes the basis for sophisticated parametrization schemes. We then explain the technical details necessary for cutting-edge numerical implementations, and further benchmark our ideas using refined implementations of both, the fRG and the parquet approximation (PA).

Zusammenfassung

Diese Doktorarbeit beschäftigt sich mit der Entwicklung neuer Ansätze für die Behandlung von Korrelationseffekten in Materialien. Mit Hilfe quantenfeldtheoretischer Methoden steht dabei besonders die korrekte Berücksichtigung von zwei-Teilchen Streuprozessen im Vordergrund, die für die Beschreibung konkurrierender Instabilitäten essenziell ist. Zu deren Verständnis hat die funktionale Renormierungsgruppe (fRG), die die verschiedenen Streukanäle sowie deren Wechselspiel gleichermaßen beinhaltet, in den letzten Jahren wesentlich beigetragen. Trotz der hohen Flexibilität in der Anwendung weist die fRG als perturbative Methode aber Einschränkungen auf. Wir stellen hier einen allgemeinen Ansatz für eine Erweiterung über das Regime schwacher Kopplung hinaus vor, in dem ein exakt lösbares Referenzsystems als Startpunkt für den Renormierungsgruppenfluss verwendet wird. Die systematische Entwicklung um diese Lösung ermöglicht es Korrelationseffekte sowohl auf dem ein-Teilchen (Selbstenergie) als auch auf dem zwei-Teilchen Niveau (Vertex-Funktionen) nicht-perturbativ einzubeziehen. Die numerische Handhabung von zwei-Teilchen Vertex-Funktionen stellt jedoch für die fRG wie auch für zahlreiche andere moderne Vielteilchenmethoden eine große Herausforderung dar. In dieser Arbeit präsentieren wir eine umfassende diagrammatische Analyse der Frequenz- und Impulsstrukturen der Vertex-Funktionen sowie deren physikalische Interpretation. Die daraus gewonnen neuen Einsichten bilden die Grundlage für die Entwicklung effizienterer Parametrisierungen. Wir diskutieren die technischen Details der numerischen Implementierung und testen diese am Beispiel der fRG und der parquet Näherung (PA).

List of publications

I N. Wentzell, S. Florens, T. Meng, V. Meden, and S. Andergassen
Magneto-electric spectroscopy of Andreev bound states in Josephson quantum dots
Phys. Rev. B **94**, 085151 (2016)

II N. Wentzell, C. Taranto, A. Katanin, A. Toschi, and S. Andergassen
Correlated starting points for the functional renormalization group
Phys. Rev. B **91**, 045120 (2015)

III G. Li, N. Wentzell, P. Pudleiner, P. Thunström, and K. Held
Efficient implementation of the parquet equations: Role of the reducible vertex function and its kernel approximation
Phys. Rev. B **93**, 165103 (2016)

IV N. Wentzell, G. Li, A. Tagliavini, C. Taranto, G. Rohringer, K. Held, A. Toschi, and S. Andergassen
High-frequency asymptotics of the vertex function: diagrammatic parametrization and algorithmic implementation
in preparation

Contents

Introduction 11

1 Introduction & Motivation 13
- 1.1 Andreev bound states in Josephson quantum dots . . . 14
- 1.2 fRG beyond the perturbative regime . . . 15
- 1.3 Towards an efficient treatment of two-particle quantities . . . 16

2 Structure 19

High-frequency asymptotics of the vertex function: diagrammatic parametrization & algorithmic implementation 21

3 Diagrammatic formalism at the two-particle level 23

4 Parametrization of the vertex asymptotics 27

5 Implementation 31
- 5.1 Decomposing the atomic limit vertex . . . 33
- 5.2 Implementation for the fRG solver . . . 36
- 5.3 Implementation for the parquet approximation . . . 39

6 Comparison to exact results of the SIAM 41
- 6.1 Neglecting the asymptotics . . . 45
- 6.2 Higher order corrections in fRG . . . 46
- 6.3 Efficiency of simplified parametrization schemes . . . 47

7 Conclusion 49

Appendix 51

A Notations 53

B An alternative approach to the asymptotic extraction 57

C Symmetries **61**
C.1 Symmetries of $\mathcal{K}_1$ and $\mathcal{K}_2$ 61
C.2 Symmetries of $\mathcal{R}$ 63

Supplements **65**

Personal contribution to publications **67**

I Magneto-electric spectroscopy of Andreev bound states in Josephson quantum dots **69**

II Correlated starting points for the functional renormalization group **85**

III Efficient implementation of the parquet equations: role of the reducible vertex function and its kernel approximation **97**

Bibliography **111**

Acknowledgments **125**

Introduction

Chapter 1

Introduction & Motivation

Electronic correlations give rise to a wealth of interesting physics in condensed matter systems, ranging from the Mott metal-insulator transitions [1] over high-temperature superconductivity [2,3] to the variety of novel phenomena observed in optical lattices [4]. The physics of these systems is typically governed by many different energy scales. Some of them are intrinsic, like the microscopic Coulomb interaction U and kinetic energy t, but the most exciting phenomena of correlated systems are also influenced by emergent energy scales like the magnetic exchange interaction J, transition temperatures T_c, the superfluid stiffness, etc. that are based upon the presence of electronic correlations. These energy scales can easily span, on the whole, multiple orders of magnitudes, and their correct description as well as the proper treatment of their mutual feedback poses one of the most challenging tasks in the field of contemporary condensed matter theory. What makes the theoretical treatment so hard (and likely the related phenomena so interesting) is the impossibility of performing a plain mean-field or low order perturbation expansion. In this respect, the renormalization group (RG) approaches have surely played a substantial role over the last decades. Historically, their first applications in the field of condensed matter were focused on scale invariant systems, as e.g. in the block-spin approaches [6], and they have since contributed significantly to the description of critical phenomena and phase transitions in classical as well as quantum systems. The main concept behind the RG approaches is, in fact, a scale ordered treatment of all degrees of freedom. This ordering allows to successively integrate out the degrees of freedom beginning from one end of the scale, e.g. high energies, to devise an effective theory for the remaining scales,

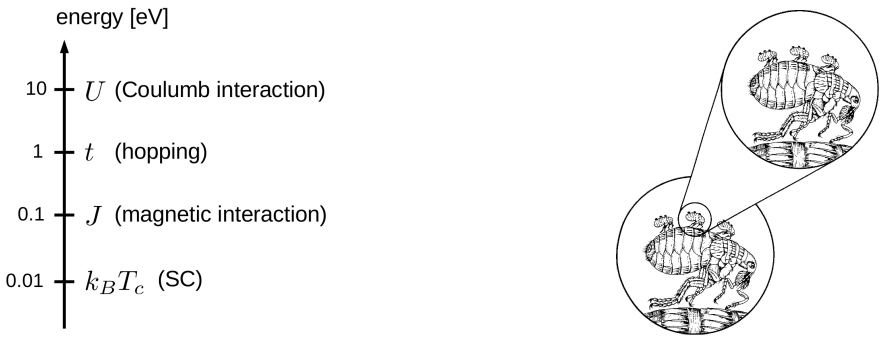

Figure 1.1.: Schematic illustration of the different energy scales (left) and the scale invariance (right) [5].

e.g. the low-energy degrees of freedom. Extending these ideas to a more general field theoretical frame has lead to the well-known Wetterich equation [7], which allows to apply the RG-based concept to a large variety of quantum many-body problems. In particular, the Wetterich equation is an exact reformulation of the physical problem at hand by means of a functional flow equation for the generating functional of the one-particle irreducible (1PI) vertex functions, also referred to as "effective action". An expansion in orders of the fields yields an infinite hierarchy of flow equations for the 1PI vertex functions, which is the basis of the functional renormalization group (fRG) [8–17] approach. The latter is a very flexible and unbiased tool for the treatment of correlated fermion systems, and has been applied in a variety of different systems for analyzing e.g. competing instabilities, spontaneous symmetry breaking, quantum criticality and correlation effects in quantum wires and quantum dots. As a showcase, I will briefly outline in the following an application of the fRG to a so-called Josephson quantum dot, as it was described in the manuscript presented in Supp. I.

1.1 Andreev bound states in Josephson quantum dots

Quantum dots coupled to superconducting leads have been an active research topic in recent years, both in theory [18–75] and experiments [76–110] , motivated to a large extent by their potential use as quantum information devices [111]. They can be modeled theoretically by a single atomic site[1] with an on-site energy ϵ and a local Coulomb repulsion U, that is coupled to one or two superconducting leads of BCS type, with superconducting gap Δ and phases φ_1 and φ_2 respectively. Such a setup is illustrated in the left panel of Fig. 1.2. The proximity effect will then lead to a gapped local density of states (see right panel of Fig. 1.2) on the atomic site, with discrete in-gap states, the so-called Andreev bound states (ABS). They emerge due to resonant Andreev reflection processes, where an electron is reflected as a hole at the interface to the superconductor, creating a Cooper pair in this process.

These bound states play a crucial role in the Josephson current that is transferred across the quantum dot, even at zero bias voltage, in case of a finite phase difference between the leads. They have been analyzed extensively [18, 19, 24, 27, 30, 33, 34, 38, 40, 41, 44, 47, 49, 51, 53, 54, 56, 58, 60–62, 65–67, 69, 70, 72–74, 80, 84, 91, 96, 102–107, 109, 110], while a full theoretical analysis in presence

[1] Assuming sufficiently low temperature and large level spacing.

Figure 1.2.: The left panel shows an illustration of a single atomic site with energy ϵ and local Coulomb repulsion U, tunnel coupled (vertical bars) to two superconducting leads with gap Δ and phases φ_1 and φ_2 respectively. The gapped density of states with the discrete ABS is depicted on the right.

of both a local magnetic field and a finite Coulomb interaction was still missing. Both parameters can induce a quantum phase transition in the Josephson quantum dot from a non-magnetic singlet ground-state, typically denoted as 0-phase, to a ground state with a localized magnetic moment, the so-called π-phase. This phase-transition induces a sign-change in the Josephson current, directly connected, in turn, with a shift of spectral weight between the Andreev states.

In our work presented in Supp. I we investigate the ABS by means of two complementary approaches: the static fRG and the self-consistent Andreev bound states (SCABS) theory [54,99,112]. Their flexibility enabled us to study the physical behavior of the ABS for varying on-site energy ϵ, phase-difference φ, superconducting gap Δ, and, in particular, for varying magnetic field B. We further supplement these results by analytical calculations in the large-gap limit.

Overall, we find a good agreement of the results in the range of validity of the two approaches. However, the fRG approach turned out to be problematic concerning the description of Andreev bound states in the π-phase for vanishing magnetic field. In order to improve in this respect, we considered an alternative fRG approach which takes into account the exact solution of the large-gap limit from the very beginning in the flow. This idea triggered the subsequent development of extending the fRG to correlated starting points. In Supp. II we worked out the details of the theoretical framework in a general way, as will be outlined in the following.

1.2 fRG beyond the perturbative regime

In the functional renormalization group approach, the dependence on a scale Λ is introduced into Gaussian part of the system, i.e. the non-interacting propagator $G_0(i\nu) \to G_0^\Lambda(i\nu)$. At the initial scale Λ_{inital} the system should be exactly solvable, such that the initial values of all flowing 1PI vertex functions can be determined, while at the final scale Λ_{final} we should recover the action of the system of interest, i.e. $G_0^{\Lambda_{\text{final}}}(i\nu) = G_0(i\nu)$. This allows for a large freedom, not only in the choice of the initial action, but also in the path, or cutoff-scheme, used for the fRG flow (see left panel of Fig. 1.3). While this choice will not have any effect on the final results as long as the full hierarchy of flow equations for the 1PI vertices is considered, an error with respect to the exact correlation functions ($\mathcal{G}_{\text{full}}$) is introduced during the integration of the flow equations if truncations of the hierarchy are performed (see right panel of Fig. 1.3), as is necessary for numerical implementations. In the conventional fRG schemes, the typical choice is $G_0^{\Lambda_{\text{initial}}}(i\nu) = 0$, such that all 1PI vertex functions are trivially determined by their microscopic bare values. This choice of the initial action freezes propagation at all scales, and does thus not allow for correlation effects. The idea behind the extension to strong coupling is to improve on the choice of the starting point, such that the most correlation effects possible are included from the very beginning in the fRG flow. I.e., one can consider as a starting point an interacting reference system described by an action $\mathcal{S}_R$, that has a close physical connection to the system of interest, but is still exactly solvable. By using this new starting point, one can expect to reduce the error on the final correlation functions induced by the truncation of the hierarchy (red path in right panel of Fig. 1.3). This very idea has recently been implemented in first pioneering studies in the case of correlated electron systems [15, 113, 114] as well as spin-models [115, 116].

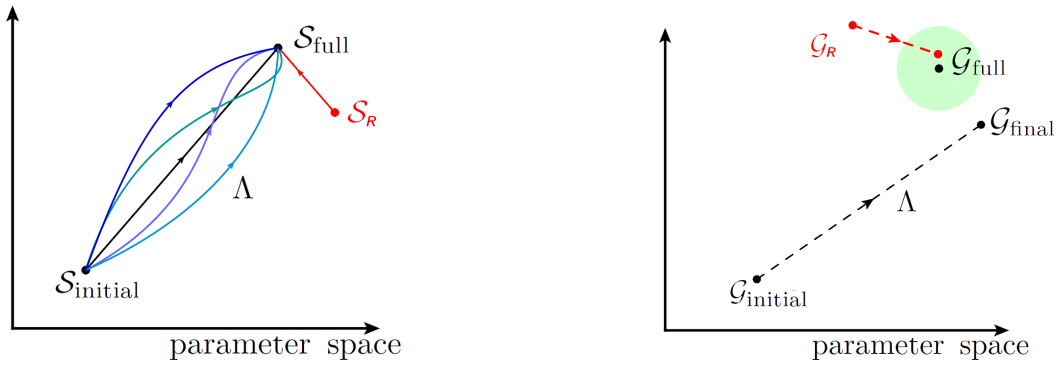

Figure 1.3.: In the fRG, certain choices for the initial action (left) can potentially reduce the truncation error introduced into the correlation functions $\mathcal{G}$ by the flow equations (right). Reproduced from [16].

The concept of setting up a perturbative expansion around the solution of an interacting reference system is not new [117]. By means of a Hubbard-Stratonovich transformation, one can reformulate the physical problem for new auxiliary degrees of freedom that include the exact reference system solution already in their quadratic part. Further, their free propagator contains a new small parameter, that is, the difference between the physical and the reference system $\Delta = g^{-1} - g_R^{-1}$, partially justifying perturbative series even for larger values of the interaction. This idea has found extensive use in the dual fermion [16, 118–127] approaches, where an effective impurity model determined by means of dynamical mean-field theory (DMFT) [128–131] is assumed as a reference system for correlated electrons on a lattice. However, while the dual fermion approaches perform perturbative or ladder expansions for these auxiliary degrees of freedom, we propose in Supp. II to use the fRG to solve the auxiliary problem. Further, we could establish a precise connection to the fRG approaches that, as described in the previous paragraph, also choose a correlated starting point, while working directly with the physical degrees of freedom (e.g. the DMF^{2}RG [15]).

As for the practical implementation of these non-perturbative schemes in the common truncation at the two-particle level, it is not sufficient to consider as a starting point of the fRG flow only the one-particle quantities of the reference system. The two-particle vertex function of the interacting reference system will also enter into the fRG calculation from the very beginning, and its renormalization must be considered during the flow.

1.3 Towards an efficient treatment of two-particle quantities

The considerations at the end of the previous section lead us to the topic presented in the main part of this thesis, that is, the correct treatment of two-particle quantities and their high-frequency asymptotics in particular. A two-particle vertex function $F(\xi_1, \xi_2, \xi_3, \xi_4)$, in its most general form, is a function of four composite indices ξ_i, where $\xi = (i\nu, \mathbf{k}, \sigma, s)$ is a composite index with Matsubara frequency $i\nu$, momentum $\mathbf{k}$, spin σ and orbital quantum number s. Even in the case of an $SU(2)$ symmetric single-band lattice model like the Hubbard model, this vertex function has $N_\nu^3 \times N_\mathbf{k}^3$ components, where N_ν denotes the number of Matsubara frequencies considered and $N_\mathbf{k}$ is the number of discretization points considered to parametrize the Brillouin zone. If one assumes

e.g. $N_\nu = N_\mathbf{k} = 50$ with 16 bytes of memory for every vertex value, a stunning 320GB is already required to store a single momentum-dependent two-particle vertex! It is thus very obvious that the limits of current as well as future computing resources will be quickly exhausted by a plain algorithmic treatment of two-particle quantities. For this reason it is essential to gain a deeper understanding of their frequency and momentum structures [132, 133], such that efficient, and physically guided, parametrization schemes can be devised. In particular, effort should be made to simplify the problem, wherever this does not entail an appreciable loss of information.

For the numerical treatment of two-particle quantities, an approximation widely used in state of the art fRG implementations decomposes the full vertex F into a sum of three terms [134] (in the frequency domain),

$$F(\nu_1, \nu_2, \nu_3) \approx U + K_{\mathrm{eff},pp}^{\Omega_{pp}=\nu_1+\nu_3} + K_{\mathrm{eff},ph}^{\Omega_{ph}=\nu_2-\nu_1} + K_{\mathrm{eff},\overline{ph}}^{\Omega_{\overline{ph}}=\nu_3-\nu_2}, \tag{1.3.1}$$

each of them depending on a single bosonic *transfer* frequency Ω. This approximation holds in the weak-coupling regime, and can be motivated by perturbation theory arguments under consideration of the so-called parquet equation [135, 136]

$$F = \Lambda_{2\mathrm{PI}} + \Phi_{pp} + \Phi_{ph} + \Phi_{\overline{ph}}. \tag{1.3.2}$$

This equation is depicted numerically in Fig. 1.4 for the purely local case of a SIAM, as explicitly discussed in Chap. 6 of this thesis. The parquet equation decomposes the full 1PI two-particle vertex by classifying its scattering diagrams according to the level of two-particle reducibility. The first term, the so-called fully irreducible vertex function $\Lambda_{2\mathrm{PI}}$, contains all scattering diagrams that are two-particle irreducible (2PI), i.e., that cannot be separated into two parts by cutting two internal propagator lines. This holds trivially for the diagram containing only the bare interaction, while the next leading order diagram scales already as U^4 (see also Fig. 1.4 for the leading order diagrams). The remaining terms of the parquet equation are referred to as the reducible vertex functions Φ, and contain all the diagrams that are two-particle *reducible*. This class can be further divided into the three scattering channels, particle-particle (pp), particle-hole (ph) and transverse particle-hole ($\overline{ph}$), depending on which of the external indices remain connected after the cut[2]. Their leading order diagrams, as depicted in the upper row of Fig. 1.4, contain the particle-particle as well as the particle-hole bubbles, and are of leading order U^2 or U^3. These lowest order diagrams, due to their structure, do not depend on all of the external arguments, but rather on a single transfer frequency. If one approximates the fully irreducible vertex by its lowest order contribution, i.e. $\Lambda_{2\mathrm{PI}} \approx U$, and considers the leading order contributions for the remaining terms, one finds that the approximation presented in Eq. (1.3.1) holds.

The idea of identifying scattering contributions that exhibit a reduced dependence on the external arguments of the scattering process plays an essential role in identifying the high-frequency structures of the two-particle vertex functions, and is developed into a sophisticated diagrammatic vertex

[2] Note that reducibility is always channel-exclusive.

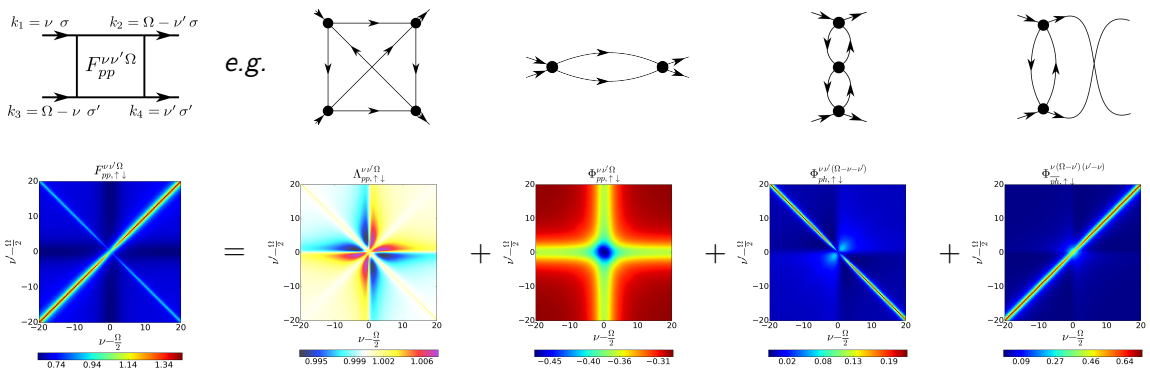

Figure 1.4.: The bottom row depicts the parquet equation (1.3.2) numerically for the SIAM described in Chap. 6 for $U = 1$ and $\beta = 20$ using the *pp*-notation for zero transfer frequency ($\Omega = 0$). The upper row shows the lowest order diagrams (excluding the bare interaction) included in the contributions from the different vertex functions (notations according to App. A). In the diagrammatic representations used throughout this thesis, all external propagators (legs) are excluded.

decomposition scheme in Chap. 4 of this thesis. This deepened understanding of the two-particle vertex has allowed us to reduce the numerical costs of a full treatment, while at the same time posing the basis for advanced vertex parametrization schemes. We have implemented these ideas in a first numerical study in Supp. III, and the corresponding numerical implementation techniques are extended thoroughly in Chap. 5 of this thesis.

We want to stress that these insights (and the related algorithmic improvements) are not only of benefit to the fRG, but are crucial for performant applications of all many-body approaches based on two-particle vertex functions, like the dynamical vertex approximation (DΓA) [121, 131, 137–140] and the dual fermion approaches [16, 118–127, 141], which are diagrammatic extensions of DMFT [15, 122, 137, 141–148], as well as numerical calculations that solve directly the parquet equations [149–165]. In this perspective, the concepts and the results presented in the central part of this thesis pave a definite route towards an efficient treatment of *both* spatial and temporal electronic correlations *beyond* the one-particle level. Because of its impact on cutting-edge method developments and on the predictive power of the theory, this represents, in fact, one of the most important challenges for the quantum many-body physics of the forthcoming years.

Chapter 2

Structure

Let us briefly outline the structure and content of this thesis. In Chap. 1 we set the stage by giving a general introduction, focusing in particular on renormalization group approaches for condensed matter theory. We further introduce our published manuscripts, beginning with Supp. I, that is, an exemplary application of the fRG approach to a so-called Josephson quantum dot. The work presented in Supp. II, on the other hand, discusses recent ideas to extend conventional fRG approaches to the regime of stronger couplings by using correlated starting points, and elaborates on their generalization. In this respect, the correct description of two-particle quantities and their high-frequency asymptotics plays an essential role. This topic is discussed thoroughly in the main part of this thesis, which is the basis of a forthcoming joint publication [166], and is also addressed in a numerical study of the parquet equations in Supp. III.

The main part of this thesis begins with a summary of the diagrammatic formalism at the two-particle level in Chap. 3, to then proceed in Chap. 4 with the discussion of a general two-particle vertex decomposition scheme, that, based solely on diagrammatic arguments, allows for an efficient parametrization of the high-frequency asymptotics. In the following Chap. 5 we discuss the practical implementation of these ideas in numerical and analytical calculations, considering as examples the atomic limit vertex (Sec. 5.1), and numerical implementations of the fRG (Sec. 5.2) and the parquet approximation (Sec. 5.3). We check the validity of our implementation schemes in Chap. 6, by comparing the results we obtain for a SIAM against the exact solution of the exact diagonalization (ED). In order to check the correct description of two-particle quantities, we focus first on the weak-coupling regime, where fRG and PA, being perturbative approaches, are expected to perform well. After having shown that our implementations correctly take into account all high frequency asymptotics, we address the inherent limitations of fRG and PA in the regime of stronger coupling. In particular, we demonstrate the importance of a correct numerical treatment of two-particle quantities in Sec. 6.1, and conclude our discussions by considering the effect of fRG corrections and common simplified parametrization schemes in Sec. 6.2 and Sec. 6.3 respectively. We then summarize our findings in Chap. 7, and give a brief outlook.

In App. A we present details on the notations utilized throughout this thesis. Further, we elaborate in App. B on an alternative numerical approach to extract vertex asymptotics directly from the full one-particle irreducible vertex function. Finally, we summarize the symmetries of the newly

introduced asymptotic and vertex functions in App. C.

High-frequency asymptotics of the vertex function: diagrammatic parametrization & algorithmic implementation

Chapter 3

Diagrammatic formalism at the two-particle level

In this chapter we present a concise summary of the general formalism for two-particle vertex functions. In particular, we recall how their high-frequency asymptotic behavior can be qualitatively related to the lowest-order perturbation theory diagrams. While a comprehensive investigation of the corresponding physical interpretation can be found in Chap. 4 and in Refs. [132, 167], we focus here mainly on aspects which are relevant for the algorithmic development and the applications presented in this thesis.

Although most of the following considerations are valid for a wide range of many-body Hamiltonians, we will restrict ourselves, for the sake of notational simplicity, to one-band systems with a local Coulomb interaction. Specifically, we consider the following Hamiltonian:

$$\hat{\mathcal{H}} = \sum_{ij,\sigma} t_{ij}(\hat{c}^{\dagger}_{i\sigma}\hat{c}_{j\sigma} + \hat{c}^{\dagger}_{j\sigma}\hat{c}_{i\sigma}) + \sum_{i} U_i \hat{n}_{\uparrow}\hat{n}_{\downarrow}, \tag{3.1}$$

where $\hat{c}^{(\dagger)}_{i\sigma}$ annihilates (creates) an electron with spin σ at the lattice site $\mathbf{R}_i$ and $\hat{n}_{i\sigma} = \hat{c}^{\dagger}_{i\sigma}\hat{c}_{i\sigma}$. t_{ij} denotes the hopping amplitude for an electron between the lattice sites i and j (for $i = j$ this corresponds to setting the energy-level for an electron at site i). U_i is a (site-dependent) local interaction between electrons of opposite spin.

From the Hamiltonian in Eq. (3.1) one retains the standard Hubbard model by choosing the parameters $t_{ij} = -t$ if i and j are nearest neighbors and $t_{ij} = 0$ otherwise, and $U_i = U$ (site independent). The restriction $t_{ij} = V_j\delta_{i0}$, $t_{ii} = \varepsilon_i$ and $U_i = U\delta_{i0}$, on the other hand, corresponds to the SIAM, where lattice site $\mathbf{R}_0$ is the impurity.

In the following we will consider the two-particle Green's function for the model in Eq. (3.1), where for the SIAM we will restrict ourselves to the corresponding (purely local) correlation functions at the impurity site. Considering the time -and for the Hubbard model also space- translational invariance of the system, we can work more conveniently in frequency (and momentum) space. To this end, we will adopt both for the SIAM and the Hubbard model the following generalized notation for the frequency and momentum arguments of the Green's functions: k denotes a generalized fermionic, q a generalized bosonic index. For the Hubbard model, this corresponds to the four-vector notation $k = (\nu, \mathbf{k})$ and $q = (\Omega, \mathbf{q})$, where ν is a fermionic and Ω a bosonic Matsubara frequency and $\mathbf{k}$ and $\mathbf{q}$ are momenta in the first Brillouin zone. For the case of the SIAM, k and q correspond simply to

the fermionic and bosonic Matsubara frequencies ν and Ω, respectively.

The general definition of the two-particle Green's function G_2 is given explicitly in App. A, alongside the general relation between the two-particle Green's functions and the corresponding irreducible (1PI) vertex function, i.e., the (full) vertex F. The latter is obtained from G_2 by first removing all unconnected parts, and by subsequently amputating all outer legs [132, 145, 168]. From a physical perspective, F represents the quasi-particle scattering rate between particles and holes (in parameter regimes where such excitations are well-defined [169]). Diagrammatically, F consists of all connected two-particle diagrams, i.e., all (connected) Feynman diagrams with *two incoming* and *two outgoing* lines (see leftmost diagram in Fig. 1.4).

As described in Chap. 1, the full two-particle vertex F can be decomposed into *four* distinct classes of diagrams, that differ in their two-particle irreducibility. This decomposition is summarized in the so-called parquet equation (1.3.2), where F is split into the fully irreducible vertex Λ, and the three reducible vertex functions Φ_{pp}, Φ_{ph} and $\Phi_{\overline{ph}}$. In the lower panels of Fig. 1.4, such a decomposition is illustrated for an actual case (namely the SIAM, see discussion in Chap. 6), by means of the results of our numerical calculations. All quantities are presented in the *pp*-notation[1] for a fixed bosonic transfer frequency $\Omega = 0$, as functions of the fermionic frequency arguments ν and ν' (compare App. A). While we restrict ourselves here to the $\uparrow\downarrow$ spin combination, we stress that analogous features are observed when decomposing $F_{\uparrow\uparrow}$.

Investigating the full vertex $F^{\nu\nu'(\Omega=0)}_{pp,\uparrow\downarrow}$ (leftmost panel) we can identify three main features [132]: (i) There is a constant background *different* from the (constant) bare Coulomb interaction U. (ii) We observe two diagonal structures which we will refer to as main (for $\nu = \nu'$) and secondary (for $\nu = -\nu'$) diagonal. (iii) $F^{\nu\nu'(\Omega=0)}_{pp,\uparrow\downarrow}$ exhibits also a "plus"-like structure, i.e., an enhanced scattering rate along the lines $\nu = \pm\pi/\beta$ and $\nu' = \pm\pi/\beta$. Remarkably, these features do *not* decay, even in the limit of large fermionic frequencies and give, hence, rise to a highly non-trivial asymptotic behavior of the vertex functions. In order to explain their origin, we will analyze in the following the frequency structures of the four building blocks of F. Our strategy will be guided by the comprehension of the frequency behavior of the lowest order perturbation diagrams for each of these sub-parts.

As for the fully irreducible vertex $\Lambda^{\nu\nu'(\Omega=0)}_{\mathrm{2PI},pp,\uparrow\downarrow}$, we can see that it decays uniformly in all directions of the two-dimensional (Matsubara) frequency space. Hence, $\Lambda^{\nu\nu'(\Omega=0)}_{\uparrow\downarrow}$ does not contribute to the asymptotic structures of the two-particle scattering amplitude $F^{\nu\nu'(\Omega=0)}_{\uparrow\downarrow}$ (except for the trivial constant background given by the interaction U). Beyond its numerical observation, this asymptotic behavior of Λ can be also justified through the analysis of its diagrammatic structure, exemplified by the "envelope"-diagram (second diagram from the left in Fig. 1.4). As discussed in detail in Ref. [132], Λ does indeed depend explicitly on ν and ν' (and Ω) and, hence, it decays in all frequency directions[2].

[1] Note that Φ_{ph} and $\Phi_{\overline{ph}}$ were explicitly translated from their respective natural mixed notation to the one of the *pp*-channel.

[2] Every frequency dependence of a diagram originates from the frequency dependence of the corresponding Green's functions. The latter decay in the asymptotic high frequency regime as $1/i\nu$.

Figure 3.1.: The so called "eye"-diagrams in the particle-particle channel.

Turning to the diagrams reducible in the particle-particle scattering channel, i.e., $\Phi_{pp,\uparrow\downarrow}^{\nu\nu'(\Omega=0)}$ (third panel in Fig. 1.4), they exhibit *two* of the three asymptotic frequency structures of $F_{pp,\uparrow\downarrow}^{\nu\nu'(\Omega=0)}$. Specifically, one can identify a constant background and a well-defined "plus"-structure. The background can be immediately understood by analyzing the second order diagram depicted above the plot of $\Phi_{pp,\uparrow\downarrow}$. This is given by the bubble-term

$$\frac{U^2}{\beta}\sum_{\nu_1} G(\nu_1)G(\Omega-\nu_1), \tag{3.2}$$

which -evidently- does not depend explicitly on ν and ν'. Hence, bubble diagrams of this type are responsible for the constant background observed in the particle-particle reducible vertex, and, consequently, in the full vertex F. The "plus"-structure, on the other hand, originates, in lowest order, from the so-called "eye"-diagrams (see Fig. 3.1), which either on their left or on their right hand side collapse into a bare vertex U. For this reason (as detailed in Chap. 4), they cannot explicitly depend on both ν and ν', thus remaining constant upon increasing the corresponding (unnecessary) frequency [132].

Let us now consider the vertex function reducible in the particle-hole (longitudinal) channel, i.e., $\Phi_{ph,\uparrow\downarrow}^{\nu\nu'(\Omega=0)}$ (fourth density plot from the left in Fig. 1.4). One can clearly see that this vertex exhibits a secondary diagonal structure along $\nu' = -\nu$. Again, we can gain insight about the origin of this feature by analyzing the lowest order perturbative diagram. For the $\uparrow\downarrow$-channel considered here, this is of third order in U, as the bare bubble term vanishes. It is given by the fourth diagram (from the left) in Fig. 1.4, and reads

$$\frac{U^3}{\beta^2}\left[\sum_{\nu_1} G(\nu_1)G(\nu_1+\nu+\nu')\right]^2, \tag{3.3}$$

i.e., it depends only on the bosonic frequency $\nu+\nu'$ rather than the two fermionic frequencies ν and ν' separately. Consequently, its value remains constant along a line $\nu+\nu' = \text{const}$ and, thus, generates the secondary diagonal structure.

Finally, we turn our attention to the vertex reducible in the transverse particle-hole channel, $\Phi_{\overline{ph},\uparrow\downarrow}^{\nu\nu'(\Omega=0)}$. Obviously, it accounts for the main diagonal in the full scattering amplitude $F_{pp,\uparrow\downarrow}^{\nu\nu'(\Omega=0)}$. Once again, the analysis of its lowest order (bubble) contribution allows for an intuitive explanation

of this feature. It is given by the last diagram in Fig. 1.4, which reads explicitly

$$\frac{U^2}{\beta}\sum_{\nu_1} G(\nu_1)G(\nu_1+\nu'-\nu), \tag{3.4}$$

and depends only on the bosonic frequency $\nu'-\nu$. Consequently, its value remains constant along a line $\nu'-\nu=$ const and, hence, generates the main diagonal structure.

The above analysis demonstrates that the high-frequency asymptotic features of the vertex functions in the weak coupling regime are determined at the second and third order in U by two-particle reducible bubble- and "eye"-like diagrams. A generalization of these conclusions to the non-perturbative regime will be discussed in the following Chapter.

Chapter 4

Parametrization of the vertex asymptotics

In the following, we will generalize the discussion of the previous chapter about the main (asymptotic) structures of the various vertex functions to the non-perturbative situation. To this end, we first note that the reduced complexity of specific diagrams regarding their frequency and momentum dependence is *not* a peculiarity of low(est) order perturbation theory but rather a general consequence of the frequency and momentum independence of the bare Coulomb (Hubbard) interaction U. In fact, if any two external lines of the vertex, e.g., the incoming momenta and frequencies k_1 and k_3, are attached to the same bare vertex U, energy and momentum conservation requires $k_1 + k_3 = k' + k''$ where k' and k'' denote internal frequencies/momenta which are summed. Obviously, in this situation the entire diagram does depend only on the linear combination $k_1 + k_3$ rather than k_1 and k_3 separately. Such a behavior has been already observed for lowest order perturbative (bubble and "eye") diagrams in the previous chapter, and does not change, as a matter of course, upon dressing these diagrams by means of vertex corrections. These insights hence suggest the following subdivision of the reducible vertex function $\Phi_{pp}^{kk'q}$ (and correspondingly for the other two channels) into three distinct classes, that are depicted diagrammatically in Fig. 4.1:

- Class 1: The ingoing *and* outgoing frequencies/momenta are attached to the same bare vertex. These diagrams correspond to (dressed) bubble diagrams (see first line of Fig. 4.1), and can hence be parametrized by a *single* (bosonic) transfer frequency and momentum $q = k_1 + k_3$. The sum of all diagrams of this class will be denoted by $\mathcal{K}_{1,pp}^{q}$.

- Class 2: Either the incoming *or* the outgoing frequencies/momenta are attached to the same bare vertex. These diagrams correspond to (dressed) eye diagrams (see, e.g., Fig. 3.1 and first two diagrams in the second line of Fig. 4.1). These diagrams depend on the bosonic transfer frequency/momentum $q = k_1 + k_3$ and one fermionic frequency $k = k_1$ or $k' = k_4$, respectively. The sum of such types of diagrams will be denoted as $\mathcal{K}_{2,pp}^{kq}$ and $\overline{\mathcal{K}}_{2,pp}^{k'q}$.

- Class 3: Every external frequency/momentum is attached to a different bare vertex. These diagrams depend independently on *all three* external arguments. Their sum will in the following be referred to as the "rest" function, denoted by $\mathcal{R}_{pp}^{kk'q}$. It is illustrated diagrammatically by the last diagram in the second row of Fig. 4.1.

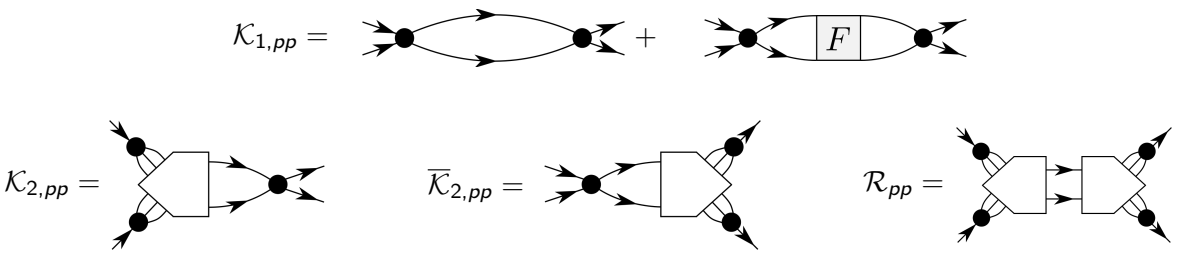

Figure 4.1.: Diagrammatic representation of the asymptotic functions for the particle-particle channel. For a more rigorous definition see Appendix B.

Based on this classification, we can thus introduce an (a priori exact) decomposition of each reducible Φ-function into these four terms[1]. In the particle-particle channel it reads[2]

$$\Phi_{pp}^{kk'q} = \mathcal{K}_{1,pp}^{q} + \mathcal{K}_{2,pp}^{kq} + \overline{\mathcal{K}}_{2,pp}^{k'q} + \mathcal{R}_{pp}^{kk'q}. \tag{4.1}$$

In the same way we can decompose also the other scattering channels *ph* and $\overline{ph}$. It is important to note, that the structures arising due to $\mathcal{K}_1$, $\mathcal{K}_2$ and $\overline{\mathcal{K}}_2$ extend to infinitely large frequencies and, hence, generate a highly non-trivial high-frequency asymptotic behavior of the corresponding vertex function.

On the contrary, the diagrammatic content of $\mathcal{R}$ implies a decay in all frequency directions, since each external fermionic frequency will enter directly one of the inner diagrammatic propagator lines by means of the frequency conservation at its attached bare vertex. These decay properties are verified numerically in Chap. 6, and motivate our proposed approximation for treating the vertex asymptotics. Our strategy will be the following: We will explicitly consider the full frequency dependence of the Φ-functions only in a small frequency window, while the third class of diagrams ($\mathcal{R}$) will be neglected at larger frequencies, i.e.,

$$\Phi_{pp,\text{asympt.}}^{kk'q} \approx \mathcal{K}_{1,pp}^{q} + \mathcal{K}_{2,pp}^{kq} + \overline{\mathcal{K}}_{2,pp}^{k'q}. \tag{4.2}$$

One can see that the reducible vertex $\Phi_{pp}^{kk'q}$ is described by functions of *at most two* arguments in the asymptotic regime, which drastically lowers the cost for its numerical treatment. This way, we are able to (i) determine the reducible vertex Φ_{pp} up to arbitrarily large frequencies with a reduced computational effort, and (ii) avoid any problem arising from boundary effects due to finite-size frequency grids in vertex-based numerical algorithms.

Let us stress that, whenever momenta are considered, the decay of $\mathcal{R}$ in the frequency domain implies, that the reducible vertices Φ exhibit their full momentum dependence only in the domain

[1] Note that for $\mathcal{K}_1$, $\mathcal{K}_2$ and $\overline{\mathcal{K}}_2$ respectively, the index denotes the reduced number of external arguments required to describe them. These shall in the following be referred to as 'necessary' arguments for the corresponding term.

[2] Let us remark, that the concrete form of the argument(s) for $\mathcal{K}_{1,pp}/\mathcal{K}_{2,pp}$ depend(s) on the chosen frequency/momentum convention. The dependence on one/two *single* argument(s) becomes apparent only in its natural notation, while for other conventions, $\mathcal{K}_{1,pp}/\mathcal{K}_{2,pp}$ will depend on one/two linear combination(s) of all frequencies/momenta. Nevertheless, these functions will be constant along two-dimensional planes/one-dimensional lines in the space of three frequencies/momenta (in the natural notation these planes/lines are parallel to the coordinate axes).

of small frequencies. At larger frequency values, where the reducible vertex function is determined by at most two of the asymptotic functions, the momentum dependence is reduced alongside the frequencies. This matter will become evident in the following Chap. 5. The same argument holds for the fully irreducible vertex $\Lambda_{2\mathrm{PI}}$, which decays to the value of the bare interaction in all frequency directions. As a consequence, strongly momentum dependent parts of the vertex F, e.g. the contributions responsible for a d-wave scattering amplitude, have to be localized in the frequency domain.

Let us now discuss the physical content of the asymptotic functions $\mathcal{K}_1$ and $\mathcal{K}_2$. The former is directly linked to the susceptibility in the corresponding scattering channel [132, 145, 167]. In fact, they are equal up to a prefactor U^2, i.e.

$$\mathcal{K}_1^q = -U^2 \chi^q, \tag{4.3}$$

with χ^q defined according to Appendix A.

$\mathcal{K}_2$ on the other hand encodes information about how the electrons couple to different bosonic degrees of freedom. For instance, for the generalized density in Fourier space $n_q = \int\!\!\!\!\!\!\diagup dk \ \sum_\sigma c_\sigma^\dagger(k) c_\sigma(k+q)$, we find the relation

$$U \times \langle \mathcal{T} n_q c_\sigma(k+q) c_\sigma^\dagger(k) \rangle_c = G_\sigma(k) G_\sigma(k+q) \sum_{\sigma'} \left(\mathcal{K}^q_{1,ph,\sigma\sigma'} + \mathcal{K}^{kq}_{2,ph,\sigma\sigma'} \right). \tag{4.4}$$

Here, $\langle ... \rangle_c$ considers only connected contractions, and the imaginary time-ordering acts inside the Fourier-integrals. The above equation relates $\mathcal{K}_1$ and $\mathcal{K}_2$ to the electron-boson coupling (three-point or Hedin) vertex as used in the ladder version of DΓA [137, 170] and the recently introduced TRILEX [147] approach.

Chapter 5

Implementation

In this chapter, we describe how the ideas presented in the previous chapter can be practically exploited in analytical and numerical calculations based on two-particle vertex functions. After a general presentation of the main concepts, we will explicitly discuss the application of our scheme for analytic calculations based on the atomic limit vertex, and for numerical implementations of the fRG in its second order truncation and the parquet approximation.

The observation that any diagram vanishes if one of its necessary frequency arguments is taken to infinity allows us to select the different diagrammatic contributions by taking the corresponding limits in the frequency domain, i.e.

$$\lim_{|\nu|\to\infty}\lim_{|\nu'|\to\infty} \Phi^{kk'q}_{r,\sigma\sigma'} = \mathcal{K}^{q}_{1,r,\sigma\sigma'}, \tag{5.1a}$$

$$\lim_{|\nu'|\to\infty} \Phi^{kk'q}_{r,\sigma\sigma'} = \mathcal{K}^{q}_{1,r,\sigma\sigma'} + \mathcal{K}^{kq}_{2,r,\sigma\sigma'}, \tag{5.1b}$$

$$\lim_{|\nu|\to\infty} \Phi^{kk'q}_{r,\sigma\sigma'} = \mathcal{K}^{q}_{1,r,\sigma\sigma'} + \overline{\mathcal{K}}^{k'q}_{2,r,\sigma\sigma'}, \tag{5.1c}$$

where $r \in \{pp, ph, \overline{ph}\}$. We stress again the fact that, by taking limits in the frequency domain, we find not only a reduced frequency, but also a reduced momentum dependence. The remaining diagrammatic class 3 introduced in Chap. 4, or rest function $\mathcal{R}$, which requires the full dependence on all arguments, can then be acquired by inverting Eq. (4.1)

$$\mathcal{R}^{kk'q}_{r,\sigma\sigma'} = \Phi^{kk'q}_{r,\sigma\sigma'} - \mathcal{K}^{q}_{1,r,\sigma\sigma'} - \mathcal{K}^{kq}_{2,r,\sigma\sigma'} - \overline{\mathcal{K}}^{k'q}_{2,r,\sigma\sigma'}. \tag{5.2}$$

One advantage of performing this limiting procedure based on the reducible vertex, is that Eq. (5.1a) holds equally if $|\nu|$ and $|\nu'|$ are taken to infinity at the same time, i.e.

$$\lim_{\substack{|\nu|\to\infty \\ |\nu'|\to\infty}} \Phi^{kk'q}_{r,\sigma\sigma'} = \mathcal{K}^{q}_{1,r,\sigma\sigma'}. \tag{5.3}$$

This property allows for a simplified scanning procedure to numerically extract asymptotic functions, which, depending on the frequency ranges and parameters, provide a good approximation. The procedure is straightforward and applicable in all channels (see also Fig. 5.1 and Ref. [165]):

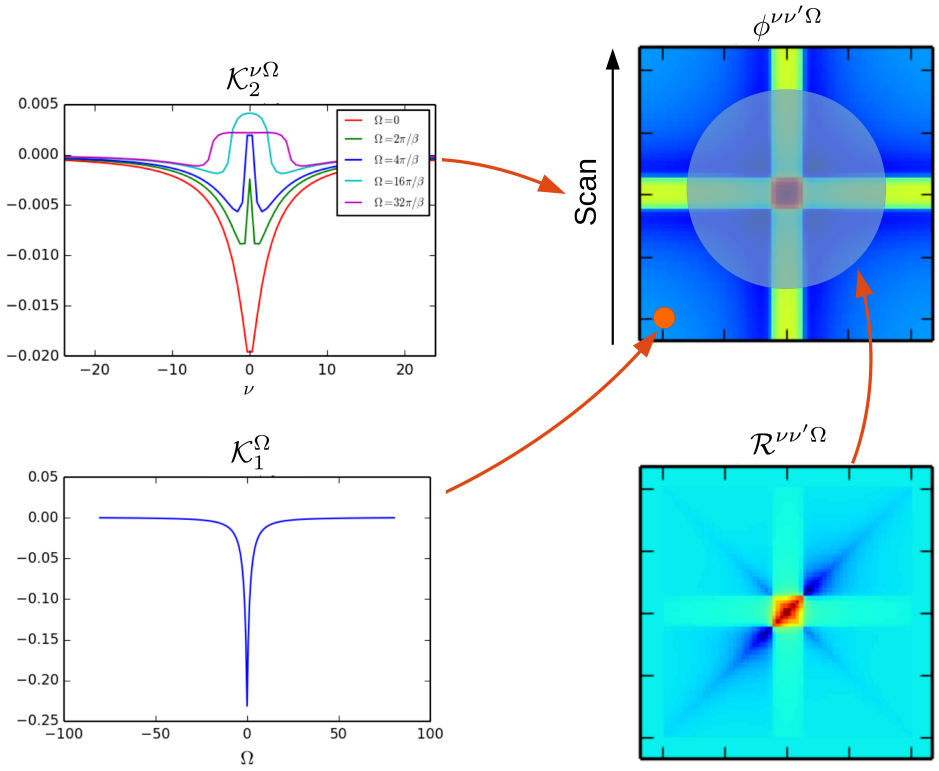

Figure 5.1.: Schematic representation of the scanning procedure, that extracts the asymptotic functions from the reducible vertex function.

- I: For large $|\nu|$ and $|\nu'|$ vary the transfer four-vector q to acquire $\mathcal{K}_1^q$.

- II: For large $|\nu'|$, vary k and the transfer four-vector q and subtract $\mathcal{K}_1^q$ in order to obtains $\mathcal{K}_2^{kq}$.

- III: Repeat II by replacing $\nu' \to \nu$ and $k \to k'$ to determine $\overline{\mathcal{K}}_2^{k'q}$.

The above described procedure proposed to determine $\mathcal{K}_1$ and $\mathcal{K}_2$ has some limitations. Firstly, one can easily see that if the scanning is not performed at sufficiently large $|\nu|$ ($|\nu'|$), the rest function might not be fully decayed, giving rise to an error in the $\mathcal{K}_1$ and $\mathcal{K}_2$ extraction. We found this error to be particularly pronounced in the strong coupling regime ($U = 4$ for the comparisons in Chap. 6) where the rest function becomes comparable with the asymptotic functions in the domain of small frequencies. Secondly, the scanning procedure requires the knowledge of the reducible vertex functions Φ_r, which are not directly available in some algorithms, as e.g. for the exact diagonalization. This raises the question whether a similar set of limits can be formulated also for

F. And in fact, as will be clarified in the following, the limits presented in Eq. (5.1) still hold, i.e.

$$\lim_{|\nu|\to\infty}\lim_{|\nu'|\to\infty} F^{kk'q}_{r,\sigma\sigma'} - (1-\delta_{\sigma,\sigma'})U = \mathcal{K}^{q}_{1,r,\sigma\sigma'}, \tag{5.4a}$$

$$\lim_{|\nu'|\to\infty} F^{kk'q}_{r,\sigma\sigma'} - (1-\delta_{\sigma,\sigma'})U = \mathcal{K}^{q}_{1,r,\sigma\sigma'} + \mathcal{K}^{kq}_{2,r,\sigma\sigma'}, \tag{5.4b}$$

$$\lim_{|\nu|\to\infty} F^{kk'q}_{r,\sigma\sigma'} - (1-\delta_{\sigma,\sigma'})U = \mathcal{K}^{q}_{1,r,\sigma\sigma'} + \overline{\mathcal{K}}^{k'q}_{2,r,\sigma\sigma'}, \tag{5.4c}$$

where again F_r denotes the representation of F in one of the three mixed notations. However, the numerical equivalent of the limiting procedure, i.e. the scanning procedure previously described for the Φ-functions, is not feasible in the case of F, which is directly related to the fact that Eq. (5.3) does not hold equally for F. In order to numerically extract the asymptotics from F directly we thus suggest an alternative approach detailed in Appendix B. We implemented this diagrammatic extraction to determine the exact asymptotic functions, as presented in Chap. 6, from ED calculations.

The limiting procedure Eq. (5.4) is however particularly suited in the case that analytical expressions for F are available, as demonstrated for the atomic limit case in Sec. 5.1. Let us thus argue why this generalization of Eq. (5.1) holds. It relies on the property that any reducible diagram vanishes if the corresponding transfer frequency, being a necessary argument, is sufficiently large, i.e.

$$\lim_{|\Omega|\to\infty} \Phi^{kk'q}_{r,\sigma\sigma'} = 0. \tag{5.5}$$

We have to further consider, that in order to take the limits in Eq. (5.4), we should formulate Eq. (1.3.2) in the corresponding mixed notation. E.g. for the particle-particle channel we have to translate Φ_{ph} and $\Phi_{\overline{ph}}$ to the pp-notation as follows

$$F^{kk'q}_{pp,\sigma\sigma'} = \Lambda^{kk'q}_{\mathrm{2PI},pp,\sigma\sigma'} + \Phi^{kk'q}_{pp,\sigma\sigma'} + \Phi^{kk'(q-k'-k)}_{ph,\sigma\sigma'} + \Phi^{k(q-k')(k'-k)}_{\overline{ph},\sigma\sigma'}. \tag{5.6}$$

It now becomes clear that for fixed Ω and ν', the bosonic frequencies of the ph and $\overline{ph}$ channel, that is $\Omega-\nu'-\nu$ and $\nu'-\nu$, will lead to a vanishing of the respective scattering channels for $|\nu|\to\infty$. This behavior can also be observed in Fig. 1.4, and holds equally for the other scattering channels. Since Λ_{2PI} decays in all frequency directions to the bare interaction, we conclude that $\lim_{|\nu|\to\infty} F^{kk'q}_{r,\sigma\sigma'} - (1-\delta_{\sigma,\sigma'})U = \lim_{|\nu|\to\infty} \Phi^{kk'q}_{r,\sigma\sigma'}$, while the same argument can be made for the other limits in Eq. (5.4).

5.1 Decomposing the atomic limit vertex

As a first showcase of these ideas we discuss the vertex decomposition for a system that can be treated analytically, i.e., the atomic limit, whose Hamiltonian reads

$$\hat{\mathcal{H}} = U\left[\hat{n}_\uparrow\hat{n}_\downarrow - \frac{1}{2}(\hat{n}_\uparrow+\hat{n}_\downarrow)\right]. \tag{5.1.1}$$

Here, $\hat{n}_\sigma = \hat{c}_\sigma^\dagger \hat{c}_\sigma$ is the number operator for fermions of spin σ, and we have imposed the half-filling (particle-hole symmetry) condition $\mu = U/2$. The Hilbert space is spanned by the four eigenstates $|0\rangle$, $|\uparrow\rangle$, $|\downarrow\rangle$ and $|\uparrow\downarrow\rangle$, allowing for a direct calculation of the two-particle Green's functions by means of the Lehmann representation. The resulting two-particle vertex function [113, 120, 132] is, for our purposes, split into four terms (note $\mathcal{F}_r \neq F_r$)

$$F_{\uparrow\downarrow} = \mathcal{F}_{\text{odd}} + \mathcal{F}_{pp} + \mathcal{F}_{ph} + \mathcal{F}_{\overline{ph}}, \tag{5.1.2}$$

which are defined in the following. The first term contains only odd orders in the interaction, and takes the most compact form in the purely fermionic notation

$$\mathcal{F}_{\text{odd}}^{\nu_1\nu_2\nu_3\nu_4} = U - \frac{U^3}{8}\frac{\sum_i \nu_i^2}{\prod_i \nu_i} - \frac{3U^5}{16}\prod_i \frac{1}{\nu_i}, \tag{5.1.3}$$

while the functions $\mathcal{F}_r$ with $r \in \{pp, ph, \overline{ph}\}$ are more conveniently expressed in their respective mixed notation (see Appendix A)

$$\mathcal{F}_{pp}^{\nu\nu'\Omega} = -\beta\,\delta_{\Omega,0}\frac{U^2}{2}\mathcal{D}^{\nu\nu'} f\left(\frac{U}{2}\right), \tag{5.1.4a}$$

$$\mathcal{F}_{ph}^{\nu\nu'\Omega} = -\beta\,\delta_{\Omega,0}\frac{U^2}{4}\mathcal{D}^{\nu\nu'}\left[f\left(\frac{U}{2}\right) - f\left(-\frac{U}{2}\right)\right], \tag{5.1.4b}$$

$$\mathcal{F}_{\overline{ph}}^{\nu\nu'\Omega} = \quad \beta\,\delta_{\Omega,0}\frac{U^2}{2}\mathcal{D}^{\nu\nu'} f\left(-\frac{U}{2}\right), \tag{5.1.4c}$$

with $\mathcal{D}^{\nu\nu'} = \frac{1}{\nu^2\nu'^2}\left(\nu^2 + \frac{U^2}{4}\right)\left(\nu'^2 + \frac{U^2}{4}\right)$ and the Fermi function $f(\epsilon) = \frac{1}{1+e^{\beta\epsilon}}$. Note that, at this stage, the decomposition for the full vertex F is motivated solely by algebraic reasons, while the connection to the physical scattering channels will be established in the following.

Let us now use the limits in Eqs. (5.4) to identify the contributions arising from the different diagrammatic classes. This task can be performed by considering each term in Eq. (5.1.2) separately. Let us illustrate this procedure for the *pp*-channel, beginning with the first term, $\mathcal{F}_{\text{odd}}$. Here, we have to translate from the purely fermionic notation to the mixed one of the *pp*-channel:

$$\mathcal{F}_{\text{odd,pp}}^{\nu\nu'\Omega} = \mathcal{F}_{\text{odd}}^{\nu,\Omega-\nu',\Omega-\nu,\nu'} = U - \frac{U^3}{8}\frac{\nu^2 + (\Omega-\nu')^2 + (\Omega-\nu)^2 + \nu'^2}{\nu(\Omega-\nu')(\Omega-\nu)\nu'} - \frac{3U^5}{16}\frac{1}{\nu(\Omega-\nu')(\Omega-\nu)\nu'}. \tag{5.1.5}$$

The large frequency limits then result in

$$\lim_{|\nu|\to\infty}\lim_{|\nu'|\to\infty} \mathcal{F}^{\nu\nu'\Omega}_{\text{odd,pp}} = U, \tag{5.1.6a}$$

$$\lim_{|\nu'|\to\infty} \mathcal{F}^{\nu\nu'\Omega}_{\text{odd,pp}} = U - \frac{U^3}{4}\frac{1}{\nu}\frac{1}{\nu-\Omega}, \tag{5.1.6b}$$

$$\lim_{|\nu|\to\infty} \mathcal{F}^{\nu\nu'\Omega}_{\text{odd,pp}} = U - \frac{U^3}{4}\frac{1}{\nu'}\frac{1}{\nu'-\Omega}. \tag{5.1.6c}$$

As for the limits of the second term, $\mathcal{F}_{pp}$, we have

$$\lim_{|\nu|\to\infty}\lim_{|\nu'|\to\infty} \mathcal{F}^{\nu\nu'\Omega}_{pp} = -\beta\,\delta_{\Omega,0}\frac{U^2}{2} f\left(\frac{U}{2}\right), \tag{5.1.7a}$$

$$\lim_{|\nu'|\to\infty} \mathcal{F}^{\nu\nu'\Omega}_{pp} = -\beta\,\delta_{\Omega,0}\frac{U^2}{2}\left[1+\frac{U^2}{4}\frac{1}{\nu^2}\right] f\left(\frac{U}{2}\right), \tag{5.1.7b}$$

$$\lim_{|\nu|\to\infty} \mathcal{F}^{\nu\nu'\Omega}_{pp} = -\beta\,\delta_{\Omega,0}\frac{U^2}{2}\left[1+\frac{U^2}{4}\frac{1}{\nu'^2}\right] f\left(\frac{U}{2}\right). \tag{5.1.7c}$$

Determining the contributions from the remaining terms $\mathcal{F}_{ph}$ and $\mathcal{F}_{\overline{ph}}$, which involves a translation from their respective mixed notation to the *pp*-notation, we find that their contributions vanish. This leads to the final expressions for the asymptotic functions in the *pp*-channel

$$\mathcal{K}^{\Omega}_{1,pp,\uparrow\downarrow} = -\beta\,\delta_{\Omega,0}\frac{U^2}{2} f\left(\frac{U}{2}\right), \tag{5.1.8a}$$

$$\mathcal{K}^{\nu\Omega}_{2,pp,\uparrow\downarrow} = \frac{U^2}{4}\frac{1}{\nu}\frac{1}{\nu-\Omega}\left(\mathcal{K}^{\Omega}_{1,pp,\uparrow\downarrow} - U\right), \tag{5.1.8b}$$

while the $\overline{\mathcal{K}}_2$ can be acquired by means of the symmetry properties reported in Appendix C. Performing the analogous procedure for the remaining two channels yields

$$\mathcal{K}^{\Omega}_{1,ph,\uparrow\downarrow} = -\beta\,\delta_{\Omega,0}\frac{U^2}{4}\left[f\left(\frac{U}{2}\right) - f\left(-\frac{U}{2}\right)\right], \tag{5.1.9a}$$

$$\mathcal{K}^{\nu\Omega}_{2,ph,\uparrow\downarrow} = \frac{U^2}{4}\frac{1}{\nu}\frac{1}{\nu+\Omega}\left(\mathcal{K}^{\Omega}_{1,ph,\uparrow\downarrow} - U\right), \tag{5.1.9b}$$

for the *ph*-channel, and

$$\mathcal{K}^{\Omega}_{1,\overline{ph},\uparrow\downarrow} = \beta\,\delta_{\Omega,0}\frac{U^2}{2} f\left(-\frac{U}{2}\right), \tag{5.1.10a}$$

$$\mathcal{K}^{\nu\Omega}_{2,\overline{ph},\uparrow\downarrow} = \frac{U^2}{4}\frac{1}{\nu}\frac{1}{\nu+\Omega}\left(\mathcal{K}^{\Omega}_{1,\overline{ph},\uparrow\downarrow} - U\right). \tag{5.1.10b}$$

in the $\overline{ph}$ case.

Now that we have determined all asymptotic functions of the atomic limit vertex, let us consider its structures that are localized in the frequency domain. We proceed again in a term-wise fashion, beginning with $\mathcal{F}_{\text{odd}}$. By subtracting all asymptotic contributions arising from this term, we find

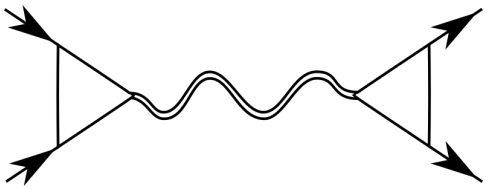

Figure 5.2.: Schematic diagrammatic representation of the localized structure presented in Eq. (5.1.11).

that only the fifth order term $-\frac{3U^5}{16}\prod_i \frac{1}{\nu_i}$ survives, while it remains unclear whether this term can be attributed to the fully irreducible vertex function or the rest functions.

For the $\mathcal{F}_r$ terms, let us again consider the *pp*-channel as an example. Here we find

$$\begin{aligned}&\mathcal{F}_{pp}^{\nu\nu'\Omega} - \lim_{|\nu'|\to\infty} \mathcal{F}_{pp}^{\nu\nu'\Omega} - \lim_{|\nu|\to\infty} \mathcal{F}_{pp}^{\nu\nu'\Omega} + \lim_{|\nu|\to\infty}\lim_{|\nu'|\to\infty} \mathcal{F}_{pp}^{\nu\nu'\Omega} \\ &= \left(\frac{U^2}{4}\frac{1}{\nu}\frac{1}{\nu-\Omega}\right) \times \mathcal{K}_{1,pp,\uparrow\downarrow}^{\Omega} \times \left(\frac{U^2}{4}\frac{1}{\nu'}\frac{1}{\nu'-\Omega}\right).\end{aligned} \tag{5.1.11}$$

This term contains three factors, i.e. a fermion-boson vertex [148] that describes the coupling to a pairing field, the bosonic propagator in the *pp*-channel, and an additional fermion-boson vertex, as depicted schematically in Fig. 5.2. We can thus argue diagrammatically that this localized term belongs to the rest function $\mathcal{R}_{pp,\uparrow\downarrow}$. For the other channels, we find equally that the localized structures belong to the respective rest function, and hence $\mathcal{F}_r \in \Phi_{r,\uparrow\downarrow}$.

Note that, to obtain the full rest functions as well as the fully irreducible vertex function, it would require the analytic expressions for all the reducible Φ functions, that have so far never been reported in the literature. Their calculation requires the very involved procedure of inverting analytically the Bethe-Salpeter equations, which goes beyond the scope of this thesis. The resulting expressions should reproduce the multiple vertex divergencies [133, 171–173] appearing in the Φ functions for $T \leq \frac{\sqrt{3}}{2\pi}U$. As these divergent terms are not present in the full vertex F, they must be subjected to cancellations between $\Lambda_{2\text{PI}}$ and one (or more) of rest functions.

5.2 Implementation for the fRG solver

The functional renormalization group approach [13,174] implements Wilson's renormalization group idea in a general field-theoretical frame. By introducing a scale-dependence into the quadratic part of the action, i.e. the non-interacting propagator

$$G_0(i\nu) \to G_0^{\Lambda}(i\nu),$$

one can derive an exact functional flow equation [7] for the 1PI generating functional, also named "effective action". This flow equation describes the gradual evolution of all correlation functions as the scale Λ is varied from the initial to the final value. Being an exact reformulation of the initial problem, it serves as a basis for further approximations, and has been used in many different applications ranging from high-energy physics to condensed matter theory. In the fRG, this approximation consists in an expansion in orders of the fields, resulting in an infinite hierarchy of

coupled ordinary differential equations for all 1PI n-particle vertex functions, e.g. the self-energy Σ, the two-particle vertex F and so on. This hierarchy is typically truncated at the two-particle level, rendering the fRG perturbative in the interaction strength.

For the flow-parameter dependence, we consider in the following two different schemes: The so-called Ω-flow [12]:

$$G_0^\Lambda(i\nu) = \frac{\nu^2}{\nu^2 + \Lambda^2} G_0(i\nu), \tag{5.2.1}$$

and the U-flow [9]:

$$G_0^\Lambda(i\nu) = \Lambda \cdot G_0(i\nu). \tag{5.2.2}$$

The Ω-flow introduces an energy cutoff into the system, that allows to successively integrate out the different energy scales from high to low. This approach is very much in the spirit of other renormalization group approaches. The U-flow on the other hand introduces a frequency-independent regulator into the Green function that treats all energy scales on a equal footing. In this sense, the U-flow is more similar to common perturbative approaches.

The flow-equations resulting from a second order truncation of the flow-equation hierarchy can be summarized as follows. At the level of the self-energy, the derivative takes the simple form

$$\dot{\Sigma}(k)^\Lambda = \sum\!\!\!\!\!\!\int dk'\, S^\Lambda(k') \times \left[F_{ph,\uparrow\downarrow}^{\Lambda,kk'(q=0)} + F_{ph,\uparrow\uparrow}^{\Lambda,kk'(q=0)} \right], \tag{5.2.3}$$

where we have introduced the so-called single-scale propagator

$$S^\Lambda(i\nu) = \partial_\Lambda G^\Lambda(i\nu)|_{\Sigma^\Lambda \text{ fixed}}.$$

At the level of the 1PI two-particle vertex, the flow-equation is composed of contributions from three scattering channels (particle-particle, particle-hole and transverse particle-hole)

$$\dot{F}^\Lambda = \mathcal{T}_{pp}^\Lambda + \mathcal{T}_{ph}^\Lambda + \mathcal{T}_{\overline{ph}}^\Lambda, \tag{5.2.4}$$

where

$$\mathcal{T}_{pp,\uparrow\downarrow}^{\Lambda,kk'q} = \sum\!\!\!\!\!\!\int dk'' \left[S^\Lambda(k'') G^\Lambda(q-k'') + S \leftrightarrow G \right] \times F_{pp,\uparrow\downarrow}^{\Lambda,qkk''} F_{pp,\uparrow\downarrow}^{\Lambda,qk''k'}, \tag{5.2.5a}$$

$$\mathcal{T}_{ph,\uparrow\downarrow}^{\Lambda,kk'q} = -\sum\!\!\!\!\!\!\int dk'' \left[S^\Lambda(k''+q) G^\Lambda(k'') + S \leftrightarrow G \right] \times \left[F_{ph,\uparrow\uparrow}^{\Lambda,kk''q} F_{ph,\uparrow\downarrow}^{\Lambda,k''k'q} + F_{\uparrow\uparrow} \leftrightarrow F_{\uparrow\downarrow} \right], \tag{5.2.5b}$$

$$\mathcal{T}_{\overline{ph},\uparrow\downarrow}^{\Lambda,kk'q} = \sum\!\!\!\!\!\!\int dk'' \left[S^\Lambda(k''+q) G^\Lambda(k'') + S \leftrightarrow G \right] \times F_{\overline{ph},\uparrow\downarrow}^{\Lambda,kk''q} F_{\overline{ph},\uparrow\downarrow}^{\Lambda,k''k'q}. \tag{5.2.5c}$$

These terms can be depicted diagrammatically as shown in Fig. 5.3 for the pp-channel. To understand the diagrammatic content generated by each channel let us refer to the previously introduced parquet equation, that holds for any scale Λ

$$F^\Lambda = \Lambda_{2\text{PI}}^\Lambda + \Phi_{pp}^\Lambda + \Phi_{ph}^\Lambda + \Phi_{\overline{ph}}^\Lambda. \tag{5.2.6}$$

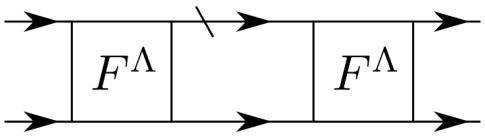

Figure 5.3.: Diagrammatic representation of the particle-particle contribution $\mathcal{T}_{pp}$ (5.2.5a) in the vertex flow equation. The dashed line denotes the single-scale propagator S^Λ.

Considering the vertex flow equation Eq. (5.2.4), it is obvious that at this level of truncation, the only diagrammatic content than can be generated by the flow is two-particle reducible, meaning $\Lambda^\Lambda_{\text{2PI}} = \overline{\Lambda}^{\Lambda_{\text{ini}}}_{\text{2PI}}$. We can thus separate the different two-particle reducible terms in Eq. (5.2.4), and identify

$$\dot{\Phi}^\Lambda_{pp} = \mathcal{T}_{pp}, \quad \dot{\Phi}^\Lambda_{ph} = \mathcal{T}_{ph}, \quad \dot{\Phi}^\Lambda_{\overline{ph}} = \mathcal{T}_{\overline{ph}}. \tag{5.2.7}$$

This allows us to make use of the parametrization scheme described in Chap. 4 during the fRG flow. While keeping track of the reducible vertex functions on a finite frequency grid, we also track the flow of the previously introduced asymptotic functions. In fact, we can directly perform the limits in Eq. (5.1) to compute the corresponding derivatives

$$\dot{\mathcal{K}}^{\Lambda,q}_{1,r,\sigma\sigma'} = \lim_{|\nu|\to\infty} \lim_{|\nu'|\to\infty} \dot{\Phi}^{\Lambda,kk'q}_{r,\sigma\sigma'}, \tag{5.2.8a}$$

$$\dot{\mathcal{K}}^{\Lambda,kq}_{2,r,\sigma\sigma'} = \lim_{|\nu'|\to\infty} \dot{\Phi}^{\Lambda,kk'q}_{r,\sigma\sigma'} - \dot{\mathcal{K}}^{\Lambda,q}_{1,r,\sigma\sigma'}, \tag{5.2.8b}$$

$$\dot{\overline{\mathcal{K}}}^{\Lambda,k'q}_{2,r,\sigma\sigma'} = \lim_{|\nu|\to\infty} \dot{\Phi}^{\Lambda,kk'q}_{r,\sigma\sigma'} - \dot{\mathcal{K}}^{\Lambda,q}_{1,r,\sigma\sigma'}. \tag{5.2.8c}$$

In practice, these limits are performed numerically by setting the corresponding frequency to an arbitrarily large value. In doing this, we have to determine F^Λ in the large frequency domain by making use of Eq. (4.2). In addition to the flow of the Φ-functions we then track, using Eqs. (5.2.8), the flow of the asymptotic functions.

Due to the numerical costs involved in treating the full argument dependence of the vertex function, a simplified parametrization scheme [134]

$$\Phi^{kk'q}_{pp} \approx \mathcal{K}^q_{\text{eff},pp} = \mathcal{K}^q_{1,pp} + \mathcal{K}^{(\lceil\Omega/2\rceil-\nu_0,\mathbf{k})q}_{2,pp} + \overline{\mathcal{K}}^{(\lceil\Omega/2\rceil-\nu_0,\mathbf{k}')q}_{2,pp} + \mathcal{R}^{(\lceil\Omega/2\rceil-\nu_0,\mathbf{k})(\lceil\Omega/2\rceil-\nu_0,\mathbf{k}')q}_{pp} \tag{5.2.9}$$

has found extensive use in the fRG community. Here, $\nu_0 = \frac{\pi}{\beta}$ denotes the first positive Matsubara frequency, and $\lceil ... \rceil$ will round up to the next bosonic Matsubara frequency [1]. This scheme considers only the dominant transfer frequency dependence of the $\mathcal{K}_2$ and $\mathcal{R}$ functions, and will be compared to the full parametrization in Sec. 6.3. Performing the same approximation in the momentum

[1] The parametrization scheme presented in Eq. (5.2.9) was originally implemented at zero temperature, where the flow of each channel was determined for vanishing transfer frequency of the other two channels. At finite temperature, this choice is only possible for every other transfer frequency, as the condition $\left(\frac{\beta}{2\pi}\sum_r \Omega_r\right) \bmod 2 = 1$ needs to hold. This leads to ambiguities in the definition.

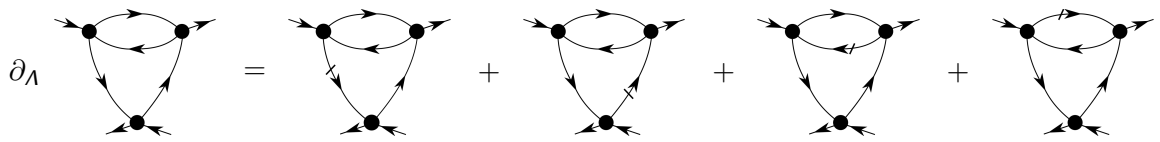

Figure 5.4.: Derivative of the lowest order contribution to $\mathcal{K}^{\Lambda}_{2,ph}$.

domain limits the scattering to the s-wave type, while higher harmonics can be captured by means of a form-factor expansion [175].

The fRG flow equations in their second order truncated form account for the feedback of F^{Λ} into the flow up to the second order. If we in addition consider partially the neglected contribution of the 1PI three-particle vertex in the flow equations, it is possible to account fully for the feedback up to $\mathcal{O}[(F^{\Lambda})^3]$. In practice this is achieved by taking into account both self-energy[2], and vertex corrections from diagrams with overlapping loops [10, 14], which is possible with a manageable numerical effort. These corrections will in the following be referred to as two-loop (2ℓ) corrections to distinguish this scheme from the conventional one-loop (1ℓ) one.

When considering the flow of the asymptotic functions, we find that including the two-loop corrections gives a substantial improvement of the two-particle vertex results. While a quantitative comparison between the one- and two-loop scheme will be presented in Sec. 6.2, we can already understand from a simple diagrammatic argument that the lowest order contribution to $\mathcal{K}_2$ is not captured in the one-loop scheme. Here, the derivative includes four contributions, as depicted in Fig. 5.4. The one-loop scheme accounts only for the first two diagrams, while the two-loop scheme includes all of them. In particular for the U-flow, the contribution from all four diagrams is equal, meaning that in its one-loop implementation the flow reproduces exactly $\frac{1}{2}$ of the exact value for $U \to 0$. This is verified numerically in Sec. 6.2 (see Fig. 6.10). A similar argument can be made for the lowest order diagram of $\mathcal{R}$, where the resulting factor is $\frac{1}{3}$.

5.3 Implementation for the parquet approximation

In this section we describe the implementation of the parquet approximation using the proper treatment of the vertex asymptotics. Let us begin by presenting in detail the essential equations. The Bethe-Salpeter equations[3], as depicted also diagrammatically in Fig. 5.5, read[4]

[2] The self-energy correction $S \to \partial_{\Lambda} G^{\Lambda}$ is generally referred to as Katanin-substitution [10].

[3] The Bethe-Salpeter equations can be channel-diagonalized by switching to the density (d), magnetic (m), singlet (s) and triplet (t) channels. While this simplifies their exact inversion, this change of description is unnecessary for the iterative procedure described in the following.

[4] We want to point out the fond similarity between Eqs. (5.3.1), which are the basis for the iterative parquet approximation solver, and the channel-resolved fRG flow Eqs. (5.2.5), which technically allows for very similar implementations of the two approaches.

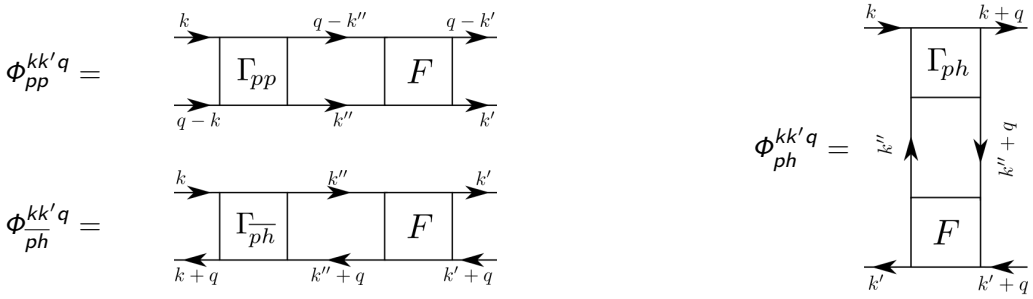

Figure 5.5.: Compact diagrammatic representation of the Bethe-Salpeter equations in all scattering channels.

$$\Phi_{pp,\uparrow\downarrow}^{kk'q} = \sum\!\!\!\!\!\!\int dk''\; G(k'')G(q-k'') \times \Gamma_{pp,\uparrow\downarrow}^{qkk''} F_{pp,\uparrow\downarrow}^{qk''k'}, \tag{5.3.1a}$$

$$\Phi_{ph,\uparrow\downarrow}^{kk'q} = -\sum\!\!\!\!\!\!\int dk''\; G(k''-q)G(k'') \times \left[\Gamma_{ph,\uparrow\uparrow}^{kk''q} F_{ph,\uparrow\downarrow}^{k''k'q} + \Gamma_{ph,\uparrow\downarrow}^{kk''q} F_{ph,\uparrow\uparrow}^{k''k'q}\right], \tag{5.3.1b}$$

$$\Phi_{\overline{ph},\uparrow\downarrow}^{kk'q} = \sum\!\!\!\!\!\!\int dk''\; G(k''-q)G(k'') \times \Gamma_{\overline{ph},\uparrow\downarrow}^{kk''q} F_{\overline{ph},\uparrow\downarrow}^{k''k'q}, \tag{5.3.1c}$$

where

$$\Gamma_r = \Lambda_{2\mathrm{PI}} + \sum_{r'\neq r} \Phi_{r'}, \tag{5.3.2}$$

while F is finally obtained by means of the parquet equation (1.3.2) (or Eq. (5.6) for the explicit version in the *pp*-channel). If we supplement these equations by the so-called Schwinger Dyson equation of motion for the self-energy

$$\Sigma(k) = U \sum\!\!\!\!\!\!\int dk_i\; G(k_1)G(k_2)G(k_1+k_2-k) F_{\uparrow\downarrow}^{k_1 k k_2}, \tag{5.3.3}$$

we acquire a closed set of equations, the parquet equations, that can in principle can be solved, if e.g. the fully irreducible vertex function $\Lambda_{2\mathrm{PI}}$ is known. Their solution is numerically very delicate though, and has posed a great challenge in numerical physics over the last years, one of the main obstacles being the correct description of the vertex symmetries [164] and asymptotics [165].

If we approximate the fully irreducible vertex by its lowest order contribution, i.e. $\Lambda_{2\mathrm{PI}} \approx U$, we obtain the so-called *parquet approximation* (PA) scheme, that we will consider in the following. The steps that we employed for a numerical solution of the parquet approximation can be formulated in a straightforward way as follows

- I: Initialize Σ as well as the Φ-,$\mathcal{K}_1$- and $\mathcal{K}_2$-functions to 0 or make some educated guess for their starting values.
- II: Based on their current values, update the Σ, Φ's, $\mathcal{K}_1$'s and $\mathcal{K}_2$'s according to Eqs. (5.3.3),(5.3.1) and (5.1), while making use of Eq. (1.3.2), Eq. (5.3.2) and Eq. (4.2) to correctly treat the high-frequency asymptotics.
- III: Repeat II till convergence.

Results obtained by this approach for a SIAM are presented in the following Chap. 6.

Chapter 6

Comparison to exact results of the SIAM

In this chapter we illustrate the high quality of the description of the vertex asymptotics obtained using the algorithmic implementations discussed in the previous chapters.

In particular, we present results for the asymptotic functions as obtained from the fRG (Ω-flow including two-loop corrections) and PA for a single impurity Anderson model and compare them with exact diagonalization data, which were acquired following the procedure outlined in Appendix B. Besides the asymptotic functions, also results for the rest function and the self-energy will be shown. In Sec. 6.2 we will further discuss a detailed comparison between the fRG in its one- and two-loop implementation for both the Ω- as well as the U-flow. We first consider the regime, where the fRG and the PA, as approximation schemes, are expected to be quantitatively correct. Hence, in this regime, the comparison with the exact results of ED will represent a stringent test for our treatment of the high-frequency asymptotics. After having demonstrated that the error introduced in the high-frequency asymptotics of the vertex function is negligible, we proceed by applying our fRG and PA algorithms, including the high-frequency treatment, to the intermediate to strong coupling regime. In this case, the comparison to the ED will allow us to assess directly the intrinsic performance of the two approximations in the non-perturbative parameter region, because no spurious effects are introduced by an incorrect treatment of the high-frequency part anymore.

The system of interest in this chapter is a SIAM, i.e. a single impurity site with local repulsive Coulomb interaction U coupled to a non-interacting bath (see Chap. 3, Eq. (3.1)). In our individual case, we consider a box-like density of states

$$\rho(\omega) = \frac{1}{2D}\Theta(D - |\omega|), \tag{6.1}$$

where D denotes the half-bandwidth, which will be used as our unit of energy, i.e. $D = 1$. This bath is coupled to our impurity site by means of a hopping $t = \sqrt{2/\pi}$, such that the resulting hybridization function reads $\Delta(\omega) = \pi t^2 \rho(\omega) = 2\rho(\omega)$. This choice results in $\Delta(0) = D = 1$, allowing us to directly relate our unit of energy to the one used in wide-band limit calculations [134], namely the hybridization function evaluated at the chemical potential.

However, the exact diagonalization of the SIAM is not possible for $\rho(\omega)$ of Eq. (6.1). Hence, we have determined a set of four optimized bath energy levels ϵ_n and hoppings t_n with the resulting

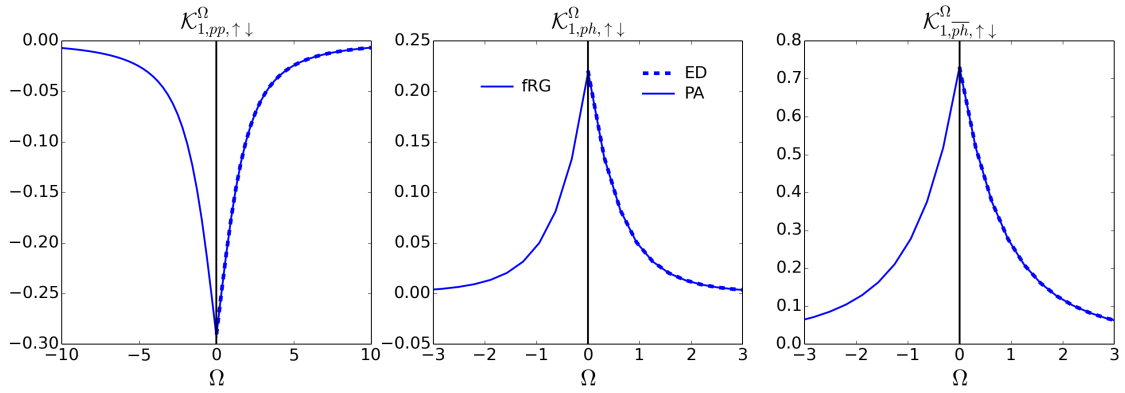

Figure 6.1.: $K^{\Omega}_{1,\uparrow\downarrow}$ for all three scattering channels. We present results obtained by fRG (left, solid), PA (right, solid) and ED (right, dashed) for the SIAM with $U = 1$, $\beta = 20$ and $\Delta(0) = D = 1$. [166]

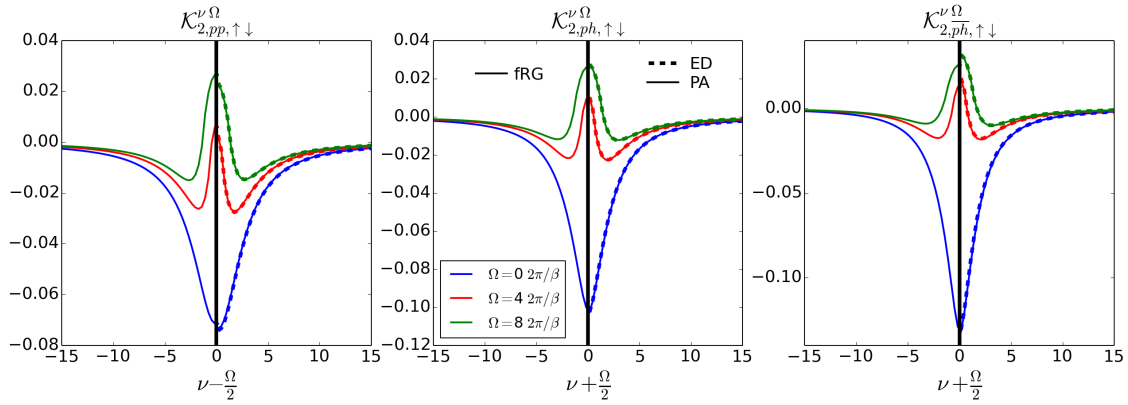

Figure 6.2.: $K^{\nu\Omega}_{2,\uparrow\downarrow}$ for all three scattering channels as a function of ν and for different values of Ω. We present results obtained by fRG (left, solid), PA (right, solid) and ED (right, dashed) for the SIAM with $U = 1$, $\beta = 20$ and $\Delta(0) = D = 1$. [166]

hybridization function

$$\Delta^{\mathrm{ED}}(i\nu) = \sum_{n=1}^{4} \frac{t_n^2}{i\nu - \epsilon_n}, \tag{6.2}$$

in order to mimic the continuous bath of Eq. (6.1) in the best way possible within a discretized ED scheme. Following a somewhat similar strategy as in the ED algorithms for DMFT, we determine our bath parameters such that the norm

$$\sum_{i\nu} |\Delta^{\mathrm{ED}}(i\nu) - \Delta(i\nu)|^2 \tag{6.3}$$

is minimized. For an inverse temperature $\beta = 20$, which was used for all numerical calculations presented in this thesis, we have $\epsilon_n = -0.7, -0.15, 0.15, 0.7$ and $t_n = 0.45, 0.34, 0.34, 0.45$. Note also that, since we are considering the particle-hole symmetric case, all two-particle quantities are purely real, while the self-energy is purely imaginary. Unless mentioned otherwise, calculations are performed with a frequency grid of $128 \times 128 \times 256$ Matsubara frequencies for the Φ-functions,

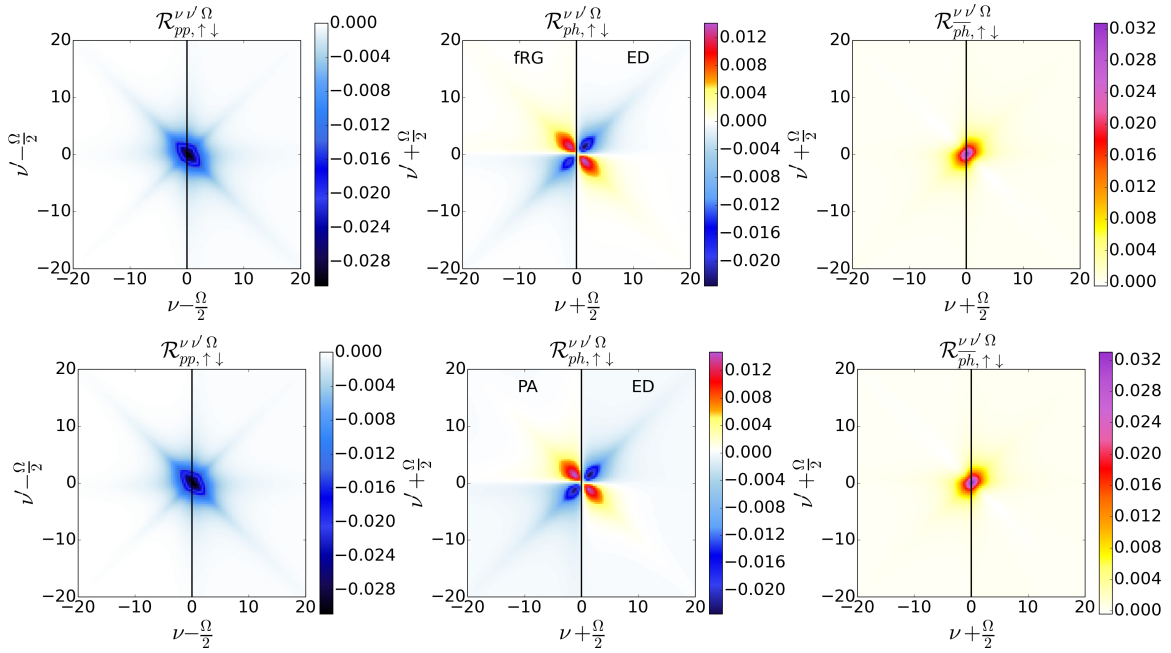

Figure 6.3.: Rest function $\mathcal{R}^{\nu\nu'\Omega}_{\uparrow\downarrow}$ for all three scattering channels as a function of ν and ν' plotted for $\Omega = 0$. We present results obtained by fRG (1st row, left) and PA (2nd row, left) for the SIAM with $U = 1$, $\beta = 20$ and $\Delta(0) = D = 1$. The right side always shows the corresponding ED result. [166]

while grids of 128×256 and 256 are chosen for $\mathcal{K}_2$ and $\mathcal{K}_1$ respectively.

Let us start considering the weak-coupling case ($U = 1$). The data for $\mathcal{K}_{1,\uparrow\downarrow}$, $\mathcal{K}_{2,\uparrow\downarrow}$ and $\mathcal{R}_{\uparrow\downarrow}$ are presented in Fig. 6.1, Fig. 6.2 and Figs. 6.3, 6.4 respectively[1]. For this parameter choice, we find an excellent agreement between the different approaches and the exact solution for all quantities. At the level of the asymptotic function $\mathcal{K}_{1,\uparrow\downarrow}$, no distinction can be made between the results of the different schemes, while for $\mathcal{K}_{2,\uparrow\downarrow}$ the fRG shows some minor deviations w.r.t. PA and ED in the *pp* and $\overline{ph}$ channel. Even at the level of the rest function $\mathcal{R}_{\uparrow\downarrow}$, which has as a leading order U^4, we find excellent agreement between PA and ED, while only minor deviations are again observed for the fRG. Note that, contrary to the plotting conventions adopted in previous Refs. [132, 165], the fermionic frequencies are shifted by $\pm\Omega/2$ for $\mathcal{K}_2$ and $\mathcal{R}$, because the main frequency structures move outwards as Ω is increased. This observation suggests to include a corresponding shift also in the notation used in the numerical implementation, such that the localized frequency structures can be more efficiently captured by means of the finite grid even in the case of finite transfer frequency. Similar trends are observed for the self-energy shown in the left panel of Fig. 6.5. While PA and ED agree perfectly, we find that the fRG self-energy deviates from the exact results, especially in its tail.

All this numerical evidence proves the reliability of our treatment of the high frequency asymptotics within the different schemes (see also the results for $U = 2$ in the supplements), allowing us to

[1] The contour plots are created such that every small square of equal color represents the value of the function at the bottom left corner of this square.

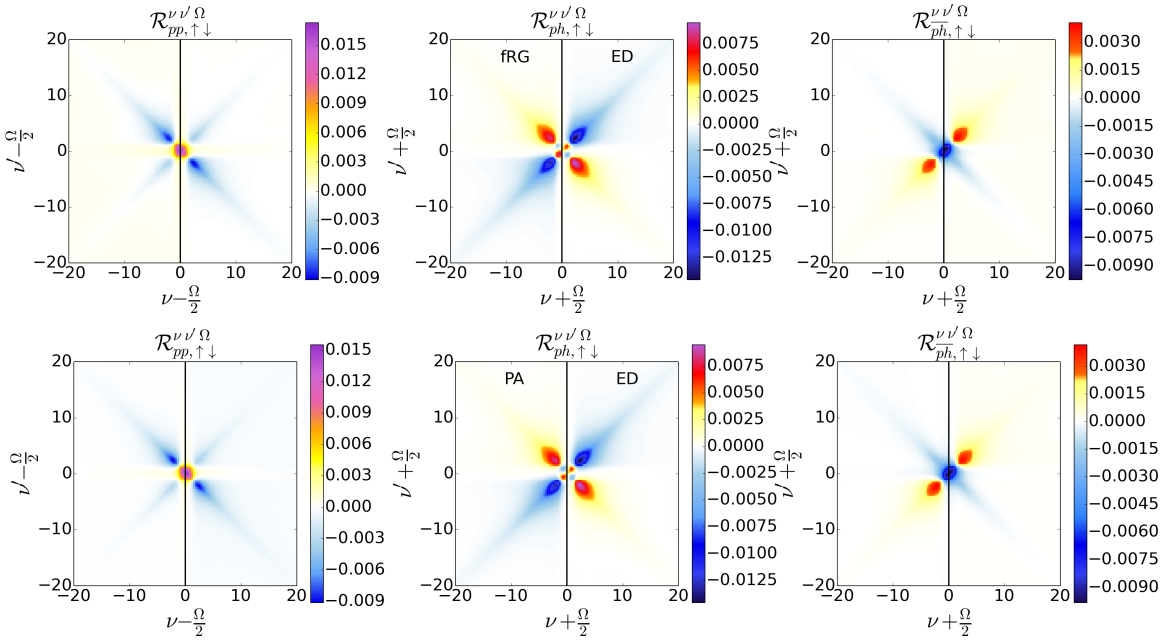

Figure 6.4.: Same as Fig. 6.3, but for a finite transfer frequency $\Omega = 8\frac{2\pi}{\beta}$. [166]

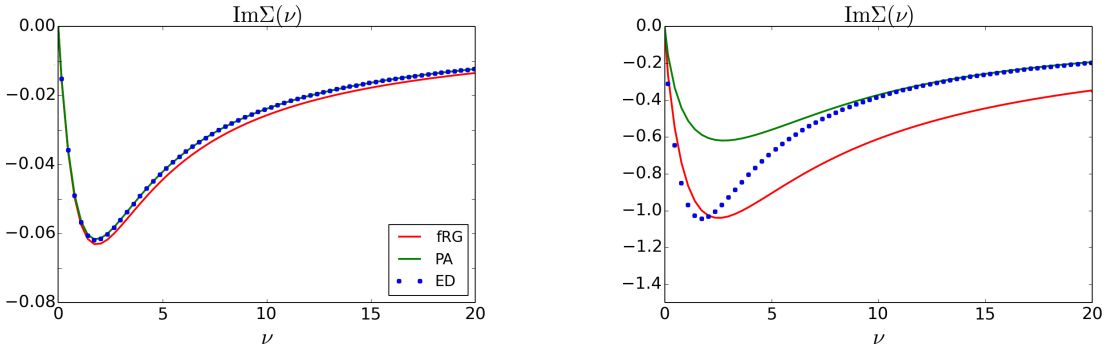

Figure 6.5.: Im $\Sigma(i\nu)$ as obtained by fRG (red, solid), PA (green, solid) and ED (blue, dotted) for the SIAM with $\beta = 20$, $\Delta(0) = D = 1$ and for $U = 1$ (left) and $U = 4$. [166]

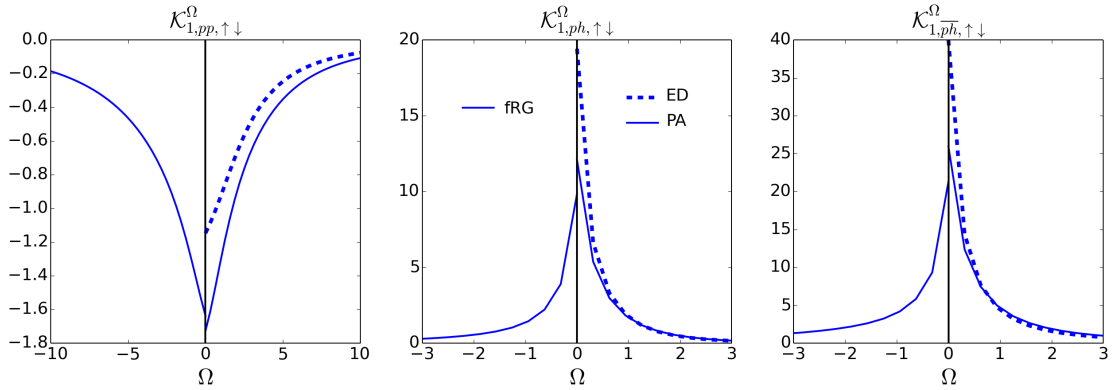

Figure 6.6.: Same as Fig. 6.1, but for $U = 4$. [166]

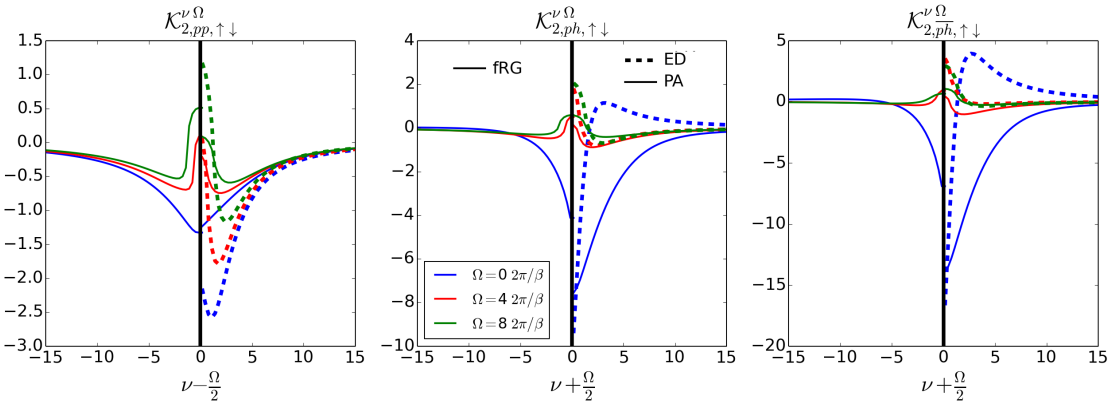

Figure 6.7.: Same as Fig. 6.2, but for $U = 4$. [166]

evaluate in an unbiased way their intrinsic performance in the most challenging strong-coupling regime.

Due to the perturbative nature of fRG and PA, the situation changes drastically in the regime of stronger coupling. The corresponding results for $U = 4$ are presented for $\mathcal{K}_{1,\uparrow\downarrow}$ and $\mathcal{K}_{2,\uparrow\downarrow}$ in Figs. 6.6 and 6.7 respectively. Note that, for this value of the interaction, we are clearly in the non-perturbative regime, as divergencies [123, 133, 171, 172, 176] are already present in the exact vertices obtained by ED. For both, PA and fRG, $\mathcal{K}_{1,\uparrow\downarrow}$ shows already strong deviations from the exact results, while the qualitative structures are still captured. These deviations are particularly enhanced in the *ph* and $\overline{ph}$ channel. In the case of $\mathcal{K}_{2,\uparrow\downarrow}$ qualitative features are missed by the PA and fRG, in particular for $\Omega = 0$, while a qualitative agreement is still achieved for finite transfer frequency. Also for the self-energy, shown in the right panel of Fig. 6.5, strong deviations are observed in both cases. As the main structures of the rest function $\mathcal{R}$ are neither reproduced by PA nor by fRG, we show only one example for this comparison in Fig. 6.8 (the full vertices are reported in the supplements). Since this diagrammatic class is at least fourth order in the interaction, the strongest deviations were to be expected here.

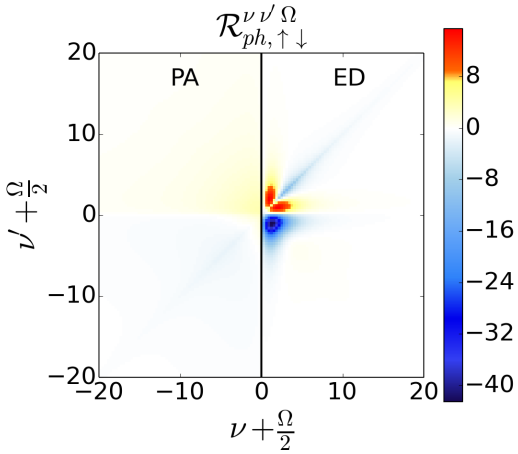

Figure 6.8.: Comparison of $\mathcal{R}_{ph,\uparrow\downarrow}$ obtained by means of PA with the exact result. Here, $U = 4$. [166]

6.1 Neglecting the asymptotics

Let us now discuss the importance of considering asymptotic functions in numerical implementations. In this regard, we present in Fig. 6.9 results for $\mathrm{Im}\,\Sigma(i\nu_0)/U^2$ as a function of U calculated by fRG and PA, with and without asymptotic functions, and compare them with the exact ED data. For these calculations, a frequency grid of $64 \times 64 \times 128$ Matsubara frequencies was used for the

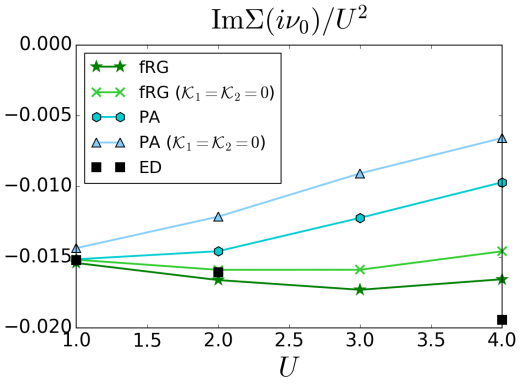

Figure 6.9.: Comparison of $\mathrm{Im}\,\Sigma(i\nu_0)/U^2$ for the SIAM with $\beta = 20$ and $\Delta(0) = D = 1$ as obtained by fRG and PA with and without ($\mathcal{K}_1 = \mathcal{K}_2 = 0$) high-frequency asymptotics, compared with ED for $\nu_0 = \frac{\pi}{\beta}$.

reducible vertex functions. In the large frequency domain, we used Eq. (4.2) and $\Phi_{r,\text{asympt.}} \approx 0$ respectively. We observe that the results for both, fRG and PA, are strongly affected if we include the asymptotic functions in the calculations: The comparison with the exact result improves by a substantial amount. This is a strong indication of the importance of a correct description of the high-frequency part of the vertex function in all vertex-based numerical implementations.

6.2 Higher order corrections in fRG

In this section, we provide a quantitative comparison between the SIAM results as obtained by means fRG in its one- and two-loop implementation. To this aim, we compare in Fig. 6.10 the quantities $\mathcal{K}^{\Omega=0}_{1,ph,\uparrow\downarrow}$, $\mathcal{K}^{\nu_0(\Omega=0)}_{2,ph,\uparrow\downarrow}$, as well as $\max_{\nu\nu'} |\mathcal{R}^{\nu\nu'(\Omega=0)}_{ph,\uparrow\downarrow}|$ normalized by their leading order[2] in U, to the exact ED results as well as to the PA. Consistently to our expectations, we find that the two-loop corrections yield a systematic improvement of the $\mathcal{K}_1$, $\mathcal{K}_2$ and $\mathcal{R}$ functions acquired during the flow, in particular for larger values of the interaction.

More specifically, for $\mathcal{K}_{1,ph,\uparrow\downarrow}$ the two-loop corrections have a minor effect in the weak-coupling regime, whereas an excellent agreement with the exact results is achieved already at the one-loop level. At larger U, the one-loop scheme strongly overestimates $\mathcal{K}_{1,ph,\uparrow\downarrow}$. Here, the two-loop corrections yield a substantial improvement over the one-loop scheme, while underestimating $\mathcal{K}_{1,ph,\uparrow\downarrow}$. We also note the strongly improved agreement of the two-loop fRG with the PA, which is a trend to be expected, since the two-loop scheme allows to include higher orders of the reducible diagrams in an exact way.

As for $\mathcal{K}_{2,ph,\uparrow\downarrow}$, we observe that already in the limit $U \to 0$ the one-loop scheme *fails* to reproduce the exact result. This can be attributed to the fact that the lowest order diagram in $\mathcal{K}_{2,ph,\uparrow\downarrow}$ is of order U^3, and is thus not captured exactly in the one-loop scheme. In particular for the U-flow, we numerically verify the factor $\frac{1}{2}$ (w.r.t. the exact result) already predicted diagrammatically at the end of Sec. 5.2, while for the Ω-flow we find, numerically, a factor of ~ 0.89 in all channels.

[2] For the particle-hole channel in the $\uparrow\downarrow$ spin configuration the bare bubble vanishes, resulting in a leading order $\mathcal{O}(U^3)$.

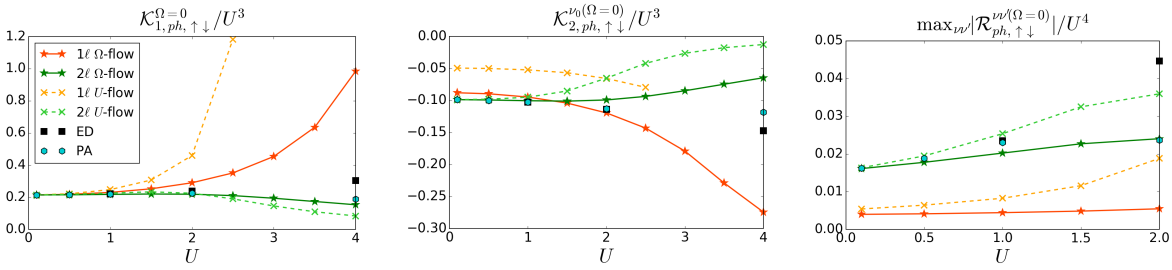

Figure 6.10.: Comparison of $\mathcal{K}^{\Omega=0}_{1,ph,\uparrow\downarrow}/U^3$, $\mathcal{K}^{\nu_0(\Omega=0)}_{2,ph,\uparrow\downarrow}/U^3$, and $\max_{\nu\nu'}|\mathcal{R}^{\nu\nu'(\Omega=0)}_{ph,\uparrow\downarrow}|/U^4$ ($\nu_0 = \frac{\pi}{\beta}$) for fRG in the one-loop (1ℓ) and two-loop (2ℓ) implementation, for both the Ω- and U-flow, with ED and PA. We note that the one-loop U-flow diverges for $U = 3$ or larger.

For larger values of U, we observe a behavior similar to the one described for $\mathcal{K}_{1,ph,\uparrow\downarrow}$, that is, a systematic improvement of the results if the two-loop corrections are included in fRG.

For $\mathcal{R}_{ph,\uparrow\downarrow}$ the trend is similar, while, being a function of $\mathcal{O}(U^4)$, the relative deviations from the exact results increase substantially. The predicted factor $\frac{1}{3}$ for $U \to 0$ is verified numerically, while for the Ω-flow we find factors 0.78, 0.25 and 0.78 in the *pp*, *ph* and $\overline{ph}$ channel respectively.

As for the comparison between the flow-schemes, consistently with the ratios in the weak-coupling regime, we observe that the simpler U-flow performs in general worse than the Ω-flow.

6.3 Efficiency of simplified parametrization schemes

In this section we preset results for the simplified parametrization scheme [134] presented in Eq. (5.2.9). It has found extensive use in the fRG community, as it allows for a substantial speedup of numerical calculations. In the left two panels of Fig. 6.11 we compare the self-energy at the first Matsubara frequency ($\mathrm{Im}\,\Sigma(i\nu_0)/U^2$) as well as its tail ($\lim_{\nu\to\infty} \mathrm{Im}\,\nu\Sigma(i\nu)/U^2$) for fRG one-loop and two-loop in their full and simplified ($\mathcal{K}_{\mathrm{eff}}$) implementation with PA and the exact results from ED.

For the self-energy at the first Matsubara frequency, we find a good agreement between the simplified parametrization scheme and the fully parametrized fRG implementation for both the one- and two-loop scheme, while the simpler scheme performs slightly worse in reproducing the exact results. In the case of the self-energy tail, the situation is reversed. Here, the aforementioned deviations of the fRG from ED are indeed cured by the simplified parametrization scheme.

To capture the effect of the simplified approximation scheme on the two-particle quantities we compare in the right panel of Fig. 6.11 the corresponding susceptibility in the *ph*-channel for the two-loop case. It is important to note, that χ cannot be directly extracted from $\mathcal{K}_{\mathrm{eff}}$ using Eq. (4.3) due to the effective inclusion of $\mathcal{K}_2$ and $\mathcal{R}$. Instead, we calculate the susceptibility after the flow by calculating explicitly the bare and vertex-corrected bubble according to equation Eq. (B.1b) (VC). This is compared, for an interaction value $U = 4$, to $\chi = \mathcal{K}_1/U^2$ and the corresponding PA and ED data. We find that the simplified parametrization fails to qualitatively reproduce the exact susceptibility, while the other approximations, although underestimating χ, compare qualitatively

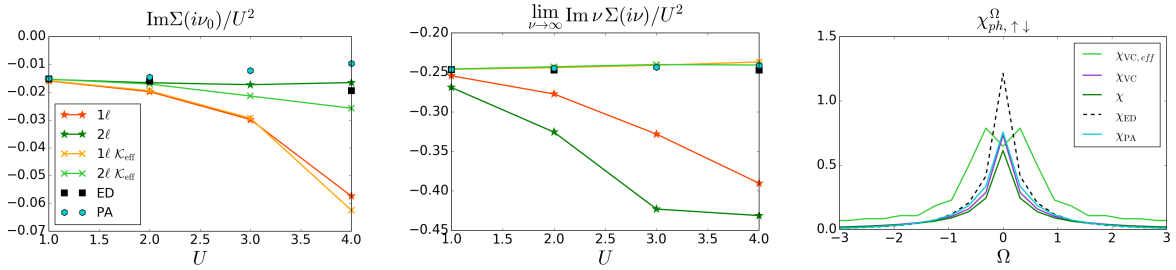

Figure 6.11.: Left two panels: Comparison of $\mathrm{Im}\,\Sigma(i\nu_0)/U^2$ and $\lim_{\nu\to\infty}\mathrm{Im}\,\nu\Sigma(i\nu)/U^2$ for fRG one-loop and two-loop with the corresponding simplified schemes introduced previously ($\mathcal{K}_{\mathrm{eff}}$, see Eq. (5.2.9)), PA and ED. Right panel: Comparison of the susceptibility χ in the *ph*-channel for $U = 4$ as obtained by means of Eq. (B.1b) after the two-loop fRG flow (χ_{VC}) in the conventional and the simplified scheme (eff). This is compared to the susceptibility χ obtained directly from Eq. (4.3) as well as the PA and ED result. [166]

well with ED[3].

While the parametrization scheme of Eq. (5.2.9) performs well for one-particle quantities, we find that the qualitative features of the susceptibility are badly reproduced. Further, we observe that the ambiguities in the definition of the flow equations for the case of finite temperatures (see p. 38) turn out to have a substantial effect on the results for larger values of the interaction. These are strong arguments for the fully parametrized schemes, that capture, consistently, all frequency structures of the two-particle vertex function.

[3]We note that χ calculated after the full two-loop flow by means of Eq. (B.1) yields a result different from $\mathcal{K}_1/U^2$. This is connected to the specific approximations introduced in the fRG, and is absent in the fully self-consistent PA.

Chapter 7

Conclusion

As it also emerges from the studies of correlated systems I performed in the first part of my PhD work, one of the most challenging aspects in the contemporary research in condensed matter physics is the theoretical treatment of correlation effects in the non-perturbative regime. While recently, several promising quantum field theoretical schemes have been proposed (including one by myself), their actual implementation calls for a significant improvement of the current algorithmic procedures. In particular, most of them are based on a Feynman diagrammatic expansion around a correlated starting point. This means to replace the bare electronic interaction with a dynamical effective one, which includes non-perturbatively, through the two-particle vertex function, a significant part of the correlations from the very beginning. As the plain treatment of these vertex functions is prohibitive in most of the cases, the development of efficient ways to include them in the current algorithms was mandatory.

To this aim, in the main part of this thesis, we have presented a detailed analysis of the diagrammatic content of the two-particle vertex functions. In particular by focusing on their two-particle reducible parts, we could identify the different contributions to their high-frequency asymptotics as diagrammatic classes with a reduced frequency (and momentum) dependence, and established a connection to the (physical) susceptibilities and the fermion-boson vertices. The gained insights allow to devise efficient parametrization schemes for the two-particle vertex functions. We then discussed the algorithmic details necessary for the application of these ideas in numerical (and analytical) studies, considering as specific examples the functional renormalization group approach and the parquet approximation. In order to verify the correct treatment of the high-frequency asymptotics, we benchmarked our numerical implementations for a SIAM against exact calculations from ED. Finally, we tested the intrinsic performance of the approaches in the most challenging strong coupling regime.

These progresses pave the way towards a full numerical treatment of correlations at the two-particle level, which is pivotal for all vertex-based quantum many-body methods. In particular, we foresee to apply these ideas to treat non-local correlations beyond the dynamical mean-field theory by means of its cutting-edge diagrammatic extensions, like the DF, the DMF^{2}RG, the DΓA and the recently introduced QUADRILEX approach [148].

Appendix

Appendix A

Notations

In this appendix we present the definitions of the two-particle Green's and (1PI) vertex functions following the notation of Refs. [132, 145, 168], and further specify the notations used throughout this thesis. Let us start by defining the two-particle Green's function G_2, which reads

$$G_{2,\sigma_1\sigma_2\sigma_3\sigma_4}(x_1, x_2, x_3, x_4) = \langle \mathcal{T}\big(c^\dagger_{\sigma_1}(x_1)c_{\sigma_2}(x_2)c^\dagger_{\sigma_3}(x_3)c_{\sigma_4}(x_4)\big)\rangle. \tag{A.1}$$

Here, $c^\dagger$ (c) represent the fermionic creation (annihilation) operators with an associated spin $\sigma = \{\uparrow, \downarrow\}$, the brackets $\langle ... \rangle$ imply a thermal expectation value, $\mathcal{T}$ denotes the time-ordering operator, and $x = (\mathbf{R}_i, \tau)$ is a four-vector including the lattice site $\mathbf{R}_i$ and the imaginary time τ. First, we note that the number of spin combinations can be reduced by considering spin conservation and the antisymmetry of the two-particle Green's function, allowing us to consider only

$$G_{2,\sigma\sigma'}(x_1, x_2, x_3, x_4) = G_{2,\sigma\sigma\sigma'\sigma'}(x_1, x_2, x_3, x_4), \tag{A.2}$$

Further, by making use of time and space-translational invariance, we can always shift all arguments such that $x_4 = 0$. This property can be exploited to yield momentum and frequency conservation, i.e.

$$G^{k_1k_2k_3k_4}_{2,\sigma\sigma'} = \beta\, V_{\mathrm{BZ}}\, \delta_{k_1+k_3,k_2+k_4} \times \underbrace{\int\!\!\!\!\!\!\diagup dx_i\; G_{2,\sigma\sigma'}(x_1, x_2, x_3, 0)e^{-ik_1x_1}e^{ik_2x_2}e^{-ik_3x_3}}_{G^{k_1k_2k_3}_{2,\sigma\sigma'}}, \tag{A.3}$$

where $k = (\mathbf{k}, i\nu)$ represents the four-vector with momentum $\mathbf{k}$ and Matsubara frequency $i\nu$. Here, we introduced the generalized four-vector integration $\int\!\!\!\!\!\!\diagup dx = \sum_{\mathbf{R}_i}\int_0^\beta d\tau$, that combines the lattice-site summation with the imaginary time integration. The corresponding object in dual space reads $\int\!\!\!\!\!\!\diagup dk = \frac{1}{V_{\mathrm{BZ}}}\int_{\mathrm{BZ}} d\mathbf{k}\frac{1}{\beta}\sum_{i\nu}$, where BZ denotes the first Brillouin zone with a volume V_{BZ}.

To obtain the two-particle vertex function F, we subtract the two possible contractions of the composite operator within the brackets (all disconnected diagrams) and subsequently cut the ex-

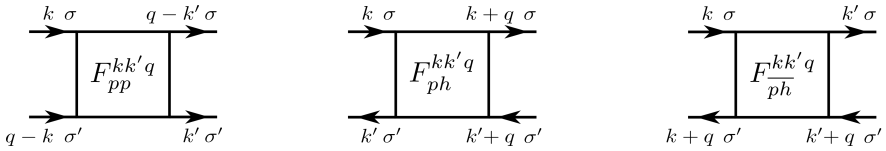

Figure A.1.: Notations of the vertex functions in the three different scattering channels.

ternal fermionic legs

$$F_{\sigma\sigma'}^{k_1k_2k_3} = -G^{-1}(k_1)G^{-1}(k_3)\Big[\underbrace{G_{2,\sigma\sigma'}^{k_1k_2k_3} - G(k_1)G(k_3)\left(\delta_{k_1,k_2} - \delta_{k_1,k_4}\delta_{\sigma,\sigma'}\right)}_{G_{2,c,\sigma\sigma'}^{k_1k_2k_3}}\Big]G^{-1}(k_2)G^{-1}(k_4). \tag{A.4}$$

Here, the additional minus sign is a matter of convention, which is commonly introduced such that the lowest order contribution of F is given by U. Note that $SU(2)$ symmetry is here and in the following explicitly assumed.

While so far we considered the two-particle Green and vertex function with purely fermionic arguments, one often introduces 'mixed' notations using a bosonic and two fermionic arguments, in order to highlight a specific scattering channel. The adoption of these notations is essential for the decomposition scheme presented in this thesis, in particular for the reducible vertex functions. Hence, we introduce the particle-particle (pp) notation

$$F_{pp,\sigma\sigma'}^{kk'q} = F_{\sigma\sigma'}^{(k)(q-k')(q-k)} \tag{A.5}$$

the particle-hole (ph) notation

$$F_{ph,\sigma\sigma'}^{kk'q} = F_{\sigma\sigma'}^{(k)(k+q)(k'+q)} \tag{A.6}$$

and the transverse particle-hole ($\overline{ph}$) notation

$$F_{\overline{ph},\sigma\sigma'}^{kk'q} = F_{\sigma\sigma'}^{kk'(k'+q)}, \tag{A.7}$$

which are defined correspondingly for G_2 and the other vertex functions ϕ, $\Lambda_{2\mathrm{PI}}$ and Γ (see Chap. 3). A diagrammatic representation of the three notations is shown in Fig. A.1. Let us note that in general, for the two-particle vertex F and also for the fully irreducible vertex $\Lambda_{2\mathrm{PI}}$, none of these notations is a priori more favorable, each of them just being an alternative way to look at the same physical object [168].

Finally, we introduce susceptibilities in all scattering channels,

$$\chi_{pp,\sigma\sigma'}^{q} = (1-\delta_{\sigma\sigma'})\sum\!\!\!\!\!\!\int dk\, dk'\, G_{2,c,pp,\sigma\sigma'}^{kk'q} + (1-\delta_{\sigma\sigma'})\sum\!\!\!\!\!\!\int dk\, G(q-k)G(k), \tag{A.8a}$$

$$\chi_{ph,\sigma\sigma'}^{q} = \sum\!\!\!\!\!\!\int dk\, dk'\, G_{2,c,ph,\sigma\sigma'}^{kk'q} - \delta_{\sigma,\sigma'}\sum\!\!\!\!\!\!\int dk\, G(k)G(k+q), \tag{A.8b}$$

$$\chi_{\overline{ph},\sigma\sigma'}^{q} = \sum\!\!\!\!\!\!\int dk\, dk'\, G_{2,c,\overline{ph},\sigma\sigma'}^{kk'q} + \sum\!\!\!\!\!\!\int dk\, G(k)G(k+q). \tag{A.8c}$$

They can be easily combined to yield the physical susceptibilities in the density, magnetic, singlet and triplet channel [132].

Appendix B

An alternative approach to the asymptotic extraction

In this part we describe an approach that extracts the asymptotic functions directly from the full vertex function F. This procedure was employed to acquire all presented high-frequency results for the ED vertices, and is based on the fact that one can write down explicit Feynman diagrams for all asymptotic functions. These consist of all possible ways of pinching two external legs of F into one bare vertex U. Since the latter is purely local in space and time, the dependence on two fermionic arguments is replaced by a single bosonic (transfer) one. The resulting diagrams for $\mathcal{K}_1$ are shown in Fig. B.1, and read explicitly

$$\begin{aligned}\mathcal{K}^{q}_{1,pp,\sigma\sigma'} = \quad & U^2(1-\delta_{\sigma\sigma'})\sum\!\!\!\!\!\!\int dk_i\, G(k_1)G(q-k_1)F^{k_1k_2q}_{pp,\sigma\sigma'}G(q-k_2)G(k_2) \\ & -U^2(1-\delta_{\sigma\sigma'})\sum\!\!\!\!\!\!\int dk_1\, G(q-k_1)G(k_1),\end{aligned} \tag{B.1a}$$

$$\mathcal{K}^{q}_{1,ph,\sigma\sigma'} = \quad U^2\sum\!\!\!\!\!\!\int dk_i\, G(k_1)G(k_1+q)F^{k_1k_2q}_{ph,\sigma\sigma'}G(k_2)G(k_2+q) + U^2\delta_{\sigma,\sigma'}\sum\!\!\!\!\!\!\int dk_1\, G(k_1)G(k_1+q), \tag{B.1b}$$

$$\mathcal{K}^{q}_{1,\overline{ph},\sigma\sigma'} = \quad U^2\sum\!\!\!\!\!\!\int dk_i\, G(k_1)G(k_1+q)F^{k_1k_2q}_{\overline{ph},\sigma\sigma'}G(k_2)G(k_2+q) - U^2\sum\!\!\!\!\!\!\int dk_1\, G(k_1)G(k_1+q). \tag{B.1c}$$

Here $\overline{\sigma}$ denotes the opposite spin of σ, and $SU(2)$ symmetry is explicitly assumed. In the case of $\mathcal{K}_2$ one introduces just one additional bare vertex, as shown in Fig. B.2. Note that here, the previously determined $\mathcal{K}_1$ has to be subtracted. The equations in all scattering channels then read

$$\mathcal{K}^{kq}_{2,pp,\sigma\sigma'} = -U\sum\!\!\!\!\!\!\int dk_1\, G(q-k_1)F^{kk_1q}_{pp,\sigma\sigma'}G(k_1) - \mathcal{K}^{q}_{1,pp,\sigma\sigma'}, \tag{B.2a}$$

$$\mathcal{K}^{kq}_{2,ph,\sigma\sigma'} = \quad U\sum\!\!\!\!\!\!\int dk_1\, G(k_1)F^{kk_1q}_{ph,\sigma\overline{\sigma'}}G(k_1+q) - \mathcal{K}^{q}_{1,ph,\sigma\sigma'}, \tag{B.2b}$$

$$\mathcal{K}^{kq}_{2,\overline{ph},\sigma\sigma'} = -U\sum\!\!\!\!\!\!\int dk_1\, G(k_1)G(k_1+q)\times\left[\delta_{\sigma\sigma'}F^{kk_1q}_{\overline{ph},\uparrow\downarrow} + (1-\delta_{\sigma\sigma'})F^{kk_1q}_{\overline{ph},\uparrow\downarrow}\right] - \mathcal{K}^{q}_{1,\overline{ph},\sigma\sigma'}. \tag{B.2c}$$

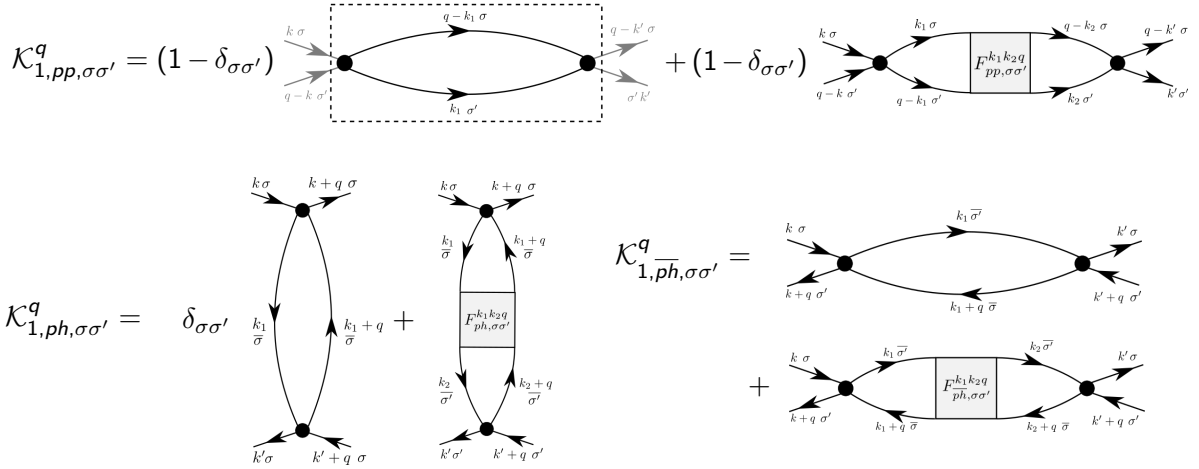

Figure B.1.: Diagrammatic representation of the $\mathcal{K}_1$ functions in the three different channels. As denoted in the first diagram, the external lines are to be excluded, making the k and k' arguments redundant. Here, $\overline{\sigma}$ denotes the opposite spin of σ.

Further, by exploiting the symmetry relations shown in Appendix C, one can easily derive $\overline{\mathcal{K}}_2$ from $\mathcal{K}_2$.

As it is typical within an ED algorithm for a SIAM, the values for F are known numerically for a finite grid in the frequency domain. Thus, in the first calculation of the aforementioned diagrams according to Eqs. (B.1) and (B.2) we have to make a rough approximation for F (i.e. $F = U$) in the large-frequency domain, which will introduce an error. To improve on this 'one-shot' calculation of the diagrams, we exploit a self-consistent scheme:

- I: Initialize the $\mathcal{K}_1$'s and $\mathcal{K}_2$'s to 0. Their grids may deviate from the grid for F.
- II: Calculate a set of new $\mathcal{K}_1$'s and $\mathcal{K}_2$'s according to Eqs. (B.1) and (B.2).
- III: Rebuild the vertex in an arbitrarily large region (as needed) using the updated asymptotic functions.
- IV: Continue from II till convergence

Once the asymptotic functions are fully converged, we can directly determine the localized structures using

$$\Lambda_{\mathrm{2PI}} + \sum_r \mathcal{R}_r = F - \left(\sum_r \mathcal{K}_{1,r} + \mathcal{K}_{2,r} + \overline{\mathcal{K}}_{2,r} \right). \tag{B.3}$$

Further, since, at this point, we have F available in the full frequency domain, we can use this additional information to determine also all the Φ functions on an arbitrarily large frequency grid by means of the Bethe-Salpeter equations (5.3.1). If needed, $\mathcal{R}$ and Λ_{2PI} can then be determined by Eq. (5.2) and Eq. (1.3.2) respectively.

The approach described in this appendix was used to compute all the exact asymptotic functions and reducible vertices presented in Chap. 6, from ED calculations, originally performed on a fermionic

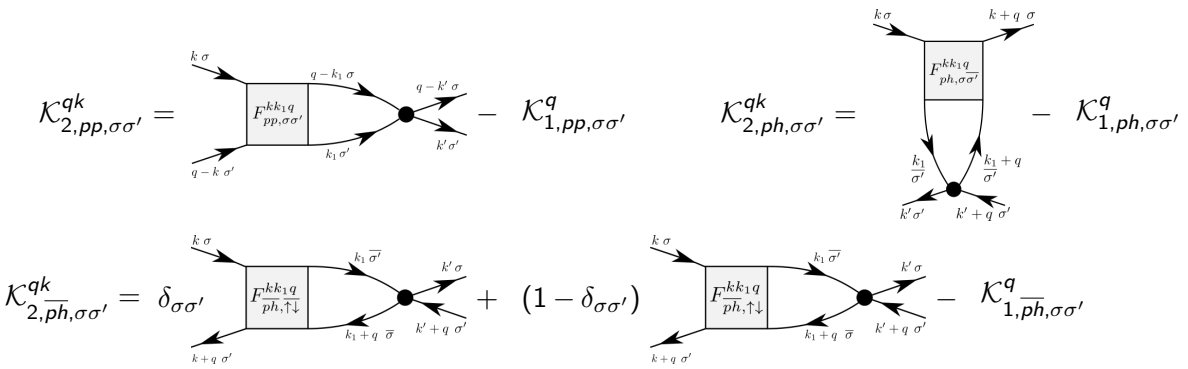

Figure B.2.: Diagrammatic representation of the $\mathcal{K}_2$ functions in the three different channels. Here, $\overline{\sigma}$ denotes the opposite spin of σ, while $SU(2)$ symmetry is explicitly assumed.

frequency grid of $128 \times 128 \times 128$ Matsubara frequencies. While here we are dealing with a purely local vertex, we stress that this approach is equally applicable in the non-local case.

Appendix C

Symmetries

C.1 Symmetries of $\mathcal{K}_1$ and $\mathcal{K}_2$

In this section we summarize the symmetries of the previously introduced asymptotic functions. Before addressing the specific physical symmetries of the system of our interest, which provide useful relations for $\mathcal{K}_1$ and $\mathcal{K}_2$, we provide some fundamental relations which hold [132, 177, 178] independently of the system under analysis. First, we consider the exchange of two (fermionic) annihilation operators in the time-ordered matrix element of Eq. (A.3), which, as a consequence of the Pauli-principle, yields a minus sign (also referred to as 'crossing symmetry' [132, 177, 178]). Diagrammatically speaking, this corresponds to an exchange of two outgoing lines. For $\mathcal{K}_1$, this operation leads to the following relations:

$$\mathcal{K}^q_{1,pp,\sigma\sigma'} = -\mathcal{K}^q_{1,pp,\overline{\sigma\sigma'}} \tag{C.1.1a}$$

$$\mathcal{K}^q_{1,ph,\sigma\sigma'} = -\mathcal{K}^q_{1,\overline{ph},\overline{\sigma\sigma'}} \tag{C.1.1b}$$

$$\mathcal{K}^q_{1,\overline{ph},\sigma\sigma'} = -\mathcal{K}^q_{1,ph,\overline{\sigma\sigma'}}. \tag{C.1.1c}$$

Here, $\overline{\sigma\sigma'}$ denotes a spin-flip for all external indices. While for the *pp* channel one finds relations between different spin configurations within the same channel, the *ph* and $\overline{ph}$-channel are interchanged. Similarly, for $\mathcal{K}_2$ one finds:

$$\mathcal{K}^{kq}_{2,pp,\sigma\sigma'} = -\mathcal{K}^{kq}_{2,pp,\overline{\sigma\sigma'}} \tag{C.1.2a}$$

$$\mathcal{K}^{kq}_{2,ph,\sigma\sigma'} = -\mathcal{K}^{kq}_{2,\overline{ph},\overline{\sigma\sigma'}} \tag{C.1.2b}$$

$$\mathcal{K}^{kq}_{2,\overline{ph},\sigma\sigma'} = -\mathcal{K}^{kq}_{2,ph,\overline{\sigma\sigma'}}. \tag{C.1.2c}$$

A second generic operation involves the simultaneous exchange of both annihilation and creation operators in Eq. A.3. Diagrammatically, this corresponds to an exchange of both the incoming and

Symmetries	$\mathcal{K}_{1,r}$	$\mathcal{K}_{2,r}$
SU(2)	$\mathcal{K}^{q}_{1,r,\sigma\sigma'} = \mathcal{K}^{q}_{1,r,\overline{\sigma}\,\overline{\sigma'}}$ $\mathcal{K}^{q}_{1,r,\sigma\sigma} = \mathcal{K}^{q}_{1,r,\sigma\sigma'} + \mathcal{K}^{q}_{1,r,\overline{\sigma\sigma'}}$	$\mathcal{K}^{kq}_{2,r,\sigma\sigma'} = \mathcal{K}^{kq}_{2,r,\overline{\sigma}\,\overline{\sigma'}}$ $\mathcal{K}^{kq}_{2,r,\sigma\sigma} = \mathcal{K}^{kq}_{2,r,\sigma\sigma'} + \mathcal{K}^{kq}_{2,r,\overline{\sigma\sigma'}}$
Time reversal	$\mathcal{K}^{q}_{1,r,\sigma\sigma'} = \mathcal{K}^{q}_{1,r,\sigma'\sigma}$	$\mathcal{K}^{kq}_{2,r,\sigma\sigma'} = \overline{\mathcal{K}}^{kq}_{2r,\sigma\sigma'}$
Particle hole	$\left(\mathcal{K}^{q}_{1,r,\sigma\sigma'}\right)^{*} = \mathcal{K}^{(\Omega,-\mathbf{q})}_{1,r,\sigma\sigma'}$	$\left(\mathcal{K}^{kq}_{2,r,\sigma\sigma'}\right)^{*} = \mathcal{K}^{(\nu,\mathbf{\Pi}-\mathbf{k})(\Omega,-\mathbf{q})}_{2,r,\sigma\sigma'}$

Table C.1.: Symmetry table for $\mathcal{K}_1$ and $\mathcal{K}_2$. Here, $\mathbf{\Pi} = (\pi, \pi, ...)$ represents the (d-dimensional) 'antiferromagnetic momentum' in the case of a simple (hyper)cubic lattice with lattice constant $a = 1$.

outgoing particles. In this case we end up with the following relations for $\mathcal{K}_1$:

$$\mathcal{K}^{q}_{1,pp,\sigma\sigma'} = \mathcal{K}^{q}_{1,pp,\sigma'\sigma} \tag{C.1.3a}$$
$$\mathcal{K}^{q}_{1,ph,\sigma\sigma'} = \mathcal{K}^{-q}_{1,ph,\sigma'\sigma} \tag{C.1.3b}$$
$$\mathcal{K}^{q}_{1,\overline{ph},\sigma\sigma'} = \mathcal{K}^{-q}_{1,\overline{ph},\sigma'\sigma}. \tag{C.1.3c}$$

For $\mathcal{K}_2$ one obtains:

$$\mathcal{K}^{kq}_{2,pp,\sigma\sigma'} = \mathcal{K}^{(q-k)q}_{2,pp,\sigma'\sigma} \tag{C.1.4a}$$
$$\mathcal{K}^{kq}_{2,ph,\sigma\sigma'} = \mathcal{K}^{(k+q)(-q)}_{2,ph,\sigma'\sigma} \tag{C.1.4b}$$
$$\mathcal{K}^{kq}_{2,\overline{ph},\sigma\sigma'} = \mathcal{K}^{(k+q)(-q)}_{2,\overline{ph},\sigma'\sigma}. \tag{C.1.4c}$$

While for this operation all the corresponding channels are conserved, the diagrammatic class changes from $\mathcal{K}_2$ to $\overline{\mathcal{K}}_2$ in the case of the ph and $\overline{ph}$ channel.

To conclude the discussion of the fundamental relations, we consider the complex conjugation operation, that leads to the following relations for $\mathcal{K}_1$:

$$\left(\mathcal{K}^{q}_{1,pp,\sigma\sigma'}\right)^{*} = \mathcal{K}^{-q}_{1,pp,\sigma'\sigma} \tag{C.1.5a}$$
$$\left(\mathcal{K}^{q}_{1,ph,\sigma\sigma'}\right)^{*} = \mathcal{K}^{-q}_{1,ph,\sigma'\sigma} \tag{C.1.5b}$$
$$\left(\mathcal{K}^{q}_{1,\overline{ph},\sigma\sigma'}\right)^{*} = \mathcal{K}^{q}_{1,\overline{ph},\sigma'\sigma}, \tag{C.1.5c}$$

Symmetries	$\mathcal{R}_r$
SU(2)	$\mathcal{R}^{kk'q}_{r,\sigma\sigma'} = \mathcal{R}^{kk'q}_{r,\bar{\sigma}\bar{\sigma'}}$ $\mathcal{R}^{kk'q}_{r,\sigma\sigma} = \mathcal{R}^{kk'q}_{r,\sigma\sigma'} + \mathcal{R}^{kk'q}_{r,\bar{\sigma}\sigma'}$
Time reversal	$\mathcal{R}^{kk'q}_{r,\sigma\sigma'} = \mathcal{R}^{k'kq}_{r,\sigma'\sigma}$
Particle hole	$(\mathcal{R}^{kk'q}_{r,\sigma\sigma'})^* = \mathcal{R}^{(\nu,\mathbf{\Pi}-\mathbf{k})(\nu',\mathbf{\Pi}-\mathbf{k}')(\Omega,-\mathbf{q})}_{r,\sigma\sigma'}$

Table C.2.: Symmetry table for $\mathcal{R}$. Note that the same table holds for the two-particle reducible vertex functions Φ_r.

and for $\mathcal{K}_2$:

$$\left(\mathcal{K}^{kq}_{2,pp,\sigma\sigma'}\right)^* = \mathcal{K}^{(-k)(-q)}_{2,pp,\sigma'\sigma} \tag{C.1.6a}$$

$$\left(\mathcal{K}^{kq}_{2,ph,\sigma\sigma'}\right)^* = \mathcal{K}^{(-k)(-q)}_{2,ph,\sigma'\sigma} \tag{C.1.6b}$$

$$\left(\mathcal{K}^{kq}_{2,\overline{ph},\sigma\sigma'}\right)^* = \mathcal{K}^{(-k-q)q}_{2,\overline{ph},\sigma'\sigma}. \tag{C.1.6c}$$

Using these fundamental relations, we can formulate the system-related physical symmetries, namely $SU(2)$, time reversal and particle-hole symmetry, in a channel-independent way. The results are summarized in Table C.1. Note that for the particle-hole symmetry, the relations differ for the frequency and momentum dependence. While in the purely local case, this symmetry implies a vanishing imaginary part of all two-particle quantities, this holds only for specific lattice-dependent **k** vectors in the non-local case.

C.2 Symmetries of $\mathcal{R}$

For the sake of completeness we report the symmetries of the remaining diagrammatic class, namely the rest function $\mathcal{R}$, which hold equally for the reducible vertex functions Φ. As shown above, the first set of fundamental relations results from exchanging two outgoing particles. We find the following relations for $\mathcal{R}$ in the different channels:

$$\mathcal{R}^{kk'q}_{pp,\sigma\sigma'} = -\mathcal{R}^{(k)(q-k')q}_{pp,\bar{\sigma}\sigma'} \tag{C.2.1a}$$

$$\mathcal{R}^{kk'q}_{ph,\sigma\sigma'} = -\mathcal{R}^{kk'q}_{\overline{ph},\bar{\sigma}\sigma'} \tag{C.2.1b}$$

$$\mathcal{R}^{kk'q}_{\overline{ph},\sigma\sigma'} = -\mathcal{R}^{kk'q}_{ph,\bar{\sigma}\sigma'}. \tag{C.2.1c}$$

By means of the simultaneous exchange of both incoming and outgoing particles we obtain:

$$\mathcal{R}^{kk'q}_{pp,\sigma\sigma'} = \mathcal{R}^{(q-k)(q-k')q}_{pp,\sigma'\sigma} \tag{C.2.2a}$$
$$\mathcal{R}^{kk'q}_{ph,\sigma\sigma'} = \mathcal{R}^{(k'+q)(k+q)(-q)}_{ph,\sigma'\sigma} \tag{C.2.2b}$$
$$\mathcal{R}^{kk'q}_{\overline{ph},\sigma\sigma'} = \mathcal{R}^{(k'+q)(k+q)(-q)}_{\overline{ph},\sigma'\sigma}. \tag{C.2.2c}$$

Finally, the complex conjugation operation leads to the following relations:

$$\left(\mathcal{R}^{kk'q}_{pp,\sigma\sigma'}\right)^* = \mathcal{R}^{(-k')(-k)(-q)}_{pp,\sigma'\sigma} \tag{C.2.3a}$$
$$\left(\mathcal{R}^{kk'q}_{ph,\sigma\sigma'}\right)^* = \mathcal{R}^{(-k')(-k)(-q)}_{ph,\sigma'\sigma} \tag{C.2.3b}$$
$$\left(\mathcal{R}^{kk'q}_{\overline{ph},\sigma\sigma'}\right)^* = \mathcal{R}^{(-k-q)(-k'-q)q}_{\overline{ph},\sigma'\sigma}. \tag{C.2.3c}$$

In the same way as for $\mathcal{K}_1$ and $\mathcal{K}_2$, the fundamental relations for $\mathcal{R}$ allow us to express the physical symmetries in a channel-independent way, see Table C.2.

Supplements

Personal contribution to publications

In this part I want to give a brief summary of my personal contribution to the publications that, as presented in this supplement, form the basis of this cumulative thesis. First and foremost, let me stress that the excellent guidance of my supervisor Prof. S. Andergassen as well as my co-supervisor Prof. A. Toschi have obviously had a strong influence on the development and the presentation of the ideas and calculations that are presented in this thesis.

Magneto-electric Spectroscopy of Andreev Bound States in Josephson Quantum Dots

[Phys. Rev. B **94**, 085151] (2016)

This work was initiated in the time of my master thesis at the RWTH Aachen under the supervision of V. Meden and S. Andergassen, and extended during my PhD as a collaboration with S. Florens. Generalizing previous studies [134,179–181] on the Josephson current through a quantum dot to the case of finite magnetic fields, I computed the spectral properties with the functional renormalization group in a large parameter regime. Additional analytical insights where gained by means of my study of the exactly solvable large gap limit both for finite and vanishing magnetic field, allowing for a better understanding of the physical behavior also at finite gaps. Eventually, my numerical fRG results and analytical derivations were complemented by numerical results obtained with the SCABS theory [54] by S. Florens and T. Meng. My contribution consists further in writing most of the manuscript (except for the SCABS theory section).

Correlated Starting Points for the Functional Renormalization Group

[Phys. Rev. B **91**, 045120] (2015)

In the frame of my work on Josephson quantum dots, I considered also an extended fRG approach that aimed to use the exact large-gap solution as a starting point of the functional renormalization group flow, in order to improve further the fRG results and to resolve some numerical artifacts that we observed in the case of vanishing magnetic fields in the π-phase. A similar idea had been recently proposed by our groups, that is, to perform fRG calculations starting from the non-perturbative DMFT solution of the $2d$ Hubbard model, in order to include the non-local correlations neglected by DMFT by means of the fRG flow [15]. In this frame, I investigated the connection of these recent strong-coupling fRG schemes with the similar dual fermion approaches [16, 118–127, 141]. This lead to a generalized formulation of the fRG for correlated starting points, and the deeper connection to fRG schemes operating with the auxiliary fermionic fields, as presented in Supp. I. These ideas were developed and formulated by me in collaboration with my colleague C. Taranto and under regular feedback from our collaborator A. Katanin. My own contribution also consisted

in writing most of the manuscript.

Efficient Implementation of the Parquet Equations: Role of the Reducible Vertex Function and its Kernel Approximation

[Phys. Rev. B **93** 165103 (2016)]

In the process of developing a general purpose second order functional-renormalization group code, that constitutes a substantial part of my PhD work, I had to address the problem of achieving a correct numerical treatment of two-particle vertex functions, in particular their high-frequency asymptotics. An extended scheme for this task was developed in the course of numerous discussions G. Li, and then implemented and tested independently by both of us. My contribution to this publication consists in the joint development of the ideas behind the asymptotic functions and the constant feedback in the formulation of the manuscript presented. Further, my independent implementation allowed to double-check these novel algorithmic ideas, and also to test and benchmark their performance.

Based on these initial ideas, I developed a deeper diagrammatic (and also physical) understanding of the asymptotic functions, which lead to the field-theoretical as well as algorithmic progresses presented in the main part of this thesis.

Appendix I

Magneto-electric spectroscopy of Andreev bound states in Josephson quantum dots

PHYSICAL REVIEW B **94**, 085151 (2016)

Magnetoelectric spectroscopy of Andreev bound states in Josephson quantum dots

Nils Wentzell,[1,2,3] Serge Florens,[4] Tobias Meng,[5] Volker Meden,[6] and Sabine Andergassen[1,3]
[1]*Faculty of Physics, University of Vienna, Boltzmanngasse 5, 1090 Wien, Austria*
[2]*Institute for Solid State Physics, Vienna University of Technology, 1040 Vienna, Austria*
[3]*Institut für Theoretische Physik and Center for Quantum Science, Universität Tübingen, Auf der Morgenstelle 14, 72076 Tübingen, Germany*
[4]*Institut Néel, CNRS & Université Grenoble Alpes, BP 166, F-38042 Grenoble, France*
[5]*Institut für Theoretische Physik, Technische Universität Dresden, 01062 Dresden, Germany*
[6]*Institut für Theorie der Statistischen Physik, RWTH Aachen University and JARA Fundamentals of Future Information Technology, 52056 Aachen, Germany*
(Received 31 May 2016; revised manuscript received 3 August 2016; published 30 August 2016)

We theoretically investigate the behavior of Andreev levels in a single-orbital interacting quantum dot in contact with superconducting leads, focusing on the effect of electrostatic gating and applied magnetic field, as relevant for recent experimental spectroscopic studies. In order to account reliably for spin-polarization effects in the presence of correlations, we extend here two simple and complementary approaches that are tailored to capture effective Andreev levels: the static functional renormalization group (fRG) and the self-consistent Andreev bound states (SCABS) theory. We provide benchmarks against the exact large-gap solution as well as renormalization group (NRG) calculations and find good quantitative agreement in the range of validity. The large flexibility of the implemented approaches then allows us to analyze a sizable parameter space, allowing us to get a deeper physical understanding into the Zeeman field, electrostatic gate, and flux dependence of Andreev levels in interacting nanostructures.

DOI: 10.1103/PhysRevB.94.085151

I. INTRODUCTION

Andreev bound states (ABS) in quantum dots connected to superconducting electrodes have been a subject of active research in recent years, both theoretically [1–50] and experimentally [51–84]. The understanding of ABS formation is not only of great interest for their potential use in quantum information devices, but also because they constitute a testbed for microscopic theories of nanostructures. Indeed, transport measurements in the normal state (obtained under the application of a sufficiently strong magnetic field to suppress the superconductivity in the leads) allow to extract in principle the basic parameters governing the quantum dot (local Coulomb interaction U, tunneling rate Γ, level position ϵ). These in turn determine the dispersion of the ABS in the superconducting state as a function of electrical gating, the superconducting phase difference ϕ, or with respect to a moderate magnetic field B. Several attempts for a precise description of ABS in quantum dots have been recently made in this direction [69,70,77], but only qualitative agreement could be obtained. In particular, microscopic calculations based on the widely used self-consistent Hartree-Fock approximation are not trustworthy except for the case of weak Coulomb interaction or large applied magnetic fields [40,49].

Alternative theories to mean-field approaches offer a trade-off between simplicity and accuracy. The simplest techniques are based on static renormalization group ideas, and have been formulated both within a perturbative expansion in the effective Coulomb interaction in the framework of the functional renormalization group (fRG) [48,85–88], or around the large gap limit by a self-consistent Andreev bound state picture (SCABS) [32,73,89]. Both techniques achieve surprisingly good agreement (in their range of validity) with full-scale numerical renormalization group (NRG) computations [90–100], while their low numerical cost allows us to efficiently explore the effective Andreev levels over the whole parameter space. While previous analytical renormalization group calculations have mainly focused on the particle-hole symmetric case (i.e., at the center of the odd charge Coulomb blockade diamond) and for zero magnetic field, we aim here at extending both the fRG and SCABS techniques to account for the full electric and magnetic tuning available in quantum dot devices. We will not consider here full second-order perturbation theory in the Coulomb repulsion U. Although this technique provides excellent results at particle-hole symmetry and zero magnetic field, once self-consistency on the effective pairing amplitude is properly taken into account [49,89], its accuracy is expected to degrade away from these two limits (in addition, a proliferation of diagrams makes the technique more cumbersome to use in absence of any symmetry).

The paper is organized as follows. In Sec. II we introduce the basic model of superconducting quantum dots, and describe how to obtain the position and weights of ABS from Green's function techniques in the presence of a Coulomb repulsion. The model is then solved mathematically in the special limit of infinite gap in the presence of both an external gate voltage and an applied magnetic field, which allows for a qualitative discussion of the physics. In Sec. III we briefly review the static functional renormalization group and the self-consistent Andreev bound state theory extensions to the case of finite magnetic field. Finally, we discuss our results in Sec. IV, starting with the case of zero magnetic field before considering the complete magnetoelectric spectroscopy of the Andreev levels. The various methods are tested against previous NRG results [93], in order to assess their validity range and possible breakdowns.

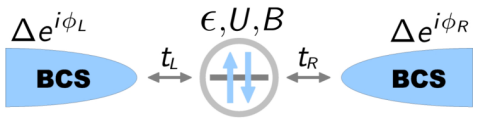

FIG. 1. Setup considered in this work. A quantum dot subject to a magnetic field B and an electrical gate ϵ is tunnel coupled to two superconducting BCS electrodes.

II. SUPERCONDUCTING QUANTUM DOT MODEL

A. The superconducting Anderson Hamiltonian

Due to strong electronic confinement in quantum dots, it is legitimate to base our study on a single-orbital level (exceptions arise however in ultraclean carbon nanotube systems, where chirality and spin-orbit physics can play an important role). We assume here for simplicity that the magnetic field has no orbital effect on the quantum dot (this applies for instance to the case of carbon nanotubes that are perpendicular to the field axis) and only lifts the degeneracy between spin up and spin down states through the Zeeman effect. In the metallic leads, the Zeeman effect is usually negligible, but a sufficiently strong orbital effect can suppress the superconducting gap. We will thus consider here relatively weak magnetic fields, such that the superconducting order parameter (gap amplitude) Δ can be assumed constant. The possibility to tune the superconducting phase difference via the magnetic field in a SQUID geometry will be accounted for via the independent phase difference ϕ across the junction. We thus investigate the model depicted in Fig. 1 that is described by the Hamiltonian

$$H = \sum_{\alpha=L,R} H_\alpha + H^{\rm dot} + \sum_{\alpha=L,R} H_\alpha^{\rm T}, \tag{1}$$

where

$$H_\alpha = \sum_{\vec{k},\sigma} \epsilon_{\vec{k}}\, c^\dagger_{\vec{k},\sigma,\alpha} c_{\vec{k},\sigma,\alpha} - \sum_{\vec{k}} (\Delta_\alpha\, c^\dagger_{\vec{k},\uparrow,\alpha} c^\dagger_{-\vec{k},\downarrow,\alpha} + \text{H.c.}), \tag{2a}$$

$$H^{\rm dot} = \sum_\sigma (\epsilon\, d^\dagger_\sigma d_\sigma + \sigma B\, d^\dagger_\sigma d_\sigma) + U\left(n_\uparrow - \frac{1}{2}\right)\left(n_\downarrow - \frac{1}{2}\right), \tag{2b}$$

$$H_\alpha^{\rm T} = \sum_{\vec{k},\sigma} (t_\alpha\, d^\dagger_\sigma c_{\vec{k},\sigma,\alpha} + \text{H.c.}). \tag{2c}$$

In the above equations $\alpha = L,R$ denotes the left and right lead, respectively, while $\sigma = \uparrow, \downarrow$ denotes the spin degree of freedom. The leads are modeled by BCS Hamiltonians H_α with a lead-independent dispersion $\epsilon_{\vec{k}}$ and superconducting gaps $\Delta_\alpha = |\Delta|\, e^{i\phi_\alpha}$ that differ only in the complex phase ϕ_α. Note that only the phase difference $\phi = \phi_L - \phi_R$ is of physical importance. We furthermore assume the leads to have a flat density of states of amplitude $\rho_0 = 1/(2D)$, where $2D$ is the total bandwidth. The leads are tunnel coupled to the quantum dot by tunneling amplitudes t_α, which we assume to be momentum independent. The dot, finally, is characterized by a level energy ϵ, an on-site Coulomb repulsion U, and a Zeeman energy B. Note that the single-particle energy was shifted, such that $\epsilon = 0$ corresponds to the particle-hole symmetric case. As discussed above, the lead parameters (such as the superconducting gap Δ and the phase difference ϕ) are considered to be effective parameters for a given magnetic field.

B. Green's functions in superconducting dots

For practical reasons we will work in the following with the Nambu operator basis

$$\Psi = \begin{pmatrix} d_\uparrow \\ d^\dagger_\downarrow \end{pmatrix} \tag{3}$$

for the dot degrees of freedom. This allows us to introduce a matrix structure for all one-particle correlation functions (defined below on the Matsubara imaginary axis), such that the off-diagonal terms capture the anomalous components, while the diagonal terms can be directly related to the normal spin-resolved ones:

$$G(i\omega) = \begin{pmatrix} G_{11}(i\omega) & G_{12}(i\omega) \\ G_{21}(i\omega) & G_{22}(i\omega) \end{pmatrix} = \begin{pmatrix} \langle d_\uparrow d^\dagger_\uparrow\rangle_{i\omega} & \langle d_\uparrow d_\downarrow\rangle_{i\omega} \\ \langle d^\dagger_\downarrow d^\dagger_\uparrow\rangle_{i\omega} & \langle d^\dagger_\downarrow d_\downarrow\rangle_{i\omega} \end{pmatrix}. \tag{4}$$

We first consider the situation of a noninteracting quantum dot ($U = 0$). In the wide band limit, i.e., $D \to \infty$ while keeping the ratio D/t^2 constant, the Green's function of the dot level is given by

$$G_0(i\omega) = \begin{pmatrix} i\tilde{\omega} - \epsilon - B & \tilde{\Delta} \\ \tilde{\Delta}^* & i\tilde{\omega} + \epsilon - B \end{pmatrix}^{-1} = \frac{1}{D_0(i\omega)} \begin{pmatrix} i\tilde{\omega} + \epsilon - B & -\tilde{\Delta} \\ -\tilde{\Delta}^* & i\tilde{\omega} - \epsilon - B \end{pmatrix}, \tag{5}$$

with the determinant

$$D_0(i\omega) = (i\tilde{\omega} - \epsilon - B)(i\tilde{\omega} + \epsilon - B) - |\tilde{\Delta}|^2.$$

We also introduced the compact notations

$$i\tilde{\omega} = i\omega\left(1 + \frac{\Gamma}{\sqrt{\omega^2 + \Delta^2}}\right), \tag{6}$$

$$\tilde{\Delta} = \frac{\Delta}{\sqrt{\omega^2 + \Delta^2}} \sum_{\alpha=L,R} \Gamma_\alpha e^{i\phi_\alpha}, \tag{7}$$

with a total hybridization $\Gamma = \sum_{\alpha=L,R} \Gamma_\alpha$, and $\Gamma_\alpha = \pi\rho_0 t_\alpha^2$. Note that Γ will in the following be used as our unit of energy.

At the one-particle level, the effects of the local Coulomb interaction U can be fully accounted for by a frequency-dependent self-energy, so that the interacting Green's function of the dot reads

$$G(i\omega) = \left(G_0^{-1}(i\omega) - \Sigma(i\omega)\right)^{-1} = \frac{1}{D(i\omega)} \begin{pmatrix} i\tilde{\omega} + \epsilon - B - \Sigma_2(i\omega) & -\tilde{\Delta} + \Sigma_\Delta(i\omega) \\ -\tilde{\Delta}^* + \Sigma_\Delta{}^*(-i\omega) & i\tilde{\omega} - \epsilon - B - \Sigma_1(i\omega) \end{pmatrix}, \tag{8}$$

with the determinant

$$D(i\omega) = [i\tilde{\omega} - \epsilon - B - \Sigma_1(i\omega)][i\tilde{\omega} + \epsilon - B - \Sigma_2(i\omega)] - |\tilde{\Delta} - \Sigma_\Delta(i\omega)|^2. \quad (9)$$

C. Andreev bound states, spectral weights, and Josephson current

The density of states of the quantum dot features discrete ABS inside the superconducting gap. They correspond to poles in the total electronic density of states

$$\rho(\omega) = -\frac{1}{\pi}\lim_{\eta\to 0^+} \mathrm{Im}[G_{11}(\omega + i\eta) - G_{22}(-\omega - i\eta)] \quad (10)$$

that can be determined by finding all roots $E_{\rm bs} \in \{\pm a, \pm b\}$ of the determinant $D(\omega)$ on the real frequency axis. Note that ABS poles will always appear in pairs symmetrically positioned around the chemical potential, while their respective spectral weights are calculated from their residuals

$$w(E_{\rm bs}) = \lim_{\eta\to 0^+} i\eta\,[G_{11}(E_{\rm bs} + i\eta) - G_{22}(-E_{\rm bs} - i\eta)]. \quad (11)$$

In addition, we will consider the weight of the anomalous component of the Nambu Green's function

$$w_\Delta(E_{\rm bs}) = \lim_{\eta\to 0^+} i\eta\, G_{21}(E_{\rm bs} + i\eta), \quad (12)$$

which contains information on the supercurrent carried by the ABS. As we will see in the following, the ABS are responsible for a substantial part of the total Josephson current [101,102] that can flow through the device in the presence of a finite superconducting phase difference ϕ. To illustrate this, let us define the Josephson current operator as the time derivative of the particle number operator N_α for the left and right lead, respectively,

$$J_\alpha = \partial_t N_\alpha = i[H, N_\alpha]. \quad (13)$$

In the absence an applied bias and at $T = 0$, the expectation value reads

$$\langle J_\alpha\rangle = \frac{2\Gamma_\alpha}{\pi}\int d\omega\ \mathrm{Im}\left[\frac{\Delta e^{i\phi_\alpha}}{\sqrt{\omega^2+\Delta^2}} G_{21}(i\omega)\right]. \quad (14)$$

This formula is valid also in the presence of interaction, provided the exact anomalous Green's function is known. To determine the contribution of the different ABS to the current, we split the Green's function G_{21} into a part containing the poles, and another part carrying the contribution of the spectrum corresponding to branch cuts in the complex plane, which is associated with the continuum above the gap:

$$G_{21}(i\omega) = G_{21}^{\rm cont.}(i\omega) + \sum_{\{\pm E_{\rm bs}\}} \frac{w(E_{\rm bs})}{i\omega - E_{\rm bs}}. \quad (15)$$

Plugging this into Eq. (14) we obtain

$$\langle J_L\rangle = \sum_{\{\pm E_{\rm bs}\}} \langle J_{E_{\rm bs}}\rangle + \langle J_{\rm cont.}\rangle, \quad (16)$$

with

$$\langle J_{E_{\rm bs}}\rangle = \frac{2\Gamma_L}{\pi}\int d\omega\ \mathrm{Im}\left[\frac{\Delta e^{i\phi/2}}{\sqrt{\omega^2+\Delta^2}}\frac{w(E_{\rm bs})}{i\omega - E_{\rm bs}}\right] \quad (17)$$

and

$$\langle J_{\rm cont.}\rangle = \frac{2\Gamma_L}{\pi}\int d\omega\ \mathrm{Im}\left[\frac{\Delta e^{i\phi/2}}{\sqrt{\omega^2+\Delta^2}} G_{21}^{\rm cont.}(i\omega)\right]. \quad (18)$$

Evaluating the integral (17) gives

$$\langle J_{E_{\rm bs}}\rangle = -2\Gamma_L\ f\left(\left|\frac{E_{\rm bs}}{\Delta}\right|\right)\mathrm{sgn}(E_{\rm bs})\mathrm{Im}[e^{i\phi/2} w_\Delta(E_{\rm bs})], \quad (19)$$

where $f(x) = [\pi - 2\arcsin(x)]/(\pi\sqrt{1-x^2})$. Note that the explicit dependence of $\langle J_{E_{\rm bs}}\rangle$ on the relative bound state position $|E_{\rm bs}/\Delta|$ is weak, so that the current amplitude is mainly determined by the sign and weight of the ABS.

D. The large gap limit

A simple physical picture of the ABS can be obtained from the limit [103] $\Delta \to \infty$. In this case, the noninteracting Green's function simplifies as

$$G_0(i\omega)^{-1} \xrightarrow{\Delta\to\infty} i\omega - \begin{pmatrix} B+\epsilon & -\Gamma_\phi \\ -\Gamma_\phi^* & B-\epsilon \end{pmatrix}, \quad (20)$$

where $\Gamma_\phi = \sum_\alpha \Gamma_\alpha e^{i\phi_\alpha}$, which, for the case of a symmetric coupling to the leads $\Gamma_L = \Gamma_R = \Gamma/2$, takes the simple form

$$\Gamma_\phi = \Gamma_\phi^* = \Gamma\cos\frac{\phi}{2}. \quad (21)$$

The key point is that the noninteracting Green function (20) coincides with the one of a system with an effective local Hamiltonian

$$H_{\rm eff}^0 = \Psi^\dagger \begin{pmatrix} B+\epsilon & -\Gamma_\phi \\ -\Gamma_\phi^* & B-\epsilon \end{pmatrix}\Psi, \quad (22)$$

where Ψ is the previously introduced Nambu spinor. This Hamiltonian can be diagonalized by means of a Bogoliubov basis transformation

$$\Psi' = \begin{pmatrix} d_+ \\ d_-^\dagger \end{pmatrix} = \begin{pmatrix} u & -v \\ v^* & u^* \end{pmatrix}\Psi, \quad (23)$$

where u and v are defined up to an arbitrary phase factor by

$$u^* v = \Gamma_\phi/(2E_\phi), \quad (24a)$$

$$|u|^2 = (1 + \epsilon/E_\phi)/2, \quad (24b)$$

$$|v|^2 = (1 - \epsilon/E_\phi)/2, \quad (24c)$$

and

$$E_\phi = \sqrt{\epsilon^2 + |\Gamma_\phi|^2}. \quad (25)$$

The possibility to reduce the problem to a local one allows us to deal with the Coulomb interaction in a simple way. In the new basis $\{|00\rangle, |01\rangle, |10\rangle, |11\rangle\}$, labeled by (n_+, n_-), the full effective Hamiltonian takes the diagonal form

$$H_{\rm eff} = E_\phi(n_+ - n_-) + B(n_+ + n_- - 1) + \frac{U}{2}(n_+ - n_-)^2, \quad (26)$$

TABLE I. Relations of the electronic dot basis to the eigenbasis of the effective interacting Hamiltonian.

Eigenvalue	Eigenbasis	Dot basis
$E_\uparrow$	$\|11\rangle$	$\|\uparrow\rangle$
$E_\downarrow$	$\|00\rangle$	$\|\downarrow\rangle$
E_+	$\|01\rangle$	$\|+\rangle = u\ \|0\rangle + v\ \|\uparrow\downarrow\rangle$
E_-	$\|10\rangle$	$\|-\rangle = v^*\|0\rangle - u^*\|\uparrow\downarrow\rangle$

with the eigenvalues

$$E_{00} = -B, \quad E_{01} = E_\phi + \frac{U}{2}, \tag{27a}$$

$$E_{10} = -E_\phi + \frac{U}{2}, \quad E_{11} = B. \tag{27b}$$

The relations to the electronic dot basis are shown in Table I. Here we have introduced the shorthands

$$E_\sigma = \sigma B, \quad E_\pm = U/2 \pm E_\phi. \tag{28}$$

Clearly (for positive B and U, which we assume from now on), the system can assume only two possible ground states, either the nonmagnetic 0-phase state $|10\rangle$, or the spin polarized π-phase state $|00\rangle$. A phase transition (level crossing) will occur under the condition $E_\downarrow = E_-$, which reads explicitly

$$(U+2B)^2 = 4\left[(\Gamma_R - \Gamma_L)^2 + 4\Gamma_L\Gamma_R\cos^2\frac{\phi}{2}\right] + 4\epsilon^2.$$

This indicates the similar role of U and B in determining the phase boundary that is an increase of either parameters will induce a transition to the π phase. However, an increase of U alone will tend in addition to renormalize strongly the electronic states on a wide energy range.

Using Lehmann's representation, one can reconstruct the exact Green's function in the large gap limit (see Appendix A), and hence the corresponding self-energies for finite magnetic fields $B \neq 0$,

$$\Sigma = \begin{cases} \frac{U}{2E_\phi}\begin{pmatrix} -\epsilon & \Gamma_\phi \\ \Gamma_\phi^* & \epsilon \end{pmatrix} & 0 \text{ phase} \\ \begin{pmatrix} \frac{U}{2} & 0 \\ 0 & \frac{U}{2} \end{pmatrix} & \pi \text{ phase} \end{cases}. \tag{29}$$

Note that, in this exactly solvable limit, the self-energy is found to be frequency independent, which is a strong argument for approaches that make the assumption of a static self-energy. On the other hand, the self-energy is completely independent from the magnitude of the magnetic field, while being purely linear in U in both phases. For finite magnetic field, this is a strong argument in favor of approaches that are perturbative in U (such as the static fRG or Hartree-Fock theory).

The situation changes drastically when we consider the case of vanishing magnetic field. While the self-energy in the 0 phase remains unchanged, the twofold degeneracy of the ground state in the π phase results in a frequency dependence as well as a U^2 scaling. At $B = 0$ we find

$$\Sigma = \begin{cases} \frac{U}{2E_\phi}\begin{pmatrix} -\epsilon & \Gamma_\phi \\ \Gamma_\phi^* & \epsilon \end{pmatrix} & 0 \text{ phase} \\ \frac{U^2}{4}\frac{1}{(i\omega)^2 - E_\phi^2}\begin{pmatrix} i\omega + \epsilon & -\Gamma_\phi \\ -\Gamma_\phi^* & i\omega - \epsilon \end{pmatrix} & \pi \text{ phase} \end{cases}. \tag{30}$$

The situation at zero magnetic fields is thus more complex for perturbative methods.

To get a more physical understanding of the Andreev bound state energies, we refer again to the Lehmann representation of the Green's function in the atomic limit. Here the poles can be identified as one-electron transitions between the eigenstates $\{|-\rangle, |+\rangle\} \leftrightarrow \{|\uparrow\rangle, |\downarrow\rangle\}$. The possible transition energies are thus

$$a_\sigma = E_- - \sigma B, \tag{31a}$$

$$b_\sigma = E_+ - \sigma B, \tag{31b}$$

and their negative values, respectively. The corresponding weights of the Andreev bound states are summarized in Table II (see Appendix A for details) for both phases in the case of finite magnetic field $B > 0$. The expressions a_σ and b_σ are plotted in Fig. 2 as a function of the on-site energy ϵ and for $U = 2\Gamma$, $B = 0.7\Gamma$, and $\phi = \pi/2$. Here solid lines were chosen whenever the corresponding weight is nonvanishing, and dashed lines are associated with zero weight, thus to a nonvisible transition.

Let us now clarify a few important points that will allow for a deeper understanding of the ABS even for the case of finite gap. First we want to point out that at finite magnetic field exactly two bound states (four, including their symmetric partners) have a nonvanishing weight, independent of whether the ground state is magnetic or not. The energies of the inner bound state pair are given by $\pm a_\downarrow$ in both phases, and can thus be tracked continuously across the phase transition. Furthermore, as the requirement for the level crossing phase

TABLE II. Spectral weights and anomalous weights of the Andreev bound states evaluated for the 0 phase and for the π phase, with the associated transitions.

	0 phase		
E_{bs}	Transition	w	w_Δ
$\pm a_\uparrow$	$\|\uparrow\rangle \leftrightarrow \|-\rangle$	$\|v\|^2, \|u\|^2$	$0, -u^*v$
$\pm a_\downarrow$	$\|\downarrow\rangle \leftrightarrow \|-\rangle$	$\|v\|^2, \|u\|^2$	$u^*v, 0$
$\pm b_\uparrow$	$\|\uparrow\rangle \leftrightarrow \|+\rangle$	0	0
$\pm b_\downarrow$	$\|\downarrow\rangle \leftrightarrow \|+\rangle$	0	0
	π phase		
E_{bs}	Transition	w	w_Δ
$\pm a_\uparrow$	$\|\uparrow\rangle \leftrightarrow \|-\rangle$	0	0
$\pm a_\downarrow$	$\|\downarrow\rangle \leftrightarrow \|-\rangle$	$\|v\|^2, \|u\|^2$	$u^*v, 0$
$\pm b_\uparrow$	$\|\uparrow\rangle \leftrightarrow \|+\rangle$	0	0
$\pm b_\downarrow$	$\|\downarrow\rangle \leftrightarrow \|+\rangle$	$\|u\|^2, \|v\|^2$	$-u^*v, 0$

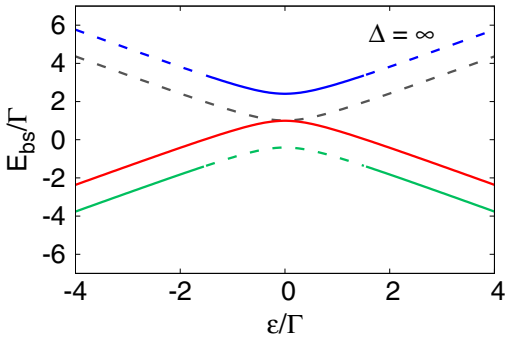

FIG. 2. The Andreev transition energies $a_\uparrow$, $a_\downarrow$, $b_\uparrow$, and $b_\downarrow$ (bottom to top) for the large-gap limit as a function of the on-site energy ϵ and $U = 2\Gamma$, $B = 0.7\Gamma$, $\phi = \pi/2$, and $\Gamma_L = \Gamma_R = \Gamma/2$. Solid lines correspond to regions of nonvanishing weight, while dotted lines denote a vanishing weight. Note that the contributions $-a_\uparrow$, $-a_\downarrow$, $-b_\uparrow$, and $-b_\downarrow$ from the symmetric ABS have not been drawn here for clarity.

transition is given by $E_\downarrow = E_-$ and thus $a_\downarrow = 0$, the inner bound state will always cross the chemical potential at the point of the phase transition, while the outer bound state pair experiences a jump in energy. While in the 0 phase the outer bound-state pair has energies $\pm a_\uparrow$, their energies change to $\pm b_\downarrow$ in the π phase. This behavior is depicted in Fig. 3 for the case of a varying level position ϵ. Here and in the following we show the inner bound states $\pm a_\downarrow$ in red, while $\pm a_\uparrow$ is shown in green and $\pm b_\downarrow$ in blue.

We finally consider the Josephson current in the large gap limit for a nonvanishing magnetic field. The total current is most straightforwardly calculated by the derivative of the ground state energy $E_{\rm GS}(\phi)$,

$$J = 2\partial_\phi E_{\rm GS}(\phi). \tag{32}$$

In the π phase, the ground state energy does not exhibit any ϕ dependence, leading to a vanishing Josephson current. In the 0 phase, the current is given by

$$J = -2\partial_\phi E_\phi = 2\Gamma_L\Gamma_R\frac{\sin\phi}{E_\phi}. \tag{33}$$

It is instructive to determine the contribution of each bound state to the total Josephson current. In the limit $\Delta \to \infty$ Eq. (19) yields

$$\langle J_{E_{\rm bs}}\rangle = -2\Gamma_L {\rm Im}[e^{i\phi/2}w_\Delta(E_{\rm bs})^*]{\rm sgn}(E_{\rm bs}), \tag{34}$$

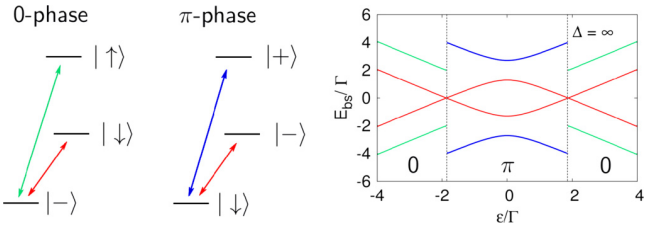

FIG. 3. The visible Andreev bound states and the corresponding transitions in and out of the ground states in the 0 and π phase for $U = 2\Gamma$, $B = 0.7\Gamma$, $\phi = \pi/2$, and $\Gamma_L = \Gamma_R = \Gamma/2$.

Since the spectrum on the dot consists only of the bound states, we get no continuum contribution to the total Josephson current. Recalling that $u^* v = \Gamma_\phi/(2E_\phi)$, the result for the 0 phase is

$$\langle J_{-a_\uparrow}\rangle = \langle J_{a_\downarrow}\rangle = \Gamma_L\Gamma_R\frac{\sin\phi}{E_\phi}, \tag{35}$$

adding up to the total Josephson current (33). In the π phase the contributions are

$$\langle J_{b_\downarrow}\rangle = -\langle J_{a_\downarrow}\rangle = \Gamma_L\Gamma_R\frac{\sin\phi}{E_\phi}, \tag{36}$$

leading to a vanishing Josephson current, as expected. Having identified the transitions associated with the different bound state energies (see Table II), we can interpret the corresponding Josephson current contribution as a measure for the relevance of the virtual intermediate state in the Cooper pair transport process. It is also interesting to note that the magnitude of the current in the 0 phase does not depend on the magnetic field at large gap, an artifact of this limit.

III. METHODS

We here briefly review two complementary approaches that are able to tackle the problem of superconducting quantum dots in the presence of both a finite Coulomb interaction and a finite gap: the static fRG and the SCABS approximation. In the description of their implementation, we focus on the aspects specific to the extension to finite magnetic fields.

A. Static functional renormalization group

The fRG [104,105] is based on Wilson's general RG idea for interacting many-body systems. By introducing a scale dependence into the noninteracting Green's function one can derive an exact functional flow equation that describes the gradual evolution of the effective action, that is, the generating functional of the one-particle irreducible vertex functions, as the scale is changed. While the action at the final scale is the one of the systems in question, we only require the initial action to be exactly solvable, giving rise to a large freedom in the choice of the initial conditions [106]. Expanding this functional flow equation in powers of the external sources yields an exact but infinite hierarchy of flow equations for the n-particle vertex functions. In practical implementations, however, this hierarchy has to be truncated at a given order. This truncation is commonly performed at the two-particle level, and yields a set of flow equations for the self-energy and the two-particle vertex functions.

We here use the fRG implementation for superconducting quantum dots formulated on the Matsubara axis [104,107] (see Ref. [48] for the extension to real-time Keldysh space) assuming that the self-energy and the two-particle vertex are both static. The underlying approximations are devised for weak to intermediate Coulomb interaction strengths and arbitrary gap, and have been checked by comparing with NRG data.

At zero temperature we use a frequency cutoff of the form

$$G_0^\Lambda = \Theta(|\omega| - \Lambda)G_0, \tag{37}$$

while the Green function at a given scale is determined by means of the Dyson equation $G^\Lambda = [(G_0^\Lambda)^{-1} - \Sigma^\Lambda]^{-1}$. In the static approximation, the self-energy contains three frequency-independent elements

$$\Sigma^\Lambda(i\omega) = \begin{pmatrix} \Sigma_1^\Lambda & \Sigma_\Delta^\Lambda \\ \Sigma_\Delta^{\Lambda *} & \Sigma_2^\Lambda \end{pmatrix}, \tag{38}$$

while the static two-particle vertex is determined by a single renormalized Coulomb interaction U^Λ. Note that the static terms Σ_1^Λ and Σ_2^Λ effectively renormalize the on-site energy and magnetic field. Introducing flowing effective physical parameters

$$\epsilon^\Lambda = \epsilon + \tfrac{1}{2}\left(\Sigma_1^\Lambda - \Sigma_2^\Lambda\right), \quad B^\Lambda = B + \tfrac{1}{2}\left(\Sigma_1^\Lambda + \Sigma_2^\Lambda\right), \tag{39}$$

the Green's function reads

$$G^\Lambda(i\omega) = \frac{1}{D(i\omega)} \begin{pmatrix} i\tilde{\omega} + \epsilon^\Lambda - B^\Lambda & -\tilde{\Delta} + \Sigma_\Delta^\Lambda \\ -\tilde{\Delta}^* + \Sigma_\Delta^{\Lambda *} & i\tilde{\omega} - \epsilon^\Lambda - B^\Lambda \end{pmatrix}, \tag{40}$$

with the determinant

$$D(i\omega) = (i\tilde{\omega} - \epsilon^\Lambda - B^\Lambda)(i\tilde{\omega} + \epsilon^\Lambda - B^\Lambda) - \left|\tilde{\Delta} - \Sigma_\Delta^\Lambda\right|^2. \tag{41}$$

The explicit flow equations for the effective parameters read

$$\partial_\Lambda \epsilon^\Lambda = \frac{U^\Lambda \epsilon^\Lambda}{\pi |D(i\Lambda)|^2}\left[\tilde{\omega}^2 + (\epsilon^\Lambda)^2 - (B^\Lambda)^2 + \left|\tilde{\Delta} - \Sigma_\Delta^\Lambda\right|^2\right]_{\omega=\Lambda}, \tag{42a}$$

$$\partial_\Lambda B^\Lambda = \frac{U^\Lambda B^\Lambda}{\pi |D(i\Lambda)|^2}\left[\tilde{\omega}^2 - (\epsilon^\Lambda)^2 + (B^\Lambda)^2 + \left|\tilde{\Delta} - \Sigma_\Delta^\Lambda\right|^2\right]_{\omega=\Lambda}, \tag{42b}$$

$$\partial_\Lambda \Sigma_\Delta^\Lambda = \frac{U^\Lambda \left(\Sigma_\Delta^\Lambda - \tilde{\Delta}\right)}{\pi |D(i\Lambda)|^2}\left[\tilde{\omega}^2 + (\epsilon^\Lambda)^2 - (B^\Lambda)^2 + \left|\tilde{\Delta} - \Sigma_\Delta^\Lambda\right|^2\right]_{\omega=\Lambda}, \tag{42c}$$

and

$$\partial_\Lambda U^\Lambda = 2\pi\left[(\partial_\Lambda B^\Lambda)^2 - (\partial_\Lambda \epsilon^\Lambda)^2 + \left|\partial_\Lambda \Sigma_\Delta^\Lambda\right|^2\right]_{\omega=\Lambda} \tag{43}$$

for the two-particle vertex, with the initial conditions

$$\epsilon^{\Lambda=\infty} = \epsilon, \quad B^{\Lambda=\infty} = B, \tag{44a}$$

$$\Sigma_\Delta^{\Lambda=\infty} = 0, \quad U^{\Lambda=\infty} = U. \tag{44b}$$

This set of ordinary differential equations is then integrated numerically from $\Lambda/\Gamma = 10^6$ to $\Lambda/\Gamma = 10^{-6}$ using a Runge-Kutta solver. An example for the evolution of the renormalized parameters during the flow is shown in Fig. 4.

Introducing the notation

$$\epsilon^{\Lambda=0} = \epsilon_r, \quad B^{\Lambda=0} = B_r, \tag{45a}$$

$$\Sigma_\Delta^{\Lambda=0} = \Sigma_\Delta, \quad U^{\Lambda=0} = U_r \tag{45b}$$

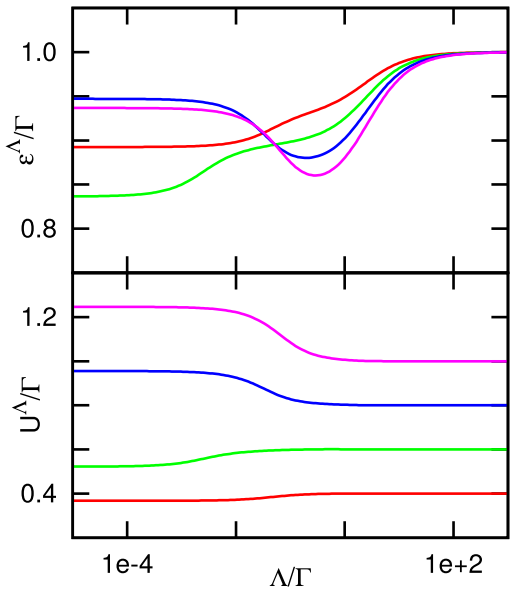

FIG. 4. Flow of the renormalized on-site energy ϵ^Λ and the effective interaction U^Λ for $\Delta = \Gamma$, $\epsilon = \Gamma$, $B = \Gamma$, $\phi = \pi/2$, $\Gamma_L = \Gamma_R = \Gamma/2$, and different values of U. $U = 0.6\Gamma$ is close to the phase transition and the flow converges at a lower energy scale. Note that the interaction is effectively reduced in the 0 phase, while an enhancement is observed in the π phase.

for the renormalized values at the end of the flow, the poles of the Green's function are determined by finding the roots of its determinant (41), e.g., by solving

$$(\tilde{\omega} - \epsilon_r - B_r)(\tilde{\omega} + \epsilon_r - B_r) - |\tilde{\Delta} - \Sigma_\Delta|^2 = 0. \tag{46}$$

The spectral weights of the associated ABS are then calculated according to Eqs. (11) and (12).

B. Self-consistent Andreev bound state theory

This alternative approach focuses again on effective Andreev levels, but, instead of a scheme based on a renormalized perturbative expansion in the Coulomb interaction, rather considers the infinite gap limit as a starting point for a perturbative treatment. The clear advantage here is that the 0 to π transition is already captured at $\Delta = \infty$, and thus the method should be able to describe both phases on an equal footing. For $\Delta = \infty$, we have previously calculated the one-particle energy levels $E_\sigma^0 = \sigma B$ and the BCS-like levels $E_\pm^0 = U/2 \pm \sqrt{\epsilon^2 + |\Gamma_\phi|^2}$. Note that we have added an additional superscript 0 to denote that these are the uncorrected energies at infinite gap. Furthermore, all following derivations will be considering the general case of a finite bandwidth $2D$, which requires the introduction of the generalized hybridization function $\Gamma_\phi(i\omega) = \frac{2}{\pi}\arctan\left(\frac{D}{\sqrt{\Delta^2 - (i\omega)^2}}\right)\sum_\alpha \Gamma_\alpha e^{i\phi_\alpha}$. In the following, $\Gamma_\phi = \Gamma_\phi(0)$.

Straightforward calculations detailed in Appendix B give the perturbative correction at lowest order

$$\delta E_\sigma = -t^2 \sum_{\vec{k}} \left[\frac{1}{E_{\vec{k}} + (E_+^0 - E_\sigma^0)} + \frac{1}{E_{\vec{k}} + (E_-^0 - E_\sigma^0)} + \frac{2\Delta}{E_{\vec{k}}} uv \left| \cos\frac{\phi}{2} \right| \left(\frac{1}{E_{\vec{k}} + (E_+^0 - E_\sigma^0)} - \frac{1}{E_{\vec{k}} + (E_-^0 - E_\sigma^0)} \right) \right], \tag{47a}$$

$$\delta E_+ = -t^2 \sum_{\vec{k},\sigma} \left(\frac{1}{E_{\vec{k}} - (E_+^0 - E_\sigma^0)} - \frac{2\Delta}{E_{\vec{k}}} uv \left| \cos\frac{\phi}{2} \right| \frac{1}{E_{\vec{k}} - (E_+^0 - E_\sigma^0)} \right) - 2|\Gamma_\phi| uv, \tag{47b}$$

$$\delta E_- = -t^2 \sum_{\vec{k},\sigma} \left(\frac{1}{E_{\vec{k}} - (E_-^0 - E_\sigma^0)} + \frac{2\Delta}{E_{\vec{k}}} uv \left| \cos\frac{\phi}{2} \right| \frac{1}{E_{\vec{k}} - (E_-^0 - E_\sigma^0)} \right) + 2|\Gamma_\phi| uv, \tag{47c}$$

with the quasiparticle energy $E_{\vec{k}} = \sqrt{\epsilon_{\vec{k}}^2 + \Delta^2}$. These expressions generalize the results of Ref. [32] to the case of finite magnetic field.

At finite Δ, the self-consistent perturbative approach considered in Ref. [32] can be generalized to the spinful case. In order to write self-consistent equations for the corrections to the Andreev transitions, $\delta a_\sigma = \delta E_- - \delta E_\sigma = a_\sigma - a_\sigma^0$ and $\delta b_\sigma = \delta E_+ - \delta E_\sigma = b_\sigma - b_\sigma^0$, one must analyze carefully the singularities appearing in their respective expressions:

$$\delta a_\sigma = -\frac{\Gamma}{\pi} \int_0^D d\epsilon \left[\sum_{\sigma'} \frac{1}{E - a_{\sigma'}^0} - \frac{1}{E + b_\sigma^0} - \frac{1}{E + a_\sigma^0} + \frac{2\Delta}{E} uv \left| \cos\frac{\phi}{2} \right| \left(\sum_{\sigma'} \frac{1}{E - a_{\sigma'}^0} - \frac{1}{E + b_\sigma^0} + \frac{1}{E + a_\sigma^0} \right) \right] + 2|\Gamma_\phi| uv, \tag{48a}$$

$$\delta b_\sigma = -\frac{\Gamma}{\pi} \int_0^D d\epsilon \left[\sum_{\sigma'} \frac{1}{E - b_{\sigma'}^0} - \frac{1}{E + b_\sigma^0} - \frac{1}{E + a_\sigma^0} + \frac{2\Delta}{E} uv \left| \cos\frac{\phi}{2} \right| \left(\sum_{\sigma'} \frac{-1}{E - b_{\sigma'}^0} - \frac{1}{E + b_\sigma^0} + \frac{1}{E + a_\sigma^0} \right) \right] - 2|\Gamma_\phi| uv. \tag{48b}$$

Recall that $E = \sqrt{\epsilon^2 + \Delta^2}$, such that singularities appear indeed whenever a one-particle transition on the dot becomes comparable to the minimum quasiparticle energy given by the gap Δ. A first important observation is that the singularities tend to cancel out together for the outer bound state correction δb_σ, which implies that these states become part of the continuum for small enough Δ. One can thus focus on analyzing the singularities related to the inner bound states a_σ, which originate from the denominators in $1/(E \pm a_\sigma^0)$. The physics here is simply an effect of level repulsion from the continuum whenever the bound state approaches the gap edges. In the case $a_\sigma^0 > 0$, which occurs typically in the regime of strong correlations $U \gg \Gamma$, only the denominators in $1/(E - a_\sigma^0)$ are singular. This leads to a downward renormalization of the bound state energy a_σ compared to the bare value a_σ^0. Conversely, an upward renormalization of the bound state occurs when $a_\sigma^0 < 0$, since the denominators $1/(E + a_\sigma^0)$ provide then the main contribution. We can thus renormalize in a self-consistent way the inner Andreev bound states according to

$$\begin{aligned} \delta a_\sigma = -\frac{\Gamma}{\pi} \int_0^D d\epsilon \Bigg[& \sum_{\sigma'} \frac{1}{E - a_{\sigma'}^0 - \Theta[-\delta a_{\sigma'}]\delta a_{\sigma'}} - \frac{1}{E + b_\sigma^0} - \frac{1}{E + a_\sigma^0} \\ & + \frac{2\Delta}{E} uv \left| \cos\frac{\phi}{2} \right| \left(\sum_{\sigma'} \frac{1}{E - a_{\sigma'}^0 - \Theta[-\delta a_{\sigma'}]\delta a_{\sigma'}} - \frac{1}{E + b_\sigma^0} + \frac{1}{E + a_\sigma^0 + \Theta[\delta a_{\sigma'}]\delta a_{\sigma'}} \right) \Bigg] + 2|\Gamma_\phi| uv, \end{aligned} \tag{49}$$

and correspondingly for b. Note the presence here of Θ functions that account for respective downward and upward renormalization, as discussed above. We thus find that δa_σ depends on both $\delta a_\uparrow$ and $\delta a_\downarrow$, such that one has to solve a coupled set of self-consistent equations for δa_σ (and similarly for δb_σ). These equations can, however, be decoupled, since $\delta a_\uparrow - \delta a_\downarrow$ is a constant that does not depend on either δa_σ (and again similarly for δb_σ, which is not written here). This simple procedure does not provide any information on the weights of the ABS, in contrast to the fRG approach of the previous section. The understanding of the allowed transitions can nevertheless be gathered from the atomic limit.

IV. RESULTS

For the results in the following we will focus on the case of symmetric coupling $\Gamma_L = \Gamma_R$ as the physics of the system does not differ from the general case. We will first describe how the case of finite gap is linked to the solution in the large-gap limit in order to understand in more detail the effect of a local magnetic field on the spectrum. This will

be followed by a detailed comparison between the fRG and the SCABS approximation, and further by a brief benchmark against available NRG results [93]. To conclude our study, we will give a small outlook towards transport calculations that are closer to actual spectroscopic experimental setups.

A. From large to small gaps using fRG

While the previously introduced SCABS approximation includes the exact large-gap limit solution by construction, this does not hold for the fRG. This allows us to benchmark fRG calculations of the Andreev bound states performed for a large gap value (e.g., $10^6\Gamma$) against the exact expressions presented previously. This comparison is shown in the left panel of Fig. 5, which shows the Andreev bound state energies (upper panels), the corresponding spectral weights (middle panels), as well as the bound-state resolved Josephson current (lower panels) as a function of the level-position ϵ for $U = 2\Gamma$, $\phi = \pi/2$. The dashed line indicates the exact solution in the large-gap limit, while solid lines denote the corresponding fRG data. Bound state colors are chosen as previously introduced. We find an excellent agreement of the fRG data with the exact solution, not only for the ABS, but also for their weights as well as the Josephson currents. Small deviations can be found in the π phase for the outer bound states $\pm b_\downarrow$ (blue), specifically close to the phase transition.

The corresponding fRG data for the same set of parameters but now a finite gap $\Delta = \Gamma$ is shown in the right panels of Fig. 5. While the qualitative behavior of the ABS is similar, we find that, due to the repulsion from the gap edge, the overall structure is squeezed in the process of closing the gap from large to small values. In particular, the outer bound states are strongly deformed due to this process. This is also mirrored in the change of the spectral weight, as the ABS tend to loose more weight the closer they are to the gap edge. In fact, for sufficiently small gap, the outer bound state pair can be absorbed completely into the continuum part of the spectrum. As the gap is lowered, we also find a nonvanishing Josephson current (gray) in π phase. Further it is interesting to note that the bound-state contributions no longer add up to the total Josephson current (which we will study in what follows), as the continuous part of the DOS now has a nonvanishing contribution to the Josephson current.

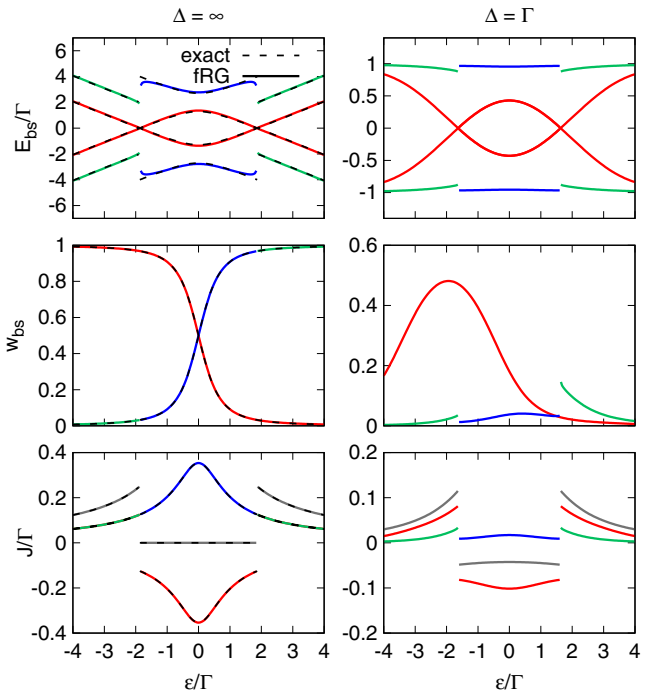

FIG. 5. Bound state energies (upper panels), the corresponding weights (middle panels), as well as the bound-state resolved Josephson currents (lower panels) defined in Eq. (19) as a function of the on-site energy ϵ. The calculation is shown for the large-gap situation (left column) and a finite gap $\Delta = \Gamma$ (right column), with $U = 2\Gamma$, $\phi = \pi/2$, and $B = 0.7\Gamma$ in all cases. Solid lines show fRG results, while dotted lines denote the exact expressions for $\Delta = \infty$. The weights shown here correspond to the bound state energies $a_\uparrow$, $a_\downarrow$, and $-b_\downarrow$ associated with their respective colors (compare Fig. 2). The gray lines denote the total Josephson current.

B. Magnetic field effects

We here discuss how the magnetic field alters the ABS in the 0 phase and by this drives the phase transition. Figure 6 shows the ABS (left) and Josephson current (right) obtained from fRG as a function of the phase-difference ϕ for $\epsilon = \Gamma$, $\Delta = \Gamma$, $U = \Gamma$, and different values of B. In the absence of a magnetic field (upper panel), the system is in the 0 phase for the whole ϕ range, and the visible ABS $a_\uparrow$ and $a_\downarrow$ are equal. Accordingly, the Josephson current shows the typical sinusoidal behavior without a jump.

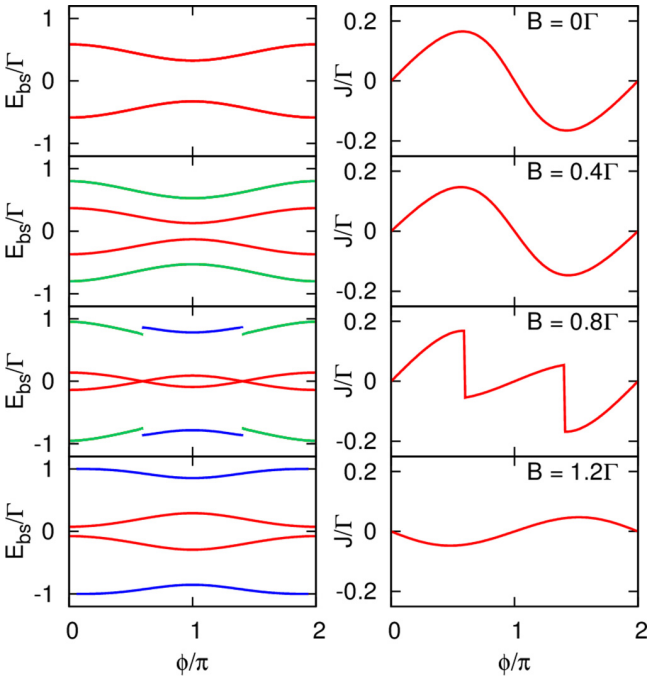

FIG. 6. Evolution of the Andreev bound states and Josephson current with ϕ as obtained from fRG for $\epsilon = \Gamma$, $\Delta = \Gamma$, $U = \Gamma$, and different values of B.

For a small magnetic field ($B = 0.4\Gamma$) the 0 phase is still the most stable, but the bound states $a_\uparrow$ and $a_\downarrow$ can now be clearly distinguished due to the Zeeman splitting. The corresponding Josephson is just mildly reduced as a consequence.

When increasing the magnetic field further ($B = 0.8\Gamma$), the inner bound states $\pm a_\downarrow$ will cross the chemical potential for ϕ close to π, thus inducing the phase transition for a finite ϕ range. In this window, the visible outer bound state changes to $\pm b_\downarrow$. A Zeeman splitting is thus no longer directly visible in this part of the spectrum. As expected, the change of the ground state is accompanied by a sign reversal in the Josephson current.

For even larger values of the magnetic field ($B = 1.2\Gamma$), the inner bound states will completely cross the chemical potential, inducing the π phase for the whole ϕ range. Accordingly, the Josephson current completely inverts its sign.

C. Comparison between fRG and the SCABS approximation

In this subsection we provide a detailed comparison between the fRG and the SCABS approximation. While the fRG, being a perturbative approach, is expected to perform better for smaller values of U/Γ, the SCABS will by construction perform better for larger Δ/Γ. We have thus chosen $U \in \{0.5\pi\Gamma, \pi\Gamma\}$ and $\Delta \in \{0.5\pi\Gamma, \pi\Gamma\}$ for our comparison, in order to span different ranges of validity of these approaches. For the other parameters we chose $\epsilon = 0$, $\phi = 0$, and $B = 0$, and then varied one of these at a time. The corresponding plots can be found in Figs. 7–9, respectively.

Overall we find a very good quantitative agreement of the results between the two methods. As expected, the largest deviations can be found for $\Delta = 0.5\pi\Gamma$ and $U = \pi\Gamma$, since both methods are then pushed away from their clear regime of applicability. Varying ϵ, we see an almost perfect agreement for $U = 0.5\pi\Gamma$. Small deviations arise close to the gap edge, which is a trend that continues throughout the whole comparison. This is tied to a weaker repulsion of the outer ABS from the gap edge in the SCABS approximation. We also note that for the choice of parameters $U = \pi\Gamma$ and $\Delta = \pi\Gamma$ we are very close to the 0-π transition. While the fRG approximation predicts the system to still be in the 0 phase, SCABS approximation results are already in the π phase. This tendency of the SCABS approximation towards the π phase is also observed throughout the whole comparison.

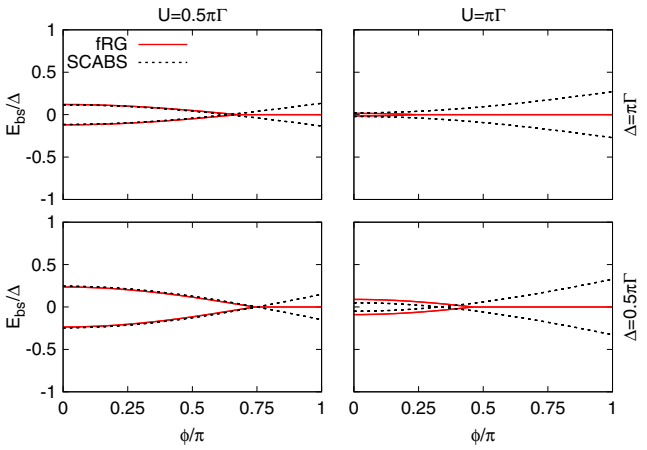

FIG. 8. Bound state energies calculated with fRG (full lines) and SCABS approximation (dashed lines) as a function of ϕ for $B = 0$, $\epsilon = 0$, and different values of U and Δ.

The data with varying ϕ show an artifact of the static fRG calculations that arise in the absence of a magnetic field. The ABS in the π phase for $B = 0$ are not described correctly, but remain pinned at the chemical potential as they cross the chemical potential at the phase transition, in disagreement with the SCABS and the previous findings in the atomic limit. This can most likely be attributed to the static approximation, as in the large-gap limit the exact self-energy is found to be frequency dependent at zero field in the π phase. Otherwise the previously described trends hold, and a good quantitative agreement is achieved in the 0 phase.

As Fig. 9 shows, increasing the magnetic field B induces the π phase rather quickly, as could already be inferred from the large-gap phase boundary defined by Eq. (29). The tendency of the SCABS approximation towards the π phase is clearly

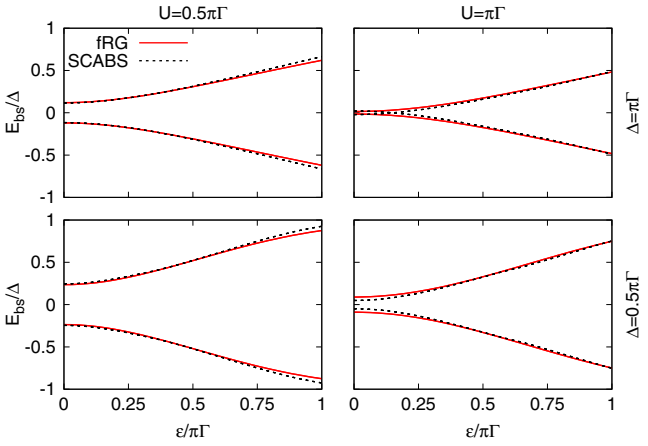

FIG. 7. Bound state energies calculated with fRG (full lines) and SCABS approximation (dashed lines) as a function of ϵ for $B = 0$, $\phi = 0$, and different values of U and Δ.

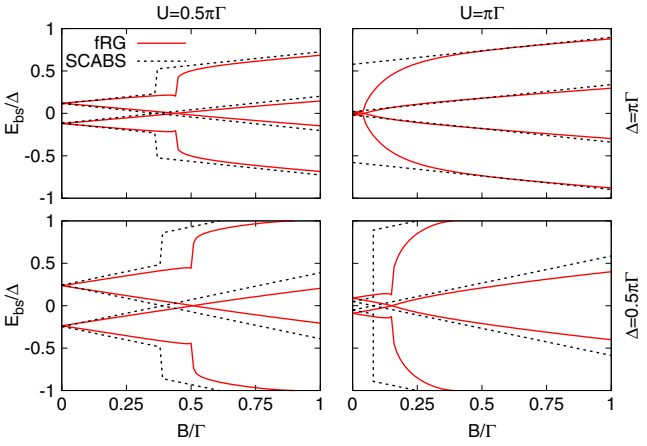

FIG. 9. Bound state energies calculated with fRG (full lines) and SCABS approximation (dashed lines) as a function of B for $\phi = 0$, $\epsilon = 0$, and different values of U and Δ.

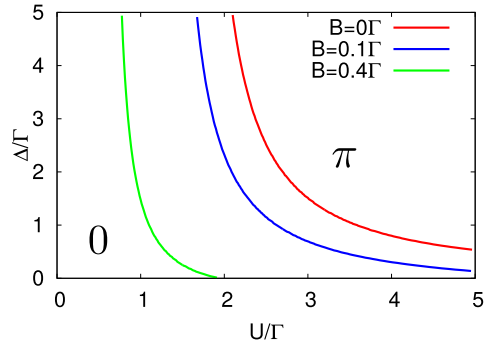

FIG. 10. Phase diagram as a function of U and Δ as obtained from the fRG at $\epsilon = 0$ and $\phi = \pi/2$ for different values of B. The lines separate the 0 phase on the left side from the π phase on the right.

visible in the B-dependent data, while the fRG shows a bending of the outer bound states in the π phase close to the phase transition. This latter behavior was also observed in Sec. II D in the comparison to the exact large-gap expressions, and was there identified as the main deviation. This effect is dominant for small values of the magnetic field B, where the renormalized interaction was found to diverge. In this limit the truncation of the hierarchy is no longer justified, as it corresponds to an expansion in the effective interaction. Similar problems using the static fRG have been found in Ref. [108], as the investigated two-level quantum dot setup was close to degeneracy.

D. Phase diagram at finite B

A detailed phase diagram for the 0-π transition determined with fRG is shown in Fig. 10, as a function of Coulomb interaction, gap amplitude, and several values of the magnetic field (for a choice of phase difference $\phi = \pi/2$). The general expected trend is a stabilization of the π phase for increasing values of U and B, which both lead to local moment formation. The π state is also favored for increasing values of Δ, as this removes the quasiparticles and thus weakens the Kondo effect responsible for the possible presence of the 0 phase at large U.

In experimental setups the magnetic field can be expected to extend beyond the quantum dot. This effect can lead to a reduction of the superconducting gap in the leads, which would stabilize the 0 phase.

E. Comparison with NRG

Figure 11 shows a comparison of fRG data (solid lines) and NRG data [93] (symbols) for the ABS and the corresponding weights for $\epsilon = 0$, $B = 0$, $\phi = 0$, and $\Delta/\Gamma = 0.0157, 0.157, 0.9425$ (red, green, blue). We find a good quantitative agreement with the NRG data up to interaction values of $U = \pi\Gamma$. For larger U values, frequency dependent self-energy effects become prominent [89], so that the static fRG cannot be expected to be precise.

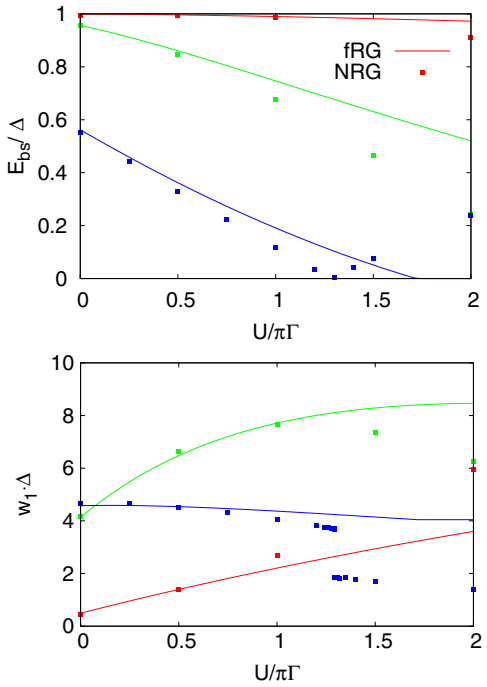

FIG. 11. Comparison with NRG data from Ref. [93] for the bound state energy and the corresponding weights as a function of the interaction strength. The parameters are $\epsilon = 0$, $B = 0$, $\phi = 0$, and $\Delta/\Gamma = 0.0157, 0.157, 0.9425$ (red, green, blue).

F. Spectroscopy

The density of states in experimental setups like the ones reported in Refs. [70,80,84] is probed by measuring the differential conductance using a weakly coupled normal lead. This has the effect that the Andreev bound states are broadened by an energy scale Γ_N, which is the corresponding hybridization to the normal contact. This effect can be easily accounted for during the fRG flow by considering the additional self-energy

$$\Sigma_N(i\omega) = \begin{pmatrix} -i\Gamma_N \operatorname{sgn}(\omega) & 0 \\ 0 & -i\Gamma_N \operatorname{sgn}(\omega) \end{pmatrix} \tag{50}$$

in the Dyson-equation $G^\Lambda = [(G_0^\Lambda)^{-1} - \Sigma^\Lambda - \Sigma_N]^{-1}$. We can then straightforwardly calculate the density of states using Eq. (10). One such calculation for a varying on-site energy ϵ and $\Gamma_N = 0.1\Gamma$, $\Delta = \Gamma$, $U = 3.5\Gamma$, and $B = 0.5\Gamma$ is shown in Fig. 12. As expected, the bound states acquire a broadening due to the presence of the normal lead, and the data compare qualitatively with measurements from Ref. [84]. Note that the outer bound states in the π phase close to $\epsilon = 0$ have already been been absorbed into the continuum, as it can be also observed in Fig. 9. In view of the experimental observation we point out that the fRG can be easily extended to multilevel quantum dot systems.

V. CONCLUSION

We have investigated electrostatic gating and magnetic field effects on the ABS of an interacting quantum dot coupled to superconducting leads by extending the static functional renormalization group and the self-consistent Andreev bound

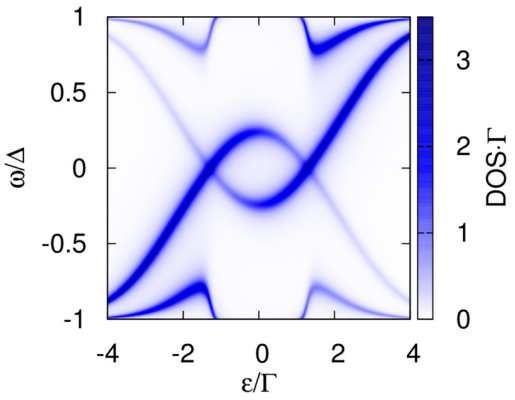

FIG. 12. fRG results for the density of states as a function of the on-site energy ϵ, for $\Gamma_N = 0.1\Gamma$, $\phi = 0$, $\Delta = \Gamma$, $U = 3.5\Gamma$, and $B = 0.5\Gamma$. The transition from the π to the 0 phase is induced at $\epsilon = \pm 1.5\Gamma$.

states theory to include finite magnetic fields. These complementary approaches allow us to capture the rich physical behavior in the large parameter space with a reduced numerical effort. According to the range of validity we found a good quantitative agreement not only between the methods, but also with NRG and the exact solution in the large-gap limit. The latter was discussed in detail for the case of a finite magnetic field, allowing for a deeper understanding of the generic finite-gap situation. We further showed how a local magnetic field induces a splitting of the ABS whenever the system is 0 phase, while this effect is absent in the π phase, and provided examples of the tunneling density of states that is typically measured in experiments.

ACKNOWLEDGMENTS

We are grateful to J. Bauer and C. Karrasch for discussions. We acknowledge financial support from the Deutsche Forschungsgemeinschaft (DFG) through FOR 723, RTG 1995, ZUK 63, SFB 1143, and SFB/TRR 21, and the Austrian Science Fund (FWF) within the Project F41 (SFB ViCoM).

APPENDIX A: GREEN'S FUNCTION IN THE LARGE GAP LIMIT

To calculate the full Green function in the large-gap limit we use the Lehmann representation for diagonal correlation functions, which reads

$$G_{AA^\dagger}(i\omega) = \sum_{mn} \frac{|\langle n|A|m\rangle|^2}{E_n - E_m + i\omega}(\rho_n + \rho_m). \tag{A1}$$

Using the eigenbasis Eq. (27b) of the effective Hamiltonian, we find

$$G_{b_+b_+^\dagger}(i\omega) = \frac{\rho_{00} + \rho_{01}}{i\omega - E_\phi - B - \frac{U}{2}} + \frac{\rho_{10} + \rho_{11}}{i\omega - E_\phi - B + \frac{U}{2}} \tag{A2}$$

and

$$G_{b_-b_-^\dagger}(i\omega) = \frac{\rho_{00} + \rho_{10}}{i\omega + E_\phi - B - \frac{U}{2}} + \frac{\rho_{11} + \rho_{01}}{i\omega + E_\phi - B + \frac{U}{2}}. \tag{A3}$$

The off-diagonal elements evaluate to $G_{b_+b_-^\dagger} = G_{b_-b_+^\dagger} = 0$. We now aim at calculating the exact self-energy expressions. For $B \neq 0$, the ground state energy is either E_{00} or E_{10}, resulting in

$$G^{-1}_{bb^\dagger}(i\omega) = i\omega - \begin{pmatrix} B + E_\phi & 0 \\ 0 & B - E_\phi \end{pmatrix} - \begin{pmatrix} \mp\frac{U}{2} & 0 \\ 0 & \frac{U}{2} \end{pmatrix}, \quad E_{00} \gtrless E_{10}. \tag{A4}$$

Using the Dyson equation $G^{-1} = i\omega - H^0 - \Sigma$, we hence obtain

$$\Sigma_{bb^\dagger} = \begin{pmatrix} \mp\frac{U}{2} & 0 \\ 0 & \frac{U}{2} \end{pmatrix}, \quad E_{00} \gtrless E_{10}, \tag{A5}$$

for the self-energy. For $B = 0$, the 0-phase calculation results in the same self-energy. For the π phase we get

$$\begin{aligned} G^{-1}_{bb^\dagger}(i\omega) &= 2\begin{pmatrix} \frac{1}{i\omega - E_\phi - \frac{U}{2}} + \frac{1}{i\omega - E_\phi + \frac{U}{2}} & 0 \\ 0 & \frac{1}{i\omega + E_\phi - \frac{U}{2}} + \frac{1}{i\omega + E_\phi + \frac{U}{2}} \end{pmatrix}^{-1} \\ &= i\omega - \begin{pmatrix} E_\phi & 0 \\ 0 & -E_\phi \end{pmatrix} - \frac{U^2}{4}\begin{pmatrix} \frac{1}{i\omega - E_\phi} & 0 \\ 0 & \frac{1}{i\omega + E_\phi} \end{pmatrix}. \end{aligned} \tag{A6}$$

The resulting self-energy

$$\Sigma_{bb^\dagger}(i\omega) = \frac{U^2}{4}\begin{pmatrix} \frac{1}{i\omega - E_\phi} & 0 \\ 0 & \frac{1}{i\omega + E_\phi} \end{pmatrix} \tag{A7}$$

is solely quadratic in the interaction U. The corresponding expressions for self-energy and Green functions in the Nambu basis can now be easily acquired by rotating back to the old basis. Executing this for the self-energy results in Eqs. (29) and (30). The Green function in the Nambu basis can be calculated straightforwardly by the Dyson equation. It will prove more useful though to write

$$\begin{aligned} G_{\varphi\varphi^\dagger} &= \begin{pmatrix} u & -v \\ v^* & u^* \end{pmatrix} G_{bb^\dagger} \begin{pmatrix} u^* & v \\ -v^* & u \end{pmatrix} \\ &= G_{b_+b_+^\dagger}\begin{pmatrix} |u|^2 & -u^*v \\ -uv^* & |v|^2 \end{pmatrix} + G_{b_-b_-^\dagger}\begin{pmatrix} |v|^2 & u^*v \\ uv^* & |u|^2 \end{pmatrix}, \end{aligned} \tag{A8}$$

since in this representation we can easily read off the bound state weights.

APPENDIX B: DERIVATION OF THE SCABS EQUATIONS

Here we want to summarize, in accordance with Ref. [32], the derivation of the SCABS equations presented in Sec. III B. Let us begin by considering the hybridization function of the leads for the case of a finite bandwidth $2D$,

$$\Gamma_\phi(i\omega) = \frac{2}{\pi}\arctan\left(\frac{D}{\sqrt{\Delta^2-(i\omega)^2}}\right)\sum_\alpha \Gamma_\alpha e^{i\phi_\alpha}. \tag{B1}$$

The noninteracting Green function of the dot then generalizes to

$$G_0(i\omega) = \begin{pmatrix} i\tilde{\omega}-\epsilon-B & \tilde{\Delta} \\ \tilde{\Delta}^* & i\tilde{\omega}+\epsilon-B \end{pmatrix}^{-1}, \tag{B2}$$

with

$$i\tilde{\omega} = i\omega\left(1+\frac{\Gamma_0(i\omega)}{\sqrt{\omega^2+\Delta^2}}\right), \tag{B3}$$

$$\tilde{\Delta} = \frac{\Delta}{\sqrt{\omega^2+\Delta^2}}\Gamma_\phi(i\omega). \tag{B4}$$

The system is then fully described by the action

$$S = S_0 + S_{\text{int}}, \tag{B5}$$

with

$$S_0 = -\frac{1}{2\pi}\int d\omega\ \bar{\Psi}(i\omega)G_0(i\omega)^{-1}\Psi(i\omega) \tag{B6}$$

and

$$S_{\text{int}} = -\frac{U}{2\pi}\int d\omega_i \left(\bar{\Psi}_1(\omega_1)\Psi_1(\omega_2)-\frac{1}{2}\right) \times\left(\bar{\Psi}_2(\omega_3)\Psi_2(\omega_4)-\frac{1}{2}\right)\delta(\omega_1-\omega_2+\omega_3-\omega_4) \tag{B7}$$

in accordance with Eq. (2b). Here $\Psi(i\omega)$ and $\bar{\Psi}(i\omega)$ denote the frequency dependent Grassmann fields corresponding to the previously introduced Nambu spinors.

We can now decompose the action into a effective part, corresponding to the limit $\Delta\to\infty$, and all other terms (compare Ref. [32])

$$S = S_{\text{eff}} + S_{\text{pert}}, \tag{B8}$$

with

$$S_{\text{eff}} = -\frac{1}{2\pi}\int d\omega\ \bar{\Psi}(i\omega)G_0^{\text{eff}}(i\omega)^{-1}\Psi(i\omega) + S_{\text{int}}, \tag{B9a}$$

$$G_0^{\text{eff}}(i\omega) = \lim_{\Delta\to\infty} G_0(i\omega), \tag{B9b}$$

as well as

$$S_{\text{pert}} = -\frac{1}{2\pi}\int d\omega\ \bar{\Psi}(i\omega)(G_0(i\omega)^{-1}-G_0^{\text{eff}}(i\omega)^{-1})\Psi(i\omega). \tag{B10}$$

Expanding to lowest order in S_{pert} allows us to compute straightforwardly the corrections to the atomic levels [32]. Note that this formulation in principle also allows us to set up a functional renormalization group flow starting from the exact atomic limit solution, following the ideas of Ref. [106].

[1] L. Glazman and K. Matveev, JETP Lett. **49**, 659 (1989).
[2] C. Beenakker and H. van Houten, in *Single-Electron Tunneling and Mesoscopic Devices*, Springer Series in Electronics and Photonics, edited by H. Koch and H. Lübbig (Springer, Berlin, 1992), Vol. 31, pp. 175–179.
[3] R. Bauernschmitt, J. Siewert, Y. V. Nazarov, and A. A. Odintsov, Phys. Rev. B **49**, 4076 (1994).
[4] S. Ishizaka, J. Sone, and T. Ando, Phys. Rev. B **52**, 8358 (1995).
[5] A. Levy Yeyati, J. C. Cuevas, A. López-Dávalos, and A. Martín-Rodero, Phys. Rev. B **55**, R6137 (1997).
[6] A. T. Alastalo, R. J. Joynt, and M. M. Salomaa, J. Phys.: Condens. Matter **10**, L63 (1998).
[7] A. V. Rozhkov and D. P. Arovas, Phys. Rev. Lett. **82**, 2788 (1999).
[8] A. A. Clerk and V. Ambegaokar, Phys. Rev. B **61**, 9109 (2000).
[9] M.-S. Choi, C. Bruder, and D. Loss, Phys. Rev. B **62**, 13569 (2000).
[10] A. V. Rozhkov and D. P. Arovas, Phys. Rev. B **62**, 6687 (2000).
[11] Y. Avishai, A. Golub, and A. D. Zaikin, Phys. Rev. B **63**, 134515 (2001).
[12] J. C. Cuevas, A. Levy Yeyati, and A. Martín-Rodero, Phys. Rev. B **63**, 094515 (2001).
[13] K. Kusakabe, Y. Tanaka, and Y. Tanuma, Physica E **18**, 50 (2003).
[14] A. Zazunov, V. S. Shumeiko, E. N. Bratus', J. Lantz, and G. Wendin, Phys. Rev. Lett. **90**, 087003 (2003).
[15] E. Vecino, A. Martín-Rodero, and A. Levy Yeyati, Phys. Rev. B **68**, 035105 (2003).
[16] M.-S. Choi, M. Lee, K. Kang, and W. Belzig, Phys. Rev. B **70**, 020502 (2004).
[17] F. Siano and R. Egger, Phys. Rev. Lett. **93**, 047002 (2004).
[18] A. Oguri, Y. Tanaka, and A. C. Hewson, J. Phys. Soc. Jpn. **73**, 2494 (2004).
[19] G. Sellier, T. Kopp, J. Kroha, and Y. S. Barash, Phys. Rev. B **72**, 174502 (2005).
[20] F. S. Bergeret, A. Levy Yeyati, and A. Martín-Rodero, Phys. Rev. B **74**, 132505 (2006).
[21] R. López, M.-S. Choi, and R. Aguado, Phys. Rev. B **75**, 045132 (2007).
[22] I. A. Sadovskyy, G. B. Lesovik, and G. Blatter, Phys. Rev. B **75**, 195334 (2007).
[23] C. Benjamin, T. Jonckheere, A. Zazunov, and T. Martin, Eur. Phys. J. B **57**, 279 (2007).
[24] M. G. Pala, M. Governale, and J. König, New J. Phys. **9**, 278 (2007).
[25] L. Dell'Anna, A. Zazunov, R. Egger, and T. Martin, Phys. Rev. B **75**, 085305 (2007).

[26] J. Sköldberg, T. Löfwander, V. S. Shumeiko, and M. Fogelström, Phys. Rev. Lett. **101**, 087002 (2008).

[27] L. Dell'Anna, A. Zazunov, and R. Egger, Phys. Rev. B **77**, 104525 (2008).

[28] M. Governale, M. G. Pala, and J. König, Phys. Rev. B **77**, 134513 (2008).

[29] D. Futterer, M. Governale, M. G. Pala, and J. König, Phys. Rev. B **79**, 054505 (2009).

[30] A. Zazunov, R. Egger, T. Jonckheere, and T. Martin, Phys. Rev. Lett. **103**, 147004 (2009).

[31] A. Zazunov, A. Schulz, and R. Egger, Phys. Rev. Lett. **102**, 047002 (2009).

[32] T. Meng, S. Florens, and P. Simon, Phys. Rev. B **79**, 224521 (2009).

[33] A. Zazunov, A. L. Yeyati, and R. Egger, Phys. Rev. B **81**, 012502 (2010).

[34] D. J. Luitz and F. F. Assaad, Phys. Rev. B **81**, 024509 (2010).

[35] R. Žitko, M. Lee, R. López, R. Aguado, and M.-S. Choi, Phys. Rev. Lett. **105**, 116803 (2010).

[36] J. Eldridge, M. G. Pala, M. Governale, and J. König, Phys. Rev. B **82**, 184507 (2010).

[37] M. Lee, T. Jonckheere, and T. Martin, Phys. Rev. B **81**, 155114 (2010).

[38] J. S. Lim, R. López, and R. Aguado, Phys. Rev. Lett. **107**, 196801 (2011).

[39] Y. Yamada, Y. Tanaka, and N. Kawakami, Phys. Rev. B **84**, 075484 (2011).

[40] A. Martín-Rodero and A. Levy Yeyati, J. Phys.: Condens. Matter **24**, 385303 (2012).

[41] I. A. Sadovskyy, G. B. Lesovik, G. Blatter, T. Jonckheere, and T. Martin, Phys. Rev. B **85**, 125442 (2012).

[42] S. Droste, S. Andergassen, and J. Splettstoesser, J. Phys.: Condens. Matter **24**, 415301 (2012).

[43] A. Brunetti, A. Zazunov, A. Kundu, and R. Egger, Phys. Rev. B **88**, 144515 (2013).

[44] J. Barański and T. Domański, J. Phys.: Condens. Matter **25**, 435305 (2013).

[45] D. Futterer, J. Swiebodzinski, M. Governale, and J. König, Phys. Rev. B **87**, 014509 (2013).

[46] A. Koga, Phys. Rev. B **87**, 115409 (2013).

[47] T. Yokoyama, M. Eto, and Y. V. Nazarov, Phys. Rev. B **89**, 195407 (2014).

[48] J. F. Rentrop, S. G. Jakobs, and V. Meden, Phys. Rev. B **89**, 235110 (2014).

[49] M. Žonda, V. Pokorný, V. Janiš, and T. Novotný, Sci. Rep. **5**, 8821 (2015).

[50] G. Kiršanskas, M. Goldstein, K. Flensberg, L. I. Glazman, and J. Paaske, Phys. Rev. B **92**, 235422 (2015).

[51] J. J. A. Baselmans, A. F. Morpurgo, B. J. van Wees, and T. M. Klapwijk, Nature (London) **397**, 43 (1999).

[52] A. Y. Kasumov, R. Deblock, M. Kociak, B. Reulet, H. Bouchiat, I. I. Khodos, Y. B. Gorbatov, V. T. Volkov, C. Journet, and M. Burghard, Science **284**, 1508 (1999).

[53] A. F. Morpurgo, Science **286**, 263 (1999).

[54] M. R. Buitelaar, T. Nussbaumer, and C. Schönenberger, Phys. Rev. Lett. **89**, 256801 (2002).

[55] M. R. Buitelaar, W. Belzig, T. Nussbaumer, B. Babić, C. Bruder, and C. Schönenberger, Phys. Rev. Lett. **91**, 057005 (2003).

[56] A. Kasumov, M. Kociak, M. Ferrier, R. Deblock, S. Guéron, B. Reulet, I. Khodos, O. Stéphan, and H. Bouchiat, Phys. Rev. B **68**, 214521 (2003).

[57] J. A. van Dam, Y. V. Nazarov, E. P. A. M. Bakkers, S. de Franceschi, and L. P. Kouwenhoven, Nature (London) **442**, 667 (2006).

[58] J.-P. Cleuziou, W. Wernsdorfer, V. Bouchiat, T. Ondarçuhu, and M. Monthioux, Nat. Nanotechnol. **1**, 53 (2006).

[59] P. Jarillo-Herrero, J. A. van Dam, and L. P. Kouwenhoven, Nature (London) **439**, 953 (2006).

[60] H. I. Jørgensen, K. Grove-Rasmussen, T. Novotný, K. Flensberg, and P. E. Lindelof, Phys. Rev. Lett. **96**, 207003 (2006).

[61] H. I. Jørgensen, T. Novotný, K. Grove-Rasmussen, K. Flensberg, and P. E. Lindelof, Nano Lett. **7**, 2441 (2007).

[62] C. Buizert, A. Oiwa, K. Shibata, K. Hirakawa, and S. Tarucha, Phys. Rev. Lett. **99**, 136806 (2007).

[63] T. Sand-Jespersen, J. Paaske, B. M. Andersen, K. Grove-Rasmussen, H. I. Jørgensen, M. Aagesen, C. B. Sørensen, P. E. Lindelof, K. Flensberg, and J. Nygård, Phys. Rev. Lett. **99**, 126603 (2007).

[64] K. Grove-Rasmussen, H. Ingerslev Jørgensen, and P. E. Lindelof, New J. Phys. **9**, 124 (2007).

[65] A. Eichler, M. Weiss, S. Oberholzer, C. Schönenberger, A. Levy Yeyati, J. C. Cuevas, and A. Martín-Rodero, Phys. Rev. Lett. **99**, 126602 (2007).

[66] A. Eichler, R. Deblock, M. Weiss, C. Karrasch, V. Meden, C. Schönenberger, and H. Bouchiat, Phys. Rev. B **79**, 161407 (2009).

[67] H. I. Jørgensen, K. Grove-Rasmussen, K. Flensberg, and P. E. Lindelof, Phys. Rev. B **79**, 155441 (2009).

[68] L. Hofstetter, S. Csonka, J. Nygård, and C. Schönenberger, Nature (London) **461**, 960 (2009).

[69] S. de Franceschi, L. Kouwenhoven, C. Schönenberger, and W. Wernsdorfer, Nat. Nanotechnol. **5**, 703 (2010).

[70] J.-D. Pillet, C. H. L. Quay, P. Morfin, C. Bena, A. L. Yeyati, and P. Joyez, Nat. Phys. **6**, 965 (2010).

[71] L. G. Herrmann, F. Portier, P. Roche, A. L. Yeyati, T. Kontos, and C. Strunk, Phys. Rev. Lett. **104**, 026801 (2010).

[72] K. J. Franke, G. Schulze, and J. I. Pascual, Science **332**, 940 (2011).

[73] R. Maurand, T. Meng, E. Bonet, S. Florens, L. Marty, and W. Wernsdorfer, Phys. Rev. X **2**, 011009 (2012).

[74] C. Ryu, P. W. Blackburn, A. A. Blinova, and M. G. Boshier, Phys. Rev. Lett. **111**, 205301 (2013).

[75] J. Bauer, J. I. Pascual, and K. J. Franke, Phys. Rev. B **87**, 075125 (2013).

[76] J.-D. Pillet, P. Joyez, R. Žitko, and M. F. Goffman, Phys. Rev. B **88**, 045101 (2013).

[77] L. Bretheau, Ç. Ö. Girit, C. Urbina, D. Esteve, and H. Pothier, Phys. Rev. X **3**, 041034 (2013).

[78] L. Bretheau, Ç. Ö. Girit, H. Pothier, D. Esteve, and C. Urbina, Nature (London) **499**, 312 (2013).

[79] B.-K. Kim, Y.-H. Ahn, J.-J. Kim, M.-S. Choi, M.-H. Bae, K. Kang, J. S. Lim, R. López, and N. Kim, Phys. Rev. Lett. **110**, 076803 (2013).

[80] W. Chang, V. E. Manucharyan, T. S. Jespersen, J. Nygård, and C. M. Marcus, Phys. Rev. Lett. **110**, 217005 (2013).

[81] A. Kumar, M. Gaim, D. Steininger, A. Levy Yeyati, A. Martín-Rodero, A. K. Hüttel, and C. Strunk, Phys. Rev. B **89**, 075428 (2014).
[82] S. Abay, D. Persson, H. Nilsson, F. Wu, H. Q. Xu, M. Fogelström, V. Shumeiko, and P. Delsing, Phys. Rev. B **89**, 214508 (2014).
[83] J. Schindele, A. Baumgartner, R. Maurand, M. Weiss, and C. Schönenberger, Phys. Rev. B **89**, 045422 (2014).
[84] E. J. H. Lee, X. Jiang, M. Houzet, R. Aguado, C. M. Lieber, and S. de Franceschi, Nat. Nanotechnol. **9**, 79 (2014).
[85] C. Karrasch, A. Oguri, and V. Meden, Phys. Rev. B **77**, 024517 (2008).
[86] C. Karrasch and V. Meden, Phys. Rev. B **79**, 045110 (2009).
[87] C. Karrasch, S. Andergassen, and V. Meden, Phys. Rev. B **84**, 134512 (2011).
[88] D. J. Luitz, F. F. Assaad, T. Novotný, C. Karrasch, and V. Meden, Phys. Rev. Lett. **108**, 227001 (2012).
[89] T. Meng, Master's thesis, Universität Karlsruhe, 2009.
[90] K. Satori, H. Shiba, O. Sakai, and Y. Shimizu, J. Phys. Soc. Jpn. **61**, 3239 (1992).
[91] O. Sakai, Y. Shimizu, H. Shiba, and K. Satori, J. Phys. Soc. Jpn. **62**, 3181 (1993).
[92] T. Yoshioka and Y. Ohashi, J. Phys. Soc. Jpn. **69**, 1812 (2000).
[93] J. Bauer, A. Oguri, and A. C. Hewson, J. Phys.: Condens. Matter **19**, 486211 (2007).
[94] Y. Tanaka, A. Oguri, and A. C. Hewson, New J. Phys. **9**, 115 (2007).
[95] R. Bulla, T. A. Costi, and T. Pruschke, Rev. Mod. Phys. **80**, 395 (2008).
[96] T. Hecht, A. Weichselbaum, J. von Delft, and R. Bulla, J. Phys.: Condens. Matter **20**, 275213 (2008).
[97] Y. Tanaka, N. Kawakami, and A. Oguri, Phys. Rev. B **78**, 035444 (2008).
[98] R. de Sousa, K. B. Whaley, T. Hecht, J. von Delft, and F. K. Wilhelm, Phys. Rev. B **80**, 094515 (2009).
[99] A. Oguri, Y. Tanaka, and J. Bauer, Phys. Rev. B **87**, 075432 (2013).
[100] R. Žitko, J. S. Lim, R. López, and R. Aguado, Phys. Rev. B **91**, 045441 (2015).
[101] B. D. Josephson, Phys. Lett. **1**, 251 (1962).
[102] F. Bloch, Phys. Rev. B **2**, 109 (1970).
[103] In the limit of infinite superconducting gap a local moment cannot be screened due to the lack of electronic states in the leads. Consequently, the Kondo effect is fully suppressed.
[104] W. Metzner, M. Salmhofer, C. Honerkamp, V. Meden, and K. Schönhammer, Rev. Mod. Phys. **84**, 299 (2012).
[105] M. Salmhofer, *Renormalization: An Introduction (Theoretical and Mathematical Physics)*, corrected ed. (Springer, Berlin, 1999).
[106] N. Wentzell, C. Taranto, A. Katanin, A. Toschi, and S. Andergassen, Phys. Rev. B **91**, 045120 (2015).
[107] C. Karrasch, T. Enss, and V. Meden, Phys. Rev. B **73**, 235337 (2006).
[108] C. Karrasch, T. Hecht, A. Weichselbaum, J. von Delft, Y. Oreg, and V. Meden, New J. Phys. **9**, 123 (2007).

Appendix II

Correlated starting points for the functional renormalization group

Correlated starting points for the functional renormalization group

N. Wentzell,[1,2,3] C. Taranto,[3] A. Katanin,[4,5] A. Toschi,[3] and S. Andergassen[1,2]
[1] *Faculty of Physics, University of Vienna, Boltzmanngasse 5, 1090 Vienna, Austria*
[2] *Institut für Theoretische Physik and CQ Center for Collective Quantum Phenomena, Universität Tübingen, Auf der Morgenstelle 14, D-72076 Tübingen, Germany*
[3] *Institute for Solid State Physics, Vienna University of Technology, 1040 Vienna, Austria*
[4] *Institute of Metal Physics, Kovalevskaya Street 18, 620990 Ekaterinburg, Russia*
[5] *Ural Federal University, 620002 Ekaterinburg, Russia*

(Received 5 November 2014; revised manuscript received 19 December 2014; published 16 January 2015)

We present a general frame to extend functional renormalization group (fRG) based computational schemes by using an exactly solvable *interacting* reference problem as starting point for the RG flow. The systematic expansion around this solution accounts for a nonperturbative inclusion of correlations. Introducing auxiliary fermionic fields by means of a Hubbard-Stratonovich transformation, we derive the flow equations for the auxiliary fields and determine the relation to the conventional weak-coupling truncation of the hierarchy of flow equations. As a specific example we consider the dynamical mean field theory (DMFT) solution as reference system, and discuss the relation to the recently introduced DMF^{2}RG and the dual-fermion formalism.

DOI: 10.1103/PhysRevB.91.045120 PACS number(s): 71.10.−w, 71.27.+a

I. INTRODUCTION

One of the main challenges in nonrelativistic quantum many-body theory is the development of powerful tools for treating correlations between fermionic particles, not limited to specific parameter regimes. These would provide the keys for understanding and controlling many of the most exciting experiments currently performed in solid-state, nanoscopic, and cold-atom physics. In fact, the state-of-the-art theoretical tools allow for an accurate treatment of quantum many-body correlations in specific cases, but their reliability is not guaranteed in general.

A very powerful method, among those currently available and widely used for performing model and realistic calculations of correlated fermions, is arguably the functional renormalization group (fRG) [1–4]. The starting point of the fRG is an exact functional flow equation, which parametrizes the gradual evolution from an exactly solvable initial action $\mathcal{S}_{\text{ini}}$ (typically of an uncorrelated problem) to the full final action $\mathcal{S}_{\text{fin}}$ of the many-body problem of interest. Expanding the functional flow equation yields an exact infinite hierarchy of flow equations for the n-particle one-particle irreducible (1PI) vertex functions. However, for most calculations, the hierarchy of equations is truncated at the two-particle level. Because of this approximation, the validity of the conventional fRG is limited to the perturbative weak-coupling regime, except for situations in which phase space restrictions suppress higher order contributions [1,5,6]. For the same reason, the accuracy of the final results depends on the choice of the initial conditions.

In spite of the limitation to the weak-coupling regime, the fRG has led to powerful new approximation schemes: In fRG, infrared singularities can be dealt with much more efficiently than within the traditional resummations of perturbation theory, due to the built-in RG structure. Moreover—differently from other perturbative approaches, such as RPA—fRG is "channel unbiased": The fRG flow equations include the contributions of *all* scattering channels (e.g., spin, charge, particle-particle) and their reciprocal interplay.

The development of novel computation schemes for extending the advantages of an fRG treatment to the strong-coupling regime, where, e.g., Mott-Hubbard metal-insulator transitions can occur, represents a very challenging but highly rewarding task. In fact, the potential of extending the fRG to the strong-coupling (SC) regime in order to overcome the main restriction of the conventional implementations has already motivated the first pioneering studies [7–9]. The underlying idea is to access the SC regime by changing the initial conditions of the fRG flow: If these are extracted from the exact solution of a suitably chosen interacting reference problem, a significant part of the correlation effects are included nonperturbatively already from the very beginning, while the remaining ones will be generated, in all scattering channels, by the fRG flow. Formally, this corresponds to taking a SC "reference" system $\mathcal{S}_R$ as an initial action $\mathcal{S}_{\text{ini}}$, provided that it allows for a reliable (numerical or analytical) solution. In the case of the Anderson impurity model (AIM), for example, the atomic limit and extensions thereof have recently been used as a reference system to define a SC starting point for the fRG flow [8,9]. For the Hubbard model on the other hand, the effective AIM determined self-consistently by dynamical mean field theory (DMFT) was chosen to define the initial conditions of the fRG flow [7]. This approach, coined DMF^{2}RG, aims at a systematic and channel-unbiased inclusion of correlations [7], beyond the purely local ones described, nonperturbatively, by the DMFT. We note that the idea of choosing a SC (or nonperturbative) reference system for the fRG flow has been recently introduced also in the context of spin models [10,11] or for systems of correlated bosons [12,13].

Irrespective of the performance in specific cases, all extensions of the conventional fRG face the challenge of proving the validity of the truncation procedures in the nonperturbative SC regime. This subject has never been explicitly addressed and calls for a systematic derivation.

The main goal of this paper is to define the properties of the fRG schemes with a nonperturbative starting point within a rigorous framework and a unified formalism. To this aim, we

consider a general starting point for the perturbative expansion: performing a Hubbard-Stratonovich transformation for the fermionic degrees of freedom *not* associated with the chosen (SC) reference system, we derive an action in terms of the auxiliary Hubbard-Stratonovich fermionic fields (referred to as "dual" fermions [14–22] in the context of the diagrammatic extensions [14–29] of DMFT). The resulting equations are compared to those derived by directly working at the level of the physical fermions, and finally, the physical contents underlying the approximations made in the different schemes are critically analyzed.

The paper is organized as follows. In Sec. II we briefly review the general procedure for decoupling the fermionic degrees of freedom associated with a given reference system with the introduction of auxiliary fermions. The formulation in terms of auxiliary fields and its physical interpretation is presented in Sec. III. In Sec. VI we derive the flow equations in the auxiliary space and in Sec. V we discuss the relation to other methods. Finally, in Sec. VI, we summarize our results and draw conclusions.

II. INTERACTING REFERENCE SYSTEM

In the following, we present a general formalism that allows for an expansion around an interacting reference system. It was first introduced to set up an expansion of the d-dimensional Hubbard model around the atomic limit [30], and has recently been used in the dual-fermion (DF) formalism [14–22] to include nonlocal correlations beyond DMFT.

Let us start with a system of fermionic particles described by a general action of the form

$$\mathcal{S}(\bar{\varphi},\varphi) = -(\bar{\varphi}, g^{-1}\varphi) + \mathcal{S}_{\text{int}}(\bar{\varphi},\varphi). \tag{1}$$

Here we use the compact notation $(\bar{\varphi},\psi) := \sum_\xi \bar{\varphi}_\xi \psi_\xi$. g denotes the noninteracting Green's function, and $\mathcal{S}_{\text{int}}$ contains quartic interaction terms in the Grassmann fields $\varphi_\xi, \bar{\varphi}_\xi$. The multi-index $\xi = (\omega_n, s)$ consists of a fermionic Matsubara frequency ω_n and a general quantum number s including, e.g., momentum, spin, and orbital index. We introduce an interacting reference system described by the action

$$\mathcal{S}_R(\bar{\varphi},\varphi) = -\left(\bar{\varphi}, g_R^{-1}\varphi\right) + \mathcal{S}_{\text{int}}(\bar{\varphi},\varphi) \tag{2}$$

written in terms of the same Grassmann fields as action (1). It differs from the latter only in the quadratic part g_R^{-1}, which is chosen such that the system is exactly solvable.

In order to expand the action

$$\mathcal{S}(\bar{\varphi},\varphi) = \mathcal{S}_R(\bar{\varphi},\varphi) - (\bar{\varphi}, \Delta\varphi) \tag{3}$$

in the difference $\Delta = g^{-1} - g_R^{-1}$ of the quadratic parts, we cannot apply Wick's theorem to the many-particle reference Green's functions because the reference action $\mathcal{S}_R$ contains the quartic terms in the fields. Instead, we perform a fermionic Hubbard-Stratonovich transformation

$$(\bar{\varphi}, nD^{-1}n\varphi) = \ln \int \frac{\mathcal{D}(\bar{\nu},\nu)}{\det D} e^{-(\bar{\nu}, D\nu)+(\bar{\nu}, n\varphi)+(\bar{\varphi}, n\nu)}, \tag{4}$$

introducing a set of auxiliary fermionic fields ν, $\bar{\nu}$. We require that the matrices $n_{\xi,\xi'}$ and $D_{\xi,\xi'}$ fulfill the condition $nD^{-1}n = \Delta$, which implies freedom in the choice of n. At this point, we can perform the integration with respect to the physical fields φ, to yield an action

$$\mathcal{S}_a(\bar{\nu},\nu) = -\left(\bar{\nu}, g_a^{-1}\nu\right) + \hat{\mathcal{V}}(\bar{\nu},\nu) \tag{5}$$

that depends on the auxiliary fields only (see Appendix A 2 for more details), with an inverse Gaussian propagator

$$g_a^{-1} = -n[G_R + \Delta^{-1}]n \tag{6}$$

that contains correlation effects already through the one-particle Green's function of the reference system G_R. The interaction of the auxiliary fields reads

$$\hat{\mathcal{V}}(\bar{\nu},\nu) = -[\ln \mathcal{G}^R(\bar{\eta},\eta) + (\bar{\eta}, G_R\eta)]\Big|_{\substack{\eta = n\nu \\ \bar{\eta} = n^T\bar{\nu}}}, \tag{7}$$

where $\mathcal{G}_R$ corresponds to the generating functional of the reference system Green's functions,

$$\mathcal{G}_R(\bar{\eta},\eta) = \frac{1}{Z_R}\int \mathcal{D}(\bar{\varphi},\varphi) e^{-[S_R(\bar{\varphi},\varphi)+(\bar{\eta},\varphi)+(\bar{\varphi},\eta)]}, \tag{8}$$

with source fields η, $\bar{\eta}$. While the freedom in the choice of n can be maintained in all following considerations, we focus on the conventional choice [14]

$$n = G_R^{-1} \tag{9}$$

for the sake of simplicity [50].

Before providing more details about the treatment of the SC problem in auxiliary space, let us briefly sketch in Fig. 1 the idea motivating the formulation of an fRG flow from a SC starting point. In contrast to the case of the conventional fRG, the initial uncorrelated generating functional $\mathcal{G}_{\text{ini}}$ is replaced by the one of the (solvable) interacting system, $\mathcal{G}_R$. A suitable choice reduces the effects of the truncation of the flow equations on the final result, which is therefore closer to the desired $\mathcal{G}_{\text{fin}}$.

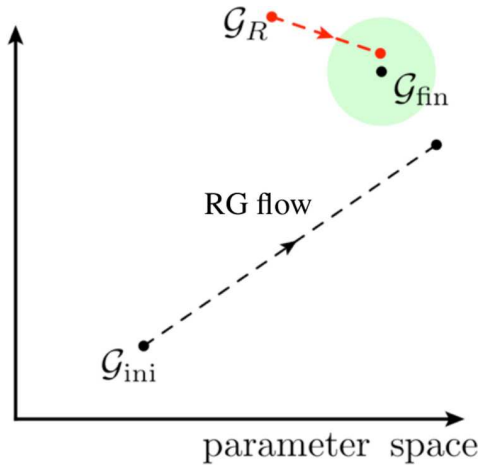

FIG. 1. (Color online) Schematic representation of the fRG flow in a general "parameter space." In conventional schemes the fRG flow starts from the generating functional of an uncorrelated problem $\mathcal{G}_{\text{ini}}$. The approximations due to the truncation lead to deviations of the result at the end of the flow from the exact final generating functional $\mathcal{G}_{\text{fin}}$. This truncation error can be reduced by using a correlated reference system (provided its generating functional $\mathcal{G}_R$ is exactly known) as a starting point for the flow.

III. THE AUXILIARY PROBLEM

Now that we have reformulated our initial problem in terms of the auxiliary fields, we derive the expansion around the reference system solution. By definition the reference system solution is contained completely in the noninteracting theory ($\hat{\mathcal{V}} = 0$) of the auxiliary fields, while any treatment of the auxiliary interaction introduces corrections that take into account the solution of the physical system. In the following, we discuss the physical interpretation of the propagator and of the interaction of the auxiliary fields, before introducing the relations between the physical quantities in auxiliary and physical space.

A. Gaussian propagator

The Gaussian propagator of the auxiliary fields (6) has interesting properties. We find that as Δ tends to zero, g_a vanishes linearly [31]:

$$g_a \xrightarrow[\Delta\to 0]{} G_R \Delta G_R. \tag{10}$$

This means that any expansion in the interaction converges asymptotically, as higher order diagrams with N internal lines will be suppressed as Δ^N. For a physical intuition of the propagation described by g_a, we write

$$g_a = \frac{1}{g^{-1} - \Sigma_R} - G_R. \tag{11}$$

The first term can be interpreted as an approximation to the physical Green's function (it actually brings the result of the 0th-order expansion in $\hat{\mathcal{V}}$), from which we subtract the full reference propagator. In this sense, g_a corresponds to the difference of the interacting propagators. Therefore it does not exhibit the typical $\sim 1/\omega$ behavior at large frequencies, but rather $\sim 1/\omega^2$.

B. Interaction

By integrating out the physical fields φ, the interaction of the auxiliary fields (7) is generated. It contains two- and multi-particle interactions that are given by the connected reference Green functions, where G_R is amputated at each external leg. We can thus schematically write

$$\begin{aligned}\hat{\mathcal{V}}(\bar{\nu},\nu) = &-\tfrac{1}{4} G_R^{(2),c}\left[\left(G_R^{-1}\bar{\nu}\right),\left(G_R^{-1}\bar{\nu}\right),\left(G_R^{-1}\nu\right),\left(G_R^{-1}\nu\right)\right] \\ &-\tfrac{1}{9} G_R^{(3),c}\left[\left(G_R^{-1}\bar{\nu}\right),\left(G_R^{-1}\bar{\nu}\right),\left(G_R^{-1}\bar{\nu}\right),\right. \\ &\left.\left(G_R^{-1}\nu\right),\left(G_R^{-1}\nu\right),\left(G_R^{-1}\nu\right)\right] + \cdots,\end{aligned} \tag{12}$$

where $G_R^{(m),c}$ $(m = 2,\ldots,\infty)$ denotes the connected m-particle reference Green's function. In Eq. (12) we introduced the notation $V_n[a_1,\ldots,a_n,a_1',\ldots,a_n']$ which is a shorthand for

$$\begin{aligned}&V_n[a_1,\ldots,a_n,a_1',\ldots,a_n']_{\xi_1,\ldots,\xi_n,\xi_1',\ldots,\xi_n'} \\ &= (a_1)_{\xi_1,\psi_1}\ldots(a_n)_{\xi_n,\psi_n} V_n(\psi_1,\ldots,\psi_n,\psi_1',\ldots,\psi_n') \\ &\quad\times (a_1')_{\psi_1',\xi_1'}\ldots(a_n')_{\psi_n',\xi_n'},\end{aligned} \tag{13}$$

where we sum over repeated indices. V_n represents a generic n-particle vertex function (e.g., connected Green's function, 1PI vertex,...) and a_i is a two-dimensional matrix in the multi-index ξ_i.

Since the treatment of infinitely many multi-particle interactions poses an impossible task, approximations to the infinite series defining the interaction have to be devised. We drop the interaction terms beyond the quartic one and thus

$$\begin{aligned}\hat{\mathcal{V}}(\bar{\nu},\nu) &\approx -\tfrac{1}{4} G_R^{(2),c}\left[\left(G_R^{-1}\bar{\nu}\right),\left(G_R^{-1}\bar{\nu}\right),\left(G_R^{-1}\nu\right),\left(G_R^{-1}\nu\right)\right] \\ &= -\tfrac{1}{4}\gamma_2^R[\bar{\nu},\bar{\nu},\nu,\nu],\end{aligned} \tag{14}$$

where γ_2^R denotes the one-particle irreducible (1PI) two-particle vertex of the reference system.

This represents an approximation based on the fundamental assumption that the effects of $(m \geqslant 3)$-particle scattering processes beyond the description of the reference system can be neglected. The impact this has on the resulting flow equations is discussed in Sec. IV. While previous works [14–22,27,30] have treated the auxiliary interaction $\hat{\mathcal{V}}$ by means of perturbation theory or ladder approaches, we propose using the fRG [4] to perform a channel-unbiased resummation of diagrams to all orders in a scale-dependent fashion, thereby further improving on the physical results.

C. Relation to physical quantities

Once the solution in the auxiliary space is obtained, we need to translate Green's and vertex functions from the auxiliary to the physical space. These relations can be formulated in a very general way by establishing the connection between the generating functionals. As shown in Appendix A 3, the generating functionals of the Green's functions fulfill

$$\mathcal{G}(\bar{\eta},\eta) = \mathcal{G}_a\left(G_R^{-T}\Delta^{-T}\bar{\eta}, G_R^{-1}\Delta^{-1}\eta\right) \times e^{-(\bar{\eta},\Delta^{-1}\eta)}, \tag{15}$$

with $G_R^{-T} = (G_R^{-1})^T$. Further relations for the generating functional of the connected Green's functions, or the effective interaction and the respective derivations, are presented in Appendix A 3. By taking the derivative of Eq. (15) with respect to the source fields we find the relation between the physical and auxiliary Green's functions,

$$G = \Delta^{-1} + \Delta^{-1} G_R^{-1} G_a G_R^{-1} \Delta^{-1}. \tag{16}$$

Translated to the self-energy, this relation reads

$$\Sigma = \Sigma_R + \frac{\Sigma_a}{\mathbb{1} + G_R \Sigma_a}, \tag{17}$$

where the fraction is to be understood as multiplication by the inverse from the right. The corresponding relation for the 1PI two-particle vertex reads (see Appendix A 3 for further details)

$$\gamma_2 = \gamma_{2,a}[\zeta,\zeta,\bar{\zeta},\bar{\zeta}], \tag{18}$$

with $\zeta = \bar{G}^{-1} G_R$ and $\bar{\zeta} = G_R \bar{G}^{-1}$, where

$$\bar{G} = \left(g_R^{-1} - \Sigma\right)^{-1}. \tag{19}$$

In the following we refer to Eqs. (11), (17), and (18) and generalizations thereof for higher order vertices as the transformation to the auxiliary fields $\mathcal{T}$.

D. DMFT as reference system

To make the procedure described above more concrete, let us focus on the example of a reference system obtained by DMFT. This allows for a direct comparison with the DF

approach and the recently introduced DMF^{2}RG [7], which is summarized in Sec. V.

DMFT can be considered the quantum extension of classical mean field theory [32,33] as it can be formally derived as the exact solution of a quantum lattice Hamiltonian in the limit of infinite spatial dimensions ($d \to \infty$) [34]. In DMFT all nonlocal spatial correlations are averaged out, and one can reduce the study of a quantum lattice problem to a self-consistently determined local impurity problem. For instance, one can consider the action of a one-band Hubbard model [35] given by

$$\mathcal{S}_{\text{lattice}} = T \sum_{\omega_n,\sigma} \int d\mathbf{k} \;\; \bar{\varphi}_{\mathbf{k},\sigma}(\omega_n) g_{\mathbf{k}}^{-1}(\omega_n) \varphi_{\mathbf{k},\sigma}(\omega_n) + U \sum_i \int d\tau \;\; [n_{i,\uparrow}(\tau) - 1/2][n_{i,\downarrow}(\tau) - 1/2], \tag{20}$$

with T being the temperature, $g_{\mathbf{k}}^{-1}(\omega_n) = (i\omega_n - \mu - \epsilon_{\mathbf{k}})$, $\epsilon_{\mathbf{k}}$ the energy dispersion of the lattice, i the lattice site index, U the Hubbard interaction, and $n_{i,\sigma}(\tau) = \bar{\varphi}_{i,\sigma}(\tau)\varphi_{i,\sigma}(0)$. The on-site (local) properties of this action are studied in DMFT by singling out a lattice site and embedding it in an effective bath which accounts for the presence of all the other sites, i.e., an Anderson impurity model (AIM) in an effective bath. To guarantee that the AIM approximates the local physics of the lattice, the effective bath (or hybridization function) $\Gamma(\omega_n)$ has to be computed self-consistently, and the resulting frequency dependence of the effective bath accounts for all purely local quantum correlations. The self-consistency condition that determines the effective bath and the propagator $g_{\text{imp}}^{-1}(\omega_n) = i\omega_n - \Gamma(\omega_n)$ (often referred to as dynamical Weiss field in the DMFT literature) of the AIM reads

$$G_{\text{DMFT}} = \int d\mathbf{k} \left(g_{\mathbf{k}}^{-1} - \Sigma_{\text{DMFT}}\right)^{-1} = \left(g_{\text{imp}}^{-1} - \Sigma_{\text{DMFT}}\right)^{-1}, \tag{21}$$

where Σ_{DMFT} is the self-energy of the self-consistent impurity problem defined by g_{imp}, and G_{DMFT} represents the DMFT approximation to the local interacting lattice Green's function. The self-consistency equation (21) follows directly from the DMFT *assumption* of locality of the lattice self-energy, which is clearly an approximation in finite-dimensional systems.

Since the AIM can be solved exactly, the action of a collection of disconnected self-consistent AIMs, one for each lattice site, is well suited as reference action to approximate the physical action (1)

$$\mathcal{S}_R = T \sum_{i,\omega_n,\sigma} \bar{\varphi}_{i,\sigma}(\omega_n) g_{\text{imp}}^{-1}(\omega_n) \varphi_{i,\sigma}(\omega_n) + U \sum_i \int d\tau \;\; [n_{i,\uparrow}(\tau) - 1/2][n_{i,\downarrow}(\tau) - 1/2]. \tag{22}$$

This way, the local physics of the system, computed at the DMFT level, is already included in the reference action. Note that assuming the action (22) as reference action is what is typically [51] done in the DF [14–22] approaches. In some cases, also the solution of a cellular DMFT [36] or a dynamical cluster approximation [37,38] calculation has been taken as a reference system [18,39]. This way one is able to include nonperturbatively in the initial conditions also the short-range spatial correlations, providing a complementary multiscale [39] framework to treat correlations beyond DMFT over all length scales. Hence, the DF reference system is defined by the momentum-independent propagator g_{imp}, while its interacting Green's function is the local DMFT one,

$$G_R^{-1} = g_{\text{imp}}^{-1} - \Sigma_{\text{DMFT}}. \tag{23}$$

Performing the Hubbard-Stratonovich transformation to introduce the auxiliary fermions relative to this reference system, one obtains for the noninteracting propagator

$$g_a = \frac{1}{i\omega_n - \epsilon_{\mathbf{k}} - \Sigma_{\text{imp}}} - G_R, \tag{24}$$

which explicitly depends on the momentum $\mathbf{k}$ through the lattice dispersion $\epsilon_{\mathbf{k}}$. The first term in Eq. (24) represents the DMFT approximation to the lattice Green's function under the assumption of a local self-energy. g_a is also referred to as the purely nonlocal propagator, as the local impurity Green's function is subtracted, and therefore it vanishes by summing over the momenta. As for the interaction between the auxiliary fields, this is, according to Eq. (14), given by the 1PI two-particle vertex of the AIM [14]. This input can be calculated [40,41] to high accuracy within the current numerical solvers for the AIM.

IV. FLOW EQUATIONS

After having reformulated the initial problem by means of the auxiliary action (5) we now address the issue of solving this problem using the fRG. This procedure is sketched on the right-hand side of Fig. 2. Integrating the flow equations in auxiliary space (which are derived in the following) results in an approximated solution for the auxiliary problem that we can eventually translate back to acquire a physical solution. This scheme is then compared to the one obtained by deriving fRG flow equations directly in the physical space.

A. General formulation

We recall that the first step to determine the fRG flow equations [4] is to substitute the noninteracting propagator g of the system in question by a scale-dependent g^Λ. This allows for the derivation of an exact functional flow equation

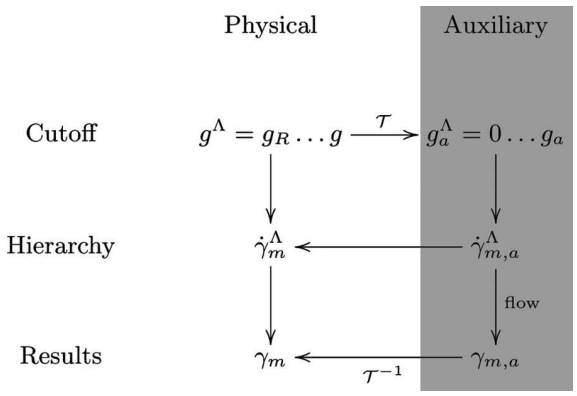

FIG. 2. Overview of the relation between the flow in physical and auxiliary space; $\mathcal{T}$ denotes the transformation to the auxiliary fields.

that describes the gradual evolution of the effective action as the cutoff scale Λ is changed. Expanding the flow equation in the 1PI vertex functions results in an infinite hierarchy of the form

$$\dot{\gamma}_m^\Lambda = f\left(\gamma_1^\Lambda, \ldots, \gamma_m^\Lambda, \gamma_{m+1}^\Lambda\right). \tag{25}$$

For practical implementations this hierarchy is typically truncated at the two-particle level by assuming that $\gamma_3^\Lambda \approx \gamma_3^{\Lambda_{\rm ini}} = 0$, reducing the hierarchy to a set of coupled flow equations for the self-energy and the 1PI two-particle vertex function

$$\dot{\Sigma}^\Lambda = -S^\Lambda \circ \gamma_2^\Lambda, \tag{26}$$

$$\dot{\gamma}_2^\Lambda = \gamma_2^\Lambda \circ (S^\Lambda \circ G^\Lambda + G^\Lambda \circ S^\Lambda) \circ \gamma_2^\Lambda. \tag{27}$$

In Eqs. (26) and (27) the $\circ$ stands for summation over internal momenta and quantum numbers according to standard diagrammatic rules as shown explicitly in Appendix A 1, while

$$S^\Lambda = -G^\Lambda[\partial_\Lambda (g^\Lambda)^{-1}]G^\Lambda = \partial_\Lambda G^\Lambda|_{\Sigma^\Lambda \text{ fix}} \tag{28}$$

denotes the single-scale propagator, with

$$G^\Lambda = [(g^\Lambda)^{-1} - \Sigma^\Lambda]^{-1}. \tag{29}$$

The scale dependence of g^Λ has to be chosen such that, at the initial scale $\Lambda_{\rm ini}$, $\Sigma^{\Lambda_{\rm ini}}$ and $\gamma_2^{\Lambda_{\rm ini}}$ can be determined exactly, while the physical propagator g is recovered at the final scale $\Lambda_{\rm final}$,

$$g^{\Lambda_{\rm final}} = g. \tag{30}$$

In conventional fRG approaches the bare propagator vanishes at the beginning of flow. We introduce the notation

$$g^\Lambda = 0 \ldots g \tag{31}$$

to describe this scale-dependence. While this choice results in trivial initial conditions that can be read off from the microscopic model action directly, recent works [7–9,11,] introduced the idea of starting the fRG flow from a reference system solution by choosing

$$g^\Lambda = g_R \ldots g. \tag{32}$$

This approach corresponds to the left-hand side of Fig. 2.

B. Flow in the auxiliary space

In contrast to the derivation in the previous subsection, we now consider the reformulated problem for the auxiliary fields, for which we set up an fRG flow in the conventional sense. For this, we introduce a scale-dependent auxiliary field propagator $g_a^\Lambda = 0 \ldots g_a$. The resulting flow equations then read as Eqs. (26) and (27), where all physical objects have to be replaced by their auxiliary equivalents. Note that the relations (17) and (18) between the scale-dependent physical and auxiliary quantities remain valid. Even though the auxiliary self-energy Σ_a^Λ vanishes at the scale $\Lambda_{\rm ini}$, the initial conditions are in general highly nontrivial, since $\gamma_{2,a}^{\Lambda_{\rm ini}} = \gamma_2^R$.

As mentioned in Sec. III B, we approximate the bare auxiliary interaction by its quartic term. This corresponds to neglecting the effect of multiparticle scattering processes when calculating corrections of the reference system solution towards the physical one. In the auxiliary fRG flow, this results in an initially vanishing scale-dependent three-particle vertex, $\gamma_{3,a}^{\Lambda_{\rm ini}} = \gamma_{3,c}^R = 0$, which justifies our truncation of the auxiliary flow equation hierarchy. Note, however, that multiparticle scattering processes are of course included in the exact solution of our reference system, and thus in the initial conditions ($\gamma_{2,a}^{\Lambda_{\rm ini}} = \gamma_2^R$) of the flow. After solving these flow equations numerically, results have to be translated back, using the transformation $\mathcal{T}^{-1}$ as described in Sec. III C.

This approach is similar in spirit to recent approaches [7–9,11] following Eq. (32), as depicted on the left-hand side of Fig. 2. In fact, any cutoff of the form (32) is translated to $g_a^\Lambda = 0 \ldots g_a$ in auxiliary space by means of (11). Without any approximations the two flow schemes yield identical results. The approximations due to the truncation of the flow equation hierarchy however induce important differences, as illustrated in the following. We compare the two paths in Fig. 2 leading to a hierarchy of physical flow equations $\dot{\gamma}_m^\Lambda$. In particular, we will compare the equations for the one- and two-particle 1PI vertex functions as relevant to common truncation schemes. Assuming that the scale dependence g_a^Λ translates into g^Λ by (11), we determine the relation between the scale-dependent Green's functions. Introducing the scale dependence in Eq. (16) and solving for G_a^Λ yields

$$G_a^\Lambda = \zeta^\Lambda (G^\Lambda - \bar{G}^\Lambda)\bar{\zeta}^\Lambda, \tag{33}$$

where $\bar{G}$, defined by Eq. (19), acquires a scale dependence via Σ^Λ. For the single-scale propagator we use the definition $S_a^\Lambda = \partial_\Lambda G_a^\Lambda|_{\Sigma_a^\Lambda \text{ fix}}$ to obtain

$$S_a^\Lambda = \zeta^\Lambda S^\Lambda \bar{\zeta}^\Lambda. \tag{34}$$

Considering that

$$\gamma_{2,a}^\Lambda = \gamma_2^\Lambda[(\zeta^\Lambda)^{-1}, (\zeta^\Lambda)^{-1}, (\bar{\zeta}^\Lambda)^{-1}, (\bar{\zeta}^\Lambda)^{-1}], \tag{35}$$

we find that each diagram contributing to the auxiliary flow can be translated to its physical counterpart by making the substitutions

$$\gamma_{2,a}^\Lambda \to \gamma_2^\Lambda, \quad S_a^\Lambda \to S^\Lambda, \quad G_a^\Lambda \to G^\Lambda - \bar{G}^\Lambda. \tag{36}$$

To relate the flow equations for the self-energy in the physical and auxiliary space we take the Λ derivative of the scale-dependent Eq. (17),

$$\dot{\Sigma}^\Lambda = \zeta^\Lambda \dot{\Sigma}_a^\Lambda \bar{\zeta}^\Lambda. \tag{37}$$

Applying the translation rules above, the corresponding flow equation in physical space remains unchanged, and is thus given by Eq. (26). The flow equations for the two-particle vertex, instead, can be obtained by taking the Λ derivative of Eq. (35). Besides the contribution arising by a direct translation of the diagrams in auxiliary space through Eq. (36), additional terms arise due to the derivative of the ζ^Λ factors attached at each leg:

$$\begin{aligned}\dot{\gamma}_2^\Lambda = {} & \dot{\gamma}_{2,a}^\Lambda[\zeta^\Lambda, \zeta^\Lambda, \bar{\zeta}^\Lambda, \bar{\zeta}^\Lambda] - \gamma_{2,a}^\Lambda[\dot{\Sigma}^\Lambda G_R, \zeta^\Lambda, \bar{\zeta}^\Lambda, \bar{\zeta}^\Lambda] \\ & - \gamma_{2,a}^\Lambda[\zeta^\Lambda, \dot{\Sigma}^\Lambda G_R, \bar{\zeta}^\Lambda, \bar{\zeta}^\Lambda] - \gamma_{2,a}^\Lambda[\zeta^\Lambda, \zeta^\Lambda, G_R \dot{\Sigma}^\Lambda, \bar{\zeta}^\Lambda] \\ & - \gamma_{2,a}^\Lambda[\zeta^\Lambda, \zeta^\Lambda, \bar{\zeta}^\Lambda, G_R \dot{\Sigma}^\Lambda].\end{aligned} \tag{38}$$

Finally, by truncating the auxiliary flow equation at the one-loop level, we get the following flow equations in physical

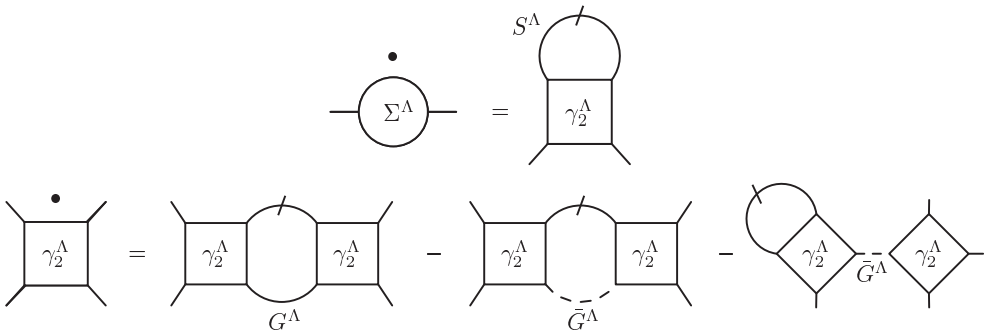

FIG. 3. Diagrammatic representation of the physical flow equations for Σ^Λ and γ_2^Λ that correspond to solving the conventional flow equations for the auxiliary fields using the second-order truncation.

space:

$$\begin{aligned}\dot{\gamma}_2^\Lambda = {} & \gamma_2^\Lambda \circ (S^\Lambda \circ G^\Lambda + G^\Lambda \circ S^\Lambda) \circ \gamma_2^\Lambda \\ & - \gamma_2^\Lambda \circ (S^\Lambda \circ \bar{G}^\Lambda + \bar{G}^\Lambda \circ S^\Lambda) \circ \gamma_2^\Lambda \\ & - \gamma_2^\Lambda[\dot{\Sigma}^\Lambda \bar{G}^\Lambda, \mathbb{1}, \mathbb{1}, \mathbb{1}] - \gamma_2^\Lambda[\mathbb{1}, \dot{\Sigma}^\Lambda \bar{G}^\Lambda, \mathbb{1}, \mathbb{1}] \\ & - \gamma_2^\Lambda[\mathbb{1}, \mathbb{1}, \bar{G}^\Lambda \dot{\Sigma}^\Lambda, \mathbb{1}] - \gamma_2^\Lambda[\mathbb{1}, \mathbb{1}, \mathbb{1}, \bar{G}^\Lambda \dot{\Sigma}^\Lambda]; \end{aligned} \quad (39)$$

for a detailed derivation we refer to Appendix A 4. The corresponding diagrams are shown in Fig. 3. The first term of Eq. (39) is identical to the flow equation Eq. (27) for the two-particle vertex in physical space, while the other terms are not present in the conventional scheme. In particular, we note that the last four terms of Eq. (39) are reducible in $\bar{G}^\Lambda$. However, this "reducibility" does not necessarily coincide with the reducibility in G^Λ and could be attributed to the specific approximation performed here. This can also be understood by considering the relation between the physical and auxiliary scale-dependent three-particle vertices, depicted in Fig. 4. Assuming that the effect of $\gamma_{3,a}^\Lambda$ on the flow is negligible, we find that the effect of the physical 1PI three-particle vertex can be described by the effect of the rightmost term in Fig. 4. By connecting two of the six external (amputated) legs of this diagram with a single-scale propagator, one obtains the one-loop correction [second term in Eq. (39)] as well as the "reducible" corrections [last four terms in Eq. (39)] to the conventional flow equation. In particular, 1PI three-particle vertex corrections are included under the assumption that the auxiliary 1PI three-particle vertex vanishes. In conventional fRG, where it is assumed that both sides of the equation depicted diagrammatically in Fig. 4 do not contribute, three-particle vertex effects are fully neglected, unless they are explicitly accounted for, e.g., by two-loop diagrams [42,43]. Let us note that a similar diagrammatic structure of the flow equations has been determined in a recent two-band fRG approach [44], where a high-energy band was included perturbatively, resulting in an effective one-particle reducible three-particle interaction of the low-energy band. The corresponding contribution to the two-particle vertex flow was subsequently considered explicitly. We emphasize that in the present approach the one-particle "reducible" (in the sense explained above) corrections to the physical self-energy [19] inferred by (17) appear at the two-particle level (as the last term in the flow equation for the vertex in Fig. 3). On the other hand, comparing the auxiliary flow equations to the ones obtained in the recently introduced 1PI approach [27] allows us to attribute the one-particle "irreducible" correction of the two-particle vertex to the the first two terms. Translated to the self-energy, for the Hubbard model with the DMFT as a starting point, these terms produce the analog of the purely nonlocal contribution to the self-energy, which contains the Green's function difference $G - \bar{G}$ in the diagrammatic series. In contrast, the contribution containing "irreducible" diagrams with at least one internal $\bar{G}$ line of the 1PI approach is absent here, since the auxiliary three-particle vertex is neglected. For the half-filled $2d$ Hubbard model with the DMFT as a starting point, this approximation is justified at relatively strong coupling, where the respective contribution was found to be largely compensated by the contribution of the other channels [27,45].

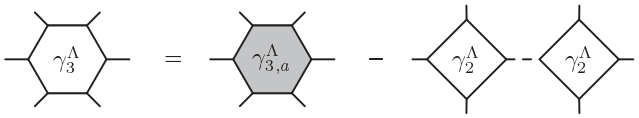

FIG. 4. Relation between the physical and auxiliary scale-dependent three-particle vertex functions.

V. RELATIONS TO OTHER METHODS

The key idea presented in the previous sections is to approach the physical problem of treating strongly interacting fermions in a channel unbiased way in two essential steps: (i) Setting up an expansion around a reference system solution by means of auxiliary fermions, and (ii) solving the auxiliary problem by the fRG. Step (i), first introduced in Ref. [30], is the basis of all the studies performed in the DF formalism [14–22] as well as of the 1PI approach [27] and in the study of impurity systems within superperturbation theory [31]. An fRG flow from an interacting starting point, that is, step (ii), has been recently proposed [7–11].

To be more concrete, in the following, we concentrate on the cases where the DMFT solution is used as a reference system solution, which corresponds to the DF approaches regarding step (i) and which has been also taken as direct input for the DMF^{2}RG flow. This corresponds to taking an action of the form of Eq. (22) as the initial action and constructing the flow

to the final action by interpolating the bare propagator from the AIM one, g_{imp}, to the final (lattice) one, g. Differently from the auxiliary field method proposed here, however, this is done directly in physical space. The important question to be addressed, then, is whether considering the flow in the auxiliary or in the physical space is more convenient. In DMF^{2}RG, one is assuming that the effect of the DMFT three-particle 1PI vertex in correcting the self-energy of the reference system is small compared to the effect of the two-particle one. In the case of conventional fRG this can be justified, at least at weak coupling, by a power counting argument [6] showing that the leading order contribution to the three-particle vertex is one order higher in the interaction compared to the leading one in the two-particle vertex. At intermediate-to-strong coupling, however, this argument does not apply anymore. Hence, in DMF^{2}RG one should rely on the fact that the main contribution of the higher order vertex functions to the truncated fRG flow is already included in the initial condition as sketched in Fig. 1. Obviously, there is no guarantee that the effect of the three-particle 1PI vertex can be neglected in general. The difference with the approach discussed here in terms of the auxiliary fields is the following: In the present approach, the *auxiliary* three-particle vertex is neglected as discussed in Sec. IV (see schematic representation in Fig. 5). At the initial scale this corresponds to neglecting the *connected* reference three-particle vertex [52] instead of the corresponding 1PI one. From the discussion above, it is clear that the crucial question is whether the physical 1PI three-particle vertex or the auxiliary one has a stronger effect on the corresponding flow. This certainly strongly depends on the problem under consideration and requires further focused investigations. Away from weak coupling this question is all but trivial, apart for some special cases, e.g., the Falicov-Kimball model [22]. Hitherto, due to its intrinsic numerical complexity, barely any knowledge about the three-particle quantities is available in the literature [46]. A noticeable exception is the case of the Falicov-Kimball model, where it has been shown [22] that the local auxiliary three-particle vertex $\gamma_{3,a}$ exactly vanishes in the particle-hole symmetric case. Here, in fact, perturbation theory considerations and the application of the Furry theorem [47] would suggest a simultaneous vanishing of the 1PI three-particle vertex for the physical fields. These results, however, cannot be directly extended to the Hubbard model. Therefore one has to critically analyze the results obtained with each approach and for each specific case. In order to compare with DF calculations, one can directly analyze the diagrammatic contributions in auxiliary space where the DF approach [14–22] usually exploits perturbation theory or ladder resummations, as additional approximations. While one cannot expect to capture diverging fluctuations by means of simple perturbation theory, ladder approaches are per definition biased towards a selected channel. On the other hand, by treating the auxiliary problem by means of the fRG one is able to treat competing scattering channels in an unbiased way. In particular, our approach allows for an improved computation of the solution of the auxiliary problem, including, although approximately, the parquet-approximation diagrams. Let us note that, differently from other nonperturbative schemes [24,25,26,29,39], the calculations are based on the 1PI two-particle vertex, and do not require the two-particle irreducible (2PI) vertex at any point of the algorithm. This way one can circumvent the technical problems arising from the recently shown [18,48,49] divergencies of the 2PI vertex at low frequencies, which are not associated with any thermodynamic transition.

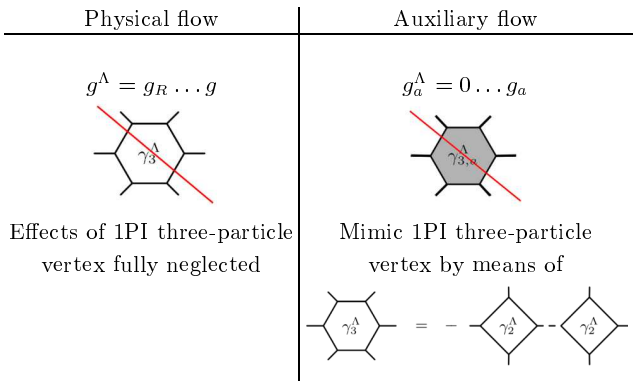

FIG. 5. (Color online) Effects of the truncation in the physical and auxiliary flow.

VI. CONCLUSION

We have demonstrated how the theory of an fRG-based expansion around a SC reference system can be rigorously formulated in the general framework of auxiliary fermionic variables. In particular, we have derived the explicit expressions for the fRG flow equations starting from a generic (exactly solvable) SC reference problem in the auxiliary fermionic fields and the corresponding transformation relations to calculate the physical quantities of the final solution. These derivations allow us to clarify the relation to the fRG flow equations formulated directly for the physical fermionic fields, including the first pioneering ones reported in the recent literature [7,8,10–12]. Furthermore, we could also elucidate the implications of the approximations introduced by truncating the hierarchy of the flow equations in the different schemes; see Fig. 5 for a summary. This represents indeed a pivotal aspect for all strong-coupling fRG algorithms, since the conventional arguments justifying the truncation do not hold any longer beyond the weak-coupling regime. Hence, a precise definition of the diagrammatic content associated with the truncation of a strong-coupling fRG flow is essential for adapting the novel algorithms to the nonperturbative physics of interest. The reported analytic and diagrammatic results, together with the physical insights which can be captured within the different formulations of the fRG with nonperturbative starting points, will provide an important reference for any future method development in this promising direction.

ACKNOWLEDGMENTS

We thank T. Costi, A. Eberlein, K. Held, C. Honerkamp, M. Kinza, V. Meden, W. Metzner, G. Rohringer, and M. Salmhofer for discussions, and S. Sproch for critically reading the manuscript. We acknowledge financial support

from FWF SFB ViCoM F4104, from DFG through ZUK 63, SFB/TRR21, and FOR 723, and from the Dynasty Foundation, Russia.

APPENDIX

1. Notation details

Here we present explicitly Eq. (26) and Eq. (27), shown in compact notation in the main text. The flow equation for the self-energy reads

$$\dot{\Sigma}(\xi_1;\xi_1') = -\frac{1}{\beta}\sum_{\omega_2}\sum_{s_2',s_2} S^{\Lambda}_{s_2';s_2}(\omega_2)\gamma_2^{\Lambda}(\xi_1,\xi_2;\xi_1',\xi_2'). \quad \text{(A1)}$$

We use the convention that for an m-particle quantity the first m arguments refer to the outgoing lines, and the last m to the incoming lines. The loop variables are $\xi_2 = (\omega_2, s_2)$ and $\xi_2'(\omega_2', s_2')$. It is implicitly assumed that the energy is conserved ($\omega_2 = \omega_2'$), while the multi-index s_2 consists of a set of continuous and discrete quantum numbers. Therefore the summations $\sum_{s_2,s_2'}$ have to be understood as integrations or summations, respectively. For example, in the case where only spin and momentum are considered for a translationally invariant system ($\mathbf{k}_2 = \mathbf{k}_2'$), Eq. (A1) reads

$$\dot{\Sigma}(\xi_1;\xi_1') = -\frac{1}{\beta}\sum_{\omega_2}\sum_{\sigma_2,\sigma_2'}\int d\mathbf{k}\; S^{\Lambda}_{\mathbf{k}_2'\sigma_2',\mathbf{k}_2\sigma_2}(\omega_2)\gamma_2^{\Lambda} \times(\omega_1\mathbf{k}_1\sigma_1,\omega_2\mathbf{k}_2\sigma_2;\omega_1'\mathbf{k}_1'\sigma_1',\omega_2'\mathbf{k}_2'\sigma_2'). \quad \text{(A2)}$$

For the 1PI two-particle vertex the flow equation is usually subdivided in three channels (particle-particle, particle-hole direct, and particle-hole crossed) corresponding to the diagrammatic contributions

$$\dot{\gamma}_2^{\Lambda}(\xi_1,\xi_2;\xi_1',\xi_2') = \mathcal{C}_{pp}(\xi_1,\xi_2;\xi_1',\xi_2') + \mathcal{C}_{pp-d}(\xi_1,\xi_2;\xi_1',\xi_2') + \mathcal{C}_{ph-c}(\xi_1,\xi_2;\xi_1',\xi_2'), \quad \text{(A3)}$$

with

$$\mathcal{C}_{pp}(\xi_1,\xi_2;\xi_1',\xi_2') = \frac{1}{\beta}\sum_{\omega_3}\sum_{s_3,s_3',s_4,s_4'}\Big[S^{\Lambda}_{s_3's_3}(\omega_3)G^{\Lambda}_{s_4',s_4}(\omega_1+\omega_2-\omega_3) + G^{\Lambda}_{s_3's_3}(\omega_3)S^{\Lambda}_{s_4',s_4}(\omega_1+\omega_2-\omega_3)\Big] \times\gamma_2^{\Lambda}(\xi_1,\xi_2;\xi_3',\xi_4')\gamma_2^{\Lambda}(\xi_3,\xi_4;\xi_1',\xi_2'), \quad \text{(A4)}$$

$$\mathcal{C}_{ph-d}(\xi_1,\xi_2;\xi_1',\xi_2') = -\frac{1}{\beta}\sum_{\omega_3}\sum_{s_3,s_3',s_4,s_4'}\big[S^{\Lambda}_{s_3's_3}(\omega_3)G^{\Lambda}_{s_4',s_4}(\omega_1-\omega_1'+\omega_3) + G^{\Lambda}_{s_3's_3}(\omega_3)S^{\Lambda}_{s_4',s_4}(\omega_1-\omega_1'+\omega_3)\big] \times\gamma_2^{\Lambda}(\xi_1,\xi_3;\xi_1',\xi_4')\gamma_2^{\Lambda}(\xi_4,\xi_2;\xi_3',\xi_2'), \quad \text{(A5)}$$

$$\mathcal{C}_{ph-c}(\xi_1,\xi_2;\xi_1',\xi_2') = \frac{1}{\beta}\sum_{\omega_3}\sum_{s_3,s_3',s_4,s_4'}\big[S^{\Lambda}_{s_3's_3}(\omega_3)G^{\Lambda}_{s_4',s_4}(\omega_1-\omega_2'+\omega_3) + G^{\Lambda}_{s_3's_3}(\omega_3)S^{\Lambda}_{s_4',s_4}(\omega_1-\omega_2'+\omega_3)\big] \times\gamma_2^{\Lambda}(\xi_1,\xi_3;\xi_2',\xi_4')\gamma_2^{\Lambda}(\xi_2,\xi_4;\xi_1',\xi_3'). \quad \text{(A6)}$$

2. Auxiliary fields

Performing the Hubbard-Stratonovich transformation (4) yields an action

$$\mathcal{S}(\bar{\varphi},\varphi,\bar{\nu},\nu) = \mathcal{S}_R(\bar{\varphi},\varphi) + \mathcal{S}_{\varphi}(\bar{\varphi},\varphi,\bar{\nu},\nu) + (\bar{\nu},n\Delta^{-1}n\nu), \quad \text{(A7)}$$

with $\mathcal{S}_{\varphi}(\bar{\varphi},\varphi,\bar{\nu},\nu) = (\bar{\nu},n\varphi) + (\bar{\varphi},n\nu)$. We determine the interaction $\hat{\mathcal{V}}$ of the auxiliary ν fermions by integrating out the φ fields and obtain

$$\int\mathcal{D}(\bar{\varphi},\varphi)e^{-\mathcal{S}_R(\bar{\varphi},\varphi)-\mathcal{S}_{\varphi}(\bar{\varphi},\varphi,\bar{\nu},\nu)} = Z_R e^{(\bar{\nu},\tilde{Q}\nu)-\hat{\mathcal{V}}(\bar{\nu},\nu)}. \quad \text{(A8)}$$

This relation defines $\hat{\mathcal{V}}$ and $\tilde{Q}$, where $\tilde{Q}$ is to be chosen such that $\hat{\mathcal{V}}$ does not contain any quadratic part in the auxiliary fermions. Note that the left-hand side is closely related to the generating functional of the reference Green's functions,

$$\int\mathcal{D}(\bar{\varphi},\varphi)e^{-\mathcal{S}_R(\bar{\varphi},\varphi)-\mathcal{S}_{\varphi}(\bar{\varphi},\varphi,\bar{\nu},\nu)} = Z_R\;\mathcal{G}^R(\bar{\eta},\eta)|_{\eta=n\nu,\bar{\eta}=n^T\bar{\nu}}. \quad \text{(A9)}$$

Inserting in Eq. (A8) and solving for $\hat{\mathcal{V}}$ we obtain

$$\begin{aligned}\hat{\mathcal{V}}(\bar{\nu},\nu) &= -[\ln\mathcal{G}^R(\bar{\eta},\eta) - (\bar{\eta},n^{-1}\tilde{Q}n^{-1}\eta)]_{\eta=n\nu,\bar{\eta}=n^T\bar{\nu}}\\ &= -[-(\bar{\eta},G_R\eta)+\mathcal{O}(\bar{\eta}^2\eta^2)-(\bar{\eta},n^{-1}\tilde{Q}n^{-1}\eta)]_{\eta=n\nu,\bar{\eta}=n^T\bar{\nu}}.\end{aligned} \quad \text{(A10)}$$

For the quadratic part of $\hat{\mathcal{V}}$ to vanish we have to choose $n^{-1}\tilde{Q}n^{-1} = -G_R$ and hence $\tilde{Q} = -nG_Rn$. Thus

$$\hat{\mathcal{V}}(\bar{\nu},\nu) = -[\ln\mathcal{G}^R(\bar{\eta},\eta) + (\bar{\eta},G_R\eta)]_{\eta=n\nu,\bar{\eta}=n^T\bar{\nu}}, \quad \text{(A11)}$$

in accordance with Eq. (7). This functional generates two-particle and multi-particle connected Green's functions, where n is appended at the outer legs. The free propagation of the auxiliary fields is then described by

$$Q_a = \tilde{Q} - n\Delta^{-1}n = -n[G_R + \Delta^{-1}]n \quad \text{(A12)}$$

as shown in Eq. (6) for $Q_a = g_a^{-1}$.

3. Relation between physical and auxiliary space

We here relate the physical to the auxiliary Green's functions. For this we determine the relation between the generating functional of the physical Green's functions,

$$\mathcal{G}(\bar{\eta},\eta) = \frac{1}{Z\,\det D}\int\mathcal{D}(\bar{\varphi},\varphi)\,\mathcal{D}(\bar{\nu},\nu)\,e^{-\mathcal{S}(\bar{\varphi},\varphi,\bar{\nu},\nu)+(\bar{\eta},\varphi)+(\bar{\varphi},\eta)}, \quad \text{(A13)}$$

and of the auxiliary Green's functions,

$$\mathcal{G}_a(\bar{\eta},\eta) = \frac{1}{Z_aZ_R}\int\mathcal{D}(\bar{\nu},\nu)\,\mathcal{D}(\bar{\varphi},\varphi)\,e^{-\mathcal{S}(\bar{\varphi},\varphi,\bar{\nu},\nu)+(\bar{\eta},\nu)+(\bar{\nu},\eta)}. \quad \text{(A14)}$$

We evaluate

$$\begin{aligned}&-\mathcal{S}(\bar\varphi,\varphi,\bar\nu,\nu)+(\bar\eta,\varphi)+(\bar\varphi,\eta)\\&\quad=-\mathcal{S}_R(\bar\varphi,\varphi)+(\bar\eta+n^T\bar\nu,\varphi)+(\bar\varphi,\eta+n\nu)-(\bar\nu,n\Delta^{-1}n\nu)\end{aligned}\tag{A15}$$

and substitute $n\nu\to n\nu'-\eta$ and $n^T\bar\nu\to n^T\bar\nu'-\bar\eta$

$$\begin{aligned}&-\mathcal{S}_R(\bar\varphi,\varphi)+(\bar\nu',n\varphi)+(\bar\varphi,n\nu')-(\bar\nu',n\Delta^{-1}n\nu')\\&\quad-(\bar\eta,\Delta^{-1}\eta)+(\bar\eta,\Delta^{-1}n\nu')+(\bar\nu',n\Delta^{-1}\eta)\\&\quad=-\mathcal{S}(\bar\varphi,\varphi,\bar\nu',\nu')-(\bar\eta,\Delta^{-1}\eta)+(n^T\Delta^{-T}\bar\eta,\nu')\\&\quad+(\bar\nu',n\Delta^{-1}\eta).\end{aligned}\tag{A16}$$

Thus

$$\mathcal{G}(\bar\eta,\eta)=\mathcal{G}_a(n^T\Delta^{-T}\bar\eta,n\Delta^{-1}\eta)\times e^{-(\bar\eta,\Delta^{-1}\eta)}.\tag{A17}$$

Taking the second derivative with respect to the source fields and setting $\bar\eta=\eta=0$ yields

$$G=\Delta^{-1}+\Delta^{-1}nG_an\Delta^{-1},\tag{A18}$$

or

$$G_a=n^{-1}\Delta G\Delta n^{-1}-n^{-1}\Delta n^{-1}.\tag{A19}$$

This translates into a physical self-energy

$$\Sigma=g^{-1}-[\Delta^{-1}+\Delta^{-1}nG_an\Delta^{-1}]^{-1},\tag{A20}$$

which can be simplified to

$$\Sigma=\Sigma_R+\frac{G_R^{-1}n^{-1}\Sigma_a}{G_Rn+n^{-1}\Sigma_a},\tag{A21}$$

as reported in Eq. (17).

After deriving the relation (A17) between the generating functionals of the physical and auxiliary Green's functions, we can now establish corresponding relations for the effective actions. Taking the logarithm of the above equation yields

$$\mathcal{W}(\bar\eta,\eta)=\mathcal{W}_a(n^T\Delta^{-T}\bar\eta,n\Delta^{-1}\eta)-(\bar\eta,\Delta^{-1}\eta),\tag{A22}$$

from which we get

$$\begin{aligned}&\mathcal{V}(\bar\nu,\nu)\\&=[\mathcal{W}(\bar\eta,\eta)+(\bar\eta,g\eta)]\ {}_{\substack{\eta=g^{-1}\nu\\ \bar\eta=g^{-T}\bar\nu}}\\&=[\mathcal{W}_a(n^T\Delta^{-T}\bar\eta,n\Delta^{-1}\eta)-(\bar\eta,\Delta^{-1}\eta)+(\bar\eta,g\eta)]\ {}_{\substack{\eta=g^{-1}\nu\\ \bar\eta=g^{-T}\bar\nu}}\\&=[\mathcal{W}_a(\bar\eta,\eta)+(\bar\eta,g_a\eta)-(\bar\eta,g_a\eta)]\ {}_{\substack{\eta=n\Delta^{-1}g^{-1}\nu\\ \bar\eta=n^T\Delta^{-T}g^{-T}\bar\nu}}\\&\quad+(\bar\nu,[g^{-1}-g^{-1}\Delta^{-1}g^{-1}]\nu)\\&=[\mathcal{W}_a(\bar\eta,\eta)+(\bar\eta,g_a\eta)]\ {}_{\substack{\eta=g_a^{-1}g_an\Delta^{-1}g^{-1}\nu\\ \bar\eta=g_a^{-T}g_a^Tn^T\Delta^{-T}g^{-T}\bar\nu}}\\&\quad-(n^T\Delta^{-T}g^{-T}\bar\nu,g_an\Delta^{-1}g^{-1}\nu)+(\bar\nu,[g^{-1}-g^{-1}\Delta^{-1}g^{-1}]\nu)\\&=\mathcal{V}_a\left(g_a^Tn^T\Delta^{-T}g^{-T}\bar\nu,g_an\Delta^{-1}g^{-1}\nu\right)\\&\quad-(n^T\Delta^{-T}g^{-T}\bar\nu,g_an\Delta^{-1}g^{-1}\nu)+(\bar\nu,[g^{-1}-g^{-1}\Delta^{-1}g^{-1}]\nu).\end{aligned}\tag{A23}$$

Some algebra yields

$$\begin{aligned}\nu^*&:=g_an\Delta^{-1}g^{-1}\nu=-n^{-1}G_R^{-1}\frac{1}{1-g\Sigma_R}\nu,\\\bar\nu^*&:=g_a^Tn^T\Delta^{-T}g^{-T}\bar\nu=-n^{-T}G_R^{-T}\frac{1}{1-g^T\Sigma_R^T}\bar\nu,\end{aligned}\tag{A24}$$

and finally [19]

$$\mathcal{V}(\bar\nu,\nu)=\mathcal{V}_a(\bar\nu^*,\nu^*)-\left(\bar\nu,\frac{\Sigma_R}{\mathbb{1}-g\Sigma_R}\nu\right).\tag{A25}$$

Aside from the relation of the physical and auxiliary self-energy, a corresponding relation for the respective 1PI two-particle vertices is easily derived by making use of relation (A22). Taking the fourth derivative with respect to the source fields we find

$$G^{(4),c}=G_a^{(4),c}[\Delta^{-1}n,\Delta^{-1}n,n\Delta^{-1},n\Delta^{-1}].\tag{A26}$$

Amputating the full one-particle Green's functions yields

$$\begin{aligned}\gamma_2=\gamma_{2,a}[&G^{-1}\Delta^{-1}nG_a,G^{-1}\Delta^{-1}nG_a,\\&\times G_an\Delta^{-1}G^{-1},G_an\Delta^{-1}G^{-1}],\end{aligned}\tag{A27}$$

which simplifies to

$$\gamma_2=\gamma_{2,a}[\zeta,\zeta,\bar\zeta,\bar\zeta].\tag{A28}$$

4. Connection between fRG and the flow in the auxiliary space

To understand how the flow for the auxiliary fields is related to the conventional fRG flow, we will in the following derive the relations between the flow equations. For this we assume that the scale dependence in Q_a^Λ is governed by a physical cutoff Q^Λ only. The self-energy relation (A21) holds also in the scale-dependent case, and we find

$$\begin{aligned}\dot\Sigma^\Lambda&=G_R^{-1}n^{-1}\dot\Sigma_a^\Lambda\left(G_Rn+n^{-1}\Sigma_a^\Lambda\right)^{-1}\\&\quad-G_R^{-1}n^{-1}\Sigma_a^\Lambda\left(G_Rn+n^{-1}\Sigma_a^\Lambda\right)^{-1}n^{-1}\\&\quad\times\dot\Sigma_a^\Lambda\left(G_Rn+n^{-1}\Sigma_a^\Lambda\right)^{-1}\\&=G_R^{-1}n^{-1}\left[1-\Sigma_a^\Lambda\left(G_Rn+n^{-1}\Sigma_a^\Lambda\right)^{-1}n^{-1}\right]\\&\quad\times\dot\Sigma_a^\Lambda\left(G_Rn+n^{-1}\Sigma_a^\Lambda\right)^{-1}\\&=\left[G_R^{-1}n^{-1}-(\Sigma^\Lambda-\Sigma_R)n^{-1}\right]\dot\Sigma_a^\Lambda\left(G_Rn+n^{-1}\Sigma_a^\Lambda\right)^{-1}\\&=\left[G_R^{-1}n^{-1}-(\Sigma^\Lambda-\Sigma_R)n^{-1}\right]\\&\quad\times\dot\Sigma_a^\Lambda[G_Rn+G_R[(\Sigma^\Lambda-\Sigma_R)^{-1}-G_R]^{-1}G_Rn]^{-1}\\&=(Q_R-\Sigma^\Lambda)n^{-1}\dot\Sigma_a^\Lambda n^{-1}(Q_R-\Sigma^\Lambda)=\zeta^\Lambda\dot\Sigma_a^\Lambda\bar\zeta^\Lambda,\end{aligned}\tag{A29}$$

with

$$\bar G^\Lambda=[Q_R-\Sigma^\Lambda]^{-1},\tag{A30}$$

where we have already included a possible scale dependence in the factors $\zeta^\Lambda=(n\bar G^\Lambda)^{-1}$ and $\bar\zeta^\Lambda=(\bar G^\Lambda n)^{-1}$. It can also be shown easily that

$$\begin{aligned}G_a^\Lambda&=n^{-1}(Q_R-\Sigma^\Lambda)\left(\frac{1}{Q-\Sigma^\Lambda}-\frac{1}{Q_R-\Sigma^\Lambda}\right)\\&\quad\times(Q_R-\Sigma^\Lambda)n^{-1}=\zeta^\Lambda(G^\Lambda-\bar G^\Lambda)\bar\zeta^\Lambda.\end{aligned}\tag{A31}$$

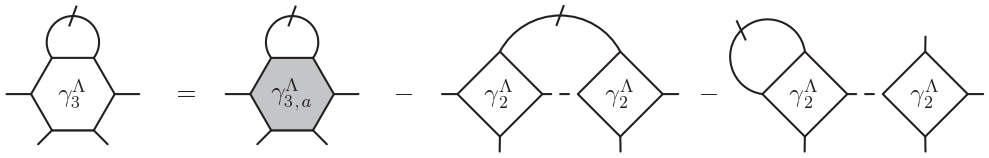

FIG. 6. Diagrammatic structure of Eq. (A39). The factors ζ^Λ appended at each leg of $\gamma_{3,a}^\Lambda$ are implicitly included in the diagram.

Let us now proceed with the single-scale propagator $S_a^\Lambda = \partial_\Lambda G_a^\Lambda|_{\Sigma_a \text{ fixed}}$. Note that keeping the auxiliary self-energy fixed in the derivative is equivalent to keeping the physical self-energy fixed. Therefore by taking the derivative of Eq. (A31) we find

$$S_a^\Lambda = \zeta^\Lambda(\partial_\Lambda G^\Lambda|_{\Sigma^\Lambda \text{ fixed}})\bar{\zeta}^\Lambda = \zeta^\Lambda S^\Lambda \bar{\zeta}^\Lambda, \tag{A32}$$

as $\bar{G}$ and thus ζ^Λ only depend on Λ through the self-energy. Looking at the flow in the physical system we find that any vertex in the diagrams effectively gets $(n\bar{G}^\Lambda)^{-1}$ appended at each connection point and internal propagators are given by $G^\Lambda - \bar{G}^\Lambda$. Let us now consider the fRG truncation at second order, thus including the vertex flow. To achieve this we solve the scale-dependent version of Eq. (A28) for $\gamma_{2,a}^\Lambda$:

$$\gamma_{2,a}^\Lambda = \gamma_2^\Lambda[(\zeta^\Lambda)^{-1},(\zeta^\Lambda)^{-1},(\bar{\zeta}^\Lambda)^{-1},(\bar{\zeta}^\Lambda)^{-1}]. \tag{A33}$$

When constructing the diagrams contributing to the auxiliary flow, the $(\zeta^\Lambda)^{-1}$ factors exactly cancel the outer expressions in G_a^Λ of (A31) and S_a^Λ of (A32) that connect to a vertex. The diagrams for the flow can thus be translated according

$$\gamma_{2,a}^\Lambda \to \gamma_2^\Lambda, \quad S_a^\Lambda \to S^\Lambda, \quad G_a^\Lambda \to G^\Lambda - \bar{G}^\Lambda, \tag{A34}$$

and the orders in $\gamma_{2,a}$ translate to the corresponding orders in γ_2. Let us now come back to the task of deriving a connection between the flow equations in physical and auxiliary space. To this end, we start by looking at the flow equation for the two-particle vertex. Since we also want to understand the effect of the truncation we first consider the exact flow equations (i.e., without truncation) that involve the 1PI three-particle vertex. This reads, respectively for the physical and auxiliary fermions,

$$\dot{\gamma}_2^\Lambda = \gamma_2^\Lambda \circ (S^\Lambda \circ G^\Lambda + G^\Lambda \circ S^\Lambda) \circ \gamma_2^\Lambda + \gamma_3^\Lambda \circ S^\Lambda, \tag{A35}$$

$$\dot{\gamma}_{2,a}^\Lambda = \gamma_{2,a}^\Lambda \circ \left(S_a^\Lambda \circ G_a^\Lambda + G_a^\Lambda \circ S_a^\Lambda\right) \circ \gamma_{2,a}^\Lambda + \gamma_{3,a}^\Lambda \circ S_a^\Lambda. \tag{A36}$$

Differentiating Eq. (A28) with respect to Λ, substituting Eq. (A36), and using Eqs. (A32), (A31), and (A28), we obtain

$$\begin{aligned}
\dot{\gamma}_2^\Lambda = {} & \dot{\gamma}_{2,a}^\Lambda[\zeta^\Lambda,\zeta^\Lambda,\bar{\zeta}^\Lambda,\bar{\zeta}^\Lambda] - \gamma_{2,a}^\Lambda[\dot{\Sigma}^\Lambda n^{-1},\zeta^\Lambda,\bar{\zeta}^\Lambda,\bar{\zeta}^\Lambda] \\
& - \gamma_{2,a}^\Lambda[\zeta^\Lambda,\dot{\Sigma}^\Lambda n^{-1},\bar{\zeta}^\Lambda,\bar{\zeta}^\Lambda] \\
& - \gamma_{2,a}^\Lambda[\zeta^\Lambda,\zeta^\Lambda,n^{-1}\dot{\Sigma}^\Lambda,\bar{\zeta}^\Lambda] - \gamma_{2,a}^\Lambda[\zeta^\Lambda,\zeta^\Lambda,\bar{\zeta}^\Lambda,n^{-1}\dot{\Sigma}^\Lambda] \\
= {} & \gamma_2^\Lambda \circ (S^\Lambda \circ (G^\Lambda - \bar{G}^\Lambda) + (G^\Lambda - \bar{G}^\Lambda) \circ S^\Lambda) \circ \gamma_2^\Lambda \\
& + \gamma_{3,a}^\Lambda[\zeta^\Lambda,\zeta^\Lambda,\zeta^\Lambda,\bar{\zeta}^\Lambda,\bar{\zeta}^\Lambda,\bar{\zeta}^\Lambda] \circ S^\Lambda \\
& - \gamma_2^\Lambda[\dot{\Sigma}^\Lambda \bar{G}^\Lambda,\mathbb{1},\mathbb{1},\mathbb{1}] - \gamma_2^\Lambda[\mathbb{1},\dot{\Sigma}^\Lambda \bar{G}^\Lambda,\mathbb{1},\mathbb{1}] \\
& - \gamma_2^\Lambda[\mathbb{1},\mathbb{1},\bar{G}^\Lambda \dot{\Sigma}^\Lambda,\mathbb{1}] - \gamma_2^\Lambda[\mathbb{1},\mathbb{1},\mathbb{1},\bar{G}^\Lambda \dot{\Sigma}^\Lambda].
\end{aligned} \tag{A37}$$

Neglecting the term proportional to $\gamma_{3,a}^\Lambda$, consistently with a one-loop approximation in auxiliary space, one directly obtains Eq. (39). To understand the connection between the three-particle physical and auxiliary vertexes, instead, let us keep all the terms and compare Eq. (A37) with Eq. (A35). A moment of inspection shows that

$$\begin{aligned}
\gamma_3^\Lambda \circ S^\Lambda = {} & \gamma_{3,a}^\Lambda[\zeta^\Lambda,\zeta^\Lambda,\zeta^\Lambda,\bar{\zeta}^\Lambda,\bar{\zeta}^\Lambda,\bar{\zeta}^\Lambda] \circ S^\Lambda \\
& - \gamma_2^\Lambda \circ (S^\Lambda \circ \bar{G}^\Lambda + \bar{G}^\Lambda \circ S^\Lambda) \circ \gamma_2^\Lambda \\
& - \gamma_2^\Lambda[\dot{\Sigma}^\Lambda \bar{G}^\Lambda,\mathbb{1},\mathbb{1},\mathbb{1}] - \gamma_2^\Lambda[\mathbb{1},\dot{\Sigma}^\Lambda \bar{G}^\Lambda,\mathbb{1},\mathbb{1}] \\
& - \gamma_2^\Lambda[\mathbb{1},\mathbb{1},\bar{G}^\Lambda \dot{\Sigma}^\Lambda,\mathbb{1}] - \gamma_2^\Lambda[\mathbb{1},\mathbb{1},\mathbb{1},\bar{G}^\Lambda \dot{\Sigma}^\Lambda].
\end{aligned} \tag{A38}$$

Using the flow equation for the self-energy in physical space, Eq. (26), and Eq. (A32) yields

$$\begin{aligned}
\gamma_3^\Lambda \circ S^\Lambda = {} & \gamma_{3,a}^\Lambda[\zeta^\Lambda,\zeta^\Lambda,\zeta^\Lambda,\bar{\zeta}^\Lambda,\bar{\zeta}^\Lambda,\bar{\zeta}^\Lambda] \circ S^\Lambda \\
& - \gamma_2^\Lambda \circ (S^\Lambda \circ \bar{G}^\Lambda + \bar{G}^\Lambda \circ S^\Lambda) \circ \gamma_2^\Lambda \\
& - \gamma_2^\Lambda\left[S^\Lambda \circ \gamma_2^\Lambda \circ \bar{G}^\Lambda,\mathbb{1},\mathbb{1},\mathbb{1}\right] \\
& - \gamma_2^\Lambda\left[\mathbb{1},S^\Lambda \circ \gamma_2^\Lambda \circ \bar{G}^\Lambda,\mathbb{1},\mathbb{1}\right] \\
& - \gamma_2^\Lambda\left[\mathbb{1},\mathbb{1},\bar{G}^\Lambda \circ \gamma_2^\Lambda \circ S^\Lambda,\mathbb{1}\right] \\
& - \gamma_2^\Lambda\left[\mathbb{1},\mathbb{1},\mathbb{1},\bar{G}^\Lambda \circ \gamma_2^\Lambda \circ S^\Lambda\right],
\end{aligned} \tag{A39}$$

which can be depicted diagrammatically as shown in Fig. 6. The last six terms on the right-hand side of this equation can be seen diagrammatically as the possible distinct ways of connecting two out of the six external points of the quantity $\gamma_2^\Lambda \circ \bar{G}^\Lambda \circ \gamma_2^\Lambda$, and therefore acquire the same diagrammatic structure of the first two terms. Hence by performing a functional derivative with respect to S^Λ we can finally write a relation between the three-particle vertex:

$$\gamma_3^\Lambda = \gamma_{3,a}^\Lambda[\zeta^\Lambda,\zeta^\Lambda,\zeta^\Lambda,\bar{\zeta}^\Lambda,\bar{\zeta}^\Lambda,\bar{\zeta}^\Lambda] - \gamma_2^\Lambda \circ \bar{G}^\Lambda \circ \gamma_2^\Lambda, \tag{A40}$$

as depicted diagrammatically in Fig. 4. Let us also note explicitly that this equation is consistent with the fact that in the beginning of the flow the auxiliary 1PI three-particle vertex is equal to the amputated connected three-particle Green's function of the reference system.

As for the flow of the self-energy one can see from Eq. (37) that no further diagrams appear by performing the flow in the auxiliary space, i.e., the self-energy flow equation Eq. (26) remains the same, and the only differences arise indirectly due to the change of the vertex during the flow discussed above.

[1] M. Salmhofer, *Renormalization: An Introduction*, Theoretical and Mathematical Physics (Springer, Berlin, Heidelberg, 1999), corrected ed.

[2] J. Berges, N. Tetradis, and C. Wetterich, Phys. Rep. **363**, 223 (2002).

[3] P. Kopietz, L. Bartosch, and F. Schütz, *Introduction to the Functional Renormalization Group*, Lecture Notes in Physics (Springer, Berlin, Heidelberg, 2010), 1st ed.

[4] W. Metzner, M. Salmhofer, C. Honerkamp, V. Meden, and K. Schönhammer, Rev. Mod. Phys. **84**, 299 (2012).

[5] M. Salmhofer, Commun. Math. Phys. **194**, 249 (1998).

[6] M. Salmhofer and C. Honerkamp, Prog. Theor. Phys. **105**, 1 (2001).

[7] C. Taranto, S. Andergassen, J. Bauer, K. Held, A. Katanin, W. Metzner, G. Rohringer, and A. Toschi, Phys. Rev. Lett. **112**, 196402 (2014).

[8] M. Kinza, J. Ortloff, J. Bauer, and C. Honerkamp, Phys. Rev. B **87**, 035111 (2013).

[9] M. Kinza and C. Honerkamp, Phys. Rev. B **88**, 195136 (2013).

[10] A. Rançon, Phys. Rev. B **89**, 214418 (2014).

[11] J. Reuther and R. Thomale, Phys. Rev. B **89**, 024412 (2014).

[12] A. Rançon and N. Dupuis, Phys. Rev. B **83**, 172501 (2011).

[13] A. Rançon and N. Dupuis, Phys. Rev. B **84**, 174513 (2011).

[14] A. N. Rubtsov, M. I. Katsnelson, and A. I. Lichtenstein, Phys. Rev. B **77**, 033101 (2008).

[15] S. Brener, H. Hafermann, A. N. Rubtsov, M. I. Katsnelson, and A. I. Lichtenstein, Phys. Rev. B **77**, 195105 (2008).

[16] H. Hafermann, S. Brener, A. N. Rubtsov, M. I. Katsnelson, and A. I. Lichtenstein, JETP Lett. **86**, 677 (2008).

[17] A. N. Rubtsov, M. I. Katsnelson, A. I. Lichtenstein, and A. Georges, Phys. Rev. B **79**, 045133 (2009).

[18] S.-X. Yang, H. Fotso, H. Hafermann, K.-M. Tam, J. Moreno, T. Pruschke, and M. Jarrell, Phys. Rev. B **84**, 155106 (2011).

[19] A. A. Katanin, J. Phys. A: Math. Gen. **46**, 045002 (2013).

[20] S. Kirchner, F. Zamani, and E. Muñoz, in *New Materials for Thermoelectric Applications: Theory and Experiment*, edited by Z. Veljko and A. Hewson, NATO Science for Peace and Security Series, B, Physics and Biophysics (Springer, Dordrecht, 2013).

[21] E. Muñoz, C. J. Bolech, and S. Kirchner, Phys. Rev. Lett. **110**, 016601 (2013).

[22] A. E. Antipov, E. Gull, and S. Kirchner, Phys. Rev. Lett. **112**, 226401 (2014).

[23] J. P. Hague, M. Jarrell, and T. C. Schulthess, Phys. Rev. B **69**, 165113 (2004).

[24] A. Toschi, A. A. Katanin, and K. Held, Phys. Rev. B **75**, 045118 (2007).

[25] K. Held, A. A. Katanin, and A. Toschi, Prog. Theor. Phys. Suppl. **176**, 117 (2008).

[26] A. Valli, G. Sangiovanni, O. Gunnarsson, A. Toschi, and K. Held, Phys. Rev. Lett. **104**, 246402 (2010).

[27] G. Rohringer, A. Toschi, H. Hafermann, K. Held, V. I. Anisimov, and A. A. Katanin, Phys. Rev. B **88**, 115112 (2013).

[28] G. Li, arXiv:1410.6861.

[29] A. Valli, T. Schäfer, P. Thunström, G. Rohringer, S. Andergassen, G. Sangiovanni, K. Held, and A. Toschi, arXiv:1410.4733 (2014).

[30] S. Pairault, D. Sénéchal, and A.-M. S. Tremblay, Phys. Rev. Lett. **80**, 5389 (1998).

[31] H. Hafermann, C. Jung, S. Brener, M. I. Katsnelson, A. N. Rubtsov, and A. I. Lichtenstein, Europhys. Lett. **85**, 27007 (2009).

[32] A. Georges and G. Kotliar, Phys. Rev. B **45**, 6479 (1992).

[33] A. Georges, G. Kotliar, W. Krauth, and M. J. Rozenberg, Rev. Mod. Phys. **68**, 13 (1996).

[34] W. Metzner and D. Vollhardt, Phys. Rev. Lett. **62**, 324 (1989).

[35] J. Hubbard, Proc. R. Soc. A **276**, 238 (1963).

[36] G. Kotliar, S. Y. Savrasov, G. Pálsson, and G. Biroli, Phys. Rev. Lett. **87**, 186401 (2001).

[37] M. H. Hettler, M. Mukherjee, M. Jarrell, and H. R. Krishnamurthy, Phys. Rev. B **61**, 12739 (2000).

[38] T. Maier, M. Jarrell, T. Pruschke, and M. H. Hettler, Rev. Mod. Phys. **77**, 1027 (2005).

[39] C. Slezak, M. Jarrell, T. Maier, and J. Deisz, J. Phys.: Condens. Matter **21**, 435604 (2009).

[40] G. Rohringer, A. Valli, and A. Toschi, Phys. Rev. B **86**, 125114 (2012).

[41] H. Hafermann, Phys. Rev. B **89**, 235128 (2014).

[42] A. A. Katanin, Phys. Rev. B **70**, 115109 (2004).

[43] A. Eberlein, Phys. Rev. B **90**, 115125 (2014).

[44] S. A. Maier and C. Honerkamp, Phys. Rev. B **85**, 064520 (2012).

[45] A. A. Katanin, Phys. Rev. B **79**, 235119 (2009).

[46] H. Hafermann, *Numerical Approaches to Spatial Correlations in Strongly Interacting Fermion Systems* (Cuvillier, Göttingen, 2010).

[47] F. Mandl and G. Shaw, *Quantum Field Theory* (Wiley, Chichester, 2010), 2nd ed.

[48] T. Schäfer, G. Rohringer, O. Gunnarsson, S. Ciuchi, G. Sangiovanni, and A. Toschi, Phys. Rev. Lett. **110**, 246405 (2013).

[49] V. Janiš and V. Pokorný, Phys. Rev. B **90**, 045143 (2014).

[50] The general expressions containing the freedom n can be found in the Appendix.

[51] Let us note that in principle, one can assume the propagator of any AIM to define the action (22), it does not need to be the self-consistent one of DMFT.

[52] By connected vertex functions we refer to connected Green's functions amputated by the *interacting* one-particle Green's function.

Appendix III

Efficient implementation of the parquet equations: role of the reducible vertex function and its kernel approximation

PHYSICAL REVIEW B **93**, 165103 (2016)

Efficient implementation of the parquet equations: Role of the reducible vertex function and its kernel approximation

Gang Li,[1,*] Nils Wentzell,[1,2] Petra Pudleiner,[1] Patrik Thunström,[1] and Karsten Held[1]
[1]*Institute of Solid State Physics, Vienna University of Technology, A-1040 Vienna, Austria*
[2]*Institut für Theoretische Physik and CQ Center for Collective Quantum Phenomena, Universität Tübingen, Auf der Morgenstelle 14, 72076 Tübingen, Germany*
(Received 18 October 2015; revised manuscript received 11 March 2016; published 4 April 2016)

We present an efficient implementation of the parquet formalism that respects the asymptotic structure of the vertex functions at both single- and two-particle levels in momentum and frequency space. We identify the two-particle reducible vertex as the core function that is essential for the construction of the other vertex functions. This observation stimulates us to consider a two-level parameter reduction for this function to simplify the solution of the parquet equations. The resulting functions, which depend on fewer arguments, are coined "kernel functions." With the use of the kernel functions, the open boundary of various vertex functions in Matsubara-frequency space can be faithfully satisfied. We justify our implementation by accurately reproducing the dynamical mean-field theory results from momentum-independent parquet calculations. The high-frequency asymptotics of the single-particle self-energy and the two-particle vertex are correctly reproduced, which turns out to be essential for the self-consistent determination of the parquet solutions. The current implementation is also feasible for the dynamical vertex approximation.

DOI: 10.1103/PhysRevB.93.165103

I. INTRODUCTION

Strong electronic correlations have led to arguably some of the most fascinating and least understood phenomena in solid-state physics, including the breakdown of Landau's [1,2] Fermi liquid theory and high-temperature superconductivity [3]. However, solving the correlated electron problem poses a great challenge to theoretical physics, since the competition between interaction and kinetic energy prohibits a simple perturbative treatment of such many-body systems. The minimal model covering this competition between localizing and delocalizing electrons is the Hubbard model [4]. Only in the special cases in which one energy scale dominates are weak- [5–10] or strong-coupling [11–13] perturbative treatments actually reliable.

Many of these perturbative approximations are functional-derivable, which is a key criterion that Baym and Kadanoff [14] discovered for a many-body theory to be conservative. They found that for any functional that is derivable with respect to the single-particle propagator, the resulting self-energy function and the Green's function satisfy the continuity equations. The central object in these conservative theories is the single-particle self-energy, which, in the Baym-Kadanoff formalism, can be calculated self-consistently. An alternative to the Baym-Kadanoff formalism, which is self-consistent also at the two-particle level, was developed by Landau, Dominicis, and Martin [15–17], and it is referred to as the parquet formalism. The central object in this theory is the two-particle vertex functions, from which the single-particle self-energy can be self-consistently calculated. The parquet formalism has built-in self-consistency at both the single- and two-particle levels, which by construction can be better than the Baym-Kadanoff theorem in this respect. However, unlike the Baym-Kadanoff theorem, the parquet equations do not explicitly guarantee that the conservation laws, such as the continuity equations, will be satisfied.

The generalization of the self-consistency from the single-particle to the two-particle level is essential to describe the behavior of individual particles and their collective excitations on an equal footing. One example of such complexity is the spin-fluctuation-mediated pairing interaction in the cuprate superconductors [18,19]. To explain how two individual particles form a Cooper pair in the particle-particle channel, one must have knowledge of the spin fluctuations in the particle-hole channel. In this problem, both the single-particle delocalization and the two-particle excitations need to be determined simultaneously, which calls for a theory with self-consistency at both the single- and the two-particle level. However, this is not limited to this particular example. In general, for any collective order that arises from the competition between different fluctuations and low-energy excitations, one needs a theory such as the parquet formalism, which satisfies the self-consistency at both the single- and the two-particle level. However, the application of the parquet equations has been limited thus far to only a few cases [20–28]. The main reason why the parquet equations are not widely applied is their numerical feasibility. The two-particle vertex depends on three independent arguments, each of which consists of both momentum and frequency. Even in the SU(2) symmetric case, solving the four coupled parquet equations for a reasonably large system at low temperature is still numerically very challenging. Here, the difficulty concerns not only the storage of the large two-particle vertices, but also how to actually preserve the asymptotic structure of the single-particle self-energy and the two-particle vertices simultaneously during the calculation. Due to the fact that the parquet self-consistency is performed on both the single- and the two-particle level, the truncation of the two-particle vertex

*Author to whom all correspondence should be addressed: gangli.phy@gmail.com

structures will unavoidably result in a wrong evaluation of the single-particle self-energy, and vice versa. In a consistent solution of the parquet equations, the correct self-energy as well as all vertex functions should be simultaneously obtained at convergence.

In this paper, we present an efficient implementation of the parquet equations that satisfies a number of important conditions. The primary goal of our implementation is to correctly reproduce the asymptotics for the single-particle self-energy and the two-particle vertex functions at each self-consistent step by employing a precise inner and an asymptotic outer frequency window, which ensures that the converged solutions are consistent and asymptotically correct.

The paper is organized as follows: For completeness, we introduce the necessary notations for the single- and two-particle vertex in Appendix. We also briefly derive the corresponding formalism for the parquet equations and the self-energy in this notation. Those readers who are familiar with the parquet formalism and are only interested in its detailed implementation can safely skip this part. In Sec. II, which is the main part of this paper, we present our philosophy for solving the parquet equations. In accordance with previous findings [29], we identify the dominant structures in the two-particle vertex. We reduce their complexity by focusing only on the parts that are reducible in a specific channel, motivating our two-level kernel approximation. In Sec. III, we solve the Anderson impurity model and a 2×2 cluster within the full parquet and the dynamical vertex approximation, respectively. For the former, we have the exact results from the dynamical mean-field theory (DMFT) [30], which in turn justifies our implementation of the parquet equations. An excellent agreement is achieved at both the single- and two-particle levels. A summary and outlook are provided in Sec. IV.

II. SOLUTION OF THE PARQUET EQUATIONS

The parquet equation is a classification of the full vertex F into the (two-particle) fully irreducible contributions Λ and the reducible contributions in the particle-hole (Φ), the transversal particle-hole (followed by symmetry), and the particle-particle channel (Ψ). Employing SU(2) symmetry, one can decouple their spin components into the density (d)/magnetic (m) and singlet (s)/triplet (t) channel, respectively. In these four channels, the parquet equation reads

$$\begin{aligned} F^{k,k'}_{d/m}(q) &= \Lambda^{k,k'}_{d/m}(q) + \Phi^{k,k'}_{d/m}(q) + c_1^{d/m}\Phi_d^{k,k+q}(k'-k) \\ &\quad + c_2^{d/m}\Phi_m^{k,k+q}(k'-k) \\ &\quad + c_3^{d/m}\Psi_s^{k,k'}(k+k'+q) \\ &\quad + c_4^{d/m}\Psi_t^{k,k'}(k+k'+q), \end{aligned} \tag{1a}$$

$$\begin{aligned} F^{k,k'}_{s/t}(q) &= \Lambda^{k,k'}_{s/t}(q) + \Psi^{k,k'}_{s/t}(q) + c_1^{s/t}\Phi_d^{k,q-k'}(k'-k) \\ &\quad + c_2^{s/t}\Phi_m^{k,q-k'}(k'-k) + c_3^{s/t}\Phi_d^{k,k'}(q-k-k') \\ &\quad + c_4^{s/t}\Phi_m^{k,k'}(q-k-k'). \end{aligned} \tag{1b}$$

$k = (\mathbf{k}, i\nu)$ is a compound index consisting of wave vector $\mathbf{k}$ and Matsubara frequency $i\nu$. The coefficients $c_{1\cdots4}^{d/m/s/t}$ take different values in the four different channels. We only briefly list here the necessary equations for the convenience of the discussions in the main part of the paper; more detailed notations and derivations can be found in Appendix. In Eq. (1), the reducible contributions are given by the Bethe-Salpeter equation (BSE) in the four channels formally as $\Phi/\Psi = \Gamma GGF$ [Eq. (A6)]. Here, Γ is the irreducible vertex in the given channel, which contains the reducible contributions from the other channels and the fully irreducible Λ; see Eqs. (A10) and (A13). The self-consistency at the single- and two-particle level are synchronized by means of the self-energy, which depends on the resulting two-particle vertex as shown in the Schwinger-Dyson equation of motion (A15).

Given the fully irreducible vertex Λ, the parquet formalism provides a set of five exact equations [(1), (A6), (A10)/(A13), (A15), (A16)] which can be solved for the five unknowns $(F, \Phi/\Psi, \Gamma, G, \Sigma)$ (where the former three equations and vertices consist of four channels each). Hence, if we know the exact Λ, we can calculate all physical, one- and two-particle, quantities exactly. However, since the exact Λ of the Hubbard model is not known, we need to make approximations. In the parquet approximation (PA) [6,31], $\Lambda \sim U$ is taken; a more sophisticated approximation that takes into account all local fully irreducible diagrams is referred to as the dynamical vertex approximation [32,33].

In this paper, we mainly discuss two problems that are practically unavoidable in solving the parquet equations, which are of critical importance for keeping the self-consistency in the single- and two-particle levels simultaneously.

The first problem arises due to the finite numbers of Matsubara frequencies that are available in the calculations. Each vertex in the parquet equation depends on three independent arguments k, k', and q, which take arbitrary values in $(-\infty, \infty)$. In practice, a finite cutoff a has to be introduced. A consequence of this cutoff is that after each self-consistency step, the interval on which the vertex is known shrinks. This can be seen as follows: take Eq. (1a) as an example and suppose k, k', and q take values in $[-a, a]$. For calculating the the right-hand side of (1a), we would need the solutions of $\Phi^{k,k+q}_{d/m}(k'-k)$ in $[-2a, 2a]$, and $\Psi^{k,k'}_{s/t}(k+k'-q)$ in $[-3a, 3a]$. Assuming that $\Phi^{k,k'}_{d/m}(q)$ and $\Psi^{k,k'}_{s/t}(q)$ are only available in $[-a, a]$, $F^{k,k'}_{d/m}(q)$ can then be calculated only in the smaller interval $[-a/3, a/3]$. Such a boundary issue only exists in the Matsubara frequency space. In momentum space, the periodic boundary condition can be applied whenever $\mathbf{k}' - \mathbf{k}$ or $\mathbf{k} + \mathbf{k}' + \mathbf{q}$ exceed the finite parameter range. However, none of the vertex functions is periodically dependent on the Matsubara frequencies $i\nu$, $i\nu'$, and $i\omega$ [27]. As a result, there exist two different parameter spaces for the vertex functions, i.e., in the bigger space ($[-a, a]$), $\Phi^{k,k'}_{d/m}(q)$ and $\Psi^{k,k'}_{s/t}(q)$ are known, while through the parquet equations $F^{k,k'}_{d/m/s/t}(q)$ can be determined only in a smaller parameter space ($[-a/3, a/3]$).

The second problem is related to the finite frequency parameter range as well. To evaluate the self-energy function in Eq. (A15), a sum over the two internal arguments k' and q has to be carried out. An example of the vertex functions

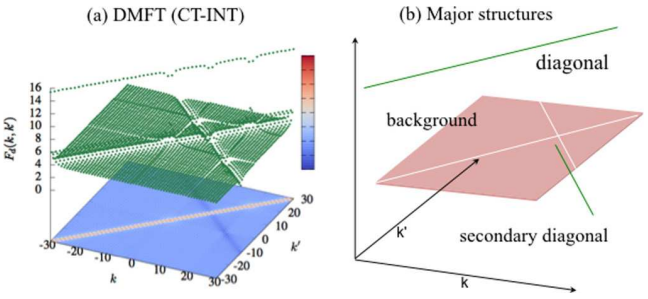

FIG. 1. (a) The green dots are the full vertex $F_d^{k,k'}(q)$ for a fixed value of q calculated from the DMFT (CT-INT) at $\beta t = 2$ and $U/t = 4$ on a square lattice. The bottom shows the intensity of $F_d^{k,k'}(q)$, which illustrates three major structures of the vertex functions. These structures are the background, diagonal, and secondary diagonal components, as illustrated in (b).

$F_d^{\nu,\nu'}(\omega)$ is shown in Fig. 1. As was already observed in Ref. [29,34], $F_d^{\nu,\nu'}(\omega)$ has structures that span the whole Matsubara frequency space. In particular, they do not decay at the boundary of any given parameter box. Thus, a sum over a finite parameter range corresponds to a truncation of these vertex functions at the boundary, which can lead to a wrong evaluation of the self-energy function.

In this paper, we propose a feasible scheme to solve these two problems, improving upon the Matsubara-frequency periodization employed hitherto [27]. Our idea is based on the observation of the central role that the reducible vertex functions play in the parquet equations, which will be explained in the following.

A. Two-level kernel approximations

To satisfy the crossing symmetry explicitly in every self-consistency step, we evaluate the full vertex $F_{d/m/s/t}$ directly from the parquet equations [27]. Figure 1 displays $F_d^{k,k'}(q)$ as a function of k and k' for a fixed q. The left plot is obtained from a DMFT calculation with the interaction-expansion continuous-time quantum Monte Carlo (CT-INT) [35,36] as an impurity solver, thus it represents a numerically exact (up to the statistical errors of the CT-INT) evaluation of the full two-particle vertex for the DMFT impurity. We will calculate this vertex in the parquet theory as well; see Sec. III. A detailed analysis of the two-particle vertex function can be found in Refs. [29,34]. In the following, we will use the exact results from DMFT as a reference to further show that, among the various two-particle vertex functions, the reducible vertex, which plays the central role in our implementation of the parquet equations, is the most important.

The right plot shows a schematic representation of the major structures of the left one. The full vertex $F_{d/m/s/t}$ can be decomposed into three main parts, i.e., the background, the diagonal, and the secondary diagonal component. Figure 1 clearly shows that the boundary of the vertex function is not periodic in frequency space, instead all three components extend to infinite values of k and k'. Due to the restricted parameter space available in practical calculations, one has to be careful with the boundary effect on these vertex functions.

The background is contributed by $\Lambda_{d/m/s/t}^{k,k'}(q)$, which is the input for the parquet equation, and it is further supplemented by the reducible vertex functions $\Phi_{d/m}^{k,k'}(q), \Psi_{s/t}^{k,k'}(q)$. The diagonal and the secondary diagonal components are predominant for $F_{d/m/s/t}^{k,k'}(q)$ with $k = k'$ and $k = -k' - q$ in the d/m channel, and for $k = k' - q$ in the s/t channel, respectively. The diagonal and secondary diagonal components are generated, in the parquet equations, by the reducible vertex $\Phi_{d/m}^{k,k+q}(k' - k), \Psi_{s/t}^{k,k'}(k + k' + q)$ in the d/m channel and $\Phi_{d/m}^{k,q-k'}(k' - k), \Phi_{d/m}^{k,k'}(q - k - k')$ in the s/t channel; see Eq. (1). We note that the above analysis on the complete vertex $F_{d/m/s/t}^{k,k'}(q)$ is not specific to the Hubbard model. In principle, it is general to any single-band model for fermions that preserves SU(2) symmetry. Among the various terms in the parquet equations, the background given by $\Lambda_{d/m/s/t}^{k,k'}(q)$ is model-dependent, i.e., its asymptotic can be different for different models, while the main and secondary diagonal structures are fully determined by the parquet equations, which are general. As a result, our approximation to the reducible vertex function, which will be discussed in the rest of this work, can in principle be applied to other models as well.

Furthermore, we also notice that these two components only depend significantly on the center-of-mass momentum and frequency (which is the momentum/frequency in the brackets); the dependence on the other two arguments (the superscript momentum/frequency) is much weaker, as will be shown in the following. Hence, the reducible vertex can be effectively approximated by single-argument-dependent functions $\tilde{\Phi}_{d/m}(q)$ and $\tilde{\Psi}_{s/t}(q)$, which we call kernel functions. The approximation of replacing the three-argument-dependent reducible vertex with a single-q-dependent kernel function, i.e., $\Phi_{d/m}^{k,k+q}(k' - k) \approx \tilde{\Phi}_{d/m}(\tilde{q} = k' - k)$, etc., is called the first-level kernel approximation. We name it the "kernel approximation" because, on the one hand, $\tilde{\Phi}(q)$ contains the most essential, i.e., core or "kernel," information of $\Phi^{k,k'}(q)$. On the other hand, we use this term because, mathematically, the kernel of our mapping $\mathcal{F} : q,k,k' \to q$ defines classes of equivalent frequency triples, whose reducible vertex $\Phi^{k,k'}(q)$ is (approximatively) the same, i.e., $\tilde{\Phi}(q)$. The parameter-reduction of the reducible vertex functions, i.e., the kernel approximation, will greatly simplify our implementation of the parquet equations. Let us emphasize that we only employ the kernel approximation when the Matsubara frequency is outside the interval $[-a,a]$ in which the vertex is known explicitly. We also note that a parametrization related to the first-level kernel approximation is used in a different context: Karrasch *et al.* use a sum of single-frequency full vertex functions for the functional renormalization-group calculations [37], where, however, this parametrization is employed for all frequencies.

We verify the simple structure of the reducible vertex functions from a DMFT calculation in Fig. 2(a), where $\Phi_d^{k,k'}(q)$ is displayed as a function of k and k' for a fixed transfer frequency $q = i\omega = -i40\pi/\beta$. First of all, we notice that the overall amplitude of the reducible vertex function for the given parameters is much smaller than that of the full vertex shown in Fig. 1 for the same parameters. Compared to Fig. 1, the reducible vertex can rather be viewed as a flat plane. Secondly, the detailed structure of the reducible vertex

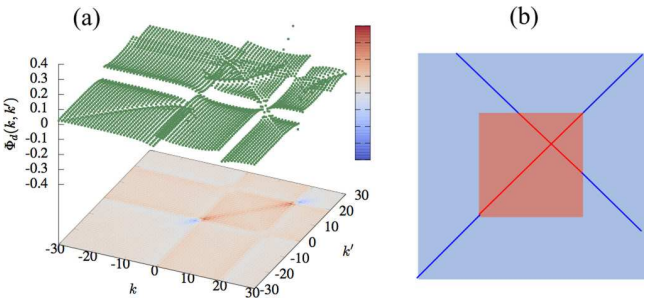

FIG. 2. (a) Reducible vertex in the density channel calculated from the DMFT (CT-INT) for the same parameter as in Fig. 1. (b) Schematic illustration of our philosophy of the kernel-approximation(s) for solving the open boundary issue in the parquet equations; see the main text for more details.

is found to consist of only two main parts, i.e., a constant background and two crossing stripes. The first-level kernel approximation discussed above corresponds to considering only the constant background. In practice, as the first-level kernel function $\tilde{\Phi}_{d/m}(q)$ [$\tilde{\Psi}_{s/t}(q)$], we take for every q the value of $\Phi^{k,k'}_{d/m}(q)$ [$\Psi^{k,k'}_{s/t}(q)$] at this q and a k,k' that is far away from the diagonal components and the stripes in Fig. 2(b). There is a certain freedom in this choice that has yet to be investigated.

For an intuitive understanding of this approximation, let us examine the first iteration of the PA. Here, $\Lambda^{k,k'}_{d/m/s/t}(q)$, $F^{k,k'}_{d/m/s/t}(q)$, and $\Gamma^{k,k'}_{d/m/s/t}(q)$ are simply taken as $(U,-U,2U,0)$. From Eq. (A6), we learn

$$\begin{aligned}\Phi^{k,k'}_{d/m}(q) &= \frac{U^2}{\beta N}\sum_{k''} G(k'')G(k''+q),\\ \Phi^{k,k'}_{s}(q) &= -\frac{2U^2}{\beta N}\sum_{k''} G(k'')G(q-k''),\\ \Phi^{k,k'}_{t}(q) &= 0,\end{aligned} \tag{2}$$

which depend on q only. For any given q, $\Phi^{k,k'}_{d/m}(q)$ and $\Psi^{k,k'}_{s/t}(q)$ are constant for all k and k'. Since in the second iteration $F^{k,k'}_{d/m/s/t}(q)$ and $\Gamma^{k,k'}_{d/m/s/t}(q)$ are no longer taking the simple values $(U,-U,2U,0)$, the stripes appear in the reducible vertex. Although $F^{k,k'}_{d/m/s/t}(q)$ and $\Gamma^{k,k'}_{d/m/s/t}(q)$ contain structures that strongly deviate from the constant background, the only structure of the reducible vertex $\Phi^{k,k'}_{d/m}(q)$ and $\Psi^{k,k'}_{s/t}(q)$ extending in Matsubara frequency space is the stripes. Other local structures inside the smaller parameter range (the light-red region), which can be pronounced in some cases, will be treated without the kernel approximation. Thus, as the first-level approximation, the choice of single-q-dependent kernel functions $\tilde{\Phi}_{d/m}(q)$ and $\tilde{\Psi}_{s/t}(q)$ is justified as an approximation for large Matsubara frequencies.

Further improvement of this kernel approximation is possible. For the second-level kernel approximation, we consider kernel functions $\tilde{\Phi}^{k}_{d/m}(q)$ and $\tilde{\Psi}^{k}_{s/t}(q)$ depending on two arguments, which is in line with the analysis of Ref. [29]. The additional dependence on k in the second-level kernel approximation allows us also to incorporate the crossing stripes of the reducible vertex functions; see Fig. 2(a). In practice, we take $\Phi^{k,k'}_{d/m}(q)$ and $\Psi^{k,k'}_{s/t}(q)$ at one of the edges of the given parameter range, for instance at $k'=-30$ in Fig. 2(a), to be the new kernel $\tilde{\Phi}^{k}_{d/m}(q)\approx\Phi^{k,-30}_{d/m}(q)$ and $\tilde{\Psi}^{k}_{s/t}(q)\approx\Psi^{k,-30}_{s/t}(q)$. The kernel function, in the second-level approximation, is then given as $\tilde{\Phi}^{k}_{d/m}(q)+\tilde{\Phi}^{k'}_{d/m}(q)-\tilde{\Phi}_{d/m}(q)$, where $\tilde{\Phi}_{d/m}(q)$ is the first-level kernel function representing the background of the reducible vertex. A similar expression can be formulated for the particle-particle channel.

The kernel approximations have strong implications for the two problems we discussed before. As our numerical study below shows, the open boundary problem of the vertex functions can be efficiently solved by supplementing the reducible vertex functions with the corresponding kernel functions whenever their arguments exceed the parameter space available in the calculations. Toward that end, we illustrate our philosophy of the kernel approximation in Fig. 2(b), where we show the two different parameter spaces discussed in the beginning of this section as light-blue and light-red squares. Only inside the smaller parameter space (light-red square) can the full vertex $F^{k,k'}_{d/m/s/t}(q)$ be calculated from the reducible vertex functions $\Phi^{k,k'}_{d/m}(q)$ and $\Psi^{k,k'}_{s/t}(q)$. Outside of the light-red region, in the first-level kernel approximation, the full vertex functions are calculated from $\tilde{\Phi}_{d/m}(q)$ and $\tilde{\Psi}_{s/t}(q)$, or in the second-level kernel approximation from $\tilde{\Phi}^{k}_{d/m}(q)+\tilde{\Phi}^{k'}_{d/m}(q)-\tilde{\Phi}_{d/m}(q)$ and $\tilde{\Psi}^{k}_{s/t}(q)+\tilde{\Psi}^{k'}_{s/t}(q)-\tilde{\Psi}_{s/t}(q)$. In this way, $F^{k,k'}_{d/m/s/t}(q)$ and $\Gamma^{k,k'}_{d/m/s/t}(q)$ can be calculated in the full parameter space defined in the calculations.

B. High-frequency regulation

To close the self-consistent loop for the parquet equations, the self-energy also needs to be updated. As explained before, the sum in Eq. (A15) is performed in a finite interval, which corresponds to a truncation of the vertex functions at the boundary. Generally, for a sum in a finite interval $(-a,a)$, the truncation effect can only be eliminated when a is large enough so that the quantity to be summed becomes negligibly small at the boundary. However, this is not the case for the vertex functions, which extend to infinite values of k and k'. In this section, we show that, based on the two-level kernel approximation introduced above, we can write down auxiliary vertex functions that match the exact complete vertex $F^{k,k'}_{d/m/s/t}(q)$ at and beyond the interval boundary. Thus their difference becomes zero at the boundary, and they can be safely summed over in the finite interval. As a principle, such an auxiliary function has to be free of the boundary issue, as it is supposed to account for the asymptotics that is not available in the finite parameter space.

We propose the following auxiliary function for the full vertex in the density channel (very similar asymptotic functions can be readily formulated for other channels):

$$\begin{aligned}\tilde{F}^{k,k'}_{d}(q) = U &+ \tilde{\Phi}_d(q) - \tfrac{1}{2}\tilde{\Phi}_d(k'-k) - \tfrac{3}{2}\tilde{\Phi}_m(k'-k)\\ &+ \tfrac{1}{2}\tilde{\Psi}_s(k+k'+q) + \tfrac{3}{2}\tilde{\Psi}_t(k+k'+q).\end{aligned} \tag{3}$$

In terms of Fig. 2(b), this is equivalent to calculating $F^{k,k'}_{d}(q)$ from the (approximate) kernel functions in both the smaller and larger intervals. Here, for a simple demonstration, Eq. (3)

is constructed from the first-level kernel functions. Similarly, one can also construct this function by using the second-level kernel functions. The resulting auxiliary functions $\tilde{F}_d^{k,k'}(q)$ will then become a better approximation to the exact complete vertex $F_d^{k,k'}(q)$.

Instead of using Eq. (A15), with the help of this auxiliary vertex function we now calculate the self-energy as

$$\begin{aligned}\Sigma(k) = \tilde{\Sigma}(k) &- \frac{UT^2}{4N}\sum_{k',q} G(k+q)G(k'+q)G(k') \\ &\times\left[\Delta F_d^{k,k'}(q) - \Delta F_m^{k,k'}(q)\right] \\ &- \frac{UT^2}{4N}\sum_{k',q} G(q-k')G(q-k)G(k') \\ &\times\left[\Delta F_s^{k,k'}(q) + \Delta F_t^{k,k'}(q)\right]. \end{aligned} \tag{4}$$

Here, $\Delta F_{d/m/s/t}^{k,k'}(q) = F_{d/m/s/t}^{k,k'}(q) - \tilde{F}_{d/m/s/t}^{k,k'}(q)$, and $\tilde{\Sigma}(k)$ is the self-energy calculated from the kernel functions in all channels.

To faithfully account for full vertex functions at arbitrary k, k', and q in $(-\infty,\infty)$, we further split $\tilde{\Sigma}(k)$ into $\tilde{\Sigma}_1(k)$ and $\tilde{\Sigma}_2(k)$, where $\tilde{\Sigma}_1(k)$ contains only the contribution from the $(U, -U, 2U, 0)$ components, while $\tilde{\Sigma}_2(k)$ contains the rest of the auxiliary functions [see Eq. (3)]. $\tilde{\Sigma}_1(k)$ can then be efficiently calculated as follows:

$$\begin{aligned}\tilde{\Sigma}_1(k) &= -\frac{U^2T^2}{2N}\sum_{k',q}[G(k+q)G(k'+q)G(k') \\ &\quad + G(q-k')G(q-k)G(k')] \\ &= -U^2\mathcal{F}FT^{-1}[G^2(r)G(-r)]. \end{aligned} \tag{5}$$

Here, $G(r)$ is the Fourier component of $G(k)$, and $\mathcal{F}FT^{-1}$ is the (fast) Fourier transformation between these (in this transformation, the antiperiodic boundary condition in the imaginary-time space has been taken into account). Thus, $\tilde{\Sigma}_1(k)$ incorporates the contribution from the lowest-order complete vertex function, i.e., the bare Coulomb interaction, for all frequencies and momentum variables. $\tilde{\Sigma}_1(k)$ is merely the self-energy from the second-order Feynman diagram. As for $\tilde{\Sigma}_2(k)$, we perform the direct sum over k' and q in a much larger parameter space, which is possible thanks to the kernel approximation. In practice, we usually take this space two or three times larger than the bigger parameter space used for calculating the various vertex functions [the light-blue region in Fig. 2(b)].

The full vertex does not decay asymptotically but extends with finite values to the largest k, k', and q. However, due to the three single-particle propagators G in Eq. (A15), the product $GGGF$ still goes to zero asymptotically for large k, k', and q. While it is usually difficult for the full vertex functions to work in a large parameter space in practice, this is not a problem for the kernel functions, which depend only on one or two arguments. Thus, the evaluation of $\tilde{\Sigma}_2(k)$ can be carried out in a much larger parameter space. We note that the high-frequency regulation explained above is very important for $\tilde{\Sigma}(k)$ to reproduce the asymptotic tail of the self-energy function in frequency space correctly, which is crucial for maintaining the correct high-frequency behavior of the two-particle vertex functions, and vice versa.

III. RESULTS

A. Validation against DMFT at half-filling

In this section, we present numerical results to justify our implementation of the parquet equations and to validate the accuracy of the kernel approximation. Toward that end, we consider the Hubbard model on a 2D square lattice with nearest-neighbor hopping t and interaction U at inverse temperature β. We solve this model using both the DMFT methodology and the parquet equations at a single-momentum point. Unless mentioned otherwise, the results presented in this section represent the solutions with the second-level kernel function and the high-frequency regulation for the self-energy asymptotics introduced in the previous section.

More specifically, we use CT-INT as an impurity solver for the DMFT equations, yielding both the single-particle self-energy and the two-particle vertex function, in a numerically precise way. The DMFT solution provides an unbiased reference for benchmarking our implementation of the parquet equations. For a fair comparison, we take the converged DMFT Weiss function $\mathcal{G}(i\nu_n)$ as input for the parquet equations. For the other input, i.e., the fully irreducible vertex function $\Lambda_{d/m/s/t}^{k,k'}(q)$, we take two different values: In one calculation, we take the lowest-order approximation $\Lambda_{d/m/s/t}^{k,k'}(q) \approx (U, -U, 2U, 0)$, which corresponds to the PA for the DMFT impurity model. In the other (full parquet) calculation, we take the CT-INT calculated $\Lambda_{d/m/s/t}^{k,k'}(q)$ as input. Since (in contrast to DΓA) we do not include a k dependence here, this calculation exactly reproduces the DMFT results for F and Σ if the parquet equations are solved on an infinite frequency interval and if statistical errors in CT-INT are negligible. For the given finite frequency interval, this is hence a test for the accuracy of the proposed kernel approximation.

We show the corresponding full parquet self-energy in Fig. 3 as empty circles. It nicely reproduces the DMFT solution (empty squares), validating the accuracy of the kernel approximation. Also, the PA solution (open triangles) agrees well with the DMFT, except for a small deviation at the first two Matsubara frequencies. In particular, the high-frequency tail of the self-energy is nicely reproduced by both parquet solutions. This is an essential check for the algorithm. As explained before, a direct truncation of the vertex at the boundary of the available parameter space will lead to the wrong solution of the self-energy, which is mainly reflected in the violation of the high-frequency behavior.

Such a violation is a rather common issue appearing in most of the diagrammatic approaches when evaluating the self-energy with only a finite numbers of Matsubara frequency. To achieve a correct high-frequency tail in the self-energy, a few hundred or even more Matsubara frequencies usually have to be adopted in these approaches [10,18], which is significantly larger than the number taken in our parquet calculations for similar parameters. That is, in all calculations presented in this paper, no more than 60 Matsubara frequencies in each argument are taken, which significantly reduces the

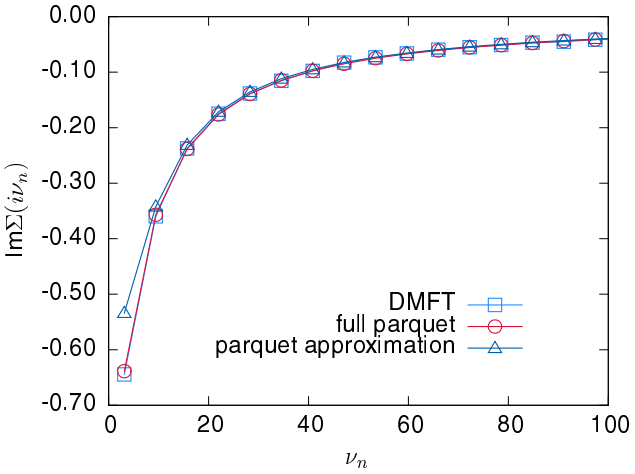

FIG. 3. Single-particle self-energy obtained from the parquet equations in the PA and the (local) full parquet calculation employing the kernel approximation. The latter reproduces the DMFT solution with high precision, but the PA also shows quite good agreement, except for the lowest two Matsubara frequencies. The parameters for the 2D Hubbard model in DMFT are $\beta = 1, U = 4$ (here and in the following, $t \equiv 1$). In the parquet equation, 60 Matsubara frequencies have been taken into account in the inner interval of Fig. 2(b), with the kernel approximation being employed in the outer interval.

demand on the memory for storing all vertex functions. Correctly reproducing the high-frequency tail with significantly fewer Matsubara frequencies is one of the highlights of our algorithm.

At a lower temperature $\beta = 2$, the full parquet calculation still yields results that agree very well with the DMFT solution, as shown in Fig. 4. The PA results, on the other hand, deviate more strongly from the DMFT at low frequencies. This is expected since approximating the fully irreducible vertex by the bare Coulomb interaction is correct only asymptotically for small U. As discussed before, the difference between the PA and the full parquet solutions results from the different

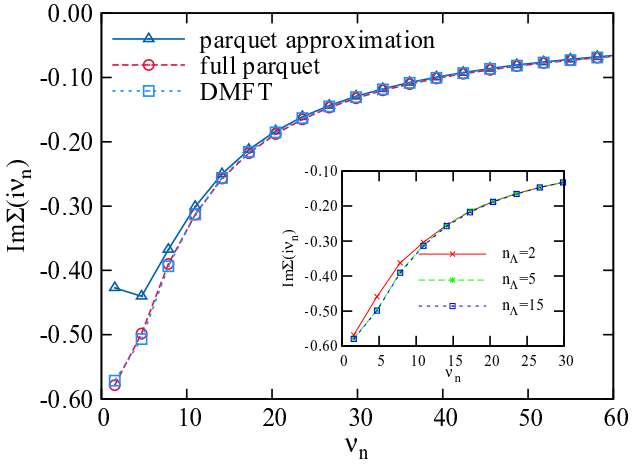

FIG. 4. Same as Fig. 3 but for $U = 4$ and $\beta = 2$. The inset shows the convergence of $\mathrm{Im}\Sigma(i\nu_n)$ with the increase of the frequency cutoff in $\Lambda_{d/m/s/t}$; see the main text for more details.

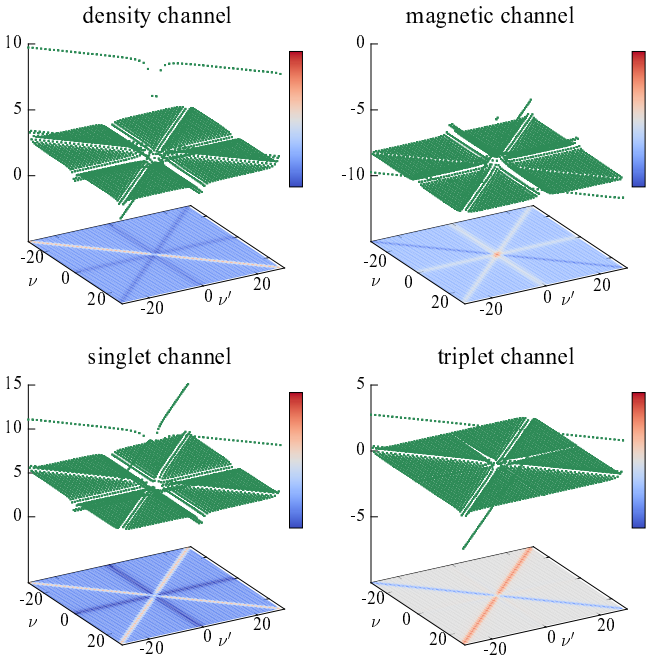

FIG. 5. Two-particle full vertex functions in the four channels as calculated from the parquet equations taking the fully local irreducible vertex from DMFT as an input. The parameters are the same as in Fig. 3.

values for the fully irreducible vertex function $\Lambda^{k,k'}_{d/m/s/t}(q)$ used in the calculations. More specifically, in the full parquet calculation, we take $\Lambda^{k,k'}_{d/m/s/t}(q)$ obtained from the DMFT (CT-INT) with 30 Matsubara frequencies for each argument, i.e., k, k', and q are in $[-n_\Lambda, n_\Lambda] = [-14, 15]$, and then we extend $\Lambda^{k,k'}_{d/m/s/t}(q)$ to $[-30, 30]$ by supplementing it with the lowest-order values of these vertices, i.e., $(U, -U, 2U, 0)$. In the PA calculations, we take $\Lambda^{k,k'}_{d/m/s/t}(q)$ as $(U, -U, 2U, 0)$ everywhere in $[-30, 30]$. To see the convergence of the full parquet calculation with respect to n_Λ, the inset of Fig. 4 shows solutions of the full parquet calculation for three different cutoffs n_Λ. We find a converged solution for $n_\Lambda \geqslant 5$. As is known, to obtain the fully irreducible vertex $\Lambda^{k,k'}(q)$ with large frequency cutoff is numerically very challenging. The inset of Fig. 4 shows that a relatively small value of cutoff n_Λ is sufficient to converge the solution (if there exists a convergence) to the correct values.

Such excellent agreement is not only achieved for the self-energy. We also find that the full parquet equations give almost identical two-particle vertex functions in all channels (Fig. 5) when compared to the DMFT. In Fig. 6, we calculate their relative difference $\sum_{\nu,\nu'} |\Delta F^{\nu,\nu'}_{d/m/s/t}(\omega)| / |\sum_{\nu,\nu'} |F^{\mathrm{DMFT},\nu,\nu'}_{d/m/s/t}(\omega)|$ by summing up the two fermionic frequencies ν, ν', and we show it as a function of the transfer frequency ω_n. Here, $\Delta F^{\nu,\nu'}_{d/m/s/t}(\omega) = F^{\mathrm{PARQUET},\nu,\nu'}_{d/m/s/t}(\omega) - F^{\mathrm{DMFT},\nu,\nu'}_{d/m/s/t}(\omega)$. The overall amplitude of their differences is small, and the biggest deviation appears at $\omega_n = 0$. This is expected as, in the reducible vertex, for any ν and ν' the largest absolute value is at $\omega_n = 0$. It is then easier for an error of the reducible vertex at $\omega_n = 0$ to propagate to the complete vertex $F^{\nu,\nu'}_{d/m/s/t}(\omega_n)$. In the

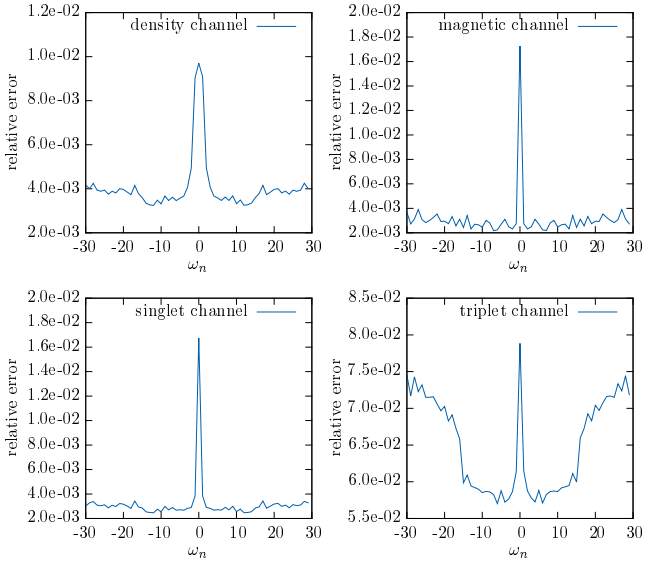

FIG. 6. The relative error of the complete vertices in Fig. 5 with respect to those calculated in DMFT using CT-INT. The relative error is summed up for the two fermionic frequencies and is shown as a function of the transfer frequency ω_n; see the text for more details. Note that this relative error is also subject to the propagation of the statistical error of CT-INT.

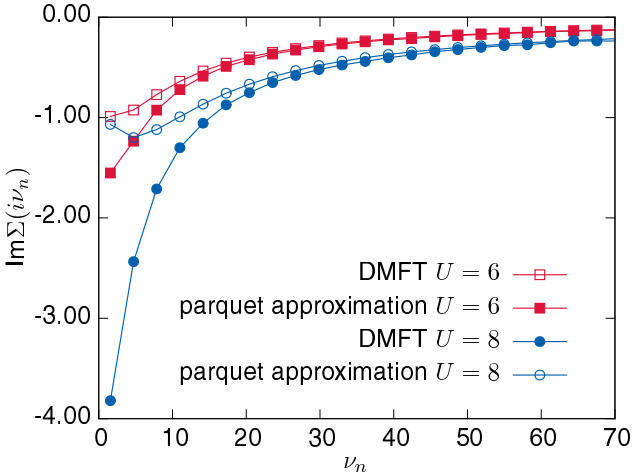

FIG. 7. With the kernel approximation and high-frequency regulation, the convergence at $U = 6$ and 8 can also be achieved in the PA. Here the inverse temperature is the same as in Fig. 4.

triplet channel, we also notice that the relative error is large at larger frequencies, too. This is due to the statistical error of the CT-INT and the extrapolation error in the fully localized vertex function $\Lambda_t^{\nu,\nu'}(\omega)$, which was only calculated up to $|\omega_n| = 15$ in the CT-INT. Let us emphasize that the two-particle vertex $F_{d/m/s/t}^{k,k'}(q)$ at larger frequencies is calculated from the kernel approximation. The small error in this regime, especially in the density, magnetic, and singlet channels, shows that the kernel approximation correctly reproduces the asymptotics of the two-particle vertex functions.

The agreement in both the single- and two-particle quantities clearly demonstrates that our implementation of the parquet equations fully respects the self-consistency at both the singe- and two-particle levels. It should be noted that the availability of the two-particle vertex function as output is one of the striking features of the parquet theory. The two-particle vertex functions play a crucial role in various diagrammatic approaches [32,38–44] that construct nonlocal correlations starting from a local DMFT [30] solution. In the dual-fermion (DF) [39–41] functional renormalization-group enhanced DMFT (DMF^{2}RG) [45], the nonlocal expansion (NLE) [44] and the three-leg vertex (TRILEX) [46] approaches to the full vertex functions $F_{d/m/s/t}^{k,k'}(q)$ are used to restore the nonlocal dependence in the self-energy. In ladder DΓA [32,38] and the one-particle irreducible (1PI) approach [43], the channel-dependent irreducible vertex functions $\Gamma_{d/m/s/t}^{k,k'}(q)$ are the building blocks for the nonlocal self-energy diagrams. Full parquet DΓA [28] starts, as we do here, with the most compact and local object, i.e., the fully irreducible vertex $\Lambda_{d/m/s/t}^{k,k'}(q)$. To obtain these necessary vertex functions is not a trivial task. Exact numerical methods, such as quantum Monte Carlo (QMC) or exact diagonalization (ED), are usually employed. We have shown in this paper that, in addition to these approaches, the parquet equations provide another tool that is more flexible than the QMC and ED in many situations, as it can be applied to cases out of half-filling, cluster systems, multiorbital materials, etc. We believe that our implementation of the parquet equations paves the way for other many-body methods [39–41,44,45] that are based on the two-particle vertex.

Another feature of our parquet implementation is the improved convergence of the algorithm. As displayed in Fig. 7, with the kernel approximation, $U = 6$ and 8 can also be converged, which is difficult to achieve in other implementations [26,27]. The improved convergence is mainly due to the correct understanding of the vertex structure and the subsequently proposed kernel approximation. In implementations without auxiliary high-frequency functions, one has to enlarge the frequency range to achieve a better convergence. However, the rapid growth in the memory demand usually forbids one to do so. Comparing Fig. 7 with Fig. 4 immediately implies that, with the increase of interaction strength, the deviations of the PA from the DMFT become more and more pronounced. The parquet approximation works better in the weak-coupling regime. This is corrected when the full parquet calculations are performed. However, we noticed that the convergence in the full parquet calculation is generally slower than in the PA, and for these values of interactions, i.e., $U = 6,8$ and even larger, we did not achieve the convergence in the full parquet calculations, which is mainly due to the almost singular value of $\Lambda_{d/m/s/t}^{k,k'}(q)$ occurring at larger values of U [47].

B. Validation against DMFT away from half-filling

The parquet formula decouples the complete two-particle vertex functions according to its reducibility in different channels. As a result, the parquet formula entangles particle-particle and particle-hole channels. Both, the full two-particle vertex functions and the single-particle self-energy are subject to contributions from both particle-hole and particle-particle fluctuations. At half-filling, the particle-hole, especially the

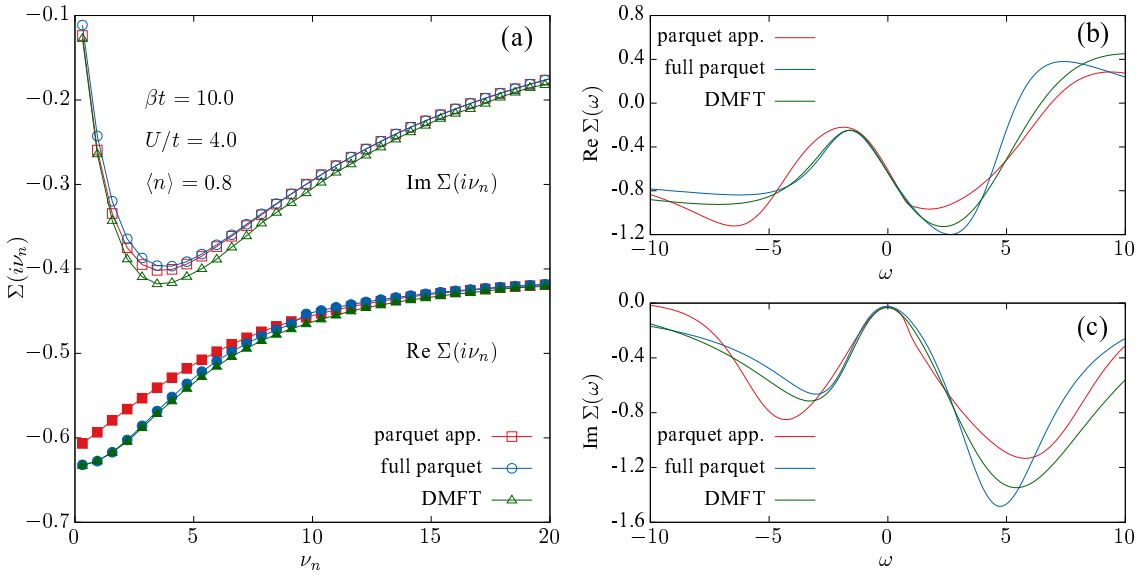

FIG. 8. The self-energy functions calculated from the parquet approximation and full parquet at $\beta t = 10.0$ and $U/t = 4.0$ with average particle number $\langle n \rangle = 0.8$. (a) Both the real and imaginary parts are compared to the corresponding DMFT solution. (b) and (c) The same self-energy functions as in (a) but in the real-frequency domain. Analytical continuation is carried out with the Padé approximation.

magnetic channel, is the channel displaying the strongest fluctuations. Thus, the low-energy physics at half-filling is dominated mainly by magnetic fluctuations from the particle-hole excitations. Here we further benchmark our kernel approximation for the hole-doped case, where the magnetic fluctuations are suppressed while the charge and pairing fluctuations are enhanced. The doped single-band Hubbard model is very appealing due to the interest in the pseudogap of unconventional superconductors. In the normal phase of cuprate superconductors, it is believed that due to the strong competition between particle-hole and particle-particle fluctuations, a pseudogap forms as a precursor of the superconducting gap below the transition temperature.

As the parquet formulation equally describes particle-particle and particle-hole fluctuations, the doped Hubbard model is indeed a good testing case for our implementation. In Fig. 8, we show the results for $\beta t = 10$ and $U/t = 4.0$, and we compare the parquet approximation (red square), the full parquet (blue circle) calculations, and the numerically exact DMFT solutions (green triangle). The particle concentration is taken as $\langle n \rangle = 0.8$. To keep $\langle n \rangle$ fixed in the self-consistent parquet calculations, we adjust the chemical potential μ in each self-consistency iteration. Compared to the results presented in the previous section, the temperature is much lower and the doping level is close to the optimal doping for cuprate superconductivity.

In the doped case, the real part of the self-energy becomes nonzero. For this effective single impurity problem, the static part of the self-energy is completely given by the Hartree contribution, which accounts for the hole doping. As is clearly displayed in Fig. 8, the asymptotics of both real and imaginary parts of the self-energy from the parquet approximation and the full parquet solutions agree well with that of the DMFT. In the low-frequency regime, the imaginary part of the parquet approximation and the full parquet solutions is similar to the DMFT exact solution, while in the real part the discrepancy between the parquet approximation and the DMFT is nicely improved by the full parquet solution with a local fully irreducible vertex as an input. Such an improvement is also seen for real frequencies [see Figs. 8(b) and 8(c)], where the low-frequency part of the DMFT solution is nicely reproduced by the full parquet results, while the parquet approximation solution deviates slightly from the other two. Here, of course, the Padé fit leads to some numerical noise.

As already noted before, in the full parquet calculations we take the fully irreducible vertex function $\Lambda^{\nu,\nu'}(\omega)$ obtained from DMFT (QMC) as input. In this low-temperature study, we have $\Lambda^{\nu,\nu'}(\omega)$ only in a limited parameter space $\nu,\nu' \in [-8.48 : 8.48]$ and $\omega \in [-8.8 : 8.8]$, which corresponds to a Matsubara frequency index in $[-14 : 15]$. Increasing the number of Matsubara frequencies in DMFT (QMC) is basically hindered by a fundamental problem of QMC, i.e., the statistical error of the two-particle vertex functions at larger frequencies. The inversion of the Bethe-Salpeter equation in DMFT (QMC) becomes unstable in this case. The problem of a limited number of Matsubara frequencies available in $\Lambda^{\nu,\nu'}(\omega)$ is more serious in this study than in the high-temperature cases studied before. This numerical noise may be the source of the discrepancies in the imaginary part. Let us note that for this set of parameters, it is not even necessary to work with the $\Lambda^{\nu,\nu'}(\omega)$ calculated by means of QMC. As one can see from Fig. 8, the parquet approximation with $\Lambda^{\nu,\nu'}_{d/m/s/t}(\omega) = (U, -U, 2U, 0)$ behaves reasonably at both high and low frequencies. By doping, electronic correlations are reduced so that the parquet approximation, which works better at weak coupling, becomes more justified. Of course, a better estimation of $\Lambda^{\nu,\nu'}(\omega)$ can further improve the parquet approximation.

C. Dynamical vertex approximation

In this section, we go beyond the DMFT solution of the Hubbard model discussed in the preceding section, where

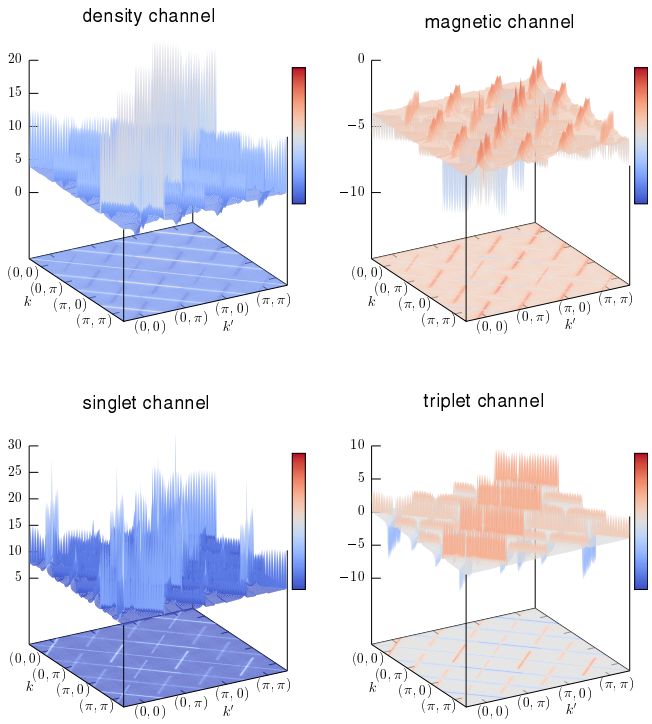

FIG. 9. Nonlocal full vertex obtained by DΓA at $\beta t = 2, U/t = 4$ for a 2×2 momentum patch. $F^{k,k'}_{d/m/s/t}(q)$ is shown as a function of k and k' for fixed $q = 0$.

the parquet equations are solved without k dependence (for a single k point). Instead, we solve the parquet equations for a 2×2 patch-grid in momentum space using the local fully irreducible vertex as an input. This is the parquet DΓA, which includes nonlocal correlations beyond DMFT [28]. Figure 9 shows the nonlocal, full vertex functions at $\beta = 2$ and $U = 4$ ($t \equiv 1$) as functions of k and k' with $q = 0$. In each compound index k, there are four different momenta, which results in 64 momentum patches for each vertex function. Figure 9 shows the 16 patches for $q = 0$. It is obvious from Fig. 9 that the full vertex shows a strong momentum dependence that is also very channel-dependent. While we only show results here for a 2×2 patch-grid, solving the parquet equations for larger clusters is possible due to the economic use of memory in our kernel approximation. We found our implementation to be feasible also for calculations on 4×4 clusters. Further algorithmic improvements regarding parallelization and memory management should allow for even larger cluster sizes.

IV. SUMMARY AND OUTLOOK

In this paper, we have proposed an implementation of the parquet equations and applied it to the one-band Hubbard model in DMFT and DΓA. We found that it is crucial to respect the correct structure of the vertex functions to simultaneously maintain the self-consistency at both single- and two-particle levels. Among the various two-particle vertex functions, the reducible vertex in each channel plays an important role in the parquet equations in the sense that it generates the major structure of the other vertex functions. This important observation motivates us to propose a two-level kernel approximation on the reducible vertex $\Phi^{k,k'}_{d/m}(q)$ and $\Psi^{k,k'}_{s/t}(q)$, which effectively reduces its three-argument dependence to a one-/two-argument dependence. Employing this two-level kernel approximation in a larger frequency interval greatly simplifies the calculation. In particular, it faithfully respects the open boundary condition of the vertex functions in Matsubara frequency space. Based on the kernel function, we also proposed an auxiliary function to carefully incorporate the high-frequency information missing in the finite sum evaluation of the self-energy.

We showed that the two-level kernel approximation and the high-frequency regulation are efficient for solving the parquet equations. For the single-impurity Anderson model, a very impressive agreement with the DMFT can be achieved that validates our approach. We also demonstrate that the PA works quite well as long as U is not too large. Let us note that the kernel approximation and the high-frequency regulation also improve the convergence, which further enhances the applicability of this approach. The calculated two-particle vertex functions can be used as a starting point by other many-body approaches, such as the ladder-DΓA, the 1PI approach, DMF^{2}RG, DF, NLE, and TRILEX.

The proposed two-level kernel approximations and the high-frequency regulations are compatible with the PA and the full parquet DΓA, which we were able to perform in two dimensions. Physically, the advantage over previously employed ladder DΓA [48,49] is that in the full parquet DΓA the particle-particle (Cooper) channel is also included. This allows us to study spin-fluctuation mediated superconductivity [18,19] and instabilities toward stripe phases [50]. Let us note that nonlocal interactions can also be included straightforwardly. For example, it is possible to study an extended Hubbard model with nearest-neighbor interaction and the competition between the long-range magnetic and charge instabilities.

ACKNOWLEDGMENTS

We want to thank S. Andergassen, G. Rohringer, and A. Toschi for the valuable comments. We acknowledge support from European Research Council under the European Union's Seventh Framework Programme (FP/2007-2013)/ERC through Grant Agreement No. 306447 (AbinitioDΓA). We are grateful for the hospitality of the Aspen Center for Physics, which is supported by National Science Foundation Grant No. PHY-1066293. The computational results presented were achieved using the Vienna Scientific Cluster (VSC).

APPENDIX: FORMULATION OF THE PARQUET EQUATIONS

In this appendix, we present the necessary notations that are used in this paper. Based on these notations, the parquet equations are derived under SU(2) symmetry. The complete derivation of the parquet formulation concerns two parts: the coupled equations for the two-particle vertex functions in all channels, and the one-particle self-energy.

Throughout this paper, we considered the half-filled single-band Hubbard model on a square lattice and used its DMFT

solution as a benchmark for testing the numerical feasibility of our approach. The Hubbard Hamiltonian reads

$$H = \sum_{\mathbf{k},\sigma} \epsilon_{\mathbf{k}} c^{\dagger}_{\mathbf{k},\sigma} c_{\mathbf{k},\sigma} + U \sum_{i} n_{i\uparrow} n_{i\downarrow}. \tag{A1}$$

Here, $\mathbf{k}$ represents a momentum vector in the two-dimensional (2D) square lattice, $\epsilon_{\mathbf{k}} = -2t(\cos k_x + \cos k_y)$, $c^{\dagger}_{\mathbf{k},\sigma}$ ($c_{\mathbf{k},\sigma}$) creates (annihilates) an electron with momentum $\mathbf{k}$ and spin $\sigma \in \{\uparrow, \downarrow\}$, and $n_{i\sigma} \equiv c^{\dagger}_{i,\sigma} c_{i,\sigma}$ is the number operator on lattice site i.

1. Notations

First, we introduce the definition for the two-particle susceptibility χ, from which other vertex functions can be derived. The particle-hole and particle-particle susceptibilities are defined as

$$\chi^{k,k'}_{ph,\sigma\sigma'}(q) = \sum_{ijkl} e^{-ikr_i} e^{i(k+q)r_j} e^{-i(k'+q)r_k} e^{ik'r_l} \times \langle T_\tau c^{\dagger}_{\sigma}(r_i) c_{\sigma}(r_j) c^{\dagger}_{\sigma'}(r_k) c_{\sigma'}(r_l) \rangle, \tag{A2a}$$

$$\chi^{k,k'}_{pp,\sigma\sigma'}(q) = \sum_{ijkl} e^{-ikr_i} e^{i(q-k')r_j} e^{-i(q-k)r_k} e^{ik'r_l} \times \langle T_\tau c^{\dagger}_{\sigma}(r_i) c_{\sigma}(r_j) c^{\dagger}_{\sigma'}(r_k) c_{\sigma'}(r_l) \rangle. \tag{A2b}$$

Here, $r = (\mathbf{r}, \tau)$ with lattice site $\mathbf{r}$ and imaginary time τ, $k = (\mathbf{k}, i\nu)$ with wave vector $\mathbf{k}$ and Matsubara frequency $i\nu$, and $q = (\mathbf{q}, i\omega)$ with the transfer momentum and bosonic frequency. $\sum_{ijkl}$ will be understood as $T \sum_{\mathbf{r}_i \cdots \mathbf{r}_l} \int_0^\beta d\tau_i \cdots d\tau_l$, where T is the temperature. Note that the particle-hole and particle-particle excitations are encoded in the same four-point correlator in the above equation, thus $\chi^{k,k'}_{ph,\sigma\sigma'}(q)$ and $\chi^{k,k'}_{pp,\sigma\sigma'}(q)$ are not independent but relate to each other by means of a frequency shift. That is, they are related to each other as $\chi^{k,k'}_{pp,\sigma\sigma'}(q) = \chi^{k,k'}_{ph,\sigma\sigma'}(q - k - k')$. The same relation also holds for the complete vertex F and the fully irreducible vertex Λ.

From the susceptibilities $\chi^{k,k'}_{ph,\sigma\sigma'}(q)$ and $\chi^{k,k'}_{pp,\sigma\sigma'}(q)$, the complete (full) vertex functions $F^{k,k'}_{ph,\sigma\sigma'}(q)$ and $F^{k,k'}_{pp,\sigma\sigma'}(q)$ can be easily obtained as

$$F^{k,k'}_{ph,\sigma\sigma'}(q) = -\frac{\chi^{k,k'}_{ph,\sigma\sigma'}(q) - \chi^{0,kk'}_{ph,\sigma\sigma'}(q)}{G^{k}_{\sigma} G^{k+q}_{\sigma'} G^{k'}_{\sigma'} G^{k'+q}_{\sigma}}, \tag{A3a}$$

$$F^{k,k'}_{pp,\sigma\sigma'}(q) = -\frac{\chi^{k,k'}_{pp,\sigma\sigma'}(q) - \chi^{0,kk'}_{pp,\sigma\sigma'}(q)}{G^{k}_{\sigma} G^{q-k'}_{\sigma'} G^{k'}_{\sigma'} G^{q-k}_{\sigma}}, \tag{A3b}$$

with the bare bubble susceptibilities $\chi^{0,kk'}_{ph,\sigma\sigma'}(q) = \frac{\beta}{N}[G^{k}_{\sigma} G^{k'}_{\sigma'} \delta_{q,0} - G^{k}_{\sigma} G^{k+q}_{\sigma} \delta_{k,k'} \delta_{\sigma\sigma'}]$ and $\chi^{0,kk'}_{pp,\sigma\sigma'}(q) = \frac{\beta}{N}[G^{k}_{\sigma} G^{k'}_{\sigma'} \delta_{k,q-k'} - G^{k}_{\sigma} G^{q-k}_{\sigma} \delta_{k,k'} \delta_{\sigma\sigma'}]$. Under the SU(2) symmetry, the full vertex functions (including also the other vertex functions) with different spin configurations can be cast into a more compact form in the density (d), magnetic (m), singlet (s), and triplet (t) channels; see Fig. 10:

$$F^{k,k'}_{d/m}(q) = F^{k,k'}_{ph,\uparrow\uparrow}(q) \pm F^{k,k'}_{ph,\uparrow\downarrow}(q), \tag{A4a}$$

$$F^{k,k'}_{t/s}(q) = F^{k,k'}_{pp,\uparrow\downarrow}(q) \pm F^{k,k'}_{pp,\overline{\uparrow\downarrow}}(q). \tag{A4b}$$

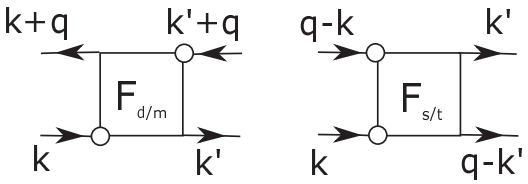

FIG. 10. Graphical representation of the vertex functions in the particle-hole (d/m) and the particle-particle (s/t) channels, which apply to all the vertices in this work.

In each channel, the full vertex function can be further decomposed into the two-particle irreducible vertex ($\Gamma_{d/m/s/t}$) and the reducible vertex ($\Phi_{d/m}, \Psi_{t/s}$) through the Bethe-Salpeter equation (BSE), which has been thoroughly discussed in many works; see, e.g., [6,34]. Here, we will only recall the BSE formulas as used in the derivation of the parquet equations:

$$F^{k,k'}_{d/m}(q) = \Gamma^{k,k'}_{d/m}(q) + \Phi^{k,k'}_{d/m}(q), \tag{A5a}$$

$$F^{k,k'}_{t/s}(q) = \Gamma^{k,k'}_{t/s}(q) + \Psi^{k,k'}_{t/s}(q), \tag{A5b}$$

where the reducible vertex functions depend on the irreducible and full vertex as follows:

$$\Phi^{k,k'}_{d/m}(q) = \frac{T}{N} \sum_{k''} \Gamma^{k,k''}_{d/m}(q) G(k'') G(k'' + q) F^{k'',k'}_{d/m}(q), \tag{A6a}$$

$$\Psi^{k,k'}_{t/s}(q) = \pm \frac{T}{2N} \sum_{k''} \Gamma^{k,k''}_{t/s}(q) G(k'') G(q - k'') F^{k'',k'}_{t/s}(q). \tag{A6b}$$

2. Derivation of the parquet equations

With the above notations and definitions, we now proceed to derive the parquet equations. The irreducible vertex $\Gamma_{d/m/s/t}$ is only irreducible in a given channel, while it becomes reducible in other channels. $\Lambda_{d/m/s/t}$, as the most fundamental one among all vertex functions, is fully irreducible in all channels. Given $\Lambda_{d/m/s/t}$, the full vertex $F_{d/m/s/t}$, the channel-dependent irreducible vertex $\Gamma_{d/m/s/t}$, and the reducible vertices $\Phi_{d/m}, \Psi_{s/t}$ can be readily calculated from the parquet equation, as represented graphically in Fig. 11. The parquet equation is merely a classification of diagrams in terms of their two-particle irreducibility. Mathematically, by taking the spin dependence of each diagram into account, we obtain the parquet equation in the particle-hole channel as

$$\Gamma^{k,k'}_{ph,\uparrow\uparrow}(q) = \Lambda^{k,k'}_{ph,\uparrow\uparrow}(q) + \Phi^{k,k'}_{\overline{ph},\uparrow\uparrow}(q) - \Psi^{k,k+q}_{pp,\uparrow\uparrow}(k + k' + q), \tag{A7a}$$

$$\Gamma^{k,k'}_{ph,\uparrow\downarrow}(q) = \Lambda^{k,k'}_{ph,\uparrow\downarrow}(q) + \Phi^{k,k'}_{\overline{ph},\uparrow\downarrow}(q) - \Psi^{k,k+q}_{pp,\overline{\uparrow\downarrow}}(k + k' + q). \tag{A7b}$$

After applying the crossing relations [34]

$$\Phi^{k,k'}_{\overline{ph},\uparrow\uparrow}(q) = -\Phi^{k,k+q}_{ph,\uparrow\uparrow}(k' - k), \tag{A8a}$$

$$\Phi^{k,k'}_{\overline{ph},\uparrow\downarrow}(q) = -\Phi^{k,k+q}_{m}(k' - k), \tag{A8b}$$

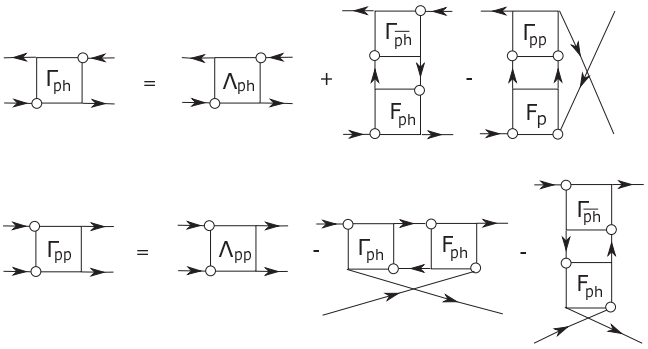

FIG. 11. Coupled diagrams for the parquet equations in the particle-hole and particle-particle channels. Here the corresponding diagrams in the particle-hole transverse channel have been omitted, as they do not lead to independent contributions to the parquet equations and can be derived from the particle-hole channel.

$$\Psi^{k,k'}_{pp,\uparrow\uparrow}(q) = \Psi^{k,k'}_{t}(q) = -\Psi^{k,q-k'}_{t}(q), \tag{A8c}$$

$$\Psi^{k,k'}_{pp,\uparrow\downarrow}(q) = -\Psi^{k,q-k'}_{pp,\uparrow\downarrow}(q) \tag{A8d}$$

to Eqs. (A7a) and (A7b), we have

$$\Gamma^{k,k'}_{ph,\uparrow\uparrow}(q) = \Lambda^{k,k'}_{ph,\uparrow\uparrow}(q) - \Phi^{k,k+q}_{ph,\uparrow\uparrow}(k'-k) + \Psi^{k,k'}_{t}(k+k'+q), \tag{A9a}$$

$$\Gamma^{k,k'}_{ph,\uparrow\downarrow}(q) = \Lambda^{k,k'}_{ph,\uparrow\downarrow}(q) - \Phi^{k,k+q}_{m}(k'-k) + \Psi^{k,k'}_{pp,\uparrow\downarrow}(k+k'+q), \tag{A9b}$$

which can be equivalently written in the density and magnetic channels as

$$\Gamma^{k,k'}_{d}(q) = \Lambda^{k,k'}_{d}(q) - \tfrac{1}{2}\Phi^{k,k+q}_{d}(k'-k) - \tfrac{3}{2}\Phi^{k,k+q}_{m}(k'-k) + \tfrac{1}{2}\Psi^{k,k'}_{s}(k+k'+q) + \tfrac{3}{2}\Psi^{k,k'}_{t}(k+k'+q), \tag{A10a}$$

$$\Gamma^{k,k'}_{m}(q) = \Lambda^{k,k'}_{m}(q) - \tfrac{1}{2}\Phi^{k,k+q}_{d}(k'-k) + \tfrac{1}{2}\Phi^{k,k+q}_{m}(k'-k) - \tfrac{1}{2}\Psi^{k,k'}_{s}(k+k'+q) + \tfrac{1}{2}\Psi^{k,k'}_{t}(k+k'+q). \tag{A10b}$$

Similarly, for the particle-particle channel in Fig. 11, the equations read

$$\Gamma^{k,k'}_{pp,\uparrow\downarrow}(q) = \Lambda^{k,k'}_{pp,\uparrow\downarrow}(q) - \Phi^{k,q-k'}_{ph,\uparrow\downarrow}(k'-k) - \Phi^{k,q-k'}_{\overline{ph},\uparrow\downarrow}(k'-k), \tag{A11a}$$

$$\Gamma^{k,k'}_{pp,\uparrow\downarrow}(q) = \Lambda^{k,k'}_{pp,\uparrow\downarrow}(q) - \Phi^{k,q-k'}_{ph,\uparrow\downarrow}(k'-k) - \Phi^{k,q-k'}_{\overline{ph},\uparrow\downarrow}(k'-k). \tag{A11b}$$

To simply these equations, we need again Eq. (A8b) and the following relation:

$$\Phi^{k,k'}_{\overline{ph},\uparrow\downarrow}(q) = -\Phi^{k,k+q}_{ph,\uparrow\downarrow}(k'-k), \tag{A12a}$$

$$\Phi^{k,k'}_{\overline{ph},\uparrow\downarrow}(q) = \Phi^{k,k'}_{m}(q). \tag{A12b}$$

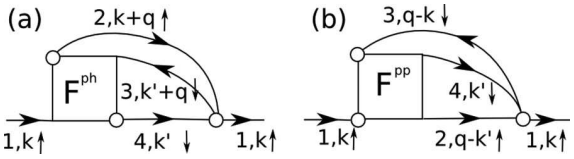

FIG. 12. The Feynman diagram for the self-energy, which contains contributions from both the particle-hole and the particle-particle channel.

The parquet equations for the particle-particle channel are then found to be

$$\Gamma^{k,k'}_{s}(q) = \Lambda^{k,k'}_{s}(q) + \tfrac{1}{2}\Phi^{k,q-k'}_{d}(k'-k) - \tfrac{3}{2}\Phi^{k,q-k'}_{m}(k'-k) + \tfrac{1}{2}\Phi^{k,k'}_{d}(q-k-k') - \tfrac{3}{2}\Phi^{k,k'}_{m}(q-k-k'), \tag{A13a}$$

$$\Gamma^{k,k'}_{t}(q) = \Lambda^{k,k'}_{t}(q) - \tfrac{1}{2}\Phi^{k,q-k'}_{d}(k'-k) - \tfrac{1}{2}\Phi^{k,q-k'}_{m}(k'-k) + \tfrac{1}{2}\Phi^{k,k'}_{d}(q-k-k') + \tfrac{1}{2}\Phi^{k,k'}_{m}(q-k-k'). \tag{A13b}$$

3. Crossing symmetry

An important symmetry that the parquet equations satisfy but that is violated in the Baym-Kadanoff formalism is the crossing symmetry, which for the full vertex reads

$$\begin{aligned} F^{k,k'}_{d}(q) &= \tfrac{1}{2}F^{k,k'}_{s}(k+k'+q) + \tfrac{3}{2}F^{k,k'}_{t}(k+k'+q),\\ F^{k,k'}_{m}(q) &= -\tfrac{1}{2}F^{k,k'}_{s}(k+k'+q) + \tfrac{1}{2}F^{k,k'}_{t}(k+k'+q),\\ F^{k,k'}_{s}(q) &= \tfrac{1}{2}F^{k,k'}_{d}(q-k-k') - \tfrac{3}{2}F^{k,k'}_{m}(q-k-k'),\\ F^{k,k'}_{t}(q) &= \tfrac{1}{2}F^{k,k'}_{d}(q-k-k') + \tfrac{1}{2}F^{k,k'}_{m}(q-k-k'). \end{aligned} \tag{A14}$$

These equations can be easily verified in the parquet equation (1) by substituting Eqs. (A10) and (A13) into Eq. (A5). A correct solution of the parquet equations certainly should respect this symmetry. It has been understood that the above crossing symmetry can be explicitly enforced at each self-consistent step by solving the parquet equations for the full vertex $F_{d/m/s/t}$, i.e., Eq. (1), instead of those for $\Gamma_{d/m/s/t}$ [27]. We note that a similar crossing symmetry also applies to the fully irreducible vertex $\Lambda_{d/m/s/t}$.

4. Self-energy from the full vertex

To close the self-consistent loop in the parquet theory, we also need to connect the two-particle full vertex functions $F_{d/m/s/t}$ with the single-particle self-energy $\Sigma(k)$, which is graphically shown in Fig. 12. This connection can be derived through the Heisenberg equation of motion and is also known as the Schwinger-Dyson equation.

In this context, it reads

$$\Sigma(k) = -\frac{UT^2}{4N}\sum_{k',q} G(k+q)G(k'+q)G(k') \times \left[F_d^{k,k'}(q) - F_m^{k,k'}(q)\right] - \frac{UT^2}{4N}\sum_{k',q} G(q-k')G(q-k)G(k') \times \left[F_s^{k,k'}(q) + F_t^{k,k'}(q)\right]. \quad \text{(A15)}$$

Here, the sum over k' and q should be done over all Matsubara frequencies. In principle, the Hartree and Fock terms need to be added to Eq. (A15), but they are not relevant for the one-band Hubbard model in the paramagnetic phase.

From Σ in turn, the Green function is obtained through the Dyson equation, which for the sake of completeness reads

$$G(k) = [i\omega - \epsilon_{\mathbf{k}} - \Sigma(k)]^{-1}. \quad \text{(A16)}$$

This Green function enters Eq. (A6), which closes the set of equations in the parquet formalism.

[1] L. D. Landau, The theory of a Fermi liquid, Sov. Phys. JETP **3**, 920 (1957).

[2] E. Lifshitz and L. P. Pitaevskii, *Statistical Physics, Part 2*, Landau and Lifshitz Course of Theoretical Physics Vol. 9 (Butterworth-Heinemann, Washington, DC, 1980).

[3] J.G. Bednorz and K.A. Mller, Possible high-T_c superconductivity in the BaLaCuO system, Z. Phys. B **64**, 189 (1986).

[4] J. Hubbard, Electron correlations in narrow energy bands, Proc. R. Soc. London, Ser. A **276**, 238 (1963).

[5] D. Bohm and D. Pines, A collective description of electron interactions. I. Magnetic interactions, Phys. Rev. **82**, 625 (1951).

[6] N. E. Bickers, Parquet equations for numerical self-consistent-field theory, Int. J. Mod. Phys. B **05**, 253 (1991).

[7] D. Pines and D. Bohm, A collective description of electron interactions: II. Collective vs individual particle aspects of the interactions, Phys. Rev. **85**, 338 (1952).

[8] D. Bohm and D. Pines, A collective description of electron interactions: III. Coulomb interactions in a degenerate electron gas, Phys. Rev. **92**, 609 (1953).

[9] P. G. J. van Dongen, Extended Hubbard model at weak coupling, Phys. Rev. B **50**, 14016 (1994).

[10] G. Esirgen and N. E. Bickers, Fluctuation-exchange theory for general lattice Hamiltonians, Phys. Rev. B **55**, 2122 (1997).

[11] S. Pairault, D. Snchal, and A.-M.S. Tremblay, Strong-coupling perturbation theory of the Hubbard model, Eur. Phys. J. B **16**, 85 (2000).

[12] J. K. Freericks and H. Monien, Strong-coupling expansions for the pure and disordered Bose-Hubbard model, Phys. Rev. B **53**, 2691 (1996).

[13] S. Schmidt and G. Blatter, Strong Coupling Theory for the Jaynes-Cummings-Hubbard Model, Phys. Rev. Lett. **103**, 086403 (2009).

[14] G. Baym and L. P. Kadanoff, Conservation laws and correlation functions, Phys. Rev. **124**, 287 (1961).

[15] L. D. Landau, A. A. Abrikosov, and I. M. Khalatnikov, On the elimination of infinities in quantum electrodynamics, Dokl. Akad. Nauk SSSR Vol. 95, 497 (1954).

[16] C. De Dominicis and P. C. Martin, Stationary entropy principle and renormalization in normal and superfluid systems. I. Algebraic formulation, J. Math. Phys. **5**, 14 (1964).

[17] C. De Dominicis and P. C. Martin, Stationary entropy principle and renormalization in normal and superfluid systems. II. Diagrammatic formulation, J. Math. Phys. **5**, 31 (1964).

[18] N. E. Bickers, D. J. Scalapino, and S. R. White, Conserving Approximations for Strongly Correlated Electron Systems: Bethe-Salpeter Equation and Dynamics for the Two-Dimensional Hubbard Model, Phys. Rev. Lett. **62**, 961 (1989).

[19] D. J. Scalapino, Superconductivity and spin fluctuations, J. Low Temp. Phys. **117**, 179 (1999).

[20] N. E. Bickers and D. J. Scalapino, Critical behavior of electronic parquet solutions, Phys. Rev. B **46**, 8050 (1992).

[21] V. M. Yakovenko, Metals in a high magnetic field: A universality class of marginal Fermi liquids, Phys. Rev. B **47**, 8851 (1993).

[22] V. Janiš and P. Augustinský, Analytic impurity solver with Kondo strong-coupling asymptotics, Phys. Rev. B **75**, 165108 (2007).

[23] P. Augustinský and V. Janiš, Multiorbital simplified parquet equations for strongly correlated electrons, Phys. Rev. B **83**, 035114 (2011).

[24] C.-X. Chen and N. E. Bickers, Numerical solution of parquet equations for the Anderson impurity model, Solid State Commun. **82**, 311 (1992).

[25] N. E. Bickers and S. R. White, Conserving approximations for strongly fluctuating electron systems. II. Numerical results and parquet extension, Phys. Rev. B **43**, 8044 (1991).

[26] S. X. Yang, H. Fotso, J. Liu, T. A. Maier, K. Tomko, E. F. D'Azevedo, R. T. Scalettar, T. Pruschke, and M. Jarrell, Parquet approximation for the 4 × 4 Hubbard cluster, Phys. Rev. E **80**, 046706 (2009).

[27] K.-M. Tam, H. Fotso, S.-X. Yang, T.-W. Lee, J. Moreno, J. Ramanujam, and M. Jarrell, Solving the parquet equations for the Hubbard model beyond weak coupling, Phys. Rev. E **87**, 013311 (2013).

[28] A. Valli, T. Schäfer, P. Thunström, G. Rohringer, S. Andergassen, G. Sangiovanni, K. Held, and A. Toschi, Dynamical vertex approximation in its parquet implementation: Application to Hubbard nanorings, Phys. Rev. B **91**, 115115 (2015).

[29] G. Rohringer, A. Valli, and A. Toschi, Local electronic correlation at the two-particle level, Phys. Rev. B **86**, 125114 (2012).

[30] A. Georges, G. Kotliar, W. Krauth, and M. J. Rozenberg, Dynamical mean-field theory of strongly correlated fermion systems and the limit of infinite dimensions, Rev. Mod. Phys. **68**, 13 (1996).

[31] N. E. Bickers, Self-consistent many-body theory for condensed matter systems, in *Theoretical Methods for Strongly Correlated Electrons*, CRM Series in Mathematical Physics, edited by D. Sènèchal, A.-M. Tremblay, and C. Bourbonnais (Springer New York, 2004), pp. 237–296.

[32] A. Toschi, A. A. Katanin, and K. Held, Dynamical vertex approximation: A step beyond dynamical mean-field theory, Phys. Rev. B **75**, 045118 (2007).

[33] K. Held, in *Dynamical Vertex Approximation*, edited by E. Pavarini, E. Koch, D. Vollhardt, and A. Lichtenstein, DMFT at 25: Infinite Dimensions, Modeling and Simulation, Vol. 4 (Verlag des Forschungszentrum Jülich, 2014).

[34] G. Rohringer, New routes towards a theoretical treatment of nonlocal electronic correlations, Ph.D. thesis, Institute of Solid State Physics, Vienna University of Technology, 2013.

[35] A. N. Rubtsov, V. V. Savkin, and A. I. Lichtenstein, Continuous-time quantum Monte Carlo method for fermions, Phys. Rev. B **72**, 035122 (2005).

[36] E. Gull, A. J. Millis, A. I. Lichtenstein, A. N. Rubtsov, M. Troyer, and P. Werner, Continuous-time Monte Carlo methods for quantum impurity models, Rev. Mod. Phys. **83**, 349 (2011).

[37] C. Karrasch, R. Hedden, R. Peters, Th. Pruschke, K. Schnhammer, and V. Meden, A finite-frequency functional renormalization group approach to the single impurity Anderson model, J. Phys.: Condens. Matter **20**, 345205 (2008).

[38] K. Held, A. A. Katanin, and A. Toschi, Dynamical vertex approximation: An introduction, Prog. Theor. Phys. Suppl. **176**, 117 (2008).

[39] A. N. Rubtsov, M. I. Katsnelson, and A. I. Lichtenstein, Dual fermion approach to nonlocal correlations in the Hubbard model, Phys. Rev. B **77**, 033101 (2008).

[40] A. N. Rubtsov, M. I. Katsnelson, A. I. Lichtenstein, and A. Georges, Dual fermion approach to the two-dimensional Hubbard model: Antiferromagnetic fluctuations and Fermi arcs, Phys. Rev. B **79**, 045133 (2009).

[41] H. Hafermann, G. Li, A. N. Rubtsov, M. I. Katsnelson, A. I. Lichtenstein, and H. Monien, Efficient Perturbation Theory for Quantum Lattice Models, Phys. Rev. Lett. **102**, 206401 (2009).

[42] H. Kusunose, Self-consistent fluctuation theory for strongly correlated electron systems, J. Phys. Soc. Jpn. **79**, 094707 (2010).

[43] G. Rohringer, A. Toschi, H. Hafermann, K. Held, V. I. Anisimov, and A. A. Katanin, One-particle irreducible functional approach: A route to diagrammatic extensions of the dynamical mean-field theory, Phys. Rev. B **88**, 115112 (2013).

[44] G. Li, Hidden physics in the dual-fermion approach: A special case of a nonlocal expansion scheme, Phys. Rev. B **91**, 165134 (2015).

[45] C. Taranto, S. Andergassen, J. Bauer, K. Held, A. Katanin, W. Metzner, G. Rohringer, and A. Toschi, From Infinite to Two Dimensions Through the Functional Renormalization Group, Phys. Rev. Lett. **112**, 196402 (2014).

[46] T. Ayral and O. Parcollet, Mott physics and spin fluctuations: A unified framework, Phys. Rev. B **92**, 115109 (2015).

[47] T. Schäfer, G. Rohringer, O. Gunnarsson, S. Ciuchi, G. Sangiovanni, and A. Toschi, Divergent Precursors of the Mott-Hubbard Transition at the Two-Particle Level, Phys. Rev. Lett. **110**, 246405 (2013).

[48] T. Schäfer, F. Geles, D. Rost, G. Rohringer, E. Arrigoni, K. Held, N. Blümer, M. Aichhorn, and A. Toschi, Fate of the false Mott-Hubbard transition in two dimensions, Phys. Rev. B **91**, 125109 (2015).

[49] G. Rohringer, A. Toschi, A. Katanin, and K. Held, Critical Properties of the Half-Filled Hubbard Model in Three Dimensions, Phys. Rev. Lett. **107**, 256402 (2011).

[50] J. Zaanen and O. Gunnarsson, Charged magnetic domain lines and the magnetism of high-T_c oxides, Phys. Rev. B **40**, 7391 (1989).

Bibliography

[1] M. Imada, A. Fujimori, and Y. Tokura. *Metal-insulator transitions*. Rev. Mod. Phys, **70**, 1039 (1998).

[2] P. A. Lee, N. Nagaosa, and X.-G. Wen. *Doping a Mott insulator: Physics of high-temperature superconductivity*. Rev. Mod. Phys, **78**, 17 (2006).

[3] Q. Si, R. Yu, and E. Abrahams. *High-temperature superconductivity in iron pnictides and chalcogenides*. Nature Reviews Materials, **1**, 16017 (2016).

[4] I. Bloch, J. Dalibard, and W. Zwerger. *Many-body physics with ultracold gases*. Rev. Mod. Phys, **80**, 885 (2008).

[5] K. Huang. *Statistical Mechanics, 2nd Edition* (Wiley, 1987), 2 edition.

[6] L. P. Kadanoff. *Scaling laws for ising models near T_c*. Physics, **2**, 192 (1966).

[7] C. Wetterich. *Exact evolution equation for the effective potential*. Phys. Lett. B, **301**, 90 (1993).

[8] M. Salmhofer and C. Honerkamp. *Fermionic Renormalization Group Flows —Technique and Theory—*. Prog. Theor. Phys., **105**, 1 (2001).

[9] C. Honerkamp, D. Rohe, S. Andergassen, and T. Enss. *Interaction flow method for many-fermion systems*. Phys. Rev. B, **70**, 235115 (2004).

[10] A. A. Katanin. *Fulfillment of Ward identities in the functional renormalization group approach*. Phys. Rev. B, **70**, 115109 (2004).

[11] C. Karrasch, R. Hedden, R. Peters, T. Pruschke, K. Schönhammer, and V. Meden. *A finite-frequency functional renormalization group approach to the single impurity Anderson model*. J. Phys.: Condens. Matter, **20**, 345205 (2008).

[12] K.-U. Giering and M. Salmhofer. *Self-energy flows in the two-dimensional repulsive Hubbard model*. Phys. Rev. B, **86**, 245122 (2012).

[13] W. Metzner, M. Salmhofer, C. Honerkamp, V. Meden, and K. Schönhammer. *Functional renormalization group approach to correlated fermion systems*. Rev. Mod. Phys., **84**, 299 (2012).

[14] A. Eberlein. *Fermionic two-loop functional renormalization group for correlated fermions: Method and application to the attractive Hubbard model*. Phys. Rev. B, **90**, 115125 (2014).

[15] C. Taranto, S. Andergassen, J. Bauer, K. Held, A. Katanin, W. Metzner, G. Rohringer, and A. Toschi. *From Infinite to Two Dimensions through the Functional Renormalization Group*. Phys. Rev. Lett., **112**, 196402 (2014).

[16] N. Wentzell, C. Taranto, A. Katanin, A. Toschi, and S. Andergassen. *Correlated starting points for the functional renormalization group*. Phys. Rev. B, **91**, 045120 (2015).

[17] D. S. de la Peña, J. Lichtenstein, and C. Honerkamp. *Competing electronic instabilities of extended hubbard models on the honeycomb lattice: A functional renormalization group calculation with high wavevector resolution* (2016).

[18] H. Shiba. *Classical Spins in Superconductors*. Prog. Theor. Phys., **40**, 435 (1968).

[19] H. Shiba and T. Soda. *Superconducting Tunneling through the Barrier with Paramagnetic Impurities*. Prog. Theor. Phys., **41**, 25 (1969).

[20] L. Glazman and K. Matveev. *Resonant josephson current through kondo impurities in a tunnel barrier*. JETP Lett., **49**, 659 (1989).

[21] C. Beenakker and H. van Houten. *Resonant Josephson Current Through a Quantum Dot*. In H. Koch and H. Lübbig (editors), *Single-Electron Tunneling and Mesoscopic Devices*, volume 31 of *Springer Series in Electronics and Photonics*, 175–179 (Springer Berlin Heidelberg, 1992).

[22] R. Bauernschmitt, J. Siewert, Y. V. Nazarov, and A. A. Odintsov. *Josephson effect in low-capacitance superconductor-normal-metal-superconductor systems*. Phys. Rev. B, **49**, 4076 (1994).

[23] S. Ishizaka, J. Sone, and T. Ando. *dc Josephson current through a quantum dot coupled with superconducting leads*. Phys. Rev. B, **52**, 8358 (1995).

[24] A. L. Yeyati, J. C. Cuevas, A. López-Dávalos, and A. Martín-Rodero. *Resonant tunneling through a small quantum dot coupled to superconducting leads*. Phys. Rev. B, **55**, 6137 (1997).

[25] A. T. Alastalo, R. J. Joynt, and M. M. Salomaa. *The Anderson model in a superconductor: Φ-derivable theory*. J. Phys. Condens. Matter, **10**, L63 (1998).

[26] A. V. Rozhkov and D. P. Arovas. *Josephson Coupling through a Magnetic Impurity*. Phys. Rev. Lett., **82**, 2788 (1999).

[27] A. A. Clerk and V. Ambegaokar. *Loss of π-junction behavior in an interacting impurity Josephson junction*. Phys. Rev. B, **61**, 9109 (2000).

[28] M.-S. Choi, C. Bruder, and D. Loss. *Spin-dependent Josephson current through double quantum dots and measurement of entangled electron states*. Phys. Rev. B, **62**, 13569 (2000).

[29] A. V. Rozhkov and D. P. Arovas. *Interacting-impurity Josephson junction: Variational wave functions and slave-boson mean-field theory*. Phys. Rev. B, **62**, 6687 (2000).

[30] Y. Avishai, A. Golub, and A. D. Zaikin. *Tunneling through an Anderson impurity between superconductors*. Phys. Rev. B, **63**, 134515 (2001).

[31] J. C. Cuevas, A. Levy Yeyati, and A. Martín-Rodero. *Kondo effect in normal-superconductor quantum dots*. Phys. Rev. B, **63**, 094515 (2001).

[32] K. Kusakabe, Y. Tanaka, and Y. Tanuma. *Numerical study of unconventional superconductor/a quantum dot/unconventional superconductor junction*. Physica E Low-Dimensional Systems and Nanostructures, **18**, 50 (2003).

[33] A. Zazunov, V. S. Shumeiko, E. N. Bratus', J. Lantz, and G. Wendin. *Andreev Level Qubit*. Phys. Rev. Lett., **90**, 087003 (2003).

[34] E. Vecino, A. Martín-Rodero, and A. L. Yeyati. *Josephson current through a correlated quantum level: Andreev states and π junction behavior*. Phys. Rev. B, **68**, 035105 (2003).

[35] M.-S. Choi, M. Lee, K. Kang, and W. Belzig. *Kondo effect and Josephson current through a quantum dot between two superconductors*. Phys. Rev. B, **70**, 020502 (2004).

[36] F. Siano and R. Egger. *Josephson Current through a Nanoscale Magnetic Quantum Dot*. Phys. Rev. Lett., **93**, 047002 (2004).

[37] A. Oguri, Y. Tanaka, and A. C. Hewson. *Quantum Phase Transition in a Minimal Model for the Kondo Effect in a Josephson Junction*. J. Phys. Soc. Jpn., **73**, 2494 (2004).

[38] G. Sellier, T. Kopp, J. Kroha, and Y. S. Barash. *π junction behavior and Andreev bound states in Kondo quantum dots with superconducting leads*. Phys. Rev. B, **72**, 174502 (2005).

[39] F. S. Bergeret, A. L. Yeyati, and A. Martín-Rodero. *Interplay between Josephson effect and magnetic interactions in double quantum dots*. Phys. Rev. B, **74**, 132505 (2006).

[40] A. V. Balatsky, I. Vekhter, and J.-X. Zhu. *Impurity-induced states in conventional and unconventional superconductors*. Rev. Mod. Phys., **78**, 373 (2006).

[41] J. Bauer, A. Oguri, and A. C. Hewson. *Spectral properties of locally correlated electrons in a Bardeen Cooper Schrieffer superconductor*. J. Phys.: Condens. Matter, **19**, 486211 (2007).

[42] R. López, M.-S. Choi, and R. Aguado. *Josephson current through a Kondo molecule*. Phys. Rev. B, **75**, 045132 (2007).

[43] I. A. Sadovskyy, G. B. Lesovik, and G. Blatter. *Continuously tunable charge in Andreev quantum dots*. Phys. Rev. B, **75**, 195334 (2007).

[44] C. Benjamin, T. Jonckheere, A. Zazunov, and T. Martin. *Controllable π junction in a Josephson quantum-dot device with molecular spin*. EPJ B, **57**, 279 (2007).

[45] M. G. Pala, M. Governale, and J. König. *Nonequilibrium josephson and andreev current through interacting quantum dots*. New J. Phys., **9**, 278 (2007).

[46] L. Dell'Anna, A. Zazunov, R. Egger, and T. Martin. *Josephson current through a quantum dot with spin-orbit coupling*. Phys. Rev. B, **75**, 085305 (2007).

[47] J. Sköldberg, T. Löfwander, V. S. Shumeiko, and M. Fogelström. *Spectrum of Andreev Bound States in a Molecule Embedded Inside a Microwave-Excited Superconducting Junction*. Phys. Rev. Lett., **101**, 087002 (2008).

[48] L. Dell'Anna, A. Zazunov, and R. Egger. *Superconducting nonequilibrium transport through a weakly interacting quantum dot*. Phys. Rev. B, **77**, 104525 (2008).

[49] M. Governale, M. G. Pala, and J. König. *Real-time diagrammatic approach to transport through interacting quantum dots with normal and superconducting leads*. Phys. Rev. B, **77**, 134513 (2008).

[50] D. Futterer, M. Governale, M. G. Pala, and J. König. *Nonlocal Andreev transport through an interacting quantum dot*. Phys. Rev. B, **79**, 054505 (2009).

[51] R. de Sousa, K. B. Whaley, T. Hecht, J. von Delft, and F. K. Wilhelm. *Microscopic model of critical current noise in Josephson-junction qubits: Subgap resonances and Andreev bound states*. Phys. Rev. B, **80**, 094515 (2009).

[52] A. Zazunov, R. Egger, T. Jonckheere, and T. Martin. *Anomalous Josephson Current through a Spin-Orbit Coupled Quantum Dot*. Phys. Rev. Lett., **103**, 147004 (2009).

[53] A. Zazunov, A. Schulz, and R. Egger. *Josephson-Current-Induced Conformational Switching of a Molecular Quantum Dot*. Phys. Rev. Lett., **102**, 047002 (2009).

[54] T. Meng, S. Florens, and P. Simon. *Self-consistent description of Andreev bound states in Josephson quantum dot devices*. Phys. Rev. B, **79**, 224521 (2009).

[55] A. Zazunov, A. L. Yeyati, and R. Egger. *Josephson effect for SU(4) carbon-nanotube quantum dots*. Phys. Rev. B, **81**, 012502 (2010).

[56] D. J. Luitz and F. F. Assaad. *Weak-coupling continuous-time quantum Monte Carlo study of the single impurity and periodic Anderson models with s -wave superconducting baths*. Phys. Rev. B, **81**, 024509 (2010).

[57] R. Žitko, M. Lee, R. López, R. Aguado, and M.-S. Choi. *Josephson Current in Strongly Correlated Double Quantum Dots*. Phys. Rev. Lett., **105**, 116803 (2010).

[58] J. Eldridge, M. G. Pala, M. Governale, and J. König. *Superconducting proximity effect in interacting double-dot systems*. Phys. Rev. B, **82**, 184507 (2010).

[59] M. Lee, T. Jonckheere, and T. Martin. *Josephson effect through a multilevel quantum dot near a singlet-triplet transition*. Phys. Rev. B, **81**, 155114 (2010).

[60] J. S. Lim, R. López, and R. Aguado. *Josephson Current in Carbon Nanotubes with Spin-Orbit Interaction*. Phys. Rev. Lett., **107**, 196801 (2011).

[61] Y. Yamada, Y. Tanaka, and N. Kawakami. *Interplay of Kondo and superconducting correlations in the nonequilibrium Andreev transport through a quantum dot*. Phys. Rev. B, **84**, 075484 (2011).

[62] A. Martín-Rodero and A. Levy Yeyati. *The Andreev states of a superconducting quantum dot: mean field versus exact numerical results*. J. Phys.: Condens. Matter, **24**, 385303 (2012).

[63] I. A. Sadovskyy, G. B. Lesovik, G. Blatter, T. Jonckheere, and T. Martin. *Andreev quantum dot with several conducting channels*. Phys. Rev. B, **85**, 125442 (2012).

[64] S. Droste, S. Andergassen, and J. Splettstoesser. *Josephson current through interacting double quantum dots with spin-orbit coupling*. J. Phys.: Condens. Matter, **24**, 415301 (2012).

[65] J. Barański and T. Domański. *In-gap states of a quantum dot coupled between a normal and a superconducting lead*. J. Phys.: Condens. Matter, **25**, 435305 (2013).

[66] D. Futterer, J. Swiebodzinski, M. Governale, and J. König. *Renormalization effects in interacting quantum dots coupled to superconducting leads*. Phys. Rev. B, **87**, 014509 (2013).

[67] A. Brunetti, A. Zazunov, A. Kundu, and R. Egger. *Anomalous Josephson current, incipient time-reversal symmetry breaking, and Majorana bound states in interacting multilevel dots*. Phys. Rev. B, **88**, 144515 (2013).

[68] A. Koga. *Quantum Monte Carlo study of nonequilibrium transport through a quantum dot coupled to normal and superconducting leads*. Phys. Rev. B, **87**, 115409 (2013).

[69] A. Oguri, Y. Tanaka, and J. Bauer. *Interplay between Kondo and Andreev-Josephson effects in a quantum dot coupled to one normal and two superconducting leads*. Phys. Rev. B, **87**, 075432 (2013).

[70] T. Yokoyama, M. Eto, and Y. V. Nazarov. *Anomalous Josephson effect induced by spin-orbit interaction and Zeeman effect in semiconductor nanowires*. Phys. Rev. B, **89**, 195407 (2014).

[71] J. F. Rentrop, S. G. Jakobs, and V. Meden. *Nonequilibrium transport through a Josephson quantum dot*. Phys. Rev. B, **89**, 235110 (2014).

[72] R. Žitko, J. S. Lim, R. López, and R. Aguado. *Shiba states and zero-bias anomalies in the hybrid normal-superconductor Anderson model*. Phys. Rev. B, **91**, 045441 (2015).

[73] M. Žonda, V. Pokorný, V. Janiš, and T. Novotný. *Perturbation theory of a superconducting 0 - π impurity quantum phase transition*. Sci. Rep., **5**, 8821 (2015).

[74] G. Kiršanskas, M. Goldstein, K. Flensberg, L. I. Glazman, and J. Paaske. *Yu-Shiba-Rusinov states in phase-biased superconductor-quantum dot-superconductor junctions*. Phys. Rev. B, **92**, 235422 (2015).

[75] N. Wentzell, S. Florens, T. Meng, V. Meden, and S. Andergassen. *Magnetoelectric spectroscopy of Andreev bound states in Josephson quantum dots*. Phys. Rev. B, **94**, 085151 (2016).

[76] J. J. A. Baselmans, A. F. Morpurgo, B. J. van Wees, and T. M. Klapwijk. *Reversing the direction of the supercurrent in a controllable Josephson junction*. Nature, **397**, 43 (1999).

[77] A. Y. Kasumov, R. Deblock, M. Kociak, B. Reulet, H. Bouchiat, I. I. Khodos, Y. B. Gorbatov, V. T. Volkov, C. Journet, and M. Burghard. *Supercurrents Through Single-Walled Carbon Nanotubes*. Science, **284**, 1508 (1999).

[78] A. F. Morpurgo. *Gate-controlled superconducting proximity effect in carbon nanotubes*. Science, **286**, 263 (1999).

[79] M. R. Buitelaar, T. Nussbaumer, and C. Schönenberger. *Quantum Dot in the Kondo Regime Coupled to Superconductors*. Phys. Rev. Lett., **89**, 256801 (2002).

[80] M. R. Buitelaar, W. Belzig, T. Nussbaumer, B. Babić, C. Bruder, and C. Schönenberger. *Multiple Andreev Reflections in a Carbon Nanotube Quantum Dot*. Phys. Rev. Lett., **91**, 057005 (2003).

[81] A. Kasumov, M. Kociak, M. Ferrier, R. Deblock, S. Guéron, B. Reulet, I. Khodos, O. Stéphan, and H. Bouchiat. *Quantum transport through carbon nanotubes: Proximity-induced and intrinsic superconductivity*. Phys. Rev. B, **68**, 214521 (2003).

[82] J. A. van Dam, Y. V. Nazarov, E. P. A. M. Bakkers, S. de Franceschi, and L. P. Kouwenhoven. *Supercurrent reversal in quantum dots*. Nature, **442**, 667 (2006).

[83] J.-P. Cleuziou, W. Wernsdorfer, V. Bouchiat, T. Ondarçuhu, and M. Monthioux. *Carbon nanotube superconducting quantum interference device*. Nat. Nanotechnol., **1**, 53 (2006).

[84] P. Jarillo-Herrero, J. A. van Dam, and L. P. Kouwenhoven. *Quantum supercurrent transistors in carbon nanotubes*. Nature, **439**, 953 (2006).

[85] H. I. Jørgensen, K. Grove-Rasmussen, T. Novotný, K. Flensberg, and P. E. Lindelof. *Electron Transport in Single-Wall Carbon Nanotube Weak Links in the Fabry-Perot Regime*. Phys. Rev. Lett., **96**, 207003 (2006).

[86] H. I. Jørgensen, T. Novotný, K. Grove-Rasmussen, K. Flensberg, and P. E. Lindelof. *Critical Current 0-π Transition in Designed Josephson Quantum Dot Junctions*. Nano Lett., **7**, 2441 (2007).

[87] C. Buizert, A. Oiwa, K. Shibata, K. Hirakawa, and S. Tarucha. *Kondo Universal Scaling for a Quantum Dot Coupled to Superconducting Leads*. Phys. Rev. Lett., **99**, 136806 (2007).

[88] T. Sand-Jespersen, J. Paaske, B. M. Andersen, K. Grove-Rasmussen, H. I. Jørgensen, M. Aagesen, C. B. Sørensen, P. E. Lindelof, K. Flensberg, and J. Nygård. *Kondo-Enhanced Andreev Tunneling in InAs Nanowire Quantum Dots*. Phys. Rev. Lett., **99**, 126603 (2007).

[89] K. Grove-Rasmussen, H. Ingerslev Jørgensen, and P. E. Lindelof. *Kondo resonance enhanced supercurrent in single wall carbon nanotube Josephson junctions*. New J. Phys., **9**, 124 (2007).

[90] A. Eichler, M. Weiss, S. Oberholzer, C. Schönenberger, A. Levy Yeyati, J. C. Cuevas, and A. Martín-Rodero. *Even-Odd Effect in Andreev Transport through a Carbon Nanotube Quantum Dot*. Phys. Rev. Lett., **99**, 126602 (2007).

[91] M. Lee, T. Jonckheere, and T. Martin. *Josephson Effect through an Isotropic Magnetic Molecule*. Phys. Rev. Lett., **101**, 146804 (2008).

[92] A. Eichler, R. Deblock, M. Weiss, C. Karrasch, V. Meden, C. Schönenberger, and H. Bouchiat. *Tuning the Josephson current in carbon nanotubes with the Kondo effect*. Phys. Rev. B, **79**, 161407 (2009).

[93] H. I. Jørgensen, K. Grove-Rasmussen, K. Flensberg, and P. E. Lindelof. *Critical and excess current through an open quantum dot: Temperature and magnetic-field dependence*. Phys. Rev. B, **79**, 155441 (2009).

[94] L. Hofstetter, S. Csonka, J. Nygård, and C. Schönenberger. *Cooper pair splitter realized in a two-quantum-dot Y-junction*. Nature, **461**, 960 (2009).

[95] S. de Franceschi, L. Kouwenhoven, C. Schönenberger, and W. Wernsdorfer. *Hybrid superconductor-quantum dot devices*. Nat. Nanotechnol., **5**, 703 (2010).

[96] J.-D. Pillet, C. H. L. Quay, P. Morfin, C. Bena, A. L. Yeyati, and P. Joyez. *Andreev bound states in supercurrent-carrying carbon nanotubes revealed*. Nat. Phys., **6**, 965 (2010).

[97] L. G. Herrmann, F. Portier, P. Roche, A. L. Yeyati, T. Kontos, and C. Strunk. *Carbon Nanotubes as Cooper-Pair Beam Splitters*. Phys. Rev. Lett., **104**, 026801 (2010).

[98] K. J. Franke, G. Schulze, and J. I. Pascual. *Competition of Superconducting Phenomena and Kondo Screening at the Nanoscale*. Science, **332**, 940 (2011).

[99] R. Maurand, T. Meng, E. Bonet, S. Florens, L. Marty, and W. Wernsdorfer. *First-Order 0-π Quantum Phase Transition in the Kondo Regime of a Superconducting Carbon-Nanotube Quantum Dot*. Phys. Rev. X, **2**, 011009 (2012).

[100] C. Ryu, P. W. Blackburn, A. A. Blinova, and M. G. Boshier. *Experimental Realization of Josephson Junctions for an Atom SQUID*. Phys. Rev. Lett., **111**, 205301 (2013).

[101] J. Bauer, J. I. Pascual, and K. J. Franke. *Microscopic resolution of the interplay of Kondo screening and superconducting pairing: Mn-phthalocyanine molecules adsorbed on superconducting Pb(111)*. Phys. Rev. B, **87**, 075125 (2013).

[102] J.-D. Pillet, P. Joyez, R. Žitko, and M. F. Goffman. *Tunneling spectroscopy of a single quantum dot coupled to a superconductor: From Kondo ridge to Andreev bound states*. Phys. Rev. B, **88**, 045101 (2013).

[103] L. Bretheau, Ç. Ö. Girit, C. Urbina, D. Esteve, and H. Pothier. *Supercurrent Spectroscopy of Andreev States*. Phys. Rev. X, **3**, 041034 (2013).

[104] L. Bretheau, Ç. Ö. Girit, H. Pothier, D. Esteve, and C. Urbina. *Exciting Andreev pairs in a superconducting atomic contact*. Nature, **499**, 312 (2013).

[105] B.-K. Kim, Y.-H. Ahn, J.-J. Kim, M.-S. Choi, M.-H. Bae, K. Kang, J. S. Lim, R. López, and N. Kim. *Transport Measurement of Andreev Bound States in a Kondo-Correlated Quantum Dot*. Phys. Rev. Lett., **110**, 076803 (2013).

[106] W. Chang, V. E. Manucharyan, T. S. Jespersen, J. Nygård, and C. M. Marcus. *Tunneling Spectroscopy of Quasiparticle Bound States in a Spinful Josephson Junction*. Phys. Rev. Lett., **110**, 217005 (2013).

[107] A. Kumar, M. Gaim, D. Steininger, A. L. Yeyati, A. Martín-Rodero, A. K. Hüttel, and C. Strunk. *Temperature dependence of Andreev spectra in a superconducting carbon nanotube quantum dot*. Phys. Rev. B, **89**, 075428 (2014).

[108] S. Abay, D. Persson, H. Nilsson, F. Wu, H. Q. Xu, M. Fogelström, V. Shumeiko, and P. Delsing. *Charge transport in InAs nanowire Josephson junctions*. Phys. Rev. B, **89**, 214508 (2014).

[109] J. Schindele, A. Baumgartner, R. Maurand, M. Weiss, and C. Schönenberger. *Nonlocal spectroscopy of Andreev bound states*. Phys. Rev. B, **89**, 045422 (2014).

[110] E. J. H. Lee, X. Jiang, M. Houzet, R. Aguado, C. M. Lieber, and S. de Franceschi. *Spin-resolved Andreev levels and parity crossings in hybrid superconductor-semiconductor nanostructures*. Nat. Nanotechnol., **9**, 79 (2014).

[111] Y. Makhlin, G. Schön, and A. Shnirman. *Quantum-state engineering with Josephson-junction devices*. Rev. Mod. Phys, **73**, 357 (2001).

[112] T. Meng. Diploma Thesis - Universität Karlsruhe (2009).

[113] M. Kinza, J. Ortloff, J. Bauer, and C. Honerkamp. *Alternative functional renormalization group approach to the single impurity Anderson model*. Phys. Rev. B, **87**, 035111 (2013).

[114] M. Kinza and C. Honerkamp. *Two-particle correlations in a functional renormalization group scheme using a dynamical mean-field theory approach*. Phys. Rev. B, **88**, 195136 (2013).

[115] A. Rançon. *Nonperturbative renormalization group approach to quantum XY spin models*. Phys. Rev. B, **89**, 214418 (2014).

[116] J. Reuther and R. Thomale. *Cluster functional renormalization group*. Phys. Rev. B, **89**, 024412 (2014).

[117] S. Pairault, D. Sénéchal, and A.-M. S. Tremblay. *Strong-Coupling Expansion for the Hubbard Model*. Phys. Rev. Lett., **80**, 5389 (1998).

[118] A. N. Rubtsov, M. I. Katsnelson, and A. I. Lichtenstein. *Dual fermion approach to nonlocal correlations in the Hubbard model*. Phys. Rev. B, **77**, 033101 (2008).

[119] S. Brener, H. Hafermann, A. N. Rubtsov, M. I. Katsnelson, and A. I. Lichtenstein. *Dual fermion approach to susceptibility of correlated lattice fermions*. Phys. Rev. B, **77**, 195105 (2008).

[120] H. Hafermann, S. Brener, A. N. Rubtsov, M. I. Katsnelson, and A. I. Lichtenstein. *Cluster dual fermion approach to nonlocal correlations*. JETP Lett., **86**, 677 (2008).

[121] H. Hafermann, G. Li, A. N. Rubtsov, M. I. Katsnelson, A. I. Lichtenstein, and H. Monien. *Efficient Perturbation Theory for Quantum Lattice Models*. Phys. Rev. Lett., **102**, 206401 (2009).

[122] A. N. Rubtsov, M. I. Katsnelson, A. I. Lichtenstein, and A. Georges. *Dual fermion approach to the two-dimensional Hubbard model: Antiferromagnetic fluctuations and Fermi arcs*. Phys. Rev. B, **79**, 045133 (2009).

[123] S.-X. Yang, H. Fotso, H. Hafermann, K.-M. Tam, J. Moreno, T. Pruschke, and M. Jarrell. *Dual fermion dynamical cluster approach for strongly correlated systems*. Phys. Rev. B, **84**, 155106 (2011).

[124] A. A. Katanin. *The effect of six-point one-particle reducible local interactions in the dual fermion approach*. J. Phys. A: Math. Theor., **46**, 045002 (2013).

[125] S. Kirchner, F. Zamani, and E. Muñoz. *Nonlinear Thermoelectric Response of Quantum Dots: Renormalized Dual Fermions Out of Equilibrium*, 129 (2013).

[126] E. Muñoz, C. J. Bolech, and S. Kirchner. *Universal Out-of-Equilibrium Transport in Kondo-Correlated Quantum Dots: Renormalized Dual Fermions on the Keldysh Contour*. Phys. Rev. Lett., **110**, 016601 (2013).

[127] A. E. Antipov, E. Gull, and S. Kirchner. *Critical Exponents of Strongly Correlated Fermion Systems from Diagrammatic Multiscale Methods*. Phys. Rev. Lett., **112**, 226401 (2014).

[128] W. Metzner and D. Vollhardt. *Correlated lattice fermions in $d = \infty$ dimensions*. Phys. Rev. Lett., **62**, 324 (1989).

[129] A. Georges, G. Kotliar, W. Krauth, and M. J. Rozenberg. *Dynamical mean-field theory of strongly correlated fermion systems and the limit of infinite dimensions*. Rev. Mod. Phys., **68**, 13 (1996).

[130] G. Kotliar and D. Vollhardt. *Strongly Correlated Materials: Insights From Dynamical Mean-Field Theory*. Physics Today, **57**, 53 (2004).

[131] G. Rohringer, A. Toschi, A. Katanin, and K. Held. *Critical Properties of the Half-Filled Hubbard Model in Three Dimensions*. Phys. Rev. Lett., **107**, 256402 (2011).

[132] G. Rohringer, A. Valli, and A. Toschi. *Local electronic correlation at the two-particle level*. Phys. Rev. B, **86**, 125114 (2012).

[133] T. Schäfer, G. Rohringer, O. Gunnarsson, S. Ciuchi, G. Sangiovanni, and A. Toschi. *Divergent Precursors of the Mott-Hubbard Transition at the Two-Particle Level*. Phys. Rev. Lett., **110**, 246405 (2013).

[134] C. Karrasch, A. Oguri, and V. Meden. *Josephson current through a single Anderson impurity coupled to BCS leads*. Phys. Rev. B, **77**, 024517 (2008).

[135] C. D. Dominicis and P. C. Martin. *Stationary entropy principle and renormalization in normal and superfluid systems. i. algebraic formulation*. J. Math. Phys., **5**, 14 (1964).

[136] C. D. Dominicis and P. C. Martin. *Stationary entropy principle and renormalization in normal and superfluid systems. ii. diagrammatic formulation*. J. Math. Phys., **5**, 31 (1964).

[137] A. Toschi, A. A. Katanin, and K. Held. *Dynamical vertex approximation: A step beyond dynamical mean-field theory*. Phys. Rev. B, **75**, 045118 (2007).

[138] A. A. Katanin, A. Toschi, and K. Held. *Comparing pertinent effects of antiferromagnetic fluctuations in the two- and three-dimensional Hubbard model*. Phys. Rev. B, **80**, 075104 (2009).

[139] T. Schäfer, F. Geles, D. Rost, G. Rohringer, E. Arrigoni, K. Held, N. Blümer, M. Aichhorn, and A. Toschi. *Fate of the false Mott-Hubbard transition in two dimensions*. Phys. Rev. B, **91**, 125109 (2015).

[140] A. Valli, T. Schäfer, P. Thunström, G. Rohringer, S. Andergassen, G. Sangiovanni, K. Held, and A. Toschi. *Dynamical vertex approximation in its parquet implementation: Application to Hubbard nanorings*. Phys. Rev. B, **91**, 115115 (2015).

[141] G. Li. *Hidden physics in the dual-fermion approach: A special case of a nonlocal expansion scheme*. Phys. Rev. B, **91**, 165134 (2015).

[142] C. Slezak, M. Jarrell, T. Maier, and J. Deisz. *Multi-scale extensions to quantum cluster methods for strongly correlated electron systems*. J. Phys. Condens. Matter, **21**, 435604 (2009).

[143] H. Kusunose. *Self-Consistent Fluctuation Theory for Strongly Correlated Electron Systems*. J. Phys. Soc. Jpn., **79**, 094707 (2010).

[144] A. N. Rubtsov, M. I. Katsnelson, and A. I. Lichtenstein. *Dual boson approach to collective excitations in correlated fermionic systems*. Ann. Phys., **327**, 1320 (2012).

[145] G. Rohringer, A. Toschi, H. Hafermann, K. Held, V. I. Anisimov, and A. A. Katanin. *One-particle irreducible functional approach: A route to diagrammatic extensions of the dynamical mean-field theory*. Phys. Rev. B, **88**, 115112 (2013).

[146] M. Kitatani, N. Tsuji, and H. Aoki. *FLEX+DMFT approach to the d -wave superconducting phase diagram of the two-dimensional Hubbard model*. Phys. Rev. B, **92**, 085104 (2015).

[147] T. Ayral and O. Parcollet. *Mott physics and spin fluctuations: A unified framework*. Phys. Rev. B, **92**, 115109 (2015).

[148] T. Ayral and O. Parcollet. *Mott physics and collective modes: An atomic approximation of the four-particle irreducible functional*. Phys. Rev. B, **94**, 075159 (2016).

[149] N. E. Bickers and D. J. Scalapino. *Conserving approximations for strongly fluctuating electron systems. I. Formalism and calculational approach*. Ann. Phys., **193**, 206 (1989).

[150] N. E. Bickers and S. R. White. *Conserving approximations for strongly fluctuating electron systems. II. Numerical results and parquet extension*. Phys. Rev. B, **43**, 8044 (1991).

[151] N. E. Bickers and D. J. Scalapino. *Critical behavior of electronic parquet solutions*. Phys. Rev. B, **46**, 8050 (1992).

[152] C.-X. Chen and N. E. Bickers. *Numerical solution of parquet equations for the Anderson impurity model*. Solid State Commun., **82**, 311 (1992).

[153] J. Luo and N. E. Bickers. *Self-consistent field studies of the negative-U Hubbard model*. Phys. Rev. B, **48**, 15983 (1993).

[154] P. Kleinert and H. Schlegel. *Parquet approximation for a disordered two-dimensional electron gas in a strong transverse magnetic field*. Physica A Statistical Mechanics and its Applications, **218**, 507 (1995).

[155] V. Janiš . *Stability of self-consistent solutions for the Hubbard model at intermediate and strong coupling*. Phys Rev. B, **60**, 11345 (1999).

[156] V. Janiš. *Parquet approach to nonlocal vertex functions and electrical conductivity of disordered electrons*. Phys Rev. B, **64**, 115115 (2001).

[157] D. Sénéchal, A.-M. S. Tremblay, and C. Bourbonnais. *Theoretical methods for strongly correlated electrons* (Springer, New York, 2004).

[158] V. Janiš and J. Kolorenč. *Mean-field theory of Anderson localization: Asymptotic solution in high spatial dimensions*. Phys Rev. B, **71**, 033103 (2005).

[159] V. Janiš and P. Augustinský. *Analytic impurity solver with Kondo strong-coupling asymptotics*. Phys Rev. B, **75**, 165108 (2007).

[160] V. Janiš and P. Augustinský. *Kondo behavior in the asymmetric Anderson model: Analytic approach*. Phys Rev. B, **77**, 085106 (2008).

[161] V. Janiš. *Integrability of the diffusion pole in the diagrammatic description of noninteracting electrons in a random potential*. J. Phys. Condens. Matter, **21**, 485501 (2009).

[162] S. X. Yang, H. Fotso, J. Liu, T. A. Maier, K. Tomko, E. F. D'Azevedo, R. T. Scalettar, T. Pruschke, and M. Jarrell. *Parquet approximation for the 4×4 Hubbard cluster*. Phys. Rev. E, **80**, 046706 (2009).

[163] P. Augustinský and V. Janiš. *Multiorbital simplified parquet equations for strongly correlated electrons*. Phys Rev. B, **83**, 035114 (2011).

[164] K.-M. Tam, H. Fotso, S.-X. Yang, T.-W. Lee, J. Moreno, J. Ramanujam, and M. Jarrell. *Solving the parquet equations for the Hubbard model beyond weak coupling*. Phys. Rev. E, **87**, 013311 (2013).

[165] G. Li, N. Wentzell, P. Pudleiner, P. Thunström, and K. Held. *Efficient implementation of the parquet equations: Role of the reducible vertex function and its kernel approximation*. Phys. Rev. B, **93**, 165103 (2016).

[166] N. Wentzell, G. Li, A. Tagliavini, C. Taranto, G. Rohringer, K. Held, A. Toschi, and S. Andergassen. *High-frequency asymptotics of the vertex function: diagrammatic parametrization and algorithmic implementation*. in preparation.

[167] S. Hummel. *Asymptotic behavior of two-particle vertex functions in dynamical mean-field theory*. Master's thesis, Vienna University of Technology (2014).

[168] O. Gunnarsson, T. Schäfer, J. P. F. LeBlanc, E. Gull, J. Merino, G. Sangiovanni, G. Rohringer, and A. Toschi. *Fluctuation Diagnostics of the Electron Self-Energy: Origin of the Pseudogap Physics*. Phys. Rev. Lett., **114**, 236402 (2015).

[169] A. A. Abrikosov. *Methods of Quantum Field Theory in Statistical Physics (Dover Books on Physics)* (Dover Publications, 1975), rev. english edition.

[170] G. Rohringer and A. Toschi. *Impact of nonlocal correlations over different energy scales: A dynamical vertex approximation study*. Phys. Rev. B, **94**, 125144 (2016).

[171] E. Kozik, M. Ferrero, and A. Georges. *Nonexistence of the Luttinger-Ward Functional and Misleading Convergence of Skeleton Diagrammatic Series for Hubbard-Like Models*. Phys. Rev. Lett., **114**, 156402 (2015).

[172] T. Schäfer, S. Ciuchi, M. Wallerberger, P. Thunström, O. Gunnarsson, G. Sangiovanni, G. Rohringer, and A. Toschi. *Non-perturbative landscape of the mott-hubbard transition: Multiple divergence lines around the critical endpoint*. arXiv:1606.03393 (2016).

[173] T. Ribic, G. Rohringer, and K. Held. *Nonlocal correlations and spectral properties of the Falicov-Kimball model*. Phys Rev. B, **93**, 195105 (2016).

[174] M. Salmhofer. *Renormalization: An Introduction (Theoretical and Mathematical Physics)* (Springer, Berlin and Heidelberg, 1999), corrected edition.

[175] C. Husemann and M. Salmhofer. *Efficient parametrization of the vertex function, Ω scheme, and the t,t′ Hubbard model at van Hove filling*. Phys. Rev. B, **79**, 195125 (2009).

[176] V. Janiš and V. Pokorný. *Critical metal-insulator transition and divergence in a two-particle irreducible vertex in disordered and interacting electron systems*. Phys. Rev. B, **90**, 045143 (2014).

[177] N. Bickers. *Self-consistent many-body theory for condensed matter systems*. In D. Sènèchal, A.-M. Tremblay, and C. Bourbonnais (editors), *Theoretical Methods for Strongly Correlated Electrons*, CRM Series in Mathematical Physics, 237–296 (Springer New York, 2004).

[178] G. Rohringer. *New routes towards a theoretical treatment of nonlocal electronic correlations*. Ph.D. thesis, Vienna University of Technology (2014).

[179] C. Karrasch and V. Meden. *Supercurrent and multiple singlet-doublet phase transitions of a quantum dot Josephson junction inside an Aharonov-Bohm ring*. Phys. Rev. B, **79**, 045110 (2009).

[180] C. Karrasch, S. Andergassen, and V. Meden. *Supercurrent through a multilevel quantum dot close to singlet-triplet degeneracy*. Phys. Rev. B, **84**, 134512 (2011).

[181] D. J. Luitz, F. F. Assaad, T. Novotný, C. Karrasch, and V. Meden. *Understanding the Josephson Current through a Kondo-Correlated Quantum Dot*. Phys. Rev. Lett., **108**, 227001 (2012).

Acknowledgments

This thesis would not have been possible without the support of many people.

First of all, I would like to express my deep gratitude to my supervisors Sabine and Alessandro for the excellent guidance during the time of my PhD. I benefited greatly from their deep physical understanding and their great intuition. While giving me a large freedom in my research choices, they encouraged my ideas and pointed me in the right direction when needed.

When I first arrived here in Vienna I felt warmly welcomed in the group of Frank Verstraete. Despite the lack of professional overlap, I really enjoyed the nice atmosphere and the numerous social activities. Thank you Valentin for introducing me to climbing, and for the fruitful discussions and advice on coding!

As Sabine moved to Tübingen for a full professorship, she and Alessandro arranged everything to allow me to finish my PhD here in Vienna, in the groups of Alessandro and Karsten. I am very thankful for the generous hospitality, and that you made this (complicated) arrangement possible! Here in the group, I felt welcomed from the very beginning and was amazed by the excellent working atmosphere and vast amount of experts around me.

I am incredibly thankful to have met Ciro, my close friend and colleague. Workwise you complemented me almost perfectly with your non-German style, and I will always miss having you as a desk-mate! We were there for each other in good an bad times, and I want to thank you for showing me again what real friendship can give you.

I want to thank you, Agnese, for being such a dear and loving friend and colleague. I will miss having you and your warm and open-minded attitude around me in the office. I will miss our perfect rice salads and the regular climbing sessions and conversations!

I want to further thank Gang, Thomas S., Patrick, Demetrio, Walter, Andreas, Georg, Thomas A. and Olivier for many fruitful discussions, that have surely had a strong influence on this thesis.

I want to also thank my other collaborators, Volker, Serge, Tobias and Andrey. It has been a pleasure working with you, and I hope for more fruitful collaborations in the future!

I thank Prof. Herbert Schoeller for his excellent and inspiring lectures on quantum theory in condensed matter, that were the pillars of most of my PhD work.

Last but not least I want to thank my parents, Rüdiger and Anja, for all the support during the years of my studies. You gave me valuable advice and encouraged me in my decisions, for which I am very thankful!

We acknowledge financial support from the Deutsche Forschungsgemeinschaft (DFG) through FOR 723, ZUK 63, SFB/TRR 21, and the Austrian Science Fund (FWF) within the Project F41 (SFB ViCoM).